CRANFIELD UNIVERSITY

J. HUTCHINGS

ADVANCING CLINICAL APPLICATION OF RAMAN SPECTROSCOPIC DIAGNOSIS OF OESOPHAGEAL PREMALIGNANCIES

CRANFIELD HEALTH

PhD. THESIS

CRANFIELD UNIVERSITY

CRANFIELD HEALTH

PhD. THESIS

Academic Year 2008-2009

J. HUTCHINGS

Advancing the clinical application of Raman spectroscopic diagnosis of oesophageal premalignancies

Supervisors: N. Stone, C. Kendall, H. Barr

January 2009

This thesis is submitted in partial fulfilment of the requirements for the degree of Doctor of Philosophy

Acknowledgements

Thank you to my friends and family for their unconditional support. My supervisors Dr. Nicholas Stone, Dr. Catherine Kendall and Prof. Hugh Barr deserve special thanks for their support, guidance and for encouraging me to be an independent scientist.

Abstract

Raman spectroscopy is a technique that utilises inelastic scattering processes to provide a biochemical fingerprint that has been shown to successfully discriminate oesophageal pathologies. The aim of this study was to develop Raman spectroscopy as a clinical tool; both *in vivo* for 'targeted biopsy', and in *ex vivo* for 'automated histopathology'.

Two different Raman probes were evaluated and compared and tissue classification models generated *ex vivo*. A preliminary classification model of a novel single collection fibre probe demonstrated potential for the probe design. Both probes were shown to discriminate three different oesophageal pathology groups. A cross-validated tissue classification model (88 samples) discriminated normal, Barrett's and neoplasia with an overall accuracy of 86.5% with a sensitivity of 83.3-89.5% and specificity of 89.2-97.1%. A novel rapid Raman mapping technique was evaluated. It was shown that sufficient biochemical information for pathology diagnosis could be extracted from low signal to noise ratio data using multivariate analysis providing the dataset was sufficiently large, thus demonstrating the feasibility of automated histopathology in a clinically realistic time frame. Furthermore, it was demonstrated that high spatial resolution imaging was not necessarily required for automated histopathology using novel interpretation of multivariate techniques. A tissue classification model generated from two rapid Raman maps containing separated substrate, normal, HGD, luminescence and fibrous connective tissue with an overall training performance of 97.5% Problems limiting clinical implementation of Raman techniques were investigated and methods of overcoming devised.

Contents

List of abbreviations

Adeno - Adenocarcinoma

ALA – Aminolevulinic acid

ANN – Artificial Neural Network

BO – Barrett's oesophagus

CCD – Charge coupled device

CM – Cardiac mucosa

DNA – Deoxyribonucleic acid

EMR – Endoscopic mucosal resection

FCT – Fibrous connective tissue

FM – Fundic mucosa

GI - Gastrointestinal

H&E – Haematoxylin and eosin

HGD – High grade dysplasia

IM – intestinal metaplasia

KMC – K-means clustering

LD (A) – Linear discriminant (analysis)

LGD – Low grade dysplasia

LIFE – Light induced fluorescence spectroscopy

NA – Numerical aperture

NIR – Near infra red

NSq – Normal squamous

OCT – Optical coherence tomography

PC (A) – Principal component (analysis)

PDT – Photodynamic therapy

RI – Refractive index

RS – Raman spectroscopy

SCC – Squamous cell carcinoma

SM – smooth muscle

SNR – Signal to noise ratio

SqDysp – Squamous dysplasia

UV – Ultraviolet

QE – Quantum efficiency

List of figures

List of tables

Chapter 1 Introduction

This thesis is concerned with the potential medical applications of Raman spectroscopy for pathology diagnosis, both *in vivo*, with the development and evaluation of Raman probes for endoscopic use and also *ex vivo*, for potential automated histopathology. The work follows on from previous work carried out within the Biophotonics Research Unit at Gloucestershire Royal NHS Foundation Trust.[1,2]

The thesis structure is set out such that a general overview of the clinical need is provided, focusing on the detection of oesophageal adenocarcinoma and premalignancies. This is followed by a review of optical technologies for pathology diagnosis and other competing technologies before introducing both Raman as the methodology of choice for both potential *in vivo* 'optical biopsy' using Raman probes and *ex vivo* 'automated histopathology' using Raman mapping. A review of the literature is included with applications in other fields and other disease sites. The methodology and results are split according to the *in vivo* and *ex vivo* studies, with a subsequent chapter covering general application issues common to both technologies. Following this is future work and a summary of conclusions.

This chapter introduces oesophageal cancer in general, the techniques currently used for diagnosing oesophageal cancer, the shortcomings of current techniques and how these can be overcome using novel optical technology which can detect early cancer. The chapter concludes with the aims of this research project.

1.1 Clinical motivation

1.1.1 Incidence of oesophageal cancer

The number of cases of oesophageal cancer is increasing (see Figure 1-1) whilst the prognosis for these patients remains poor. The reasons for this increase can not be pinpointed, although possible causes include genetic predisposition, dietary or

environmental changes. The oesophagus is lined with epithelial cells, of importance since 85-90% of all cancers originate in the epithelia. [3,4] Treatment of epithelial cancers (referred to as carcinomas), is easier and more successful when diagnosed at pre-invasive stages (before the cells penetrate the basement membrane),[3] using a range of possible techniques such as those discussed in Section 1.1.2.3. However, due to the nature of the disease, in many cases, the patient does not present until symptomatic, i.e. exhibiting dysphagia, which due to the elastic nature of the oesophagus, is only induced upon ~75% circumferential obstruction, at which point the cancer is usually advanced and often invasive.[5] At this late stage the outcome is poor. Five year survival figures range from 2-25%,[8] with Cancer Research UK quoting a figure of <10% (Figure 1-2).[6] The long term survival of patients with oesophageal cancer improves with early detection.

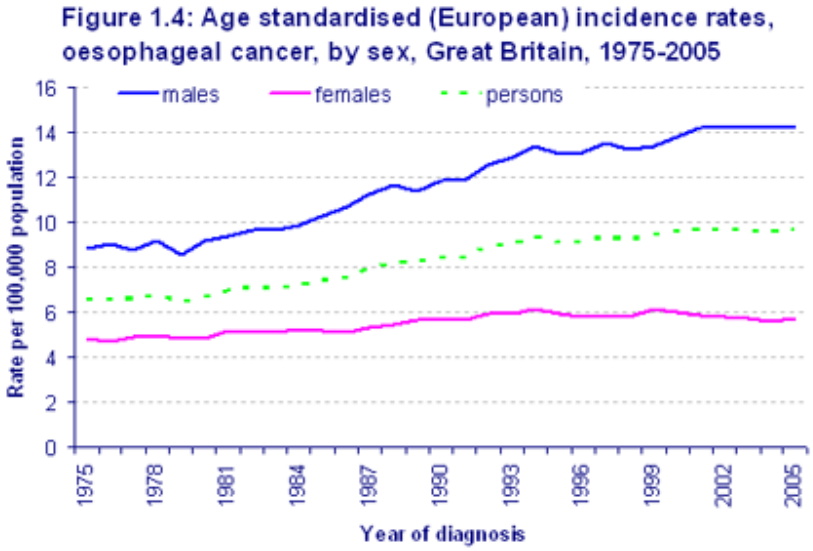

Figure 1-1 : Age-standardised incidence rates of oesophageal cancer[7]

In 2002 there were over 462,000 new cases of oesophageal cancer,[8] with over 7,400 cases in the UK in 2006.[9] Oesophageal cancer is more common in men than women[8] (see Figure 1-1). There are two types of oesophageal cancer. Squamous cell carcinomas (SCC) and adenocarcinomas (adeno). SCC originates in the squamous epithelial surface (with a pre cursor stage - squamous cell dysplasia), with risk factors associated to smoking and Helicobactor pylori infection.[5] This thesis concentrates on the second type

of cancer adenocarcinomas, which originate in the glandular or columnar epithelium. Adenocarcinoma, are of particular concern in the Western world since incidence of adenocarcinoma has increased to a level above that of SCC,[5] furthermore, the incidence of SCC has remained stable.[7]

Amongst other risk factors, there is a medical condition for which the chance of developing oesophageal cancer is increased called Barrett's oesophagus (BO), a condition caused by gastric acid reflux, where stomach and bile acids are regurgitated into the oesophagus causing irritation and inflammation, and eventually a metaplastic change.[8,10] BO is discussed further in Section 1.1.1.1.

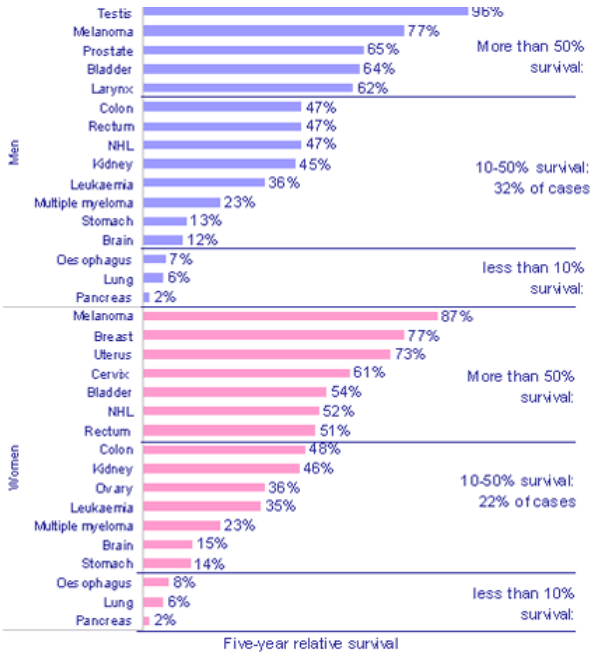

Figure 1-2: Five-year age-standardised relative survival (%), adults diagnosed 1996-1999, England and Wales by sex and site (Cancer Research UK, 2006[6])

1.1.1.1 Barrett's oesophagus (BO)

If an epithelial cell has been damaged the probability of malignant transformation is more likely. One example of this is where a cancer is formed on the basis of metaplasia, (pathological condition in which the normal mucosa is replaced by another type of mucosa) as in the case of Barrett's Oesophagus (BO), or often referred to as columnar-

line oesophagus (CLO). This is a condition in which acid reflux causes the lining of the oesophagus to undergo cellular changes characterised by the replacement of normal squamous epithelium by simple columnar epithelia as found in intestinal mucosa. This is referred to as a metaplastic change and is demonstrated in Figure 1-3, comparing normal and Barrett's oesophageal endoscope images. There are three different cell types associated with BO – fundic type mucosa (FM), cardiac mucosa (CM - junctional type mucosa) and intestinal metaplasia (IM - columnar epithelium with goblet cells).[11,12]

There is an increased risk of developing cancer of the oesophagus for patients with Barrett's oesophagus.[11] Carcinogenesis is not fully understood but is thought to follow the chain of intestinal metaplasia, low grade dysplasia (LGD), high grade dysplasia (HGD) leading to invasive cancer.[13,14,15]

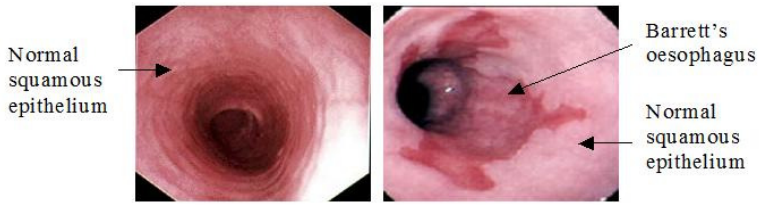

Figure 1-3: Endoscopic images of the oesophagus showing normal (left) and BO (right)[16]

1.1.1.2 Dysplasia

Dysplasia is a neoplastic epithelial change, which by the original definition by Riddell *et al.*[17], must be confined by the basement membrane of the originating gland.[11,14,18] The difference between normal and dysplastic cells is illustrated in Figure 1-4. Dysplastic cells are characterised by the following points:[3]

- Vary greatly in size and shape (pleomorphism), usually abnormally large
- Darkly stained nuclei (due to excessive chromatin)
- Abnormal mitosis may be observed
- Overall cell disorganisation
- Loss of cell maturation

Dysplasia is generally split into two categories, low and high grade dysplasia (LGD and HGD). For LGD, the changes are mild, with preservation of glandular structures/crypts.

Considering HGD, the cytological changes mentioned above are more severe, in particular more nuclear pleomorphism and hyperchroism compared to LGD.[11] These changes can be seen compared to BO in Figure 1-4.

Dysplastic cells are often described as having *malignant potential* since they always precede cancer, but do not always result in cancer. Goldblum refers to high grade dysplasia as a pre-invasive lesion of adenocarcinoma.[11] This increased risk of developing adenocarcinoma in patients with BO is reported as being in the range of 30% -120%.[3,19] There has been an increase in the number of patients diagnosed with BO and Barrett's dysplasia, but this may be explained by the increase in the number of patients undergoing endoscopy procedures and increased recognition of the condition.

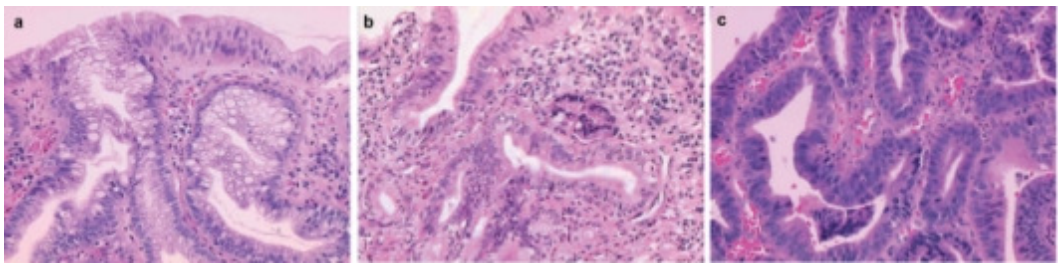

Figure 1-4: H&E comparison between a) Barrett's (IM with goblet cells), b) LGD and c) HGD[14]

Surveillance of dysplasia is considered as a vital step towards the prevention of cancer. However, surveillance using the biopsy techniques described below is hindered by the fact that dysplastic regions may be invisible to the practicing endoscopist.[3] As a result, there is significant risk that these areas can potentially be missed during random biopsy.

If oesophageal cancer or a pre-cancerous condition is diagnosed, the appropriate treatment can then be given. These treatment options are discussed in Section 1.1.2.3.

The histopathological analysis technique is currently the gold standard for diagnosing oesophageal cancer, although it has some drawbacks. These are discussed below.

1.1.2 Current diagnostic techniques

1.1.2.1 Diagnosis and surveillance using endoscopic biopsy

When a patient presents with symptoms they will undergo an endoscopic examination. A biopsy (usually several) is taken, sectioned, stained with haematoxylin and eosin (H&E) and then analysed in histopathology.

Currently, patients within certain risk categories, such as BO also undergo routine endoscopic surveillance in which biopsies are taken following a set protocol, such as the Seattle protocol in which quadrant biopsies are taken at 2 cm intervals over the length of the Barrett's region.[20,21] This biopsy process is invasive and there is a risk of infection and perforation at the biopsy site. However, it is reported that less than 10% of patients undergoing surveillance are actually diagnosed with cancer.[22] As a result there is debate as to the cost effectiveness of these surveillance programs but this is beyond the scope of this thesis. BO is confirmed by a biopsy which shows intestinal metaplasia (IM), characterised by goblet cells (also referred to as specialised mucosa).[14]

1.1.2.2 Disadvantages of endoscopic biopsy for diagnosing of oesophageal cancer

Since the biopsy samples need to be sent to histopathology for analysis, there is a delay associated with obtaining the diagnosis. This can be exacerbated by the fact that the pathologists are often required to analyse a large number of samples due to surveillance programs, many of which will not contain any neoplastic change.[23] Figure 1-5 shows the number of biopsy samples taken from one patient in a single endoscopy session.

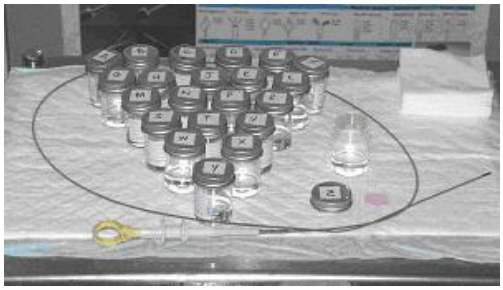

Figure 1-5 : Photograph showing the number of biopsies taken from one patient in a single endoscopy session

There is also a degree of uncertainty associated with the results since there are not strict boundaries between cell differentiation and despite comprehensive training for the histopathologist there is an element of subjectivity associated with the diagnosis. Studies have been done to assess inter and intra observer agreement, which is reportedly as low as 50% in some cases.[18] Similar results have also been demonstrated by Montgomery *et al.* who compared the opinions of twelve pathologists and Kendall *et al.* comparing the opinion of three expert pathologists, both using Kappa statistics to analyse the results.[1,24]

Furthermore, since the biopsy samples taken are small with respect to the size of the area under surveillance, there is a chance that the biopsy may miss an area of local disease even if a rigorous biopsy protocol is followed.[25] The biopsies are taken using endoscopic guidance, in which a live image of the oesophagus is viewed via the endoscope camera. Dysplastic changes may remain undiagnosed if they are not visible to the practicing endoscopist. Some protocols suggest the use of jumbo biopsy forceps to obtain larger samples, but these are still thought to miss unsuspected cancer in BO.[25] In one report by Dar *et al.*, in which patients with HGD were treated with a prophylactic oesophagectomy, 43-57% of patients were found to have undetected adenocarcinoma[26] showing that there is a need for better techniques for early diagnosis.

Ultrasound, magnification endoscopy, chromoendoscopy (a spray of Lugol's solution, which highlights glycogen depletion[27] and enhances visualisation of Barrett's[28] and inflammation) and narrow band imaging (NBI, in which improved contrast is achieved using filters are used to increase the relative amount of blue light in the image to emphasise superficial structures and blood vessels) are also used for diagnosis. The former has been reviewed by Kaffes *et al.* [29] and more recently Lennon *et al.*[30] and details of the latter techniques can be found in a recent review of imaging techniques for neoplastic changes in the oesophagus by Curvers *et al.*[31] They comment that these techniques are hindered by operator dependence, as found with the above mentioned histopathology.[31]

Alternative and adjunct methods of diagnosis are being explored. One technique investigated by Lao-Sirieix *et al.*, uses a sponge capsule which is swallowed and

retracted and samples the oesophageal epithelial surface as it is retracted[32]. However, the technique would still require cytology diagnosis, which again has the disadvantages of pathology diagnosis as described previously.

Optical diagnostic techniques such as Raman spectroscopy (RS), optical coherence tomography (OCT) and fluorescence are currently being investigated and have been shown to have potential for diagnosing many different medical conditions, in particular early cancer which will enable earlier diagnosis and hence more successful treatment. These techniques utilise lasers and other light sources to construct detailed images and obtain spectral information which can be used to determine the structure and biochemical makeup of the sample. Complex analytical techniques can be used to extract diagnostic information and hopefully remove the element of subjectivity associated with the diagnosis. The details of these techniques are discussed later in Section 1.2.

The majority of the work carried out using these optical techniques is being done *ex vivo*, in a laboratory based environment in which the techniques are compared to the current 'gold standard' histopathology result. These techniques could potentially complement the histopathology facilities, acting as a screening process to remove normal samples, thus reducing the workload on an overworked department or providing a virtual second opinion. The most significant application, however, would be the use of these techniques in a real clinical situation, *in vivo*. Currently, only a few studies have been carried out *in vivo*. This is mainly due to limitations of the equipment required, but as technological advances are made then the *in vivo* work is becoming possible. If the technology can be adapted in such a way as to make *in vivo* diagnosis possible, then the possible clinical impact would be significant. The reasons for this are summarized below.

1. **Reproducible objective results**
2. **Biochemical basis rather than morphology**
3. **Immediate diagnosis**
4. **Immediate treatment if required**

5. **Relatively non-invasive (potential for optical biopsy without tissue excision)**
6. **Potential to reduce costs**

*1.1.2.3 **Treatment options***

The treatment option will depend on the stage of disease, which is determined by the gold standard histopathology diagnosis, which as described previously is not a perfect gold standard. This serves as a reminder of the importance of the diagnostic decision and the need for improvements in diagnosis which can potentially be provided by optical techniques.

Palliative treatments of advanced cancer include stent insertion, laser ablation, and also chemo-radiotherapy.[33] Laser ablation can also be effective for the eradication of dysplasia although there is potentially a risk of perforation.[34,35]

For radical treatment, oesophagectomy (the complete removal of the oesophagus) has a high associated morbidity and mortality. However, it is still reported as being the gold standard treatment for HGD in patients with BO.[36] This is in part due to the high number of patients which are found to have invasive cancer retrospectively.[26,27] Chemotherapy and radiotherapy have a role in reducing the size of bulky tumours, which in turn makes complete resection easier.[33]

For dysplasia[37] and nodules, photodynamic therapy (PDT), endoscopic mucosal resection (EMR) and oesophagectomy are treatment options, as described by Barr *et al.*[13] An EMR is an endoscopic procedure which involves suction of the mucosa into a plastic cap which is then removed using a hot wire loop. It is being used increasingly to remove localised lesions.[20,38] For further details of treatment options, the reader is referred to the following reference.[39] Photodynamic therapy involves the administration of a drug (either topically or intravenously) which is activated by light, called a photosensitiser. The photosensitiser is excited to a metastable triple state, which produces highly unstable and reactive singlet oxygen as it returns to the ground state. The photosensitiser is preferentially retained by tumour cells (ratio of 2-3:1),[13] and

consequently the technique can be used to selectively target and destroy cells, although there is obviously a degree of damage to normal cells as well. PDT has also been shown to be a successful method of treating dysplasia.[35] PDT has also been shown to be a successful method of eradicating small tumours in patients for whom surgery is considered too risky.[40]

It is evident that the treatment options become less drastic and more successful for earlier lesions. This reiterates the need for earlier diagnosis using techniques such as optical spectroscopy. Prediction of progression to cancer would be a further potential benefit.

1.1.2.4 ***Genetic biomarkers***

Genetic instability is one of the characteristics of malignant progression and genetic biomarkers are an active area of research. The details of this are beyond the scope of this report, but further details can be found in the following references.[41,42]

A biomarker is defined as a characteristic that is measured/evaluated that is indicative of a given pathology process or therapeutic response.[41] Considering malignant progression, a biomarker would be required to be detectable at the premalignant stage and subsequently vary throughout the neoplastic transformation. Several tissue biomarkers have been evaluated, the main example being p53, a protein that controls transcription of other proteins responsible for regulating cell proliferation.[43] Further biomarkers are under investigation.[44] Tissue biomarkers can potentially provide information regarding the risk of progression, and although there are some studies which report correlation with carcinogenesis, the genetic pathway is so complex that it is difficult to isolate specific mutations or protein expressions and to date they are generally unreliable.[45]

To summarise, there are inadequacies with current diagnostic methods and suggested alternatives such as novel endoscopic imaging techniques and genetic biomarkers have not delivered to date and alternative reproducible and objective methods of diagnosis are required.

1.2 Introduction to optical diagnostic techniques

Optical diagnostic techniques have shown considerable promise as alternatives and adjuncts to current diagnostic techniques.

1.2.1 Interactions between light and tissue

When optical radiation interacts with matter different effects occur, including reflection, scatter (elastic scattering and inelastic scattering), absorption and autofluorescence. These effects, illustrated in Figure 1-6 are utilised in the following optical diagnostic techniques.

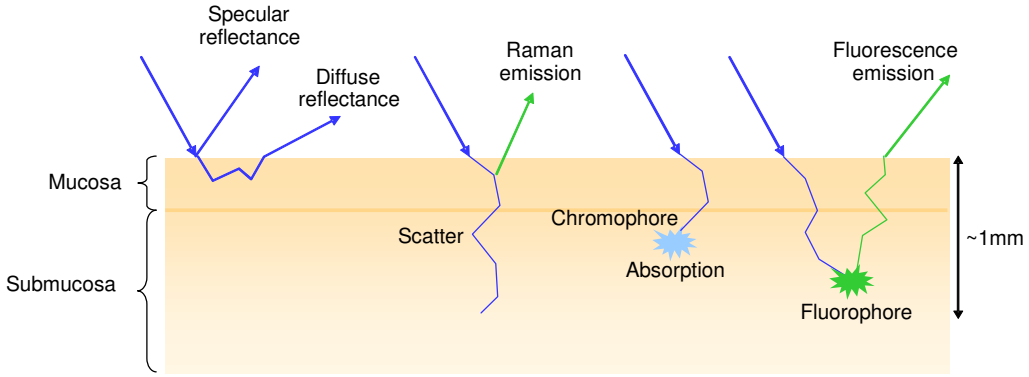

Figure 1-6: Illustration of different interactions of light with tissue

1.2.2 Light scattering spectroscopy (LSS)

This is a technique which utilises backscattered photons which have the same wavelength (elastically scattered) as the incident light to obtain morphological information about a tissue sample. Singly scattered photons provide information relating to the surface (epithelial) morphology, whilst multiple scattered photons (diffuse reflectance) provide morphological information regarding deeper stromal tissue. The technique is capable of detecting precancerous changes such as "nuclear size" and "degree of pleomorphism" (cellular atypia).[20,46] Morphological changes associated with dysplastic changes have been detected in several studies.[20,47,48,49] Recently, Dhar *et al.* have reported a larger study of 45 patients (483 spectra from 138 sites) with PCA-fed LDA classification of normal hyperplastic and dysplastic polyps and adenocarcinoma

with good sensitivity and specificity (77-85%).[50] Similar promising results have been reported by Lovat *et al*. in a cross validated multivariate model.[51]

The disadvantage of LSS is that it only probes the morphology of the tissue and not the biochemical changes, and also there is a limited sampling volume. However, the technology is simple and inexpensive making it a possible tool for *in vivo* diagnosis, or multimodal techniques.

1.2.3 Raman spectroscopy

The Raman effect was first described in 1928 was discovered by Chandrasekhara Venkata Raman, for which he was awarded the Nobel Prize in 1930.[52] The Raman effect, is an inelastic scattering process in which there is an energy exchange between light and matter which occurs when incident light causes molecular bonds to vibrate. Raman scattering is a relatively inefficient process with approximately one in a million scattered photons undergoing Raman scatter in tissue at visible wavelengths.[53]

The spectrum of scattered light (a plot of the scattered light intensity against the change in frequency with respect to the incident light) can be used to investigate matter since the characteristic peaks caused by the molecular vibrations are specific to each molecular species so the spectrum effectively provides a biochemical fingerprint. Examples of different biochemical constituents in tissue can be seen in Figure 1-7.

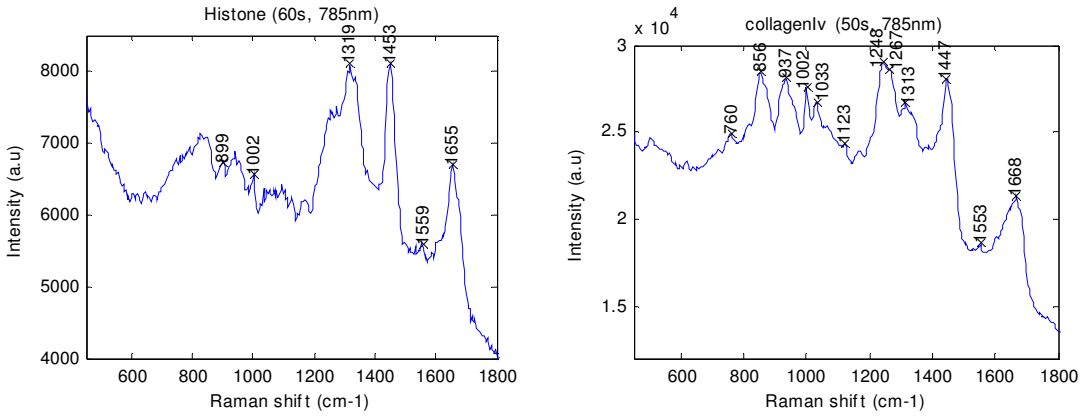

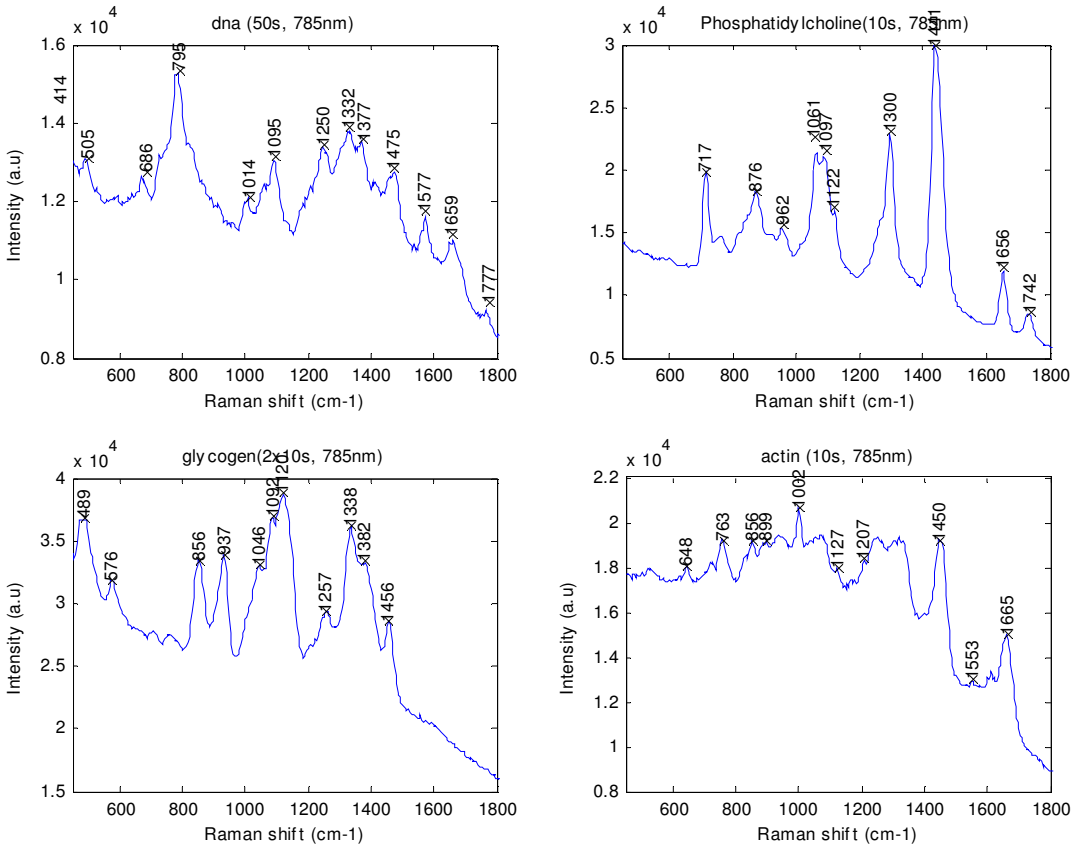

Figure 1-7: Raman spectra from biochemical standards acquired using a 785 nm excitation and x50 Leica objective, 10 s acquisition time – a) Histone - is a protein constituent of chromatin (DNA, RNA and protein which form chromosomes), b)collagen – fibrous protein which forms the extra-cellular matrix of connective tissue c) d)deoxyribonucleic acid (DNA), d) phosphotidylcholine (a phospholipid) - one of the major constituents of cell membranes, consisting of a glycerol molecule with a phosphate and nitrogen molecule attached to the third hydroxyl group e) glycogen, the major energy (carbohydrate) storage form in the body, is a branched polysaccharide (with glucose subunit), f) actin – a contractile protein is a constituent of microfilaments which are the main constituent of the cytoskeleton[3]

As mentioned previously, the peaks are characteristic of different molecular vibrations and these are labelled in the figure and can be assigned to different molecular bonds and more generally to biochemical constituents. These can be found in most biochemical constituents of tissue in varying concentrations. Some of the Raman peaks associated with the main constituents in tissue are listed below in Table 1-1. A more

comprehensive list can be seen in Appendix A. Furthermore, since the relative contributions of these peaks within the spectrum are proportional to the abundance of that constituent, [54] the entire spectrum can be utilised to obtain quantitative information making Raman spectroscopy potentially a powerful tool for diagnosis and tissue analysis.

Table 1-1: Typical biochemical constituents in oesophageal tissue and associated Raman peaks assignments from the literature and biochemical standards measured from Sigma Aldrich (above)*

	cm^{-1}
Glycogen	481-489, 576, 853-856, 937, 1046-1048, 1083-1092, 1123, 1256, 1377-1382, 1455
Protein	760, 876, 937, 1001, 1034, 1240, 1329, 1458, 1655
DNA	624, 682, 770-795, 925, 1016, 1095, 1250, 1332, 1577
Phenyl ring (breathing mode)	1001
O-P-O (DNA backbone)	785, 1090
CH_2 twisting	1299-1320
CH_2, CH_3 bending (Amide III)	1450
C=C stretch (Amide I)	1653-1658

*Peak assigments obtained from the literature and measurements above [55,56,57,58]

Raman can be used via fibre optics for *in vivo* applications[54] and also *ex vivo* in mapping studies, providing imaging of tissue sections.[59] As Raman spectroscopy is the main modality utilised within this study further details of instrumentation for Raman spectroscopy and a review of the literature are discussed in Chapter 2.

There are also other applications of Raman spectroscopy techniques including Coherent anti-Stokes Raman scattering (CARS) spectroscopy,[60] which can be used for accurate optical sectioning, and surface enhanced Raman scattering (SERS)[61] spectroscopy utilises the local electric field (surface plasmon) between noble metal particles to enhance Raman signal to an extent where the technique is capable of detecting single molecules.[62] Currently the techniques are limited to research applications, although there is the potential for fluorescence labelled dyes used in so called resonant SERS or

SERRS which could potentially have an application of genotyping *in vivo* or for histopathology.[63,64,65]

As described previously, light is scattered within turbid media. From each scattering event there is a possibility of Raman scatter. This has led to the development of techniques for obtaining Raman molecular information from deep within tissue. Depth resolution is achieved using both lateral spatial offset between excitation and detection (Spatially Offset Raman Spectroscopy (SORS)) and time gating of the collection of Raman scattered photons (Kerr gated Raman Spectroscopy).[66,67] These techniques have been applied *ex vivo* to detect deep calcifications in a breast tissue phantom,[68,69] and to detect subsurface bone.[70]

1.2.4 Infrared (IR) absorption spectroscopy

Infrared absorption spectroscopy is a technique which is commonly used as a research tool for biochemical investigations for biomedical applications.[71,72] Mid-infrared spectroscopy is a similar spectroscopic technique to Raman, but the technique utilises absorption of mid-IR radiation (not from a monochromatic source as with Raman) rather than scattering to probe vibrational molecular information. Mid-IR absorption spectroscopy is complimentary to Raman since each are sensitive to different functional groups with IR being more sensitive to polar bonds including C=O, C-O, O-H and C-H.

Detection methods do not need to be as sensitive as Raman since the signal is greater than Raman scatter and signal to noise ratio of spectra is greater, but in general there are fewer spectral peaks compared to Raman.[73] Imaging methods are also much more rapid than Raman mapping techniques. Mid-IR absorption spectroscopy, is however, hindered by water absorption which prevents (or limits) *in vivo* applications.

Considering applications on oesophageal tissue, Wang *et al*. have carried out studies of oesophageal tissues including comparison of normal and cancerous tissue,[74] as have Maziak *et al*. in a more recent study.[75] In the latter study, Maziak *et al*. reported biochemical differences in normal compared to malignant oesophageal tissue including increased nuclear to cytoplasmic ratio, a relative increase and decrease in DNA and

RNA respectively and a relative decrease in glycogen, all of which are consistent with expected biochemical changes.[3,5] More subtle biochemical changes including the structural protein changes (which results in subtle changes in the peak position/shape) and accumulation of triglycerides were also noted.

More recently, Wang *et al*. have also published a larger and more detailed FTIR study (using ATR) of premalignant (dysplastic) oesophageal tissues using partial least squares to estimate changes in biochemical constituents and LDA for tissue classification.[76] In this study they reported that dysplastic mucosa could be detected with an overall accuracy of 89% (sensitivity 92% and specificity 80%).

FTIR imaging is an established technique and there have been many applications using FTIR to detect cancer in other tissues including the skin,[77,78] cervix,[79] prostate,[80,81] brain[82,83] and breast.[84]

1.2.5 Autofluorescence

Fluorescence occurs when fluorophores in tissue are excited upon the irradiation of short wavelength light (often blue or UV). The wavelength of the emitted fluorescence is greater than that of the incident light. Since different tissues have varying biochemical constituents, different tissue types contain different naturally occurring fluorophores and this concept was first used for cancer detection by Alfano *et al*. in 1984.[85] Since then fluorescence has been widely used for both spectroscopic and imaging applications.[86]

Panjehpour *et al*. reported application of fluorescence spectroscopy for detecting cancer in the oesophagus, and initial results (from 26 cancer and 108 normal spectra) were promising and resulted in a model with a sensitivity and specificity of 100% and 98% respectively.[87] Subsequent studies have all been hindered by false-positives.[88,89] Similarly, fluorescence imaging is also hindered by false positives.[31,90]

*1.2.5.1 **Induced Fluorescence***

Photosensitisers (refer to Section 1.1.2.3), such as 5-aminolevulinic acid (ALA) can be administered to the patient, either locally (in the form of a spray or topical cream) or

systemically. These are found to localise in areas of rapid cell division, such as dysplastic regions and cancers, which can provide enhanced fluorescent signal in these areas. In one study of 47 patients, a difference was noted in the sensitivity and specificity between the two methods, although there were small numbers of patients in each group, with an increased sensitivity to the recognition of dysplastic lesions using systemic administration (80-100%) compared to only 60% when a photosensitising spray was applied.[91] A specificity of 70% was reported for the photosensitising spray, whilst poor specificity (26% and 56%) was reported for the systemic photosensitiser, which has been attributed to the presence of inflammatory cells.

1.2.6 Optical coherence tomography (OCT)

OCT is a technique analogous to ultrasound, but using light, to produce real time, high resolution (10-25microns) cross sectional images first presented by Fercher in 1990,[92] and subsequently published by Hitzenberger,[93] and a fibre optic based system by Huang *et al.*[94]. Biological examples of OCT are discussed in the review by Wong Kee Song.[90] OCT can be used to look at the morphology of tissue samples and has been used for *in vivo* imaging. This has become routine in ophthalmology applications, but is still experimental elsewhere. OCT is sensitive to small differences in tissue refractive index (RI). It may be possible to obtain a diagnosis from the image alone, although, this process, unless computer automated, will be subjective, however, it has the potential for *in vivo*[95] and even time gated use.[96] OCT has also been used in combination with other techniques such as Raman to provide a multimodal approach for diagnosis as described in Section 1.2.7.

Many groups have investigated the use of OCT in the oesophagus.[95,97] It is reported that BO can be detected, however, there have been problems detecting dysplasia.[90,95] More recently, intramucosal carcinoma and HGD have been distinguished from LGD and IM by Evans *et al*. with a sensitivity and specificity of 83% and 75%, respectively.[98] OCT is hindered by the fact that image analysis is subjective, and in a discussion of OCT for detecting dysplasia, Poneros concludes that further work is needed and eventually computer automation will be required.[99] Automation of OCT image analysis is one

possibility.[100] Further details of the advancing field of OCT can be found in many review articles.[101]

1.2.7 Multimodal optical diagnosis

As mentioned previously, these various techniques can be combined to provide a multimodal technique.

Several groups have applied this multimodal approach to diagnosis in the upper gastrointestinal tract, for example, near infrared (NIR) auto-fluorescence and LSS were recently combined to identify dysplastic oesophageal lesions by Leiber *et al*., in an *ex vivo* study on biopsy samples harvested from 20 patients. In this study, a classification model was developed to discriminate between low risk (Barrett's mucosa without dysplasia and other benign samples) and high risk (LGD, HGD, squamous cell carcinoma (SCC) and adenocarcinoma) with a sensitivity and specificity of 86% and 96% respectively.[102]

Considering Raman in particular, Huang *et al*., illustrated that the most effective diagnostic algorithms were those developed using a combination of Raman and NIR autofluorescence spectroscopy.[103] Patil *et al*. used OCT guided Raman for measuring breast tissue *ex vivo* and skin *in vivo*.[104]

*1.2.7.1 **Summary of optical diagnostic techniques***

Optical spectroscopic techniques provide the most suitable solution to one of the limiting factors of histology, since the spectroscopic information lends itself to computer automation using tissue classification models. Other techniques such as OCT and autofluorescence imaging are still vulnerable to subjectivity and inter and intra operator variability. To summarise, the above mentioned spectroscopic techniques each have advantages and disadvantages:

- LSS is simple, but provides only morphological information.

- Raman can provide detailed biochemical information, providing high molecular specificity, but interactions are weak. However, recent technological advances have meant this is no longer such a limiting factor.
- FTIR is an established spectroscopic technique for probing biochemical changes in tissue sections, but it is limited by water absorption and as a result is not suitable for *in vivo* use.
- Fluorescence spectroscopy (and imaging) may be useful for targeting biopsy but is hindered by false positives.
- OCT results are promising, but it is likely to have a place for image guided targeting rather than definitive diagnosis.

Automated diagnosis based on biochemistry rather than morphology is advantageous and furthermore, biochemical changes are likely to occur prior to morphological changes which provide the opportunity of detecting disease before it is visible to the eye. It is also suggested that standard H&E diagnosis underestimates the extent of intestinal features in BO,[105] which may potentially be visible/detected using optical techniques. Considering the sampling volumes, Raman also samples the surface epithelial layer which lends itself to detecting precancerous changes in the surface epithelium *in vivo*. As mentioned previously, IR spectroscopy is limited by water absorption, and as a result sample thickness is limited to ~10 μm. Wani *et al.* identified Raman spectroscopy as a potential modality for overcoming problems associated with 'blind biopsy'.[15] Overall, Raman appears to be the modality of choice since the technique can be used both *in vivo* for optical biopsy and also *ex vivo* for imaging.

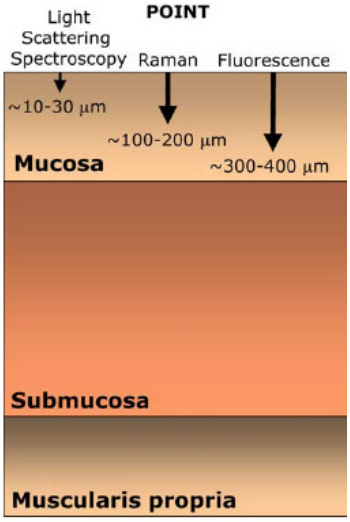

Figure 1-8: Illustration of the sampling depths of different optical diagnostic techniques (adapted from[21])

1.3 Project aims and objectives

The study outlined in this thesis has concentrated on evaluating Raman spectroscopy as a potential tool for pathology diagnosis both as an optical tool for targeted biopsy *in vivo* and also as a laboratory aid to the histopathologist. The research addresses key areas which will hopefully move Raman diagnostic techniques towards implementation in the clinical environment. The process of carcinogenesis of oesophageal adenocarcinoma is used as a typical example of an epithelial cancer. There are three aims of the study:

1) To evaluate and develop Raman probes for potential *in vivo* pathology diagnosis - referred to as 'Raman targeted biopsy'

- To evaluate the current leading fibre optic (which is no longer available commercially) Raman probe by generating a large tissue classification model *ex vivo* (Section 5.3-5.5).
- To compare novel probe designs to the current leading Raman probe using tissue equivalent phantoms, calibration standards and tissue classification models (Sections 5.2 and 5.7).

2) To evaluate the potential application of rapid Raman mapping techniques as a potential adjunct to the histopathologist by providing automated Raman histopathology

- To evaluate a novel rapid Raman mapping technique for imaging biological tissue sections and compare to previous technology (Section 6.1- 6.2).
- To investigate the feasibility of clinical implementation of rapid Raman mapping by investigating overall mapping times and mapping parameters (Section 6.4).
- To evaluate the application of rapid Raman mapping technique as a potential research tool for the elucidation of biochemical changes associated with carcinogenesis (Section 6.5).

3) To evaluate and overcome factors which limit implementation of Raman diagnostic techniques (optical biopsy and automated histopathology) into the clinical environment

This work was undertaken within the Biophotonics Research Unit based at Gloucestershire Royal NHS Foundation Trust, UK under the supervision of Dr. N. Stone, Dr. C. Kendall, Prof. H. Barr.

Chapter 2 Raman Spectroscopy

2.1 Raman theory

Raman spectroscopy is a technique used to study vibrational and rotational modes in a system. It is based on the inelastic scattering, or Raman scattering of monochromatic light, resulting in the energy of the scattered photons gaining or losing energy (to or from the interacting molecules). This gives information regarding the system under investigation and enables biochemical changes within the tissue to be probed.

When a sample is illuminated with a laser beam, several processes take place, as mentioned previously, including elastic (Rayleigh) and inelastic (Raman) scatter. The Rayleigh scattered light is filtered out (laser line filter), and the remaining light is dispersed onto a detector, most commonly a charge coupled device (CCD).

Raman scattering is very weak, typically 10^{-6} of the elastically scattered light. The intensity of the Raman scattered light is proportional to the intensity of the input light (I_{in}), the density of the Raman scattering molecules (ρ), the sampling volume (V) and the Raman cross-section (σ), according to Equation 2-1.

$$I_{out} \propto I_{in}\, \rho\, V\, \sigma$$

Equation 2-1

The Raman cross-section describes how likely it is that a photon will interact due to local electric fields. It is wavelength dependent. The density of the sample describes the concentration of scattering molecules within the sampling volume. A photon interaction is more likely for higher concentrations.

The Raman shift is given by the difference in energy of the incident and scattered photons (related to the frequency according to Energy=hν, where h is Planck's constant and ν is frequency) respectively. The Raman shift is often described in terms of wavenumber (cm^{-1}).

The vibrational energy is eventually dissipated as heat, although this is not measurable within the sample.

2.1.1 Classical Raman model

The intensity of Raman bands can be described using a simple classical model. An induced dipole moment, P is proportional to the external electric field, E. The constant of proportionality, α, is called the polarizability and describes how easily the electronic cloud around a molecule can be distorted.

$$P=\alpha E$$

Equation 2-2

The induced dipole will emit elastically scattered light at the same frequency as the incident light. However, specific vibrations within some molecules can alter the polarizability of a molecule during the vibration (described by the polarizability derivative $\delta\alpha/\delta Q$, where Q is the normal coordinate of the vibration). Raman scattering can only occur by an internal conversion of energy in the molecules during this process. It follows, that the selection rule for a Raman active vibration, is that there must be a change in the polarizability, i.e. $\delta\alpha/\delta Q\neq 0$. The Raman selection rule is analogous to that of an infrared-active vibration which states that during vibration there must be a net change in the permanent dipole. If a molecule is symmetric then it follows that there will not be a net change in the permanent dipole and hence symmetric molecules will be silent in the infrared region.

Raman scattered photons may be of lower or higher energy than the incident photon and this is referred to as Stokes and anti-Stokes scatter respectively, as illustrated in Figure

2-1. This depends on the temperature, since anti-Stokes scatter occurs when the initial state of molecule is excited (either thermally or by other means). At room temperature, anti-Stokes scatter is weak with respect to Stokes scatter.

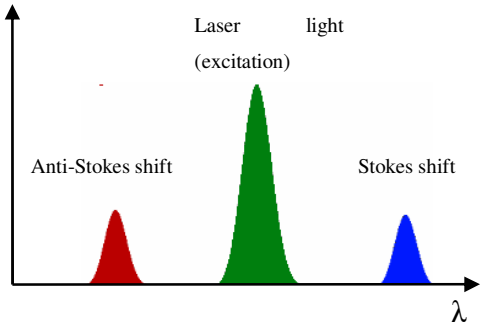

Figure 2-1: Illustration of the Stokes and anti-Stokes shift in wavelength (λ) compared to the excitation wavelength

If the vibration greatly affects the polarizability then the polarizability derivative will be large and the intensity of the Raman band will be high and vice versa. For example, in a highly polar bond such as O-H, induced polarisation due to an external electric field will be less than the larger electron cloud of the C=C double bond which is evenly distributed and easily distorted. The intensity of the Raman scatter also increases with the fourth power of the incident radiation frequency and as discussed later, this affects the choice of wavelength selected. However, the benefits of using a shorter wavelength are counteracted by possible damage to the sample, penetration depth and also fluorescence effects.

2.1.2 Quantum mechanical model

Whilst the classical explanation views the scattering process as a perturbation of the molecule's electric field, in the quantum mechanical model the scattering is described by the excitation to a virtual energy state followed almost immediately by de-excitation and a change in vibrational energy with a timescale in the order of picoseconds. The molecule can only gain or lose energy equal to the energy difference between two allowed energy states. Elastic and Raman scatter are illustrated in Figure 2-2. In the case

of elastic scatter, the scattered photon has the same energy as the incident photon and returns to the original energy state. In the case of Raman scatter, the scattered photon has more or less energy than the incident photon, referred to as anti-Stokes and Stokes scatter respectively.

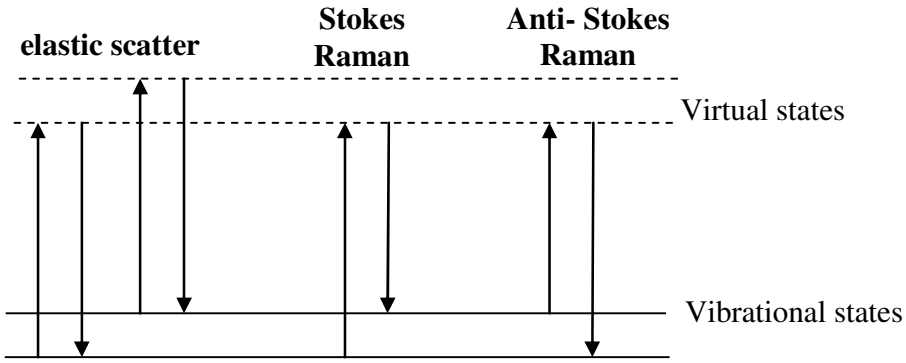

Figure 2-2: Quantum mechanical illustration of elastic and Raman scatter

2.2 History of the medical applications of Raman spectroscopy

The first interpretable biological application of Raman spectroscopy was performed by Lord *et al*. on a native protein in 1970,[106] using a He-Ne (633nm) laser. However, the use of light in the visible spectrum is limited because of the high fluorescence background from biological tissues. Some complex tissue matrices exhibit low fluorescence and visible excitation was still feasible, for example in the eye.[107] Despite background subtraction techniques, the fluorescence is the limiting factor in the visible region. For excitation in UV region, the fluorescence occurs at wavelengths beyond the Raman fingerprint region and furthermore, an increase in the signal due to resonance within the electronic transitions. However, there are problems associated with mutagenesis of biological tissue samples and the penetration depth is very small (μm). Over time there was a trend toward the near-infrared (NIR) region since there is a significant reduction in fluorescence and an increased penetration depth as discussed in a review by Hanlon *et al*.[54] Furthermore, Stone demonstrated 830 nm was optimum for Raman spectroscopic investigations of oesophageal tissues. [108]

The use of Raman confocal microscopy systems to obtain increased spatial resolution (only for a small well defined volume) has been investigated for examples on deoxyribonucleic acid (DNA) in chromosomes.[109] For more detail on confocal Raman microscopy, the reader is referred to Turrel *et al.*[110] Confocal microscopy has also been used to study subtle changes in cholesterol, phospholipids and proteins in complex tissues such as the lens cataracts.[111]

Initially studies using Raman employed Fourier transform (FT) spectrometers. In general, these were used in conjunction with Nd:YAG laser excitation (1064nm) and cooled InGaAs detectors. FT Raman systems use interferometric methods to collect all wavelengths simultaneously, also allowing a greater light collection. Early use revealed spectral peaks that were previously masked by the large fluorescence background.[112] Initial work applying Raman spectroscopy to investigate the biochemical changes associated with carcinogenesis in gynaecological lesions showed that diseased tissue could be distinguished from normal.[113] Other applications in the field of cancer diagnosis included brain tumours[114] and skin lesions.[115,116] However, the detectors used were noisy and required long spectral acquisition times (30-60minutes) Also, the laser powers required (0.5-1W) exceed maximum permissible exposure (MPE) limits for the eye and skin.

The development of low noise charge coupled device (CCD) detector technology, the use of dispersion rather than interference methods,[117,118] and the advent of small, efficient semiconductor laser sources have all contributed to the rapid advances in Raman spectroscopy.

The advent of edge and notch filters are one of the most important additions to the modern Raman spectrometer since they efficiently reject elastically scattered and stray light and have enabled more compact spectrometer designs.[117]

Studies have shown that working in the NIR region, and in particular the 800-830nm region, minimises florescence whilst utilizing the CCD to its full potential.[3,54,108,119] The

fluorescence continues to reduce at greater wavelengths, but this is counteracted by the fact that the efficiency of the CCD detector falls sharply with increased wavelength.[3]

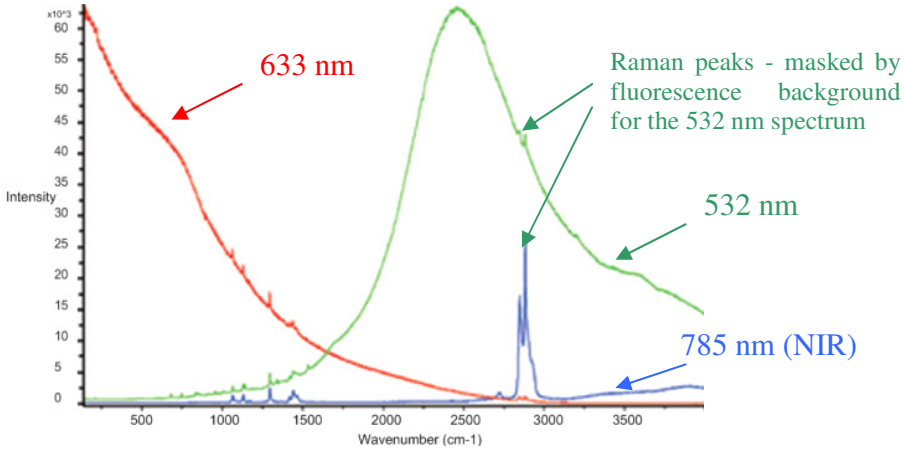

Figure 2-3: Raman spectra acquired using green (532 nm), red (633 nm) and NIR (785 nm) excitation. The fluorescence background masks the Raman peak in the red and green spectra whilst it is clearly visible in the NIR spectra. Note that the NIR wavelength is represented by the blue spectrum.[120]

There have been many biological applications of Raman spectroscopy for different pre-cancer and cancers including the oesophagus,[1,2,108,121,122,123,124] cervix,[125,126] prostate,[127] bladder,[128,155] brain,[114,128] breast[129,130,131] oral cavity,[132] larynx,[133,134] and stomach.[135] These applications are covered in many review articles.[54,73,136,137] There are also applications in other diseases besides cancer including atherosclerotic plaques[138] and dementia.[139] Several fibre optic probes have been proposed for *in vivo* applications, for use on the skin and gynaecological applications during colposcopy.[140] The first endoscopic *in vivo* use of Raman spectroscopy of human gastrointestinal tissue was reported in 2000 by Shim *et al.*[141] also detailed in a thorough review.[54]

The following sections review applications of Raman in the upper gastrointestinal tract. This is followed by instrumentation common to both Raman probes and laboratory based spectrometers. A review of both the practical considerations and applications of Raman probes for potential targeted biopsy (Section 2.3.4 and 2.4.2) and Raman mapping applications (Section 2.5) is also included.

2.2.1 Raman studies in the upper gastrointestinal tract

Locally, several studies have been carried out *ex vivo* using a customised laboratory based Raman microscopy system.[1,2,108,121,122,123] In one study carried out by Kendall *et al.*, 87 histopathologically homogeneous samples were taken from 44 patients.[1] Cross validated PCA fed LDA tissue classification models were generated to separate both three, and nine different pathology groups. The multivariate classification model developed gave sensitivities of 73-100% and specificities of 90-100%. Additional potentially useful tissue groups are discussed in the results section including, amongst others, fibrous connective tissue and smooth muscle. An important advance in these studies was that for the first time, a consensus histopathology opinion was obtained from three independent expert pathologists.[1,121,122] This partially overcomes the problem that the pathology is subjective, and improves the histopathology opinion as a 'gold standard'. This concept was used in this thesis to improve the robustness of the tissue classification models (Section 5.2). Kendall *et al.* used attributed peak assignments to biochemical constituents to support the Raman classification model, for example a decrease in glycogen levels consistent with increased proliferation,[5] increase in nucleic acids and decrease in carotenoids.[1] Further investigation of the biochemical changes using Raman mapping has supported this.[123]

2.3 Raman instrumentation and practical considerations

2.3.1 Modern Raman system components

A typical Raman microscopy system is shown in Figure 2-4, a schematic diagram of the customised Renishaw Raman spectroscopy system (System 1000, Renishaw Plc. Wotton-under-edge, UK). The individual components are described in further detail in the following sections. A cylindrical lens can be added into the path of the laser resulting in a line focussed laser beam. This has practical uses which are described in Section 2.5.2.

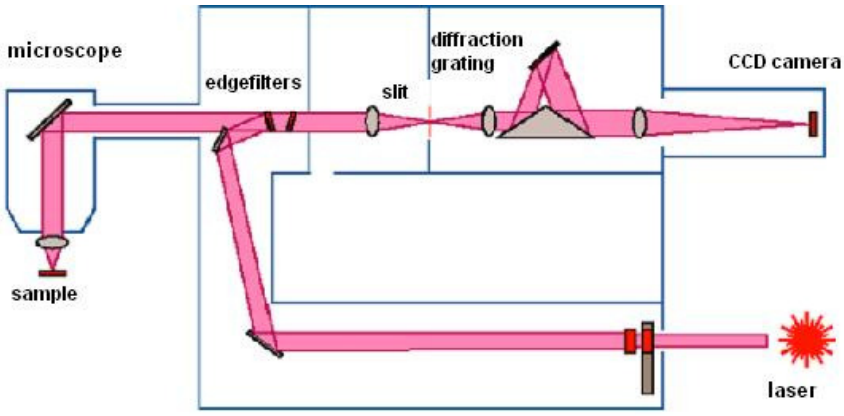

Figure 2-4: schematic diagram of the standard Raman microscopy system (Renishaw System 1000)

2.3.1.1 ***Laser***

The laser light is delivered to the system via two adjustable steering mirrors. The wavelength selection is important and as mentioned previously, there has been a general trend towards NIR wavelengths. Locally, 830nm has been shown to be optimum with reduced tissue fluorescence, whilst still working within the optimum region for the CCD.

2.3.1.2 ***Microscope***

A typical Raman microscopy system is shown in Figure 2-5, showing the microscope on the left and the spectrometer on the right. The laser is hidden behind the spectrometer. The internal components of the spectrometer were shown previously in Figure 2-4. A microscope is used to view the sample, illuminate the sample at the target volume and collect the scattered light. The collection of scattered light depends on the numerical aperture of the objective which is given by NA = sinθ. (where θ is half of the angular aperture). It also depends on the spot size, for a smaller spot size there is greater intensity of light within a smaller region, but consequently the sample volume and hence the number of molecules within it is smaller.

2.3.1.3 ***Filters, slit and gratings***

Holographic notch filter or edge filters are used to separate the Raman signal from the elastic scatter.[3] Following transmission through the edge filter, the collected beam then passes through the slit, which reduces the divergent components of the beam. Although this limits the amount of light passing through, it improves the spectral resolution. The diffraction grating disperses the light into its spectral components and disperses the light onto the detector. Multiple elements of the detector can be used to detect a range of wavelengths simultaneously. The grating density (locally this is 300 lines/mm) affects the spectral resolution. The angle of the grating determines which region of the spectral range is detected. The grating can also be moved during the spectral acquisition, referred to as a dynamic scan, to cover a wider spectral range whilst maintaining high spectral resolution, the trade off being that spectral acquisition are slower. The latter points have practical implications for Raman spectroscopic analysis since this will need to span the spectral range of interest and this is investigated in Section 6.1.2.

Figure 2-5: Photograph of the Renishaw System 1000

2.3.1.4 ***CCD camera***

A CCD is made up of an array of small detectors (~25 μm). The CCD can be rapidly read out by transferring charge from one detector element to the next in sequence. There are two main types of CCD in use for Raman spectroscopy, back thinned and deep depletion CCDs. Back thinned devices suffer from etaloning, and deep depletion CCDs are favourable for NIR applications.[117]

Calibration ensures that the correct wavelength is detected by the correct CCD element. One of the problems hindering the clinical development of Raman spectroscopy is a reliable calibration routine such that the measurements are reproducible and also comparable with spectra taken from another Raman system. This is especially important when building spectra libraries.[142]

2.3.2 Sources of noise and signal to noise ratio (SNR)

Signal to noise ratio (SNR) is related to the intensity of the incident light. It is proportional to the square of the intensity multiplied by the acquisition time, thus if the intensity is increased the collection time can be reduced to achieve the same SNR and vice versa.[143] The signal is limited by shot noise, arising due to the random quantum nature of photon interactions. It is given by $N \pm \sqrt{N}$ where N is the number of counts. Increasing the number of counts reduces the relative effect of shot noise, provided the Raman signal is greater than any background signal.

Dark noise is minimal with modern CCD detectors. Cooling the CCD reduces the number of counts generated by thermal effects. Temperature stabilization is also important and the effects of temperature on Raman spectrometers are investigated in Section 7.2.2. Cosmic rays also cause large spikes which can have a significant effect on the spectrum if not averaged out or removed (manually or using automated algorithms). This has particular implications for Raman mapping as discussed in Chapter 6.

Many groups have investigated the impact of SNR on Raman spectral analysis.[144,145,146] This is discussed further in Section 6.3, since this aspect has particular importance for rapid Raman mapping applications. De Paula *et al*. studies the use of Raman spectroscopy for identification of atherosclerotic plaques, using mathematically added noise they investigated the effect of SNR on subsequent multivariate classification. They concluded that short acquisition times, as low as 20ms, could be used to distinguish calcified, atherosclerotic and non-pathological plaques.[144] However, in this study, spectral features were very visibly different (due to strong Raman signatures for inherent calcification and lipids) and as a result the limit of PCA and other multivariate techniques was not tested.[144]

2.3.3 Spatial and spectral resolution

Resolution is defined as the ability to separate two distinct objects. Considering spectral resolution, this is the ability to resolve separated Raman peaks (in the wavenumber direction). Overlapping Raman bands makes this issue complex and derivative spectra are often calculated to highlight shoulder of Raman bands.

Spatial resolution has been investigated by many groups for Raman probe (lateral and axial)[147] and spectral mapping applications for both Raman,[148] and IR.[149,150] Bhargava has published a thorough evaluation of FTIR imaging for histology diagnosis, demonstrating the effects of imaging parameters (similar to those used for Raman mapping (see Section 2.5) in particular spatial resolution (with the step size used as a nominal spatial resolution, determined by binning data acquired at 6.25µm to larger pixels 10-50µm) and SNR (random Gaussian noised artificially added to the spectra).[150] The aim of this study is not to determine spatial resolution for Raman probe and mapping applications, however, concepts are discussed later regarding the implications for clinical histology.

2.3.4 Raman probes

Light is transmitted through fibre optics via total internal reflection. For visible wavelengths, glass or plastic fibres can be used with a similar material with a lower refractive index chosen for the cladding. However, as the wavelength approaches the IR region silica and silica doped material are used as the core and cladding respectively. The obvious problem with this is that silica is Raman active and this can cause problems when performing Raman probe spectroscopy. [151,152] Fluorescence and optical properties of other materials used to construct the probe also need to be considered, for example optically transparent glues should be used.[151]

For *in vivo* measurements in the oesophagus, a front viewing fibre is not ideal, and De Lima *et al*. report a side viewing probe suitable for fluorescence applications and have since reported on a catheter based Raman probe with manoeuvrable tip.[153]

2.3.4.1 ***Limitations of Raman Probes***

The weak Raman signal, makes rapid *in vivo* Raman diagnosis via endoscopy technically challenging. Fluorescence and Raman backgrounds are generated by the probe itself, which can mask Raman signals and contribute to shot noise. This results in subtle differences in probe spectra which require sophisticated multivariate statistical techniques.[141,151]

Scatter within the probe and optical fibres causes a background signal that must be removed using background subtraction techniques such as that discussed in Section 2.3.4.2, or by using an appropriate filter positioned at the distal probe tip, however, this is technically difficult due to the intricacies and precision required since the filters are often angular dependent.

A further problem for *in vivo* studies is the possibility of spectral artefacts caused by angle and pressure changes, however this has been investigated and analysed by PCA and found to be insignificant.[141]

2.3.4.2 ***Removing probe background and fluorescence***

The broad background spectrum is due to tissue and fibre optic autofluorescence, cross talk and backscatter.[147,154] In the literature, probe background is generally removed using a 5th order polynomial fit (for 785nm and 830nm Raman probes) to reveal narrow Raman peaks from the tissue,[133,141,155,156] however the particular fit used is dependent on the wavelength, filtering and spectrometer.

The probe background can also be removed by subtraction of a background signal. The background signal may be acquired, for example, with the probe covered by a black plastic cap,[125] or from roughened aluminium.[157] In the latter case, Boere *et al*. reported an angular dependence of the background signal, which was accounted for in the vector subtraction method.[157] Shim *et al* reported that subtraction using such methods was inconsistent.[147]

In summary, there are discrepancies regarding the source of the background signal and furthermore, background subtraction methods are unreliable, resulting in the need for alternative methods of dealing with background subtraction.

2.3.4.3 ***Safety concerns***

As mentioned previously, the power of the laser and its effect on the tissue is one of the limitations for probe design *in vivo* and consequently, the focus on probe design is to maximise the collected Raman signal and to utilise optimal data processing.[151]

At NIR wavelengths, thermal damage is possible, however, more importantly, DNA strand breaks can occur in the UV region and hence this should be avoided. Tests have been carried out to assess the temperature rise in tissue caused by NIR lasers light. A 250mW, 830nm laser focused to a spot size of 500 µm spot size did not produce a detectable temperature rise in tissue (<0.8ºC) after an exposure time of 1 minute.[141] In another study by Mahadevan-Jansen *et al*., using a laser with power of 15 mW (785nm) at the probe tip and a spot size of 900 µm, it was calculated that this power produced an increase in temperature of 1.5 ºC in 5 minutes, insufficient to cause cytotoxicity. It is also suggested that powers up to 80 mW could be used, which would cause a calculated temperature rise in cervix tissue of 6 ºC/min, enabling a reduced acquisition time of 15-20 s.[140] This reduction in acquisition time would be more clinically useful since multiple point measurements could be made. Ideally, this should be reduced further to 1-2s, and recent reports in the literature suggest this is feasible.[158] Further more it is later shown in this study that providing large spectra database is used multivariate techniques can tolerate poor signal to noise.

Considering the probe system used in this study, similar to that used by Shim *et al*., with an output power of used <80 mW at the probe tip and an exposure time of 1 minute, no thermal damage would result,[141] especially *in vivo* as perfusion of blood would reduce any temperature rise further. Studies are also carried out within this report to investigate the effect of reducing acquisition times and the effect this has on tissue classification models (Section 6.3).

2.3.5 Raman probe details

To provide some history, to date the main probe used for biological applications is the Visionex probe (Enviva, Visionex Inc, Atlanta, Georgia, USA), since this was the only commercially available probe suitable for passing down an endoscope channel. However, production of the Visionex probe (see Figure 2-6) ceased before work on this thesis commenced. Several groups have been investigating alternative designs, such as the Emvision (also shown in Figure 2-6) and also some larger probes for skin applications which are not suitable for endoscopic use.[160] The Visionex and Emvision probes are described in subsequent sections. Details of the novel single out-put fibre probe are confidential and as a result are not described, but for the proposes of this study this is not of significance and it is sufficient to consider the probe as a single out-put fibre whilst the other probes utilise multi-fibre collection.

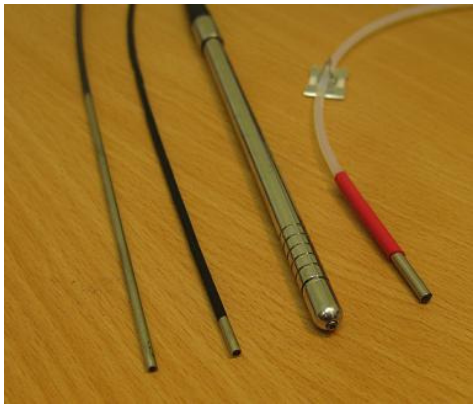

Figure 2-6: Photograph of a selection of Raman probes. From left to right: Emvision probe (830 nm), Visionex (785 nm), Visionex in a removable rigid casing (830 nm) and a novel single output fibre probe

2.3.5.1 The Visionex and Emvision probes

The Visionex probe consists of a central excitation fibre of 400µm diameter which is surrounded by seven 300 µm diameter bevelled collection fibres to maximize collection efficiency (see Figure 2-7). The angle of the bevelled fibres is described by the gaser level (5 and 10) for the Visionex probes. The higher the gaser level the smaller the sampling depth, i.e. the greater the degree of 'beam steering'.[147] The probe fibres have a numerical aperture of 0.22. A band pass filter is incorporated approximately 2.5cm from

the tip in line with the excitation fibre and a long pass filter in line with the collection fibers.[147] The probe (Figure 2-7), is approximately 2mm in diameter and can pass down the biopsy channel of an endoscope. The probe reportedly samples to a depth of 500 μm and a tissue volume of 1 mm^3 for the gaser level 10 probes.[56,155]

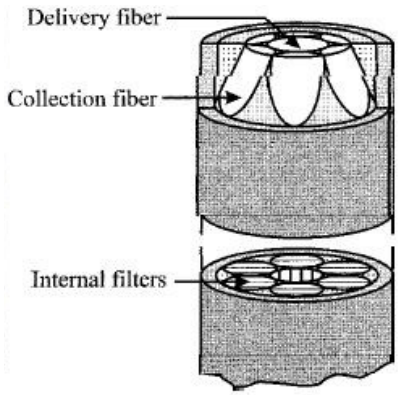

Figure 2-7: Photograph of Visionex probe and illustration of tip[56]

Two different Raman probe designs are shown in Figure 2-8, which illustrates the reduction in sampling volume for a bevelled fibre probe, which is advantageous for detecting precancerous changes in the surface epithelial layers. The Emvision probe (Figure 2-8), manufactured by Eric Marple is effectively a gaser level 0 probe, i.e. with no beam steering. Other probes are being investigated by other groups and these are discussed in the following section.

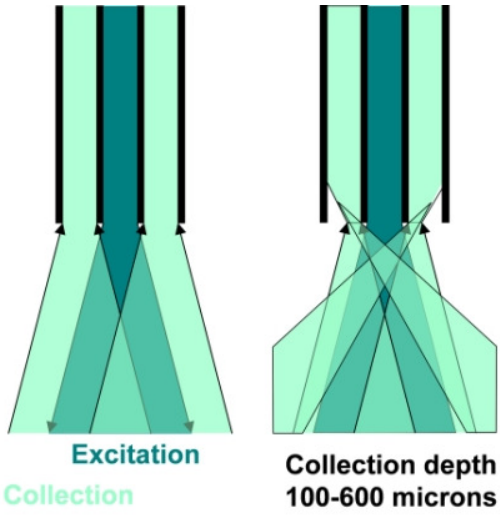

Figure 2-8: left) Schematic diagrams of the two different Raman probe designs illustrating the excitation and collection regions for an unbevelled fibre probe (e.g. Emvision), right) and a bevelled fibre probe (Visionex)

2.4 Raman probe studies for targeted biopsy

Raman probes have been extensively tested *ex vivo* for targeted biopsy and some studies have been carried out *in vivo*. In the past, the majority of the latter have been in easily accessible sites such skin, [159,160] oral cavity (tongue, teeth),[154] and cervix[140], however, there are reports of *in vivo* applications in the upper GI tract by Shim *et al*.,[141] and (a recent abstract by) Wong Kee Song *et al*..[161] There have also been reports for *in vivo* tumour margin assessment[162] and applications in stomach,[156] bladder,[155] prostate,[155] colon,[163] and lung.[164]

2.4.1 Probe studies *ex vivo*

Several groups have begun to assess the performance of *in vivo* probes *ex vivo*, as the first step towards *in vivo* measurements. *Ex vivo* measurements have the potential for diagnosis in a theatre situation since the probe systems are mobile and can potentially provide an immediate diagnosis for excised tissue samples, which may be beneficial in assessing tumour margins or allowing earlier treatment if required. In a study by Huang *et al*., a Raman probe system designed for *in vivo* measurements of the skin was used for *ex vivo* measurements of bronchial tissue samples.[165] This was the first application of

Raman spectroscopy in the bronchus. Measurements were made on 28 samples (biopsies and resected specimens) taken from 10 patients. Biopsies were taken under Laser Imaging Fluorescence Endoscopy (LIFE) guidance. The pathology results showed 12 normal samples, 6 adenocarcinoma and 10 squamous cell carcinoma. The results were grouped as either normal (normal and inflammation) or malignant (adenocarcinoma and SCC).[165] Univariate techniques were used to investigate the differences between normal and malignant with respect to the mean of the Raman intensity ratio of the 1445 and 1655cm^{-1} peaks (CH_2 bend and amide I). A peak ratio of 1 was used as the decision point, a sensitivity of 94% and specificity of 92% was achieved.

Boere *et al*. developed a multivariate classification model based on a database of spectra acquired using different Visionex probes (standard Visionex and also Visionex with a 200 µm CaF_2 offset) and on different days.[166] Raman spectra were acquired from 66 rats oesophagi opened longitudinally. A suture was placed at the point the measurements were taken so that the area could be located upon histology. The study concluded that the probe lacked reproducibility, even after filtering. The filtering methods, including correction for backscatter (see Section 2.3.4.2), caused loss of biological information which limits the diagnostic capabilities, although it was reported that >93% of spectra were correctly classified. Boere *et al*. stated that the sampling volume of the Visionex probe (830nm) was 100-600 µm, which was reduced to 400 µm with the addition of the CaF_2 offset window. However, no evidence was provided to support this.

A Visionex Raman probe system has also been used *ex vivo* to discriminate malignant and benign bladder and prostate samples with overall accuracy of 84% and 86% respectively.[155]

Several real time Raman probe systems have been reported such as that described by Motz *et al*., who reported a sapphire ball lens probe (1 excitation fibre, 15 collection fibres) capable of acquiring spectra in 1s then a further 1s for analysis.[167] Another real time software system was reported by Baker Schut *et al*., in which spectra were projected onto a previously developed LDA model in real time.[154]

High wavenumber Raman spectroscopy has also been explored since silica signal is not present at the high wavenumber region. Spectral contributions have been shown to contain similar diagnostic spectral information by Koljenovic *et al*. in a mapping study comparison to validate future high wavenumber probe applications.[128]

2.4.2 *In vivo* Raman applications

Mahadevan-Jansen *et al*. reported the first *in vivo* Raman application (Visionex probe, 785nm) in the cervix, and successfully identified high grade precancerous changes which were verified by taking biopsies at that point.[140] The algorithm based on the peak height ratios at 1659 to 1321 cm^{-1} (amide I to CH_2 twist) and 1659 to 1452 cm^{-1} (amide I to CH_2 bend) correctly identified high grade precancerous changes, but it was not stated in how many patients. Furthermore, biopsies were not taken from sites diagnosed as normal using the probe system so the histology could not be confirmed. A typical spectrum from normal and precancerous spectra was presented, considering only the region between 900 and 1800 cm^{-1}. Spectra were similar to *ex vivo* system.

A further *in vivo* study was carried out on 13 patients undergoing routine colposcopy procedures by Utzinger *et al*.[125] A univariate algorithm based on peak intensities at 1454cm^{-1} to 1656cm^{-1}, which on average was greater for dysplasia and 1656 to 1330 cm^{-1}, which on average was lower for dysplasia. Multivariate analysis was not possible due to the limited sample size. Haka *et al* reported *in vivo* tumour margin assessment during breast surgery using the sapphire ball lens probe described previously.[162]

*2.4.2.1 **Application of Raman probes in the upper GI tract***

The first *in vivo* use of Raman spectroscopy of human gastrointestinal tissue was reported in 2000 in a feasibility study.[141] Emphasis was on the investigation of artefacts from pressure and angle, both of which were found to be negligible as discussed previously in Section 2.3.4.1.[141] Raman spectra were acquired *in vivo* from 5 patients using a custom built fibre optic probe system. A diagnostic algorithm was developed using LDA, with cross validation. Barrett's samples were classified with 86% sensitivity and 88% specificity, with an overall accuracy of 87%. High risk lesions (i.e. HGD and adenocarcinoma) were classified with 88% sensitivity and 89% specificity with 89%

accuracy overall. Shim *et al*. compared the spectra of blood and oesophageal tissue and found that there was no contamination of the heme vibrational modes in the oesophageal spectra, even when measured tissue is covered in blood.[141] This and other contaminant were studied to provide negligible contributions to epithelial Raman spectra.

A larger *in vivo* study was carried out more recently by Wong Kee Song *et al.* in 2006,[161] although results are yet to be published in a scientific journal. In this study, spectra were acquired using a custom built probe at 785 nm from at least 6 Barrett's sites in each of the 100 patients. In this study, a model was developed to differentiate non-dysplastic samples from dysplasia (i.e. LGD, HGD and early adenocarcinoma) with an overall model accuracy of 80% (sensitivity 80%, specificity 79%). These results were improved to 88%, 88% and 88% respectively when the groupings were changed and LGD was included in the non-dysplastic group. This effectively creates a two group model for high risk and low risk pathologies. An important realisation in this study was that the inclusion of reactive/inflammatory changes did not alter the diagnostic accuracy.[161]

Teh *et al*. have recently reported a Raman probe study to detect gastric cancers. In this study, 76 samples/spectra from 41 patients resulted in a cross validated PCA-fed LDA model which discriminated normal and dysplastic gastric samples with good sensitivity and specificity (95.2% and 90.9%). However, it must be noted that there appear to be artefacts in the background subtracted spectra used in the classification model.[156]

2.4.3 Developmental probes

Yamamoto *et al*. reported on a miniature Raman probe comprising hollow optical fibres and a ball lens although the probe has yet to be evaluated for biological applications.[168] De Lima *et al*, reported recently on a catheter based probe (1 excitation fibre, 5 collection fibres and 1 fibre for 'optoclinical treatments') with a mechanism for manoeuvring the distal probe tip.[153] Another catheter based probe has also been reported.[169] However reports are recent and presented only in abstract form. To date little information is provided about the particulars of the probe design.

2.5 Raman mapping and applications for potential histology

A further extension of Raman spectral analysis is the combination with spatial information to produce a 3D spectral data cube which can be used for imaging, referred to as a Raman mapping. Three different methods of Raman mapping were first described by Delhaye and Dhamelincourt, including point mapping, line mapping and global imaging.[170] Raman mapping allows the possibility of multiplexed disease marker measurement without the use of stains.

As mentioned previously, Raman scatter is a relatively weak process. As time has progressed technological advances have enabled the acquisition of Raman point tissue spectra in relatively short acquisition times. Imaging applications of Raman have generally relied on point mapping, which is widely regarded as a slow technique. However, there has been some limited use of global imaging (flat field illumination coupled with liquid crystal tuneable filters and array detection (ChemImage).[59,171] Point and line mapping are described below to provide background details enabling the description of a recent technological development of line mapping referred to here as rapid Raman mapping. Global imaging is not described further here and the reader is referred to Treado and Nelson.[59]

In previous studies our group has shown that Raman spectroscopy is capable of detecting and classifying pre-cancerous and cancerous changes with a high sensitivity and specificity.[1,2] Further studies have gone on to elucidate biochemical changes occurring during the progression to cancer in the oesophagus.[123,172,173] The first demonstration of Raman mapping for the biochemical analysis of the bladder was made by Stone *et al.*[174] Other groups have used Raman mapping to investigate precancerous changes in the bladder,[175] bronchus,[176] and brain.[177] Other Raman mapping studies have been carried out on healthy tissue such as the breast,[178] and also hard tissue applications such as bone.[179] However, the long overall mapping times have limited the size of the datasets which can be acquired and consequently the biochemical information which can be gleaned using multivariate analysis. Furthermore, long overall mapping times have hindered the progression of the technique into the clinical environment.

There are limited papers published which compare different Raman mapping techniques[180] and the most recently developed techniques for rapid mapping have yet to be evaluated. For details of Raman imaging, the reader is referred to the following reference.[59] In order to explain novel technology, Raman mapping techniques are described in brief below. In the following explanations, there are some references to the results section (Section 6.2.1.1). The details of some of these new technologies are described below and compared to existing mapping techniques in Chapter 6.

2.5.1 Point Raman mapping

During point spectral mapping (Figure 2-9a), a spectrum is acquired using effectively the entire length in one dimension (actually the edges are removed to reduce noise) of the charged couple device detector (CCD) with the collection pixels region spanning the width of the laser line to maximise the collected signal. The rest of the CCD is not read out to minimise dark current readout noise and readout time. The sample is stepped along to the next position using an XY translational stage and the next spectrum is acquired and so on until a grid of spectra is obtained, often referred to as a spectral data cube. The overall mapping time is often limited by the acquisition time (per spectrum) when measuring tissue samples since they are not strong scatterers. The acquisition time may be of the order of 1-30 s depending on the tissue type and even as long as 120 s when measuring single cells.[181] Typically the total mapping time is roughly equal to the total number of spectra multiplied by the acquisition time. Additionally, there is a stage translation delay and CCD readout time delay for each of the spectra. This is of the order of 1.6s (combined CCD readout and stage translation, calculated from a 0.1 s acquisition point map using a Renishaw system 1000 – see Section 6.3.1). For shorter acquisition times, the speed of the XY translational stage and, often most significantly, the readout time of the CCD can significantly limit the rate at which spectra can be acquired. Furthermore, factors such as extended scanning and auto-focusing reduce the rate of spectral acquisition. In one study, Krafft *et al*. reported an acquisition rate of only 30 spectra per hour based on an acquisition time of 30 s whilst using auto-focus during the mapping of brain tissue[182].

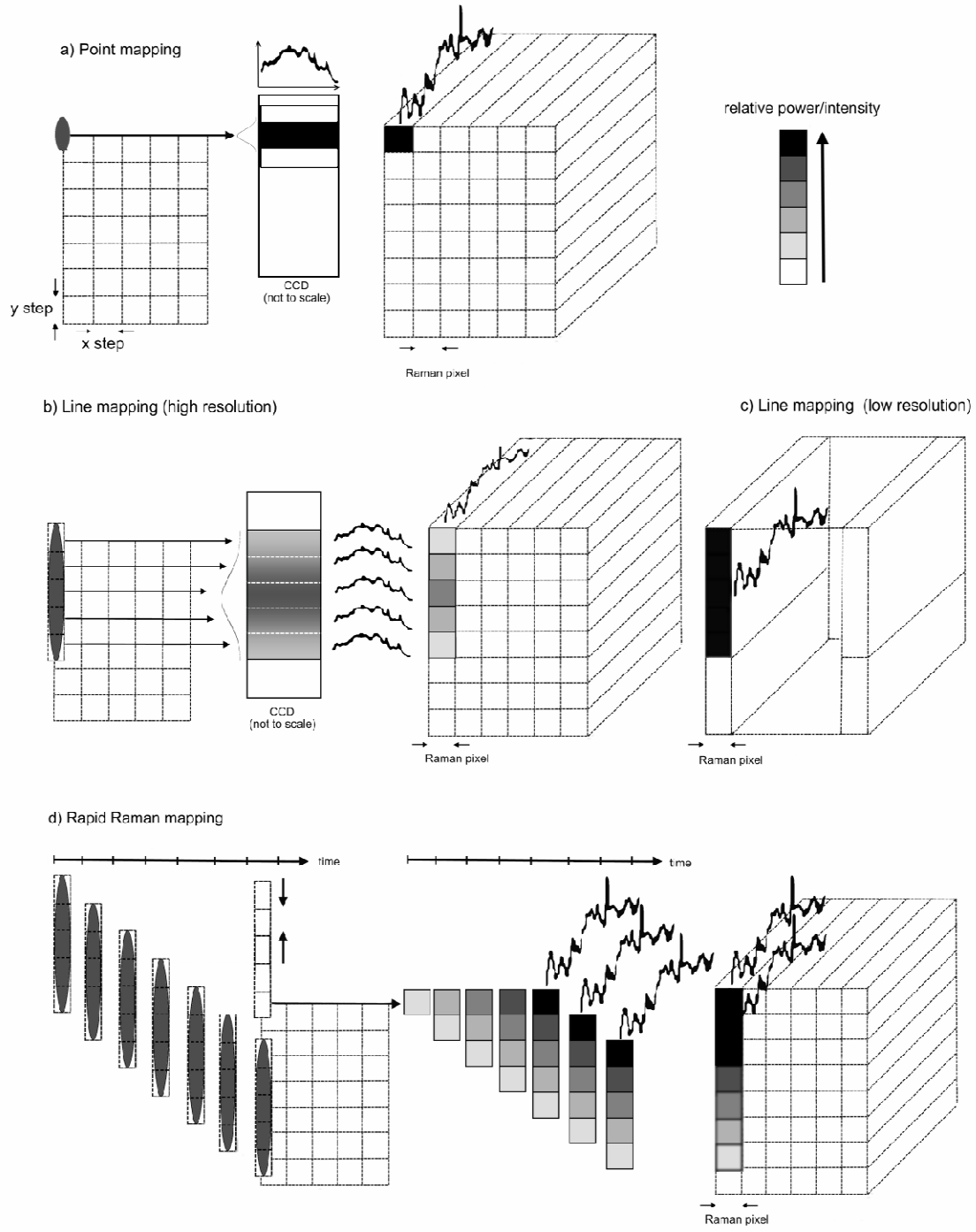

Figure 2-9: a) Illustration of point Raman mapping in which a spectrum is acquired at each position on a grid, b) High spatial resolution line mapping using a barrel lens to produce a line focused laser. Many spectra are acquired simultaneously by separating out the lines on the CCD, c) Low spatial resolution line mapping in which the entire laser line is used to sample a large area of the sample utilising vertical binning of the CCD pixels and d)

Illustration of rapid Raman mapping in which the CCD readout is synchronized with the movement of the stage to allow constant readout of Raman spectra thus reducing dead time between spectra

A development of point mapping was the introduction of a cylindrical lens to create a line-focused laser, often referred to as line mapping.

2.5.2 Line mapping

A line focused laser can be used in two different ways as illustrated in Figure 2-9b and Figure 2-9c. First, line mapping can achieve spatial separation of the laser line using the CCD pixels, resulting in an increased spatial resolution as illustrated in Figure 2-9b. This is achieved by reading out each CCD line separately creating multiple spectra, the trade off being a reduction in the signal of each spectrum since only a portion of the laser light is used to illuminate the area of the tissue imaged by that CCD pixel. A further draw-back is that since the power varies along the length (~50μm for the x50 objective used in this study) of the laser line (approximately Gaussian) this method of line mapping results in a variation in the intensity of the spectra along the laser line. A correction can be performed, but this can be unreliable for inhomogeneous samples such as biological tissue. Schlucker *et al.*,[180] concluded that the signal to noise and images of a Si and aluminium test phantom were similar for point mapping and line mapping (spatial resolution from both methods was of the order of 1.1 μm), but line mapping (corrected using a manufacturers line map correction) was faster. However, in the study by Schlucker *et al.*, the focus for the point mapping laser was reported as being 1.1 μm using a x50 objective, significantly smaller than the point focus achieved with the system in our laboratory due to the wavelength and the type of the laser used, which explains how they were able to achieve similar spatial resolutions with the two different mapping methodologies.

The second method for line mapping is to utilise the expanded laser line to sample the mapped region in fewer steps (Figure 2-9c). In this case, an increased signal to noise ratio is achieved compared to the high resolution line-focused mapping (since the entire

laser line is used to generate each spectrum), but the trade off is reduced spatial resolution.

Line mapping is still limited by CCD readout (especially for short acquisition times), although this is reduced when portions of the laser line read out independently for higher spatial resolution since the readout time is spread over multiple spectra. In fact, it is possible to set up the system to in between settings, for example using only half the line focussed laser line.

These two techniques were rigorously compared by Schlucker *et al*., along with wide field imaging concluding that depending on the application, line mapping was faster that point mapping.[180]

2.5.3 Rapid Raman mapping

Rapid mapping systems have been developed by several manufacturers including WITec (Ulm, Germany) and Renishaw. This study focuses on Renishaw StreamLine™, although the concepts discussed can potentially be applied to any imaging system capable of rapidly acquiring large Raman datasets. Considering StreamLine™ technology (Figure 2-9d), referred to as rapid Raman mapping from here forth, provides a novel and fast method of acquiring Raman maps. The sample is stepped along the laser line and the position of the stage is synchronised with the readout of the CCD (as illustrated in Figure 2-9c). Each spectrum is effectively made up of an accumulation of spectra as the entire laser line passes over each part of the sample. There is a short delay at the beginning of each column in the grid as the laser line passes over the first pixel and then following spectra are acquired at an increased rate. This enables high spatial resolution mapping without the reduction in intensity trade off (associated with spatial separation line mapping) and consequently eliminates the variation in SNR due to the laser profile, as illustrated in Figure 6-9d. There is still however a reduction in signal intensity and SNR compared to point/line mapping using the entire laser line. A further advantage is that constant readout (i.e. reduced dead time between sequential data points compared to point mapping) of spectral data results in the acquisition of spectra and maps at an increased rate. This uses the multichannel advantage of the CCD in two

dimensions simultaneously to get full spectra readout that is orders of magnitude higher than the actual exposure time per spectrum. These advances have facilitated the acquisition of thousands of spectra within a matter of minutes compared to previous mapping techniques which took hours and even days.

Compared to traditional line mapping, rapid mapping provides many advantages. There is an increased rate of spectral readout due to the synchronised readout of the CCD with movement of the XY translation stage, and also high lateral spatial resolution. High lateral spatial resolution line mapping (in which each line of the CCD is used to spatially separate the laser line) is subject to the variation in laser intensity across the laser profile (approximately Gaussian) as shown previously in Figure 6-9.

Gendrin *et al*.[183] recently reviewed the impact of spectral imaging on the field from the perspective of pharmaceuticals (with some biological examples). Discussing the advantages of obtaining both spatial and spectral information, the author also highlighted the multidisciplinary challenges raised by the advent of spectral imaging with the need for a combination of traditional spectroscopic skills (biochemical and instrumentation), chemometric, signal processing and image processing skills.

De Paula *et al*. studied the use of Raman spectroscopy for identification of atherosclerotic plaques; using mathematically added noise they investigated the effect of SNR on subsequent multivariate classification. They concluded that short acquisition times as low as 20ms which result in poor quality spectra could be used distinguishing plaques (calcified, atherosclerotic or non-pathological). However, in this study, spectral features were very visibly different (due to strong Raman signatures for inherent calcification and lipids) and as a result the limit of PCA and other multivariate techniques was not tested.[138]

2.5.4 Relevant points from FTIR mapping studies

As discussed previously, spatial resolution of spectral imaging is a key parameter. For mapping studies, it is important to distinguish the spatial resolution from the step size, which determines the pixel size. A consequence of finite spatial resolution is spectral

mixing between adjacent pixels. This has been investigated by Bhargava, who investigated the effects of nominal spatial resolution (step size) on the classification performance. They went on to attribute complications to what are referred to as "boundary pixels" which are pixels resultant of spectral mixing of neighbouring pixels, as described previously. The effect of over-sampling (increasing the number of pixels which represent a given area) was also considered, concluding that over-sampling can result in improved boundary definition, but spectral mixing is still an issue.[150]

2.6 Practical considerations for sample preparation

The substrate used for Raman spectroscopy and Raman mapping in particular, is particularly important practical consideration since it is vital that the substrate does not have a strong Raman signature. Stone and Kendall investigated different substrates concluding CaF_2 was the most suitable for Raman applications.[108,121] Various other substrates are still routinely used including glass,[131] and quartz.[169]

Formalin fixed samples are not suitable for *in vivo* mimicking Raman spectroscopy, due to the fact that the fixation process induces biochemical changes in the tissue.[184] Sample storage is also an issue, and Shetty investigated the effects of long term storage (at -80°C) of tissue samples, concluding that the effects of prolonged storage on Raman spectra was insignificant.[124] Samples should also be snap frozen in liquid nitrogen to prevent formation of ice crystals. However there are reports in the literature which do suggest there are subtle peak of the amide I due to freezing of tissue samples.[185]

Chapter 3 Data Analysis

This section summarises the techniques used for pre-processing data and subsequent chemometric techniques used for developing a classification model. The main emphasis is on techniques actually used in this study, but also touches on other competing and complementary techniques that will be investigated in the future.

3.1 Data pre-treatment

Where possible, raw data should be energy sensitivity corrected to account for CCD efficiency across the wavenumber range (see Section 4.4). Spectra are also interpolated to unitary wavenumber divisions since the spectral wavenumber values are determined by the positions of the CCD pixels.

Data pre-processing reduces systematic and random errors in the Raman spectra.[186] For single spectra, smoothing techniques such as the Savitsky-Golay filter, removes high frequency fluctuations. This is achieved by isolating low frequency fluctuations through fitting polynomial functions to a number of points around each spectral point. [187]

Normalisation eliminates differences in absolute intensity. Normalisation can either be carried out with respect to a well defined peak, but overlapping bands etc. can be problematic, or with respect to the total area. Another alternative commonly used is where the centred and normalised to a given variance (normally unity).[187]

A common approach to standardise data is mean centring in which the mean of the entire dataset is subtracted from each individual spectrum. This also allows scaling of test datasets.[187]

The elimination of background signals is also problematic and this has been discussed in Section 2.3.4.2.

3.2 Chemometrics

3.2.1 Empirical analysis

Empirical analysis includes calculation of difference spectra, peak assignment, absolute peak heights and peak ratios. Subtracting spectra is useful to give a general indication of the main differences between spectra. For example, subtraction of the mean normal spectra from the mean cancer spectra indicated shows a spectrum with peaks in the same position as glycogen showing that there is less glycogen in cancer samples as expected due to increased proliferation. Although this method is crude, it can be a useful starting point. Peak ratios take it one step further and several groups have developed successful classification models based on peak ratios. A commonly used peak ratio is 1651 cm^{-1} to 1445 cm^{-1} (Amide I C=O stretch vs lipid vibrational mode CH_2, CH_3) which has been used on several sites, including the cervix,[140,113] breast[131] and bronchus[165] to discriminate between normal and abnormal/malignant tissue samples. The technique is simple and often used for feasibility studies. However, it is limited since it only takes into account a small region of the spectra, and complex biochemical changes would affect the entire spectrum. Although using more than one intensity ratio may improve this, a significant amount of spectral information is still wasted. Multivariate methods utilise the entire spectra enabling more subtle changes to be detected.

3.2.2 Principal component analysis (PCA)

Principal component analysis (PCA) forms the basis for multivariate statistical analysis.[188] PCA is a data compression technique which removes collinear variations, variations in spectral features that arise from the same source, and retains only spectral features with independent variations. The first principal component (PC) is such that it is representative of the highest variance in the spectral dataset; the second principal component is representative of the next highest variance. This continues until the principal components represent only noise. The principal component scores represent the

fit coefficient/weight of each PC. The most significant principal components can then be used to separate different groups. This is most easily visualized by plotting the scores in principal component space, although this is difficult in multiple dimensions.

This is referred to as an unsupervised model since the process separates the groups with no prior knowledge of their classification.

Many groups have used PCA for analysis and separation of Raman (and other vibrational) spectroscopic data.[50,132,138,189] A model can be trained against a gold standard using linear discriminant analysis (LDA), for example by inputting pathology information.

3.2.3 Linear discriminant analysis (LDA)

LDA is referred to as a supervised method, since the model is generated with groups separated based on prior knowledge of the classification groups. The process of LDA maximises the variance between the different groups and minimises the variance within each group and creates a discriminant function which describes this. Many groups have used PCA fed LDA for separating different Raman spectroscopic tissue pathologies.[1,50,103,133,155,175] The number of PCs (i.e. using the minimum) used for LDA is an important variable to prevent overfitting the data (fitting noise components etc.).

Alternative chemometric techniques such as artificial neural networks are described below with regards to imaging, but these techniques can also be applied to point spectra. PCA and LDA are established techniques and as a result these are chosen for use in this study.

3.3 Model validation

Ideally, a model will be tested using an independent dataset. However, due to limitations with patient and sample numbers this is not always possible. Retaining a number of samples to generate an independent validation dataset means that the number samples to

produce the model training set is reduced, thus limiting the training model, which ideally will have as many samples/patients as possible. A method of overcoming this is leave-one-out cross validation.

3.3.1 Leave-one-out cross validation

After a model is generated, it can be tested by removing one spectra (which may include all spectra from a sample/patient) and regenerating the model. The removed spectrum is then fed into the LDA classification model to determine the classification based on the new model. This is then repeated by removing each spectrum (again this may refer to all spectra from one sample/patient) in turn.

This technique has been widely used for validating classification models in the other tissues,[133,155,192], and oesophageal tissue.[1]

3.4 Chemometrics for spectral imaging

Univariate imaging (or functional group imaging) is one of the simplest forms of displaying biochemical information from a spectral image, however, multivariate techniques as described previously, utilise the entire spectra and all of the biochemical information contained within it.

Principal component analysis has been applied by many groups for spectroscopic image processing of both Raman and FT-IR applications.[148,181,190] The reader is referred to Raman textbooks for further details.[187]

Hayden *et al*. investigated the effects of sampling parameters and compared for Raman line images using PCA, demonstrating that improved results were obtained using the higher magnification, concluding that this was due to an increased dataset size.[148]

Principal component analysis has been used by many groups as an unsupervised method of data reduction to produce pseudocolour PC score images of Raman and FTIR spectral images.[148,182,190] Various other forms of cluster analysis (Hierarchal cluster analysis, k-

means cluster analysis, fuzzy C-means) have also been used as unsupervised methods of imaging for spectral imaging. [175,178,191]

Many groups have generated supervised multivariate tissue classification models using LDA based on spectra, or mean spectra extracted from Raman maps, however, few groups have taken the step to produce images from the classification results. Supervised methods include artificial neural networks (ANN),[138,191] and LDA, although after a search of the literature, only one paper which uses (LDA) for Raman imaging could be found (based on an LDA model spectral averages from cluster analysis trained with histology).[192] Mansfield *et al*. have reported the application of LDA for FTIR imaging of skin cancer,[193] and Krafft *et al*. reported LDA applied to FTIR imaging of gliomas.[194]

Chapter 4 Materials and methods

The following chapter describes the materials and methods involved in a preliminary study carried out with the Visionex probe system for targeted biopsy *ex vivo* (described in Section 2.3.5) and how this model was developed, include trial of different preprocessing and the addition of consensus pathology. Materials and methods for the Raman mapping (for automated histopathology) studies and also studies which impact both *in vivo* and *ex vivo* clinical applications of Raman spectroscopy are also included.

4.1 Oesophageal tissue sample collection

Informed written consent was obtained from patients undergoing routine upper gastrointestinal endoscopic surveillance of Barrett's oesophagus, endoscopic mucosal resection (EMR) treatments and radical oesophagectomy. Ethical approval for this study was obtained from Gloucestershire Local Ethics Committee.

Tissue samples were collected during EMR and oesophagectomy procedures. Both EMR and resected samples were approximately 1cm in diameter. In the latter case, samples could be obtained from disease free regions of the resected oesophagus. Biopsy samples have also been harvested during routine endoscopic surveillance, including a small number of jumbo biopsies, although these have not been used in this study. Samples were placed in a cryovial and immediately snap frozen in liquid nitrogen.

Included in this preliminary study were 50 EMR and resected samples obtained from 39 patients used in this preliminary study.

4.2 Histopathology definition

Pathology information was obtained from three expert pathologists specializing in gastrointestinal pathology, Prof. N. Shepherd, Prof. K. Geboes and Prof. Bryan Warren. However, this was not possible for all samples due to time limitations and pathologist

commitments. A comparison was made between the pathology diagnosis from each histopathologist and a consensus opinion and majority diagnosis determined.

Samples were measured on fresh or defrosted samples. From the early stages of the study, following spectroscopic measurement, samples were formalin fixed after measurements, sectioned and stained with H&E for histological diagnosis. Subsequently, samples were snap frozen after measurement and frozen sections were then stained with H&E. This allowed the remainder of the sample to be retained for further spectroscopic measurements.

For rapid Raman mapping, 15-20 µm tissue sections were cut onto calcium fluoride (CaF_2) substrates which have a low background signal with only one Raman peak at ~320 cm^{-1} which is outside of the finger print region (400-1800 cm^{-1}). For these sections, consecutive 7µm sections were sectioned and stained with H&E for histological diagnosis. Furthermore, some frozen sections were stained with H&E to improve correlation of morphology and biochemistry of the Raman maps.

Although only a low number of classification groups were used in this preliminary study due to the limited number of patients/samples, the pathologist provided a range of diagnosis from 9 classifications listed below, along with abbreviations. These could be then used in the future when the model is extended. Pathologists were encouraged to highlight uncertainty, in keeping with pathology criteria in which clinical samples are diagnosed as indefinite for dysplasia.

- Normal squamous – NSq
- Cardiac mucosa – CM
- Fundic mucosa – FM
- Intestinal metaplasia – IM
- Low grade dysplasia – LGD
- High grade dysplasia – HGD
- Adenocarcinoma – Adeno

- Squamous dysplasia – SqDysp
- Squamous cell carcinoma – SCC
- Inflammation

Further tissue groups were also identified for mapping sections which often contained submucosa including:

- Fibrous connective tissue
- Smooth muscle
- Lymphoid aggregate
- Glands
- Duct
- Goblet cells
- Nerve
- Blood vessels
- Laser damage
- Fibrosis

4.3 Wavelength selection

As discussed previously, 785-830 nm is the ideal wavelength range of choice for Raman spectral measurements of biological tissue. 830 nm has been chosen as the wavelength of choice, supported by previous studies and commonly used by other groups.[108,138] In general, two different types of Renishaw spectrometers were used in this study, one for probe based studies and a laboratory based microspectrometer for mapping experiments. These are discussed in detail below. Two model variations of these were used in preliminary studies, where relevant these are noted in the methods of that particular study. System calibration issues are discussed separately below.

4.4 Raman system calibration

There must be a calibration to ensure that the conversion from channel number to wavenumber is reproducible. An intensity calibration is also required since there is wavelength dependence in the efficiency of the detector (due to filtration), efficiency of the gratings and quantum efficiency (QE) of the detector.[195] Different calibration methods are listed below:

- Offset calibration – Silicon is often used to monitor any shift in wavenumber since it gives a well defined single peak at 520cm^{-1}. Although a quick and easy test, it does not check calibration across the entire wavenumber range.
- Neon argon lamp – this can be used to test the CCD across the entire wavenumber range, however it requires that the laser light is blocked.[2,125] A calibration standard which has Raman spectra peaks has advantages over neon argon atomic emission lines.[142] Cyclohexane is also used locally (in combination with neon argon source) and by other groups since it does not require the laser line to be blocked. White light calibration (diffusely scattered by $BaSO_4$) – this provides calibration traceable to national standards. Raman intensities can be corrected for wavelength dependent detector efficiency using the emission spectrum of a calibrated tungsten band lamp.[3,196]
- Fluorescence –A recent paper by Etz *et al*. reports on a doped glass standard for relative Raman intensity calibration developed by the National Institute of Standards and Technology (NIST). However calibration is only carried out at one wavelength (785nm).[197] Locally, green glass is used as secondary standard traceable standard which can be related to the calibrated white light source.

The Raman systems within the department have been wavelength calibrated using neon argon atomic emission lines. The emission lines provide well defined bands within the wavenumber range of interest as described previously in Section 4.4. An example of three neon argon calibration spectra acquired using the probe system spectrometer can be seen in Figure 4-1.

For the probe system, the neon argon calibration was carried out when the system was initially set up. For the laboratory based spectrometers, this was also carried out, and additionally, neon argon spectra were acquired routinely before each spectral acquisition to monitor temporal changes, although the spectra are not used to calibrate the system on a daily basis, the data is merely stored in case retrospective correction is required. A full calibration is performed if the system is realigned or the laser is replaced.

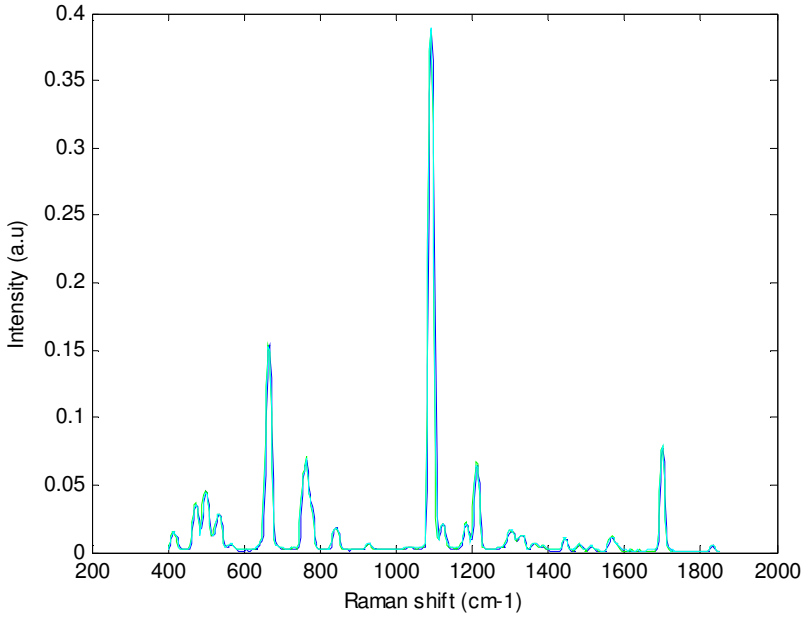

Figure 4-1: Neon argon emission lines measured with the Renishaw RA100 spectrometer (three independent measurements (blue, cyan and green) acquired from Oct 2005 to July 2007

Green glass is used as secondary standard (to an NPL calibrated tungsten lamp) for intensity calibration. For the laboratory based Raman systems, the green glass standard is measured using the x50 Leica objective (1s acquisition) prior to any tissue measurement Green glass correction is not required for mapping measurements since the data is only self-compared, i.e. data analysis is not carried out over weeks or months as tissue classification models are and thus drift in system performance is not an issue.

Green glass calibration measurements were only carried out sporadically. A 1s acquisition was used for the probe system. Green glass correction was not deemed vital for the probe model since measurements were carried out in large batches so system drift

was not generally a problem, however replacement of the CCD and realignment did result in some issues which is discussed in Section 5.5.

4.5 Methods – 1) optical biopsy

The methods section has been constructed such that the heading numbering correlates with the relevant section in the results chapters. For example, the methods described in Section 4.5.1 can be found in section 5.1 and so on.

Raman spectra were acquired from endoscopic mucosal resections (EMR) and resected tissue specimens using a Visionex probe (Gaser level 10, described previously in Section 2.3.5). A diode laser (Process Instruments) with wavelength of 830nm was used for excitation, which was connected to the excitation fibre. The collection fibres (arranged in a linear array) were passed through a further laser line rejection filter and connected to a Renishaw RA100 spectrometer (Renishaw plc., Wotton-under-edge, UK). The Renishaw System 100 spectrometer is a simple design, shown in Figure 4-2. The collection fibres direct the Raman scattered photons via a lens, mirror, and grating, onto the CCD detector. The spectral resolution of the probe spectrometer is approximately $15cm^{-1}$.

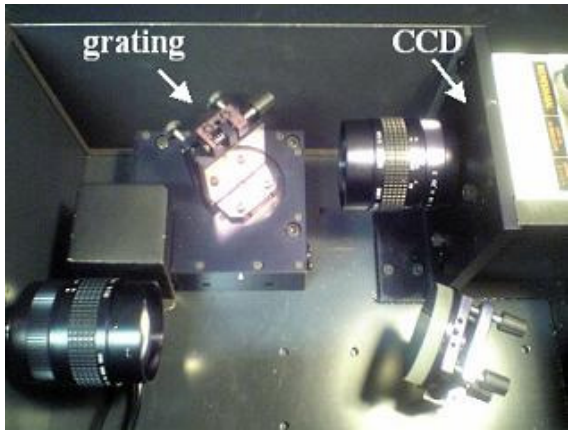

Figure 4-2: Photograph of the Renishaw System 100 spectrograph

The spectrometer and spectral acquisition is controlled via GRAMS (Graphic Relational Array Management System), a 32-bit software package for collecting Raman spectra via the Renishaw spectrometers.

The Raman probe was positioned vertically in a jig as shown in Figure 4-3. The sample was then placed on CaF_2 on a z-translation stage. The sample was raised until in (gentle) contact with the probe. Prior to each spectral tissue measurement, the probe spectrometer was calibrated using a Si standard. A 1s acquisition time was used. If a spectral offset was detected (from the expected 520cm^{-1}) position, a wavenumber offset correction was applied. For large offsets, the system was shut down and rebooted with a full system motor check and the wavenumber calibration process repeated. A tolerance of ±0.5cm^{-1} has previously been shown to be acceptable.[108]

Figure 4-3: left) Photograph of the Visionex Raman probe and spectrometer, right) photograph of the Visionex probe, z-translation stage and substrate

4.5.1 Raman probe background signal

As described previously, reports in the literature state that current methods of background subtraction are unreliable. To investigate this further, the most widely used technique was tested which involves the iterative subtraction of a polynomial described by Leiber *et al.*[198] Considering the Visionex probe, a 5th order polynomial is suggested. The technique was tested on a series of spectra acquired using the Visionex probe and Rensihaw RA100 spectrometer described above is 4.5.

An acquisition time of 4x15s was used for these measurements. Spectra from 96 samples were averaged into three pathology groups (defined by one expert pathologist). The mean spectra were compared before and after background subtraction. Artefacts due to the probe background and also from the background subtraction process itself are compared to results in the literature. The results can be found in Section 5.1

4.5.2 Comparison of Raman probes

A second probe for potential *in vivo* optical biopsy was obtained from Eric Marple, and is referred to as the Emvision probe. As described previously in Section 2.3.5.1, this probe has the same fibre set up as the Visionex probe, however the probe does not have the filters at the tip, nor the bevelled fibres which limits the collection volume/depth.

It was not evident whether or not this probe would be suitable for *in vivo* diagnosis in the oesophagus and since there appears to be no evidence of its use in the literature. It was decided that an initial comparison would need to be carried out, firstly and most importantly to investigate the sampling volume.

To compare the two different probes, depth profiles in air and water were measured, using diamond as the target sample. The Raman probes were held vertically in a jig. The sample was placed on a CaF_2 substrate on a vertical translation stage. Initially, spectra were acquired in contact with diamond chip with an acquisition time of 1s. The stage was then lowered at 50μm intervals and a spectrum acquired at each position.

The collection efficiency of the probes was determined using the magnitude of the diamond peak (with respect to the baseline), divided by the acquisition time and power at the sample. The power at the sample was measured using a calibrated power meter with optical diffuser.

Depth profiles were also plotted, with the peak intensity, normalised with respect to the value at the probe tip. This was repeated for both probes in air and water. A comparison of the calibration standards was also carried out. Results of these measurements can be seen in 5.2

4.5.3 Preliminary three group Visionex model

Previous measurements had shown that 4x15 s acquisition maximised counts and signal to noise ratio without CCD saturation so this protocol was adopted for all future tissue measurements using the Visionex probe system. 163 spectra were acquired from 50 EMRs and resected samples taken from 39 patients, a break down of the pathology can be seen in Table 5-1. The biopsies were then formalin fixed, sectioned and H&E stained for pathology diagnosis. The pathologist classified the samples as 1 of 9 groups listed in Section 4.2.1.

The majority of samples were snap frozen and defrosted before measurement, however some samples were measured fresh. Record was made of how the sample was stored prior to measurement and spectra analysed to assess the effects of fresh and frozen tissue. In addition, 6 of the samples were clinical samples (needed for diagnosis) and therefore measured fresh and the sample was subsequently put through the normal diagnostic route. PCA was used to investigate any subtle variation in spectra acquired from fresh and frozen sample, discussed and no evidence was found (see Appendix B). Clinical samples were put through the normal diagnostic route for patients undergoing routine surveillance for Barrett's oesophagus, but the pathology report did not provide sufficient detail for this study and these samples have been excluded from the classification model. They were however used in a comparison of fresh and frozen tissue spectra.

After each Raman spectrum was acquired, clinical biopsy forceps were used to localise and remove the region on the sample from which the Raman measurement was made to mimic the situation *in vivo*. The biopsy samples were then either formalin fixed or snap frozen (if required for further measurements). Subsequently, 7µm frozen sections were stained with H&E for histological diagnosis following standard H&E protocol. For the initial model, pathology opinion was obtained from one expert histopathologist. The tissue samples were large enough to allow multiple measurements to be taken from different regions. On average, three spectra were acquired from each, starting at one end

of the sample and working along, and thus on average three samples were obtained from each larger sample. These were treated independently since each has individual pathology diagnosis. Initially, the idea was to correlate these probe measurements with OCT images taken from the same regions and also the gold standard histopathological analysis. However, this proved fruitless since the OCT images were not of sufficient quality and it was impossible to correlate pathology results from inhomogeneous samples. Furthermore, OCT images were acquired from distinct borders in the tissue for example on the edge of a lesion in an attempt to emphasise the differing appearance with tissue type, but this was sub-optimal for the Raman method since a homogeneous tissue sample is required for best results and correlation with pathology.

Tissue inhomogeneity, due to the size of the biopsy samples used, was a problem. An attempt was made to overcome this problem by eliminating samples that were inhomogeneous with respect to the 3 group model, i.e. inhomogeneous samples were accepted providing the different pathologies present were all covered by umbrella of the three group definitions. This was applied between pathologists as well as within the samples, e.g. if one pathologist's diagnosis was adenocarcinoma and the second pathologist's diagnosis was HGD, the sample was accepted into the model and placed in the high risk group. Conversely, if a sample was reported as containing both NSq and HGD, the sample was rejected. The pathology break down for the preliminary model based on the opinion of one pathologist is shown in Table 4-1.

Table 4-1: Pathology break down based on the opinion of one pathologist for ALL samples measured in the preliminary Visionex study

Pathology	Number of samples/spectra
NSq	11
Barrett's CM	14
Barrett's FM	5
Barrett's IM	16
LGD	11
HGD	23
Adeno	18
SqDysp	0
SCC	0
Discarded	65
Total	163

Many samples were not used in the model since it is necessary to ensure models are trained with reliable groups and as a result, criteria for rejecting samples were relatively strict. Samples were discarded from the study if the sample only contained submuscosa (caused by sample accidentally being placed epithelial surface down), the pathologist was uncertain of the diagnosis, the sample contained mixed pathologies (i.e. not within the boundaries of the three group pathology model), or there was poor staining which prevented accurate diagnosis. A further two Barrett's FM samples were rejected since spectrally, they appeared to be stomach samples (obtained from oesophagectomy/gastrectomy) with high lipid content. This resulted in a total of 96 samples/spectra the following groupings for the preliminary Visionex probe model, as summarised in Table 4-2.

Table 4-2: Pathology breakdown based on the opinion of one pathologist for samples using in the PCA fed LDA three group tissue preliminary Visionex probe classification model

Pathology	Number of samples/spectra	Model Groups
NSq	11	NSq (11)
Barrett's CM	14	
Barrett's FM	3	Barrett's (33)
Barrett's IM	16	
LGD	11	
HGD	23	Neoplasia (52)
Adeno	18	
SqDysp	0	
SCC	0	
Discarded	67	
Total	163	96

*4.5.3.1 **Data analysis***

Data analysis was carried out using Matlab and the PLS toolbox (Eigenvector Technologies, Manson, Washington, USA). Acquisition parameters described above minimised the occurrence of saturated spectra. Cosmic rays were removed using the 'zap' function in GRAMs. Further cosmic rays (detected using the multivariate analysis process) were removed in Matlab by linear interpolation of the regions either side of the cosmic ray.

Spectra were interpolated to 1 wavenumber per point. Spectra were normalised, smoothed (Savitzky–Golay filter with a 2nd order polynomial and window of 21) and mean centred prior to principal component analysis. This was supported by previous studies within the group which also used these settings.[121] This was repeated with and without background subtraction (normalisation following background subtraction in this case) according to the procedure and Matlab program by Leiber *et al.*[199] to investigate the model performance with different pre-processing steps. Iterations of number of PCs fed into the LDA model were carried out from 3PCs to 30PCs. The final model was then cross validated by methodically removing one sample (i.e. one spectrum) and recalculating the model. (See section 5.3)

4.5.4 Visionex probe model following replacement of the CCD

The above model was extended following the same methods described previously, but due to a CCD failure, and subsequent alignment issues, the models have been separated for clarity. These results can be seen in Section 5.4

145 spectra were acquired from 145 samples obtained from 28 patients. This was reduced to 88 samples from 20 patients after rejecting samples and spectra according to the aforementioned criteria.

Table 4-3: Pathology breakdown based on the opinion of one pathologist for samples using in the PCA fed LDA three group tissue Visionex probe classification model (following realignment after CCD replacement)

Pathology	Number of samples/spectra	Model Groups
NSq	19	NSq (19)
Barrett's CM	2	
Barrett's FM	1	Barrett's (18)
Barrett's IM	15	
LGD	6	
HGD	9	Neoplasia (51)
Adeno	36	
SqDysp	1	
SCC	2	
Discarded	54	
Total	145	88

4.5.5 Visionex combined model

In order to maximise the size of the tissue classification model, methods of combining the two previously calculated models was investigated. This is also an issue which is significant for translation to a clinical environment since tissue classification models would need to be robust to changes in equipment and in particular for the probe, potential alignment issues which may occur as the spectrometer is transported in a theatre environment for example. Three different methods of combining the two datasets were compared.

The combined dataset contained 184 samples/spectra from 59 patients.

*4.5.5.1 **Combining the datasets without pre-processing***

A first step towards investigating this was to combine the raw data from both models and evaluate the subsequent tissue classification model. This was feasible since PCA fed LDA has been shown to be relatively insensitive to probe backgrounds so it was possible that variation in the background would not effect classification.

The model was recalculated simply by combining the two datasets, both normalised, smoothed and mean centred. A PCA fed LDA model was generated using 15 PCs.

*4.5.5.2 **Removal of probe background variation using PCs to independently reconstruct the datasets***

A further option is to reconstruct the dataset minus the artefact, in this case the probe background. In order to achieve this, PCA was carried out on the datasets independently, the probe background was identified in the PC loads and the date reconstructed minus the PCs in question. The two reconstructed datasets were then combined and PCA recalculated with 15 PCs fed into the LDA tissue classification model.

*4.5.5.3 **Removal of the probe backgrounds using energy sensitivity correction***

The third option for combining the datasets is to use an energy sensitivity correction as described previously in Section 4.4. Green glass calibration standards were acquired as and when possible for the probe system. Mean green glass calibration spectra were

determined for pre and post alignment issue. The mean spectra were interpolated to the same wavenumber range as the tissue spectra. A ratio of the absolute (reference green glass) and the mean green glass calibration file is used to correct for the energy sensitivity of the spectrometer. The two different datasets were corrected with the ratio for the corresponding mean green glass correction. The datasets were then combined and PCA-LDA carried out using 15PCs. The results can be seen in 5.5.3.

4.5.6 Short acquisition (4 s) Visionex probe model

Whilst the above mentioned spectra were acquired with an acquisition time of 4x15s, a spectrum of each sample was also acquired using a shorter acquisition time of only 4s. The purpose of this was to demonstrate that diagnosis is potentially feasible in clinically practicable time frames. Results of this model can be seen in Section 5.6. Datasets from the preliminary and post alignment Visionex models were combined to maximise sample numbers since consensus (of three pathologists) pathology was used to train the classification model, which resulted in a high rejection rate of samples. A breakdown of the samples in each pathology group can be seen in Table 4-4.

Considering the samples rejected after consensus pathology, the majority of disagreements were for neoplastic samples with 42 samples rejected. This was often due to pathologists failing to mention focal regions of other pathologies, e.g. Barrett's or normal within the samples. 11 Barrett's samples were also rejected, whilst only 2 NSq samples were rejected. In the latter case, the good agreement between pathologists with NSq samples is expected since identification is less subjective compared to different Barrett's sub-types and neoplastic changes.

Table 4-4: Pathology breakdown for the 4 s Visionex combined model trained with consensus pathology opinion from three expert pathologists

	# samples correctly classified
NSq	28
Barrett's	40
Neoplasia	42
Total	110

4.5.7 Single output fibre probe tissue classification model

The custom built probe, which consisted of a single excitation fibre and single collection fibre, (with diameters of 62.5 µm and 105 µm, respectively) was connected to a custom built spectrometer with similar performance characteristics to the Renishaw System 100 spectrometer used above. The probe, schematically shown in Figure 4-4, differs from other probes which generally rely on multiple collection fibres to increase collection efficiency. The probe contains a notch filter and fluorescence filter near the tip to remove elastically scattered light and reject background fluorescence signal.

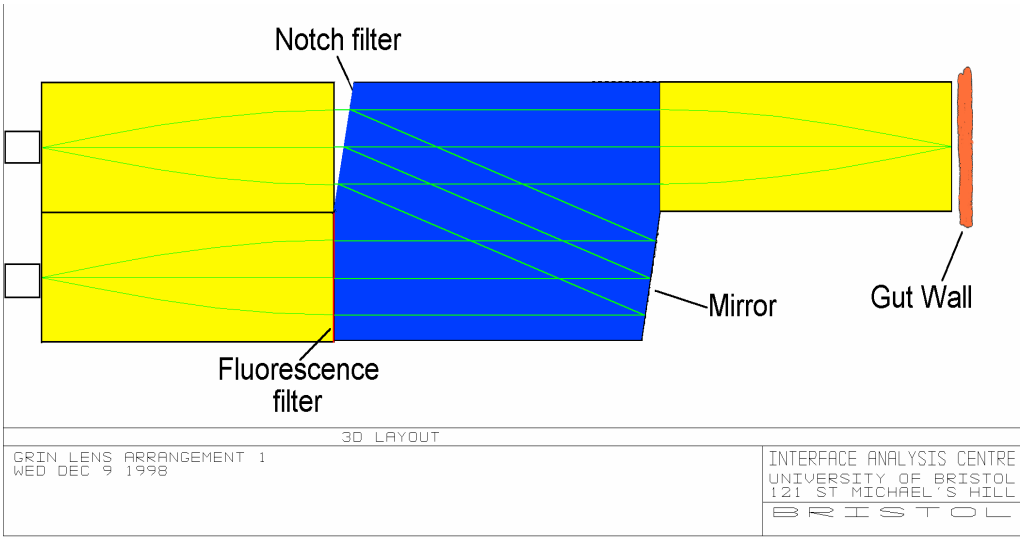

Figure 4-4: Schematic diagram of the single collection fibre probe

Thirty spectra were measured from 30 homogeneous biopsy samples from 30 different patients with an acquisition times of 4x15 s and 4 s. The samples were placed on a vertical CaF_2 and moved laterally until in contact with the (unpackaged) probe, which can be seen in Figure 4-5.

Figure 4-5: Experimental set up for the single collection fibre probe ex vivo

The consensus histology diagnosis from three expert pathologists was used to train a PC fed LDA model (15 PCs, data normalised and mean centred). A breakdown of the sample numbers in each pathology group can be seen in Table 4-5.

The consensus histology diagnosis from three expert pathologists was used to train a PCA fed LDA model.

Background subtraction was not used for the PCA-LDA model, but was performed to enable comparison of spectra with the Visionex probe spectra.

Spectra were also measured with shorter acquisition times (4s) to determine the feasibility for more realistic time scale Raman measurements. This was based on the fact that there was scope to improve throughput of the probe by a factor of 4, thus enabling 1s acquisition times in the future.

Table 4-5: Summary of the number of samples for each pathology group for the single collection fibre probe

	# samples correctly classified
NSq	13
Barrett's	8
Neoplasia	9
Total	30

4.6 Methods – 2) Rapid Raman mapping for potential automated histopathology

The general construction of a Raman microscopy system has been described previously in Section 2.3. To summarise the system components for the microscopy systems used in the mapping studies.

Typically, the core of the StreamLine instrument is a Renishaw inVia Raman microscope, although in these experiments Raman point spectra and maps were acquired using a customised Renishaw Raman System 1000 spectrometer coupled to a microscope fitted with a Leica x50 long working distance objective (NA 0.5). A diode laser with a wave-length of 830 nm was used with 70 mW at the sample (270 mW at source). A dielectric coated edge filter is used to reject Rayleigh scattered photons, which have been found to have good long term stability.[121]

A grating (300 lines/mm) was used to disperse the scattered light which was measured with a deep depletion charged couple device (CCD) detector. A peltier cooled deep depletion CCD was used. The spectral resolution of the probe spectrometer is approximately ~10cm^{-1}.

For mapping experiments, the sample is placed on an x-y translation stage which is co-registered with spectral readout. The mapping system can work in three modes, as described previously in Section 2.5 – point, line and rapid (line) mapping.

4.6.1 A preliminary study of rapid Raman mapping parameters

To test the optimum objective lens for rapid Raman mapping a series of objectives were tested using a prototype rapid mapping system (785nm) at Renishaw Plc. The rapid Raman mapping system was only set up for use with a x50 objective. Two were available for use, the NPlan x50 and the Leica x50 long working distance objective. The Nplan objective is recommended by the manufacturer due to the higher throughput, but locally the Leica x50 objective has been used for tissue classification models and mapping since the objective does not have a glass background. The thickness of the

mapping section was chosen to maximise Raman scattered photons from the tissue section (whilst not taking the section beyond 1-2 cells thick). This was based on work carried out previously in the group.[108,121,123]

Raman spectra were acquired using both spectra to compare the signal to noise for each objective. An acquisition time of 5 s was used. Raman maps (of NSq and FCT) were acquired using both objectives as a further comparison. The Nplan x50 objective map was acquired with an acquisition time of 5 s, step size of 27.5 µm step size, and Leica x50 long working distance map was acquired with a 5 s acquisition time and step size of 11 µm. The area of the 11 µm map was cropped to the same mapped area as the 27.5 µm map. Spectra were not normalised or mean centred in this case. It was decided that intensity variations may be relevant to pathology for mapping studies. The latter is also important for mapping studies containing large areas of CaF_2 since this will dominate the mean spectrum.

A 1200 lines/mm grating was available which provides improved spectral resolution over a shorter wavenumber range. This was tested by running a trial map a step size of 6.6 µm and acquisition time of 30 s. The map dimensions were 141x111 spectra resulting in a total of 15651 spectra.

4.6.2 Comparison or rapid Raman mapping with point mapping and line focus mapping

Rapid Raman mapping as described in Section 2.5 utilises spatial separation of the CCD to achieve increased lateral spatial resolution. In theory, there should be no difference in signal to noise for different step size settings, since each spectrum is effectively made up of accumulations of the entire laser length. However, it was noticed that there was a slight reduction in signal to noise with decreasing step size. Although not significant, it was necessary to investigate this since it may be necessary to increase acquisition time for small step size maps to counter act the reduction in signal to noise ratio.

To evaluate this, repeated rapid Raman maps (line maps were used to reduce dataset sizes) were carried out on both Si and tissue with a constant acquisition time of 0.1 s and 40 s respectively, with the step size varying from 52.8-1.1 μm.

Mean map spectra were compared, along with individual spectra from the same position in the map. The signal to noise ratio (at 1000 cm^{-1}) was determined, along with the signal to baseline ratio (at 1000 cm^{-1} and 1450 cm^{-1}).

4.6.3 Principal component analysis in combination with rapid Raman mapping for potential automated histopathology

In this study, two samples from two different patients have been mapped. Due to the heterogeneous nature of the samples the pathologist annotated each sample with the various pathologies according to the list defined in Section 4.2.

In the following experiments, the SNR was monitored for a range of maps methodically acquired with various combinations of acquisition time and spatial resolution parameters (step size). This study presents the results of this investigation and demonstrates that total mapping time for oesophageal biopsies can potentially be reduced to a clinically practicable timescale

Repeated maps were carried out on tissue sections, methodically varying the spectral acquisition time and step size. There are several variables to take into consideration – for a constant area map, a higher resolution map (i.e. smaller step size) results in a larger number of spectra compared to a lower resolution map (i.e. larger step size) of the same area. The total number of spectra is an important consideration since the size of the dataset has an impact on the reliability of any multivariate analysis used. However, for a lower spatial resolution map the total number of spectra is reduced, thus the acquisition time can be increased to obtain higher quality spectra in the same overall time scale. The quality of the spectral dataset is also an important factor when attempting to identify subtle biochemical changes using multivariate techniques.

Acquisition times ranged from 0.1-20 s. For each acquisition time, the step size was also varied between 7.4-25.3 µm. The mapping parameters are summarised in Table 6-3. The total mapping time was limited to a maximum of 24 h since longer maps were not practicable. The total number of spectra in each map varied between $0.9x10^4$ and $10x10^4$. The approximate mapping time using standard point mapping was calculated based on a CCD readout and XY translation delay of 1.65 s per spectra (1.2 s reported by Schlucker *et al.*[180]). This value was determined by running a map (traditional point map mode) with an acquisition time of 0.1 s, step size of 6 µm and calculating the delay according to actual map time minus the best case scenario map time (i.e. number of spectra multiplied by the acquisition time) and dividing this by the total number of spectra in the map. To account for the difference in Raman signal intensity for the rapid Raman spectra compared to point mapping (which varies with step size, in a similar manner to line mapping), the acquisition time used in the estimate of the overall point mapping time was scaled by a factor equal to the step-size divided by the length of the laser line. Including this scaling factor ensured that the advantage of rapid Raman mapping was not overestimated.

Work has also been carried out elsewhere by Sasic *et al*., to investigate the effects of reducing the acquisition time (from 30 s to 3 s) with Raman mapping of pharmaceutical beads analysed using principal component analysis.[145] In this and a previous study,[146] Sasic *et al*., used the relative standard deviation (RSD) to compare maps with varying degrees of noise within the raw spectra, but the effect of varying the size of the dataset was not considered. Since the performance of multivariate techniques improves with increased dataset size, the number of spectra within a map is an important variable to consider and this is the first paper to investigate the effects of this with Raman mapping. Krafft *et al.* also demonstrated that PCA could be used to evaluate low SNR data acquired from mapping single cells.[181] However, the focus of this study was on the recovery of biochemical information rather than the implications of reducing the total mapping time. To date, little work has been carried out to investigate the effect of reducing the total mapping time on the data obtained from biological tissue samples. Many of these studies have used mathematically modelled noise rather than actual data.[144,145]

It is well known that larger datasets improve the performance of multivariate techniques. Subsequently it was hypothesised that sufficient diagnostic information, for screening out non-relevant samples, could be extracted from low SNR spectra providing that the dataset was sufficiently large. An initial trial experiment was carried out on a sample containing normal squamous epithelium to demonstrate feasibility, and results can be seen in Appendix C.

Signal to noise (SNR) measurements were carried out on spectra measured on a relatively homogeneous tissue sample containing connective tissue and smooth muscle as diagnosed by an expert pathologist Figure 6-10. Further SNR and relative standard deviation (RSD) measurements were made using a sample containing circumferential normal squamous epithelium. To determine the optimum mapping parameters, the step size (and thus total number of spectra) was varied from 9.5-31.7 μm whilst optimizing the acquisition time to maintain a constant total mapping time of 4.5 h (Table 6-4).

Data analysis was carried out using Matlab and the PLS toolbox (Eigenvector Technologies, Manson, Washing-ton, USA). Saturated spectra and cosmic rays were re-moved by replacement with the nearest neighbour. Principal components (PCs) were calculated and pseudocolour PC score maps were generated. Any remaining cosmic rays appearing in the score maps were blanked out and the PCs recalculated so as not to distort the loads. The relative standard deviation (RSD) (the ratio between the standard deviation and the mean at a given peak position[177]) measured at the 1000cm-1 phenylalanine peak, expressed as a percentage, was used as a measure of the SNR to enable comparison between the different maps. This technique was adopted since the SNR of the raw spectra was low making it difficult to determine accurately. The focus of the laser causes variation in the spectral intensity and SNR at the edge of the sample and in areas where the calcium fluoride substrate has been measured. To overcome this, a region 1/16th of the total map area was selected over the region of connective tissue for the RSD measurements. The area was kept constant for all maps to enable direct comparison. The RSD calculations were performed on normalised data to give an indication of SNR variation only. Spectra with saturations and cosmic rays were not

included in the RSD calculations. Although not directly attributable to the acquired spectra, the 'signal to noise ratio' ('SNR') of the principal component loads was also calculated at the 932 cm^{-1} peak (the strongest peak in the 5^{th} PC load) to provide a relative comparison between the loadings for the different mapping parameters. This was done for the fifth principal component only. The fifth PC was chosen since the psuedocolour score map provided good correlation with the morphology of the H&E sections which was underpinned by good correlation biochemically with the PC load.

This is the first study reporting rapid Raman mapping of biological tissue. Raman maps containing larger numbers of spectra (100,000+ spectra) of biological tissue are presented. There is only one paper in the literature reporting Raman mapping of oesophageal tissue,[123] in which maps contained approximately 2000 spectra (see Appendix D for an examples), therefore, this study presents a significant improvement over map size and image quality (total number of spectra and spatial resolution) due to an increase in the size of the spectral dataset. The effect of varying mapping parameters and the subsequent effect on the PCA is also shown, in particular the consequences of reducing the signal to noise ratio for such large datasets is investigated. This is also the first study to demonstrate that Raman mapping times for biopsies has reduced sufficiently to enable the technique to be used as a histological screening tool.

4.6.4 Raman mapping and linear discriminant analysis to evaluate the importance of lateral spatial resolution for histology diagnosis

As described previously, fresh tissue samples were immediately snap-frozen in liquid nitrogen and stored in a -80°C freezer until measurements were carried out. For each sample, a 15 µm frozen section was cut onto a CaF_2 substrate for Raman spectral mapping, as previously described. A contiguous 7 µm section was obtained and stained with H&E for diagnosis by an expert gastrointestinal registry pathologist. Regions of connective tissue (smooth muscle (SM) and fibrous connective tissue (FCT)), normal squamous (NSq), Barrett's (BO), low grade dysplasia (LGD), high grade dysplasia (HGD) and adenocarcinoma (Ad) were identified. Biopsy samples are typically 1-2 mm in diameter.

Mapped samples were also stained with H&E following Raman mapping to enable better correlation with morphological features. The diagnosis was verified on the mapped section H&E (on CaF_2) by a second histopathologist. Two samples from two different patients have been mapped in this study.

Raman maps were acquired using a customised Renishaw Raman System 1000 spectrometer with StreamLine technology described previously in Section 2.5.3.

An initial rapid pre-scan was carried out using a crude step size (26.4 μm) and short acquisition time (0.5 s). This allowed general morphological features to be visualised so that a region of interest could be identified. Further maps were acquired with step size of 8.4, 4.2 and 2.1 μm with a 15 s acquisition time (to achieve spectra with good signal to noise ratio). It was decided that it was optimum to generate the tissue classification model using good quality spectra, with the prospect of reducing the acquisition times in the future based on results from the previous chapter.

Cosmic rays and saturated spectra were removed, followed by PCA. However, in the case of these maps, data was normalised and mean centred since the PC components would be used to generate an LDA model. Raman maps are not normally normalised and mean centred since this makes identifying changes due to tissue thickness difficult to identify. Also, normalisation including CaF_2 can bias the mean, especially if large areas of the substrate are mapped. However, since the spectra were to be later used in an LDA model (described below), of which CaF_2 would be included as a group in the model this was deemed the best pre-processing protocol.

Pseudocolour PC score maps were then generated as described previously. However, a novel method of displaying the PCs images was developed to assist with identifying different regions of pathology. The pixels of the Raman map were colour coded with the upper and lower extremes of the PC scores and those pixels falling into the central range of the scores were left transparent to enable the images to be overlaid. This represented the pixels/spectra with the most significant contributions from the positive and negative aspects of the PC loads, respectively. The corresponding PC loads were colour coded

accordingly to enable correlation of biochemical constituents from peaks within the PC loads with morphological information from the pseudocolour PC score image.

Bhargava stated that "the effect of limited spatial resolution on data classification [FTIR] in not entirely clear."[150] In this study, Bhargava investigated the effect of low spatial resolutions (nominal step size). This study looks at the converse of this and investigates the effect of high spatial resolution on classification models, the effects of which are also unclear. This was not feasible for FTIR data, highlighting the advantage of Raman spectroscopic mapping.

To compare the different step size maps, PC fed LDA was carried out (using the first 10 PCs). Spectra were selected using the threshold process described above which highlights regions of pathology. Spectra were classified as either calcium fluoride (CaF_2), tissue border (TB),[*] high grade dysplasia (HGD), fibrous connective tissue (FCT) and luminescence (Lum). Spectra which ambiguously belonged to more than one group (either due to the fact that there are not distinct boundaries or the spectra found to have overlapping PC load contributions) were classed as 'unknown'.

Two PC fed LDA models were generated for each map. The first with the unknown group included as a separate group to investigate misclassifications within the LDA. For the second model, the unknown group was excluded from the model and subsequently projected onto the classification model as an independent test data set.

To further test the tissue classification model, the number of spectra in the training dataset was refined with a stricter tolerance level on the threshold level which was used to select the spectra. A region of unknown spectra (i.e. test dataset) was also defined at the boundary of different tissue types.

---

[*] The idea of classifying pixels as border pixels was also used by Bhargava *et al*. in which they were referred to as boundary pixels and reported as a cause of misclassification.[150]

This was taken one step further by selecting small and well defined regions of each tissue pathology (and CaF_2), with the remainder of the map projected onto the model as an independent test set.

As an extension of this, two samples were stitched together to add further tissue pathologies and to test the classification between different samples. Small well defined regions of pathology were identified in the map using the threshold procedure. The remainder of the map spectra were used as an independent test dataset.

4.6.5 Rapid Raman mapping as a research tool to elucidate biochemical changes associated with carcinogenesis

Previous studies of rapid Raman mapping have investigated the limitations of the system with respect to clinical implementation of the technique. A further, additional benefit of the technique is the application of rapid Raman mapping to investigate subtle biochemical changes occurring in tissue which will help to support clinical implementation and help us to understand carcinogenesis processes.

Oesophageal tissue sections were prepared as described previously. Rapid Raman maps were acquired of two samples containing Barrett's mucosa. The first was acquired with an acquisition time of 60 s and step size of 1.1 μm and the second mapped with an acquisition time of 40 s and step size of 3.2 μm.

PCA was carried out on the samples. The larger maps were cropped to focus on regions containing only Barrett's glands to remove variance associated with other pathology types present in the sample. Peak assignments of the PC loads were carried out to investigate biochemical constituents.

4.7 Methods – 3) Factors limiting translation of Raman spectroscopy to the clinical environment

4.7.1 Comparison of the Raman probe spectra and Raman microscopy spectra

Previous work has been based on Raman microscopy systems ex vivo. To compare the two systems, Raman spectra from two cancer samples were measured using both the Visionex probe (4x15 s acquisition time) and the Raman System 1000 microspectrometer (4x15 s acquisition time) with the x50 Leica long working distance objective.

Spectra were normalised and plotted to enable comparison of the background and Raman peaks.

4.7.2 Practical considerations

Clinical implementation of Raman spectroscopy for histological diagnosis will require large scale clinical studies to validate methods and to develop large spectral libraries. In order to achieve this, optimum parameters must be determined to maximise collected data for both accuracy of diagnosis and widespread population and pathology representation.

Highly accurate models are clearly fundamental. In a perfect situation, classification models will be infinitely large and comprising of high quality spectra. In a practical sense this is not possible and as with all medical techniques there are trade offs. Considering Raman probe applications for targeted biopsy and Raman mapping for automated histopathology, it is evident that this trade of is spectral quality vs. spectral quantity.

*4.7.2.1 **Ambient light sources***

A range of ambient light sources were tested for peaks within the Raman spectral fingerprint region. This was in part rule out spectral contamination sources for

laboratory experiments (tissue classification models etc.) and also for prospective clinical implementation in a theatre environment. Confounding factors are presented with recommendations for practical implementation both experimentally and in a clinical environment.

*4.7.2.2 **The effect of ambient temperature Raman spectrometers***

The Visionex probe and microspectrometer have been described previously in Sections 4.5 and 4.6.

As described previously, the silicon peak (Si) is used to perform a wavenumber calibration. If the peak was not positioned correctly, an offset correction was applied. The system was switched on and allowed to stand for at least 30 minutes before measurements were carried out. This was to allow the system to stabilize since problems with Si peak position drift were encountered within this time.

To investigate the effect of ambient temperature on peak position, the air conditioning unit setting was altered in 2ºC intervals ranging from 19 to 31ºC (the actual room temperature was also measured). Polymer spectra were acquired using two Renishaw System 1000 spectrometers (830 nm, 5 s, x50 objective) and a Visionex probe system in combination with a Renishaw System 100 spectrometer (830 nm, 30 s). Spectra were also acquired from a neon argon lamp (1 s). At each air-conditioner setting, the systems were allowed to reach temperature equilibrium for 2 hours. Peak positions were plotted against actual room temperature.

A Raman map of the polymer standard was also acquired whilst ramping the temperature up from 19-28ºC using S1000 (1). A 2 mm square was mapped with a step size of 2 µm, with acquisition time of 2 s.

*4.7.2.3 **Reproducibility and transferability***

One of the key areas currently limiting clinical implementation of Raman spectroscopy is reproducibility and transferability. Comparison of spectra between systems will be

vital for generating large tissue classification models in the future. These areas are investigated and potential methods for comparing systems suggested.

4.7.3 The combination of chemometric analysis and Raman spectroscopy for pathology diagnosis – data quality versus data quantity

To investigate this, the classification performance of different models was assessed from a perspective of practical clinical implementation, with the aim of determining optimum parameters for future clinical implementation studies. The number of pathology groups included, dataset size and spectral quality were considered. The overall experimental time and analysis time was also considered.

4.7.3.1 ***Determining optimum parameters for large scale clinical trials***

The final step before clinical implementation is large scale clinical trials to validate techniques. Considering both the Raman probe and also Raman mapping, pitfalls are discussed and recommendations made for robust protocols.

Chapter 5 Results and discussion: 1) Evaluating Raman probes for potential *in vivo* optical biopsy

5.1 Raman probe background signal

The background subtraction process can successfully remove the large background, although as mentioned previously, the consistency of this method still requires further validation. A further area of concern is the broad spectral artefacts in the regions 600-750 cm^{-1}, 750-900 cm^{-1} and 1150-1230 cm^{-1}, marked by an asterisk in Figure 5-1. The latter has also been identified in other studies using the Visionex probe and attributed to silica,[56] although, the lower wavenumber region was not included in this study, the peak in the 750-900 cm^{-1} region is shown in one figure, although not mentioned in the paper itself. However, it is referenced one of the later papers.[141] From measurements obtained in this group, it is believed the background signal may also be attributable to system alignment since the probe background has been seen to vary after realignment. Further work is needed to investigate the sources of the background signal.

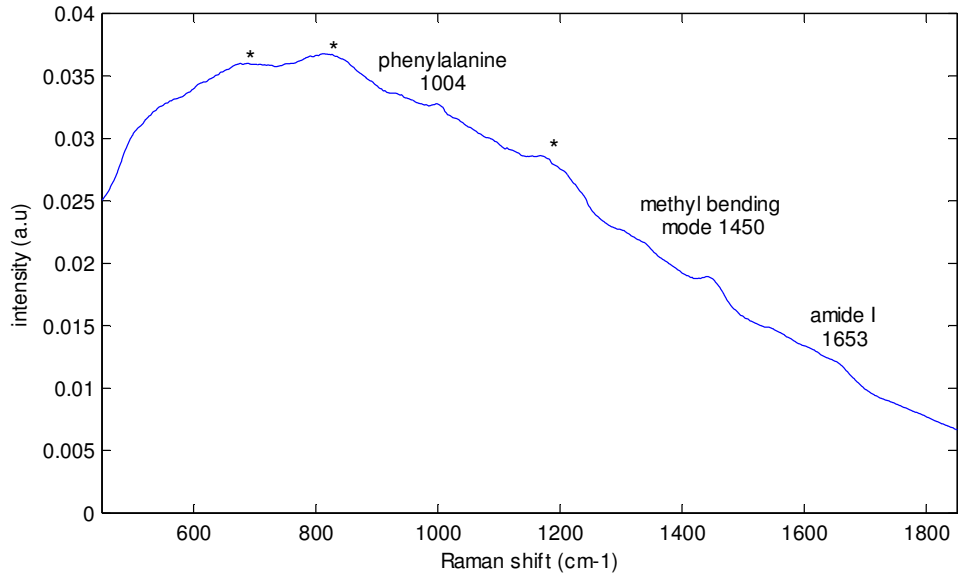

Figure 5-1: Mean spectrum (96 spectra acquired using the Visionex probe 4x15 s acquisition time) illustrating silica peaks marked with *

5.1.1 Background subtraction using iterative subtraction of fifth order polynomial

An example of three mean spectra (taken from the preliminary three group Visionex probe model) can be seen in Figure 5-2. The mean background subtracted spectra (subtraction of a 5th order polynomial)[199] in each of the three classification groups (normal, Barrett's and neoplasia) are shown in Figure 5-3. From the background subtracted spectra, it can be seen that more spectral peaks are evident. However, peak assignment with these spectra should be treated with caution due to silica spectral contributions and possible artefacts resulting from the background subtraction process.

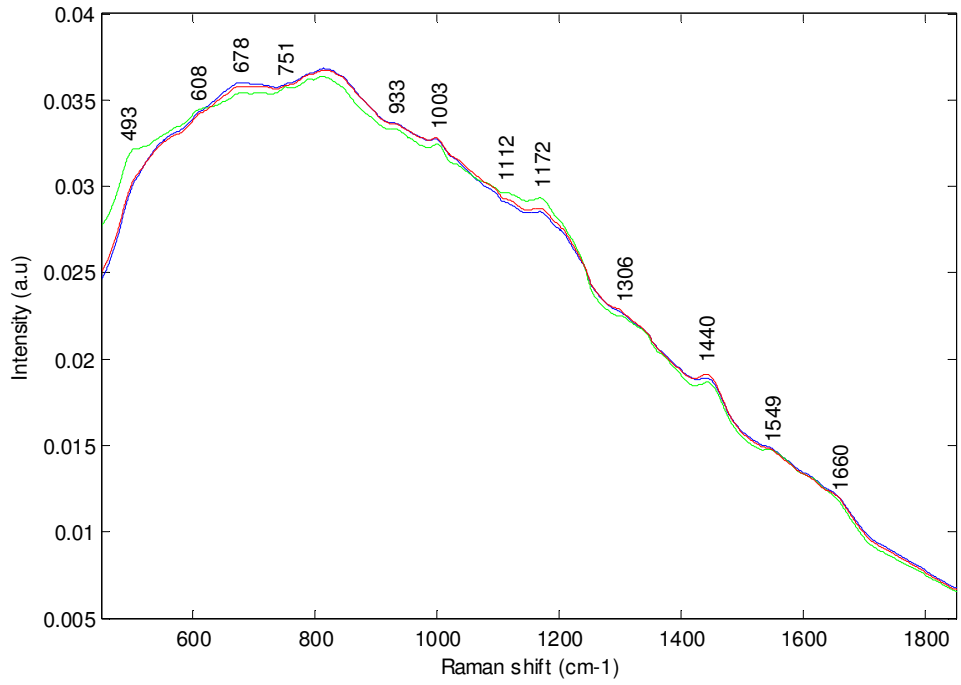

Figure 5-2: Mean spectra from Visionex probe - Green (normal squamous), blue (Barrett's) and red (neoplasia)

Considering peaks common to each tissue groups at 1660 cm^{-1} (amide I), 1140 cm^{-1} (CH_2 and CH_3 deformation), 1172cm^{-1} (C-N stretch, protein, hydroxyproline).

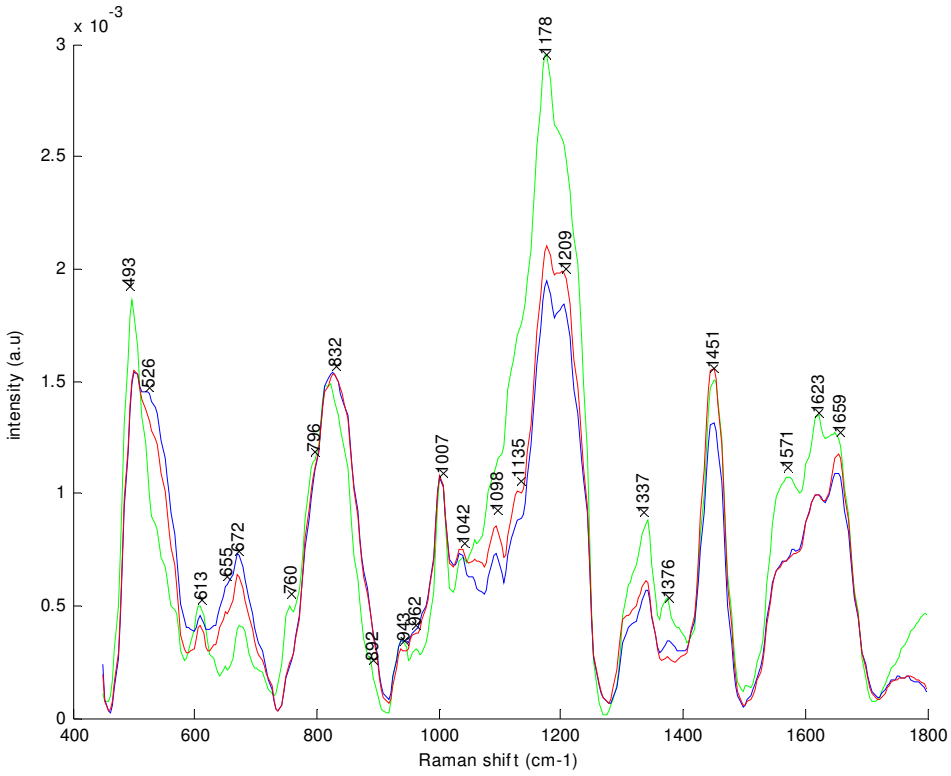

Figure 5-3: Mean spectra Visionex probe (background subtracted) for normal (green), Barrett's (blue) and neoplasia (red)

It is evident that the background subtraction process removes variation at the lower wavenumber regions and broad spectral background peaks are evident in the regions 1150-1230 cm^{-1} and 750-900 cm^{-1}, previously attributed to silica in accordance with literature. This reduction in the variance at lower wavenumbers using background subtraction is also evident in the mean centred spectra (see following sections). However, it remains unknown as to whether or not removing this variance is correct or even beneficial.

Although it is useful to note that there is spectral information superimposed on the peak in the region 1150-1230 cm^{-1}, other spectral peaks in this region could also be attributed to collagen/glycogen (shoulder at 1130 cm^{-1}), tyrosine from protein, collagen (hydroxyproline)(1175 cm^{-1} and 1201 cm^{-1}). This suggests that there is an increased

amount of glycogen in normal tissue, as expected, since glycogen is the cellular energy store which is used up in rapidly proliferating cells.[5]

Peaks can also be identified in the amide I region (1653-1658 cm^{-1}), CH_2, CH_3 deformation (1446-1455 cm^{-1}) and phenylalanine (1005 cm^{-1}). Although, due to uncertainty regarding the background subtraction process it is difficult to draw any real conclusions from these peaks at this stage and more work is required in this area

The peak at 493 cm^{-1} is tentatively attributed to glycogen, which appears to be narrower and shifted to the lower wavenumber range compared to Barrett's and neoplastic mean spectra. However, background peaks have been noticed in this region when measuring thin tissue biopsy samples, which is potentially due to the substrate (CaF_2). Although unlikely since the tissue samples are bulk tissue samples, 5-8 mm thick, without knowing the sampling volume (reported to be of the order of 500 μm in the literature[155]) some substrate contribution is possible since the optical properties of the tissue may vary with pathology for example considering the dense nature of tumour tissues, which potentially could be more optically opaque than normal epithelium. Potential contributions should not be disregarded since the investigation of the optical properties of tissue pathology is an active area of research in itself. To investigate the effects of sampling depth further, the depth profile of two different Raman probes were measured since sampling volume, based on the above mentioned details was considered an important parameter. The results of this are discussed below.

5.2 Comparison of Raman probes

The first comparison of the Raman probes was their signal collection efficiency. Firstly, the power at the laser source, which was measured as 320 mW, was compared to the power measured at the probe tip. The power at the probe tips was measured to be 50 mW and 25 mW for the Visionex and the Emvision probes respectively. The throughput of the excitation fibre for the Emvision probe was approximately half that of the Visionex probe. This agreed with previous measurements using an alternative connection fibre (to link the laser and excitation fibre for the probe), the power at the

probe tip was found to be 22 mW and 9 mW for the Visionex and Emvision probes respectively. In both cases there are considerable losses, although this is expected when working with fibre optics. This poor throughput for the Emvision probe is attributed to the fact the probe system alignment is optimised for the Visionex probe.

Throughput of collection fibres is more important for collection efficiency considerations. The collection efficiency of the two probes was calculated using the height of the diamond peak with respect to the baseline and found to be $3.4x10^4$counts/mW/s for both the Visionex and Emvision respectively. Therefore the probes have equal collection efficiency, but the Visionex returns higher single due to higher illumination powers with the current set up. There is scope for improving throughput as technology relating to fibre connections, and fibre optics is constantly improving.

A key further consideration for Raman probe designs is sampling volume, as discussed previously. To recap, since precancerous changes occur in the epithelial layer, it was concluded that the sampling volume should not exceed 100-200 µm in depth to prevent significant spectral mixing with underlying stromal tissue. To briefly investigate the sampling depth, a study was carried out in which a diamond chip was placed at the bottom of a beaker of water. Spectra were acquired (1s) at 50 µm intervals. The resultant spectra for the Visionex and the Emvision probe can be seen in Figure 5-4.

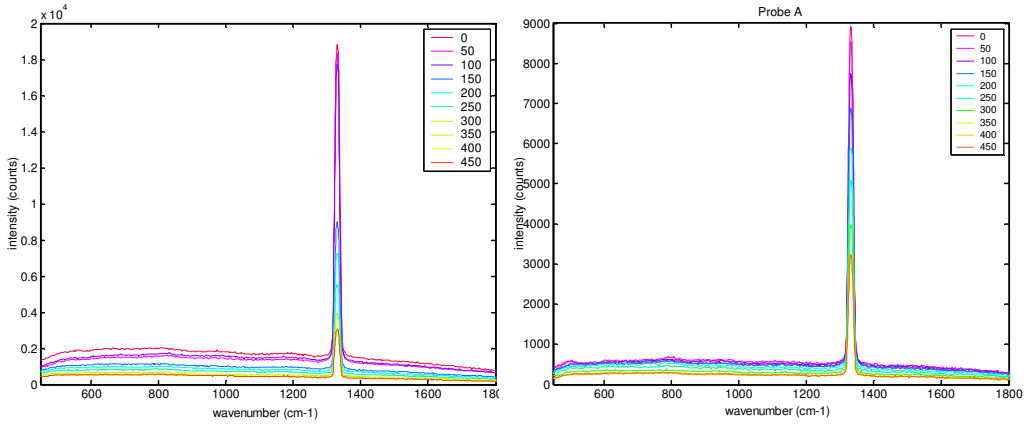

Figure 5-4: Series of depth profile spectra of diamond in water using left: Visionex probe and right: Emvision A probe (first Emvision prototype probe)

It can be seen that there is a variation in signal intensity, and also background between the probes. This was in part accountable by the power output at the probe tip (discussed above. To enable better comparison, the ratio of the peak height (at the maximum signal intensity at the probe tip, i.e. 0 µm) was plotted against distance from the probe tip (in microns), as shown in Figure 5-5. The distance from the probe tips at which the intensity is reduced to half the initial intensity were found to be 150 µm and 280 µm in air for the Visionex and Emvision probes respectively. In water the half intensity depths were found to be 90 µm and 305 µm respectively.

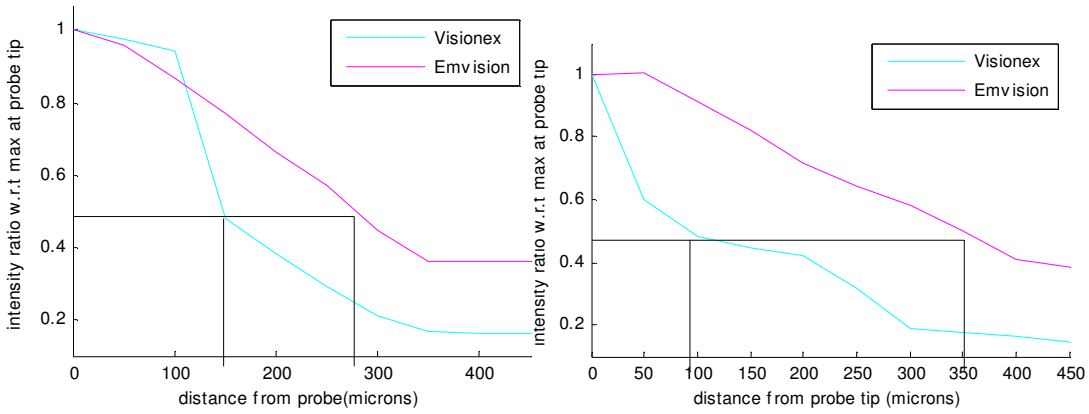

Figure 5-5: The ratio of the peak maximum (at the 1332 cm^{-1} diamond peak) with the peak maximum at 0 µm distance from the Visionex probe in left) air and right) water.

The results agree with the expected profile based on the delivery and excitation volumes described in Figure 2-8, since the signal intensity rapidly falls off with the Visionex probe compared to the Emvision probe. Also, considering the Emvision probe, the ratio rises above 1 at 50 µm from the probe tip indicating that the intensity at this point is slightly greater than that at the probe tip (i.e. 0 µm). This is also expected since, considering the collection and delivery fibres shown in Figure 2-8, there is a region for which, on the central axis, there is a volume for which there is no overlap between the collection and excitation regions. This is less so in the Visionex probe and not evident in the depth profile. The refractive index of water will affect the beam steering, which is the likely cause of why the beam steering is more affected).

This could also be due to issues with the experimental setup since Raman spectra from crystal lattices are known to be dependent on the angle of interface and since diamond was used as the Raman scatterer, this may account for the variation in intensity with distance from the diamond. The position of the diamond was kept constant for both experiments to minimise effects, but this cannot be ruled out. This potential void in the sampling volume may be significant for detecting precancerous changes in surface epithelial layers, so it was concluded that further work would need to be done in the future to investigate the sampling volume in more detail. One potential method of overcoming this problem was to introduce an offset to the Emvision probe tip. This offset would need to be reproducible, for example a physical barrier e.g. on the probe tip to create an air gap. Another option is to use calcium fluoride or quartz, substances which are commonly used as Raman substrates. However, in the latter case, work would need to be carried out to investigate the effects at refractive index boundaries, and also to investigate the optimum offset since to determine the thickness of the offset window, depth profiles would need to be measured using the offset material as a test medium. Offset windows are also likely increase background signals.[166]

There are some other minor issues with the design of this experiment, including the fact that water does not mimic the scattering properties of tissue. Also, it was difficult to ensure that the diamond was on axis, especially at depth. It was decided that maximising the signal at each depth by adjusting the position of the diamond laterally was not feasible since that assumed maximum intensity was on the central axis. Lateral profiles would be required to confirm this. Also, the depth profile appeared to vary with medium, as expected, since neither had the same scattering and attenuation properties of tissue quantification of the sampling volume and depth would have been fruitless. Generating a suitable scattering phantom with the same scattering and attenuation coefficients as tissue was not a trivial study in itself.

Due to the number of points raised in this study it was concluded that significant work needed to be carried out on this area, which was beyond the scope of this thesis. As a result an MSc student took on the project to investigate these issues in more detail and investigations are ongoing.

As a simple test, the diamond chip was measured through an EMR sample which was estimated to be 4-5 mm thick. The diamond peak could be detected with both probes with an acquisition time of only 1s. Although diamond is an extremely strong Raman scatterer, and Raman signals from tissue constituents are not of the same magnitude, this demonstrates that Raman signals can potentially be detected at depth which will have implications for spectral mixing.

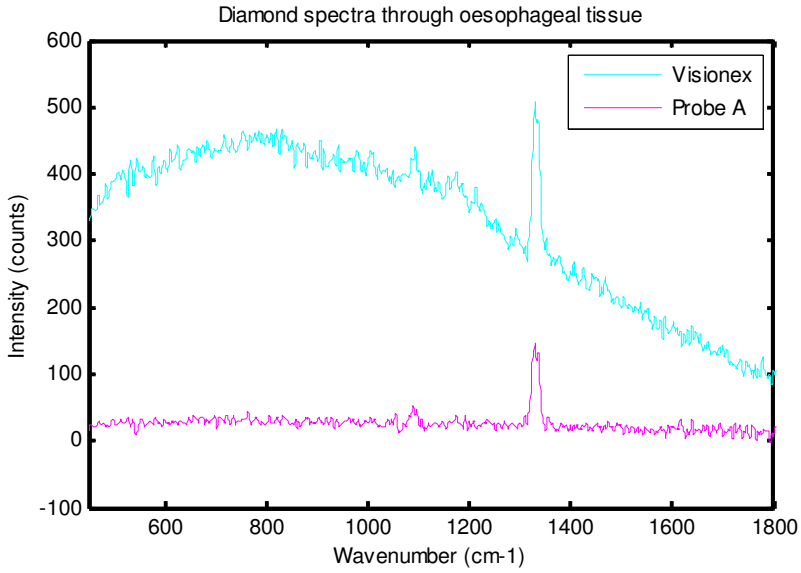

Figure 5-6: diamond chip measured through an oesophageal EMR (1 s acquisition)

As discussed above, the sampling depth of the Emvision probe is greater than the Visionex probe. However, it has been found in a study by our group (results not published), supported by other reports in the literature,[200,201] that there is a biochemical difference between stroma from normal and diseased regions.

Based on this there is also an argument for using Raman probes with a larger penetration depth in combination with probes with a smaller sampling depth, but for tissue classification in both cases it is important to know which depths of spectral contributions so that spectral mixing can be accounted for.

5.2.1 A comparison of probes using calibration standards

Calibration standards measured with the Visionex and Emvision probe illustrate that the background broad spectral peaks may not necessarily be attributable to silica since the spectral peaks are in different positions. They appear to be the effect of a broad luminescence background that is transmitted through the filters.

However, this does imply that green glass correction may be a potential method of background subtraction since the background peaks may be specific to the broad probe background shape. A correction is made for the energy sensitivity throughput of the system using mean luminescence spectra measured from a green glass calibration standard measured at each spectrometer configuration. The results of this are discussed in Section 5.5.3.

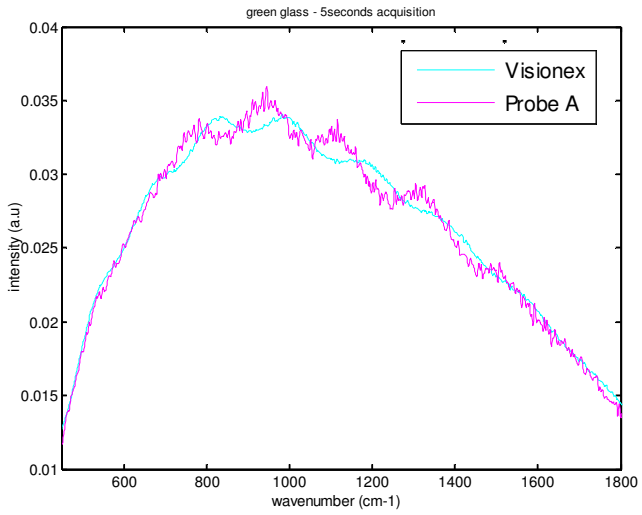

Figure 5-7: Green glass calibration spectra for the Visionex and Emvision probe (Renishaw system 100 spectrometer), measured in contact, with a 1 s acquisition time.

5.3 Preliminary three group Visionex model

5.3.1 Preliminary three group Visionex model with background subtraction

No differences were noted between fresh and frozen samples as found by previous studies within the group.[108,121] Background subtracted spectra acquired from the oesophageal samples with the Visionex probe were used to generate a PC (15PCs) fed LDA model. The LDA model was trained using the pathology diagnosis from each sample (which could be correlated to each individual spectrum). Samples were separated into three different pathology groups, defined as NSq, Barrett's (including IM, fundic and cardiac Barrett's) and neoplasia (which includes LGD, HGD, adenocarcinoma and SCC). Figure 5-8 shows the scatter plot of the linear discriminant (LD) scores, with the normal, Barrett's and neoplasia represented by green, blue and red respectively.

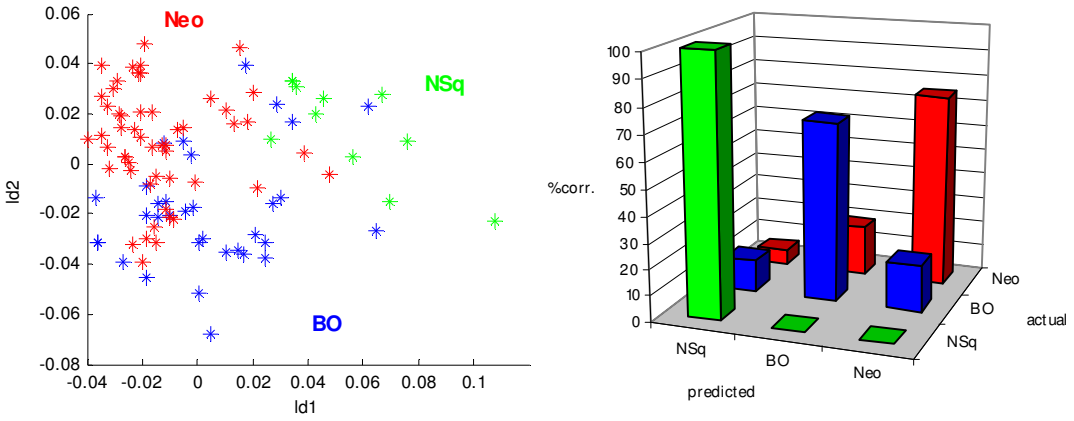

Figure 5-8: Left) Scatter plot of LD1 vs. LD2 for the three group training (normal – green, Barrett's – blue, neoplasia – red) right) Plot showing the percentage classified in each of the 3 groups

Separation can be seen between the three groups visually, although there is some overlap. This can probably be attributed to the fact that the sample numbers are small and the spectral differences are subtle due to the large probe background. The overall training performance of the classification model is illustrated in Figure 5-8. Reasonable correlation can be seen between the Raman prediction and the pathology opinion. The

overall training performance was 76%. Sensitivities were calculated in the range 70.0-100.0% and specificity in the range 84.1-91.8%.

In addition to the relatively poor Raman signal (compared to microscopy based Raman spectra which were used to generate previous classification models), discrepancies can be attributed to the fact that there are not discrete steps in the progression to cancer and as a result, subtle changes between the spectra may cause spectra to be misclassified. Artefacts due to the background subtraction process may also cause problems.

Furthermore, the pathology opinion, used to train the model is not a perfect 'gold standard' due to the difficulties in classifying samples based on morphology. Obtaining a consensus opinion will improve this. The number of spectra and % correctly classified is summarized in Table 5-1.

Table 5-1: The number of spectra in each group and the percentage of spectra correctly classified for the preliminary three group PCA-LDA model with background subtraction

	# spectra	% correct
Normal	11 (out of 11)	100.0
Barrett's	23 (out of 33)	70.0
Neoplasia	39 (out of 52)	75.0
Total	96	

It is evident that the number of spectra in each group is not balanced, with the number of normal spectra significantly lower than the Barrett's and neoplasia groups. This is due to the fact that normal tissue samples are difficult to obtain (only available from patients undergoing the oesophagectomy procedure). It is also important to note that although these samples are defined as normal, they are harvested from normal regions of the oesophagus of patients who have advanced cancer in another region. For this reason, the normal results should be treated with caution since there may be subtle biochemical changes that are picked up in the spectra, but not in the histopathological diagnosis.

5.3.1.1 *Interpretation of PC loads for the Visionex probe tissue classification model*

PC loads for the preliminary Visionex probe model (three groups) are shown in Figure 5-9.

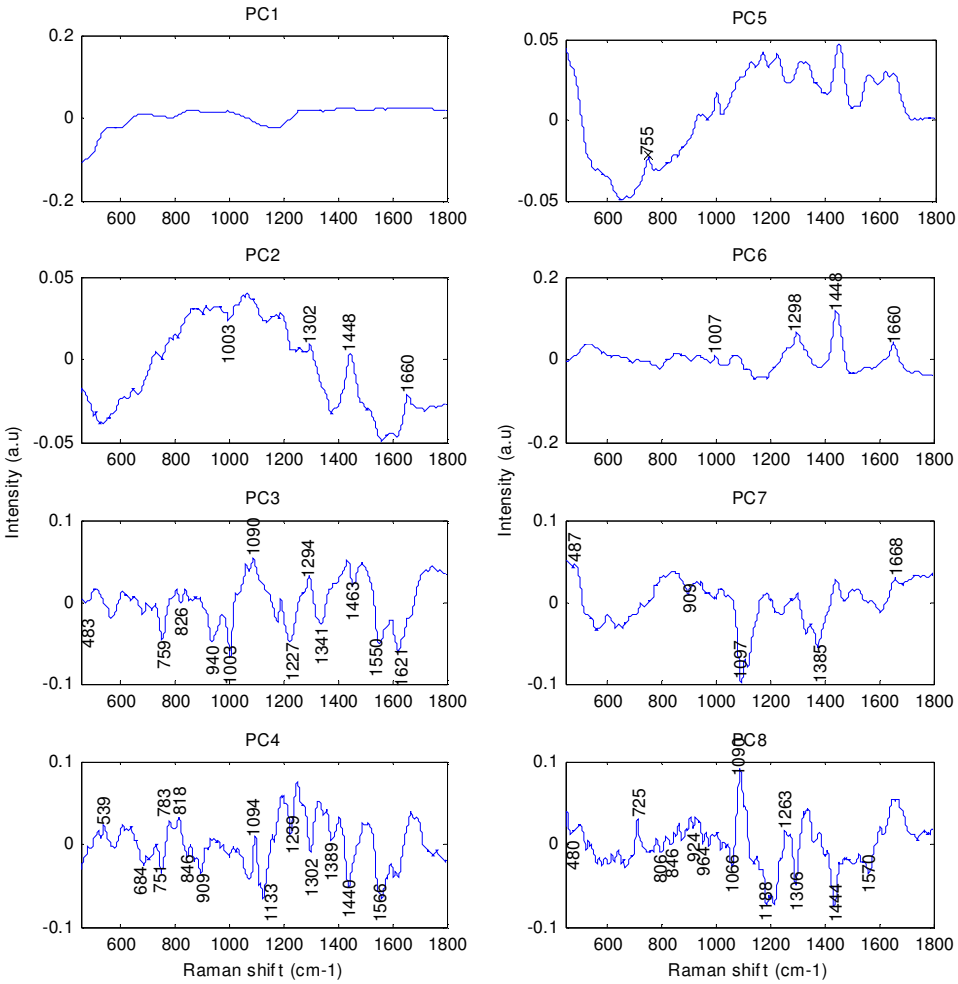

Figure 5-9: PC loads 1-6 for the preliminary Visionex probe (background subtracted) tissue classification model).

The first PC load identifies the probe background. Further PCs identify biochemical constituents which enable the separation of the different pathology groups. General peak assignments indicate protein contributions (1005, 1453-1463, 1640 cm^{-1}) and peaks at 487, and 1089-1110 cm^{-1} which can tentatively be attributed to glycogen. The peak at

785 cm^{-1} could possibly be attributed to the strongest peak in the DNA fingerprint region.

In general, peak assignments on the PC loads are difficult, especially for the probe spectra which are of poorer spectral resolution than Raman microscopy spectra.

Of particular concern is the evidence of the probe background despite background subtraction. To investigate this further, the model was recalculated without background subtraction.

5.3.1.2 Three group Visionex model – analysis without background subtraction

The process was repeated without the background subtraction to check the effectiveness of the process. The overall training performance of the PCA-LDA model was 83.3% with sensitivity and specificity of 81.8-90.1% and 87.3-95.3% respectively. The results are summarised in Figure 5-10 and Table 5-2.

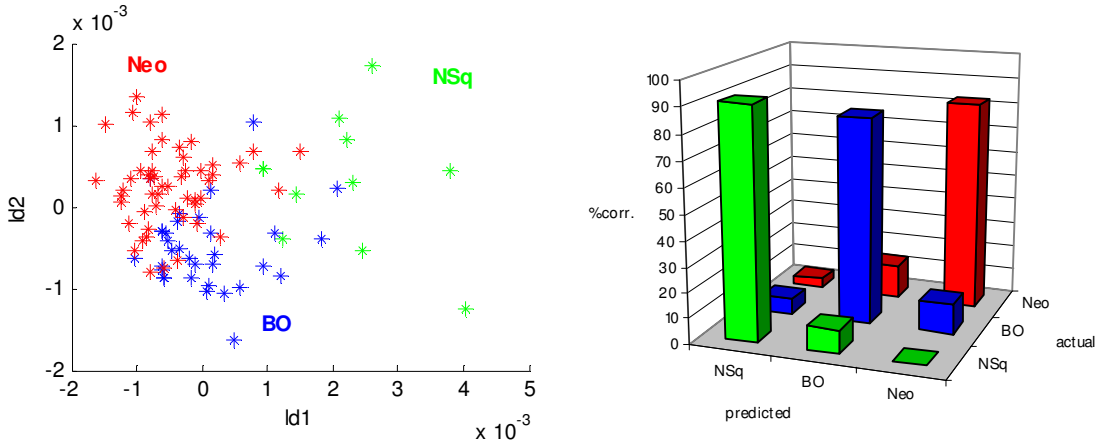

Figure 5-10: left) Plot of LD1 vs. LD2 for the three group training model generated without background subtraction right) Performance of the classification model generated without background subtraction

Table 5-2: The number of spectra in each group and the percentage of spectra correctly classified for the preliminary three group PCA-LDA model without background subtraction

	# spectra	% correct
Normal	10 (out of 11)	90.1
Barrett's	27 (out of 33)	81.8
Neoplasia	43 (out of 52)	82.7
Total	96	

An improved performance was demonstrated, which shows that the PCA-LDA process is sensitive enough to detect subtle biochemical changes despite the large fluorescence background, and perhaps is less of an issue than previously thought. These results also suggest that the process of background subtraction does not adequately remove background signal and accentuates silica peaks which could be potentially mistaken for spectral peaks relating to biochemistry. It is proposed that background subtraction should be not used for multivariate models without further validation. The benefit of the background subtraction, however, is that it clarifies the peaks used when determining the constituent components of the spectrum which further supports the model. The mean background subtracted spectra have been shown in Figure 5-3. However, if the background subtraction process is unreliable as suggested previously, the usefulness of this is in doubt. Investigation of further techniques is required in this area.

It is possible that the mean centring process acts to remove the background sufficiently since the background is actually contained within the mean spectrum. The plot of the mean centred spectra (Figure 5-11) highlights a possible problem at the low wavenumber region suggesting that the background is less consistent in this region.

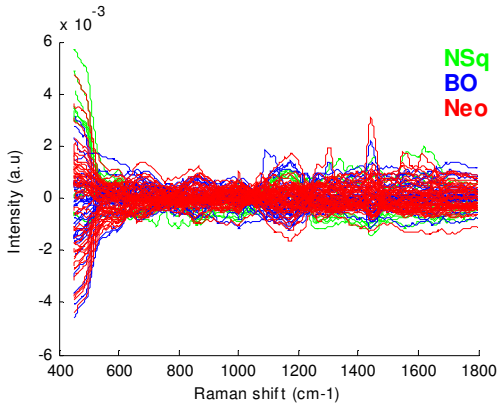

Figure 5-11: Mean centred spectral data colour coded with pathology group

It is evident that there is significant variation at the lower wavenumber range (i.e. 450-600 cm^{-1}), likely to be caused by variation in the probe background. This indicated truncation to remove this region was potentially beneficial (as investigated in Section 5.3.3.

PC loads 1-6 can be seen in Figure 5-12 for comparison with the previously calculated model with background subtraction. In general, the background appears to be represented in PC load 1 and 2, with the remaining PC loads containing similar peak.

Results suggest that background subtraction should not be used for PCA fed LDA tissue classification models, which is also supported by Shaver.[187] Since an improved training performance was achieved without background subtraction, and it is advantageous to minimise data processing, especially if artefacts are introduced, it was decided that further models would be generated without background subtraction. To confirm this, model iterations were carried out varying the number of PCs used to train the model.

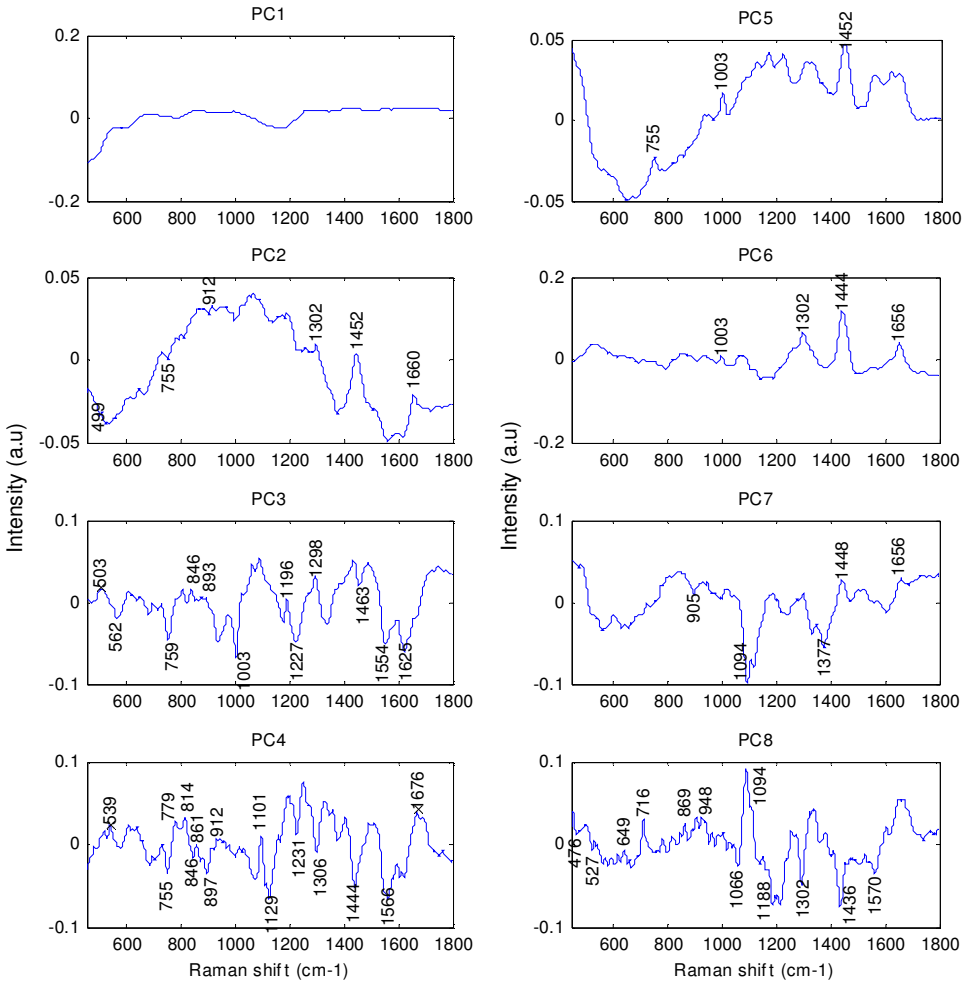

Figure 5-12: PC loads 1-6 for the three group preliminary Visionex probe model (without background subtraction)

5.3.2 Assessment of the number of PCS for training model generation

Figure 5-13 shows the overall accuracy for the preliminary probe tissue classification model trained with different numbers of PCs. The number of PC loads contributing to the model was increased from 3 to 30 and the model recalculated. This was repeated for both models with and without background subtraction. Similarly, the sensitivity and specificity ranges are also shown in Figure 5-14.

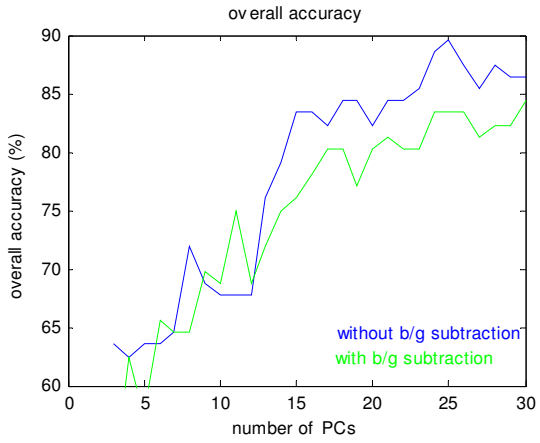

Figure 5-13: Overall accuracy of the three group preliminary Visionex PC-fed LDA model (trained with the pathology opinion from 1 pathologist) calculated for with (green) and without (blue) background subtraction

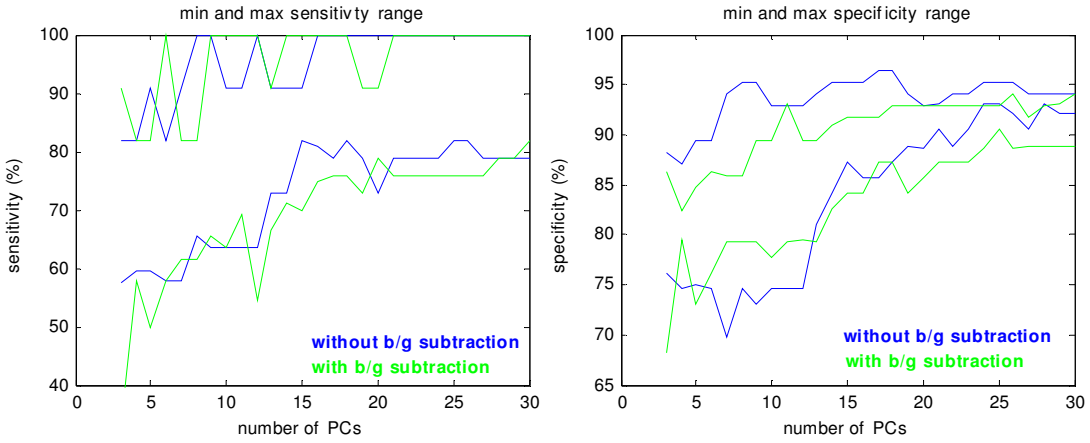

Figure 5-14: sensitivity range for the three group preliminary Visionex PCA-fed LDA model (trained with 1 pathologist opinion) – with background subtraction (green) and without background subtraction (blue)

The overall training performance was generally higher without background subtraction. The sensitivity ranges were similar, whilst there was a slight improvement in specificity. This is a useful finding supported by Shaver who states that background subtraction of polynomials should be used with caution when used with multivariate analysis since the background subtraction routine can introduce large variance which can detract multivariate techniques from more subtle and real variance.[187]

5.3.2.1 ***Cross validation of the three group model***

Leave one spectrum (i.e. sample) out cross validation was carried out on the three group model generated without background subtraction. One spectrum was acquired from each sample, so leave one spectrum out is a reasonable test of the model. However, it must be remembered that more than one biopsy sample is harvested from each EMR, and furthermore, in some cases, more than one EMR is harvested from the patient, so leave one EMR out or leave one patient out would be a more rigorous test, and this will be carried out in the future once a consensus pathology opinion is obtained.

The model performance dropped when leave one spectrum out cross validation was carried out, with only 70.0% of the spectra correctly classified compared to 83.3% previously. The main cause is limited sample numbers, in particular in the NSq group. Therefore further samples are required to validate the model.

5.3.3 Trial model with the wavenumber truncation

It is also noted that there is significant probe background below 800 cm^{-1} and reports in the literature[140,155] suggest that this region should be excluded from the analysis. The model performance could potentially be improved by eliminating this region from the analysis, or possibly selecting regions of interest in the spectra. Since the only problematic region is below 600 cm^{-1} the spectra were truncated to this value. There was no improvement in training model performance, with an overall training performance of 82.3% (based on 15PCs fed into the LDA model) with sensitivity and specificity of 72.7-100% and 84.1-95.3% respectively. The results are summarised below.

Table 5-3: The number of spectra in each group and the percentage of spectra correctly classified for the preliminary three group PCA-LDA model without background subtraction and truncated to 600-1800cm^{-1}

	# spectra	% correct
Normal	11 (out of 11)	100.0
Barrett's	24 (out of 33)	72.7
Neoplasia	44 (out of 52)	84.6
Total	96	

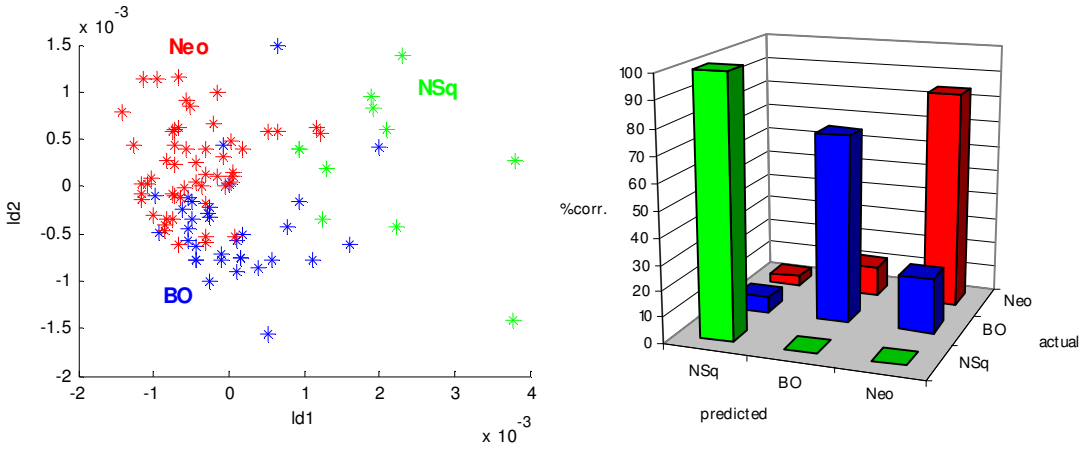

Figure 5-15: left) Scatter plot of LD1 vs LD2 and right) Performance for the three group training model generated without background subtraction and truncated to 600-1800 cm^{-1}

5.4 Visionex model (following CCD replacement)

It is well known, as discussed previously that energy sensitivity correction is required to correct for CCD sensitivity across the wave number range of interest. In particular this is required to correct for alignment issues which alters the light collection path causing subtle variations in the energy sensitivity profile. It has also been touched upon that this will vary from system to system which introduces issues with transferability of data. The following applies within a system when the alignment is changed, for example following the replacements of a major component such as the CCD. The following results were acquired after a laboratory relocation and also CCD replacement on the Renishaw system RA100 spectrometer which is used in combination with the Visionex probe. Based on the calibration data (see Figure 5-24), it was possible to pinpoint the source of variation in the probe background to the CCD change and exclude the laboratory move as the source of the alignment change.

In this model, a significant portion of the spectra were removed due to poor tissue staining and therefore uncertain pathology diagnosis, cosmic rays and also mixed pathology samples.

The initial model was generated including all samples to investigate the effects of mixed samples and cosmic rays on the model performance. The model performance was less than 70% with very poor sensitivity and specificity. Upon recalculation, with cosmic rays and mixed samples removed, model performance improved to 90.1% with sensitivity and specificity 89.5-94.4% and 92.9-100% respectively. This highlights the importance of filtering the training dataset before model generation.

There were still misclassifications, but upon further investigation, these were two Nsq samples which were classified as neoplasia. These two samples actually came from a larger sample which also contained adenocarcinoma (1 pathologist reported this as mucin, the second reported as query cancer – these spectra were excluded from the model since pathology was uncertain.). However, spectra from the NSq regions of this sample were included since a definitive diagnosis was given (by two expert pathologists).

Table 5-4: The number of spectra in each group and the percentage of spectra correctly classified for the three group PCA-LDA model without background subtraction following CCD replacement/alignment

	# spectra correctly classified	% correct
Normal	17 (out of 19)	89.5
Barrett's	17 (out of 18)	94.4
Neoplasia	46 (out of 51)	90.2
Total	88	

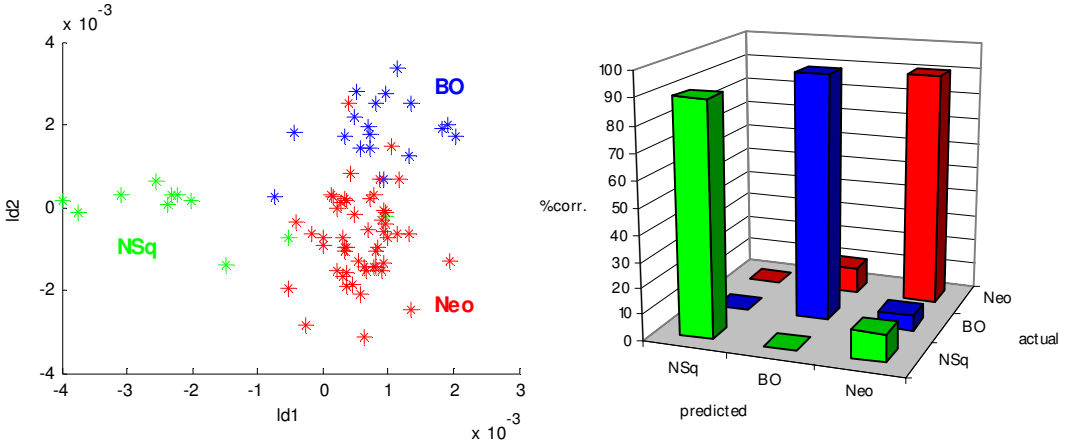

Figure 5-16: Three group probe training model generated using the Visionex probe after system realignment

5.4.1 Cross validation

The cross validation of the model resulted in an overall model performance of 86.4% with a sensitivity and specificity of 83.3-89.5% and 89.2-97.1% respectively. The scatter plot is shown below in Figure 5-17. This model was more robust, most likely to be due to the higher sample numbers in the NSq group.

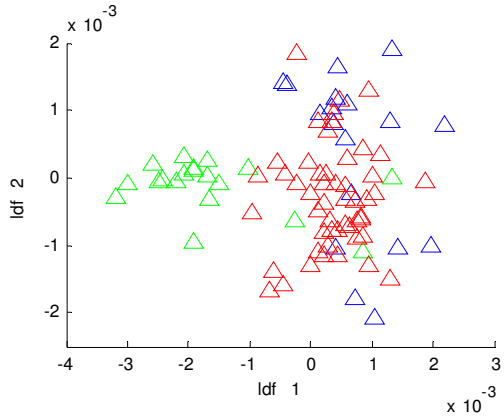

Figure 5-17: Cross validated (leave one sample/spectrum out) for the three group Visionex probe training model generated with 15PCs

5.5 Combined Visionex probe model (pre and post CCD replacement/realignment)

5.5.1 Combining the datasets without processing to remove variation in background

The combined dataset consisted of 184 spectra obtained from 184 biopsy samples from 59 patients. A three group LDA model generated based on the histology diagnosis from one expert histopathologist (Prof. N. Shepherd). The three pathology groups were defined as Normal squamous, Low Risk (Barrett's and Low Grade Dysplasia (LGD)) and High Risk (High Grade Dysplasia (HGD) and cancer). The results can be seen in Figure 5-18 and summarised in Table 5-5. The overall performance of the classification model was 72% with a sensitivity and specificity of 78.4-83.3% and 83.5-96.1% respectively. The majority of misclassifications were between LGD and HGD in the Low risk and High risk groups.

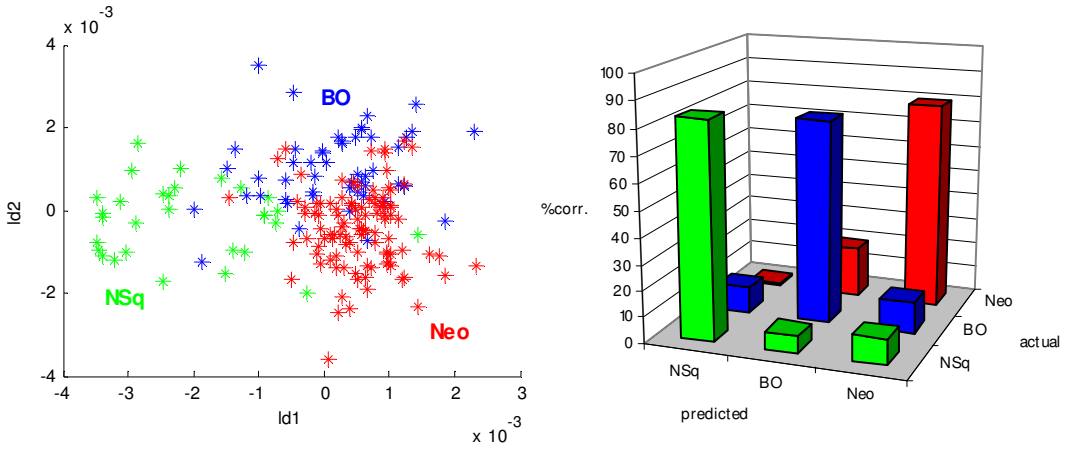

Figure 5-18: LDA classification model trained using the pathology opinion of 1 expert pathologist for the combined (pre and post alignment) Visionex probe

Table 5-5: The number of spectra in each group and the percentage of spectra correctly classified for the combined (pre and post alignment) three group PCA-LDA model without background subtraction

	# spectra correctly classified	% correct
Normal	25 (out of 30)	83.3
Barrett's	40 (out of 51)	78.4
Neoplasia	82 (out of 103)	79.6
Total	184	

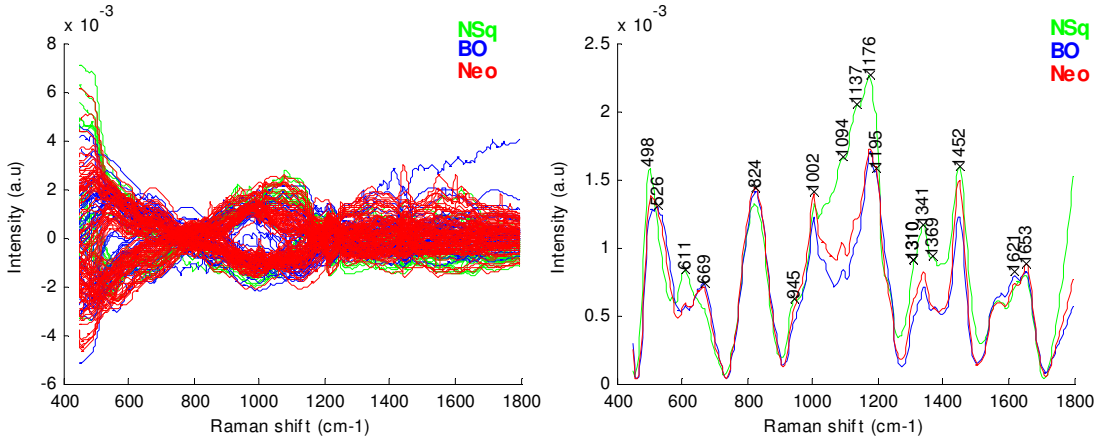

Figure 5-19:left) Mean centred spectra for the combined dataset without pre-processing to remove probe backgrounds (colour coded for pathology group (NSq – green, Barrett's – blue and neoplasia – red), right) mean spectra for each group background subtracted

5.5.2 Removal of probe background variation using PCs to independently reconstruct the datasets

A further option is the removal of the PCs relevant to the CCD background by performing PCA on the separate models, identifying the relevant PC, removing this PC and reconstructing the dataset from the PC scores and PC loads. The two different datasets, could in theory then be recombined and PCA re-run in the absence of the background PCs.

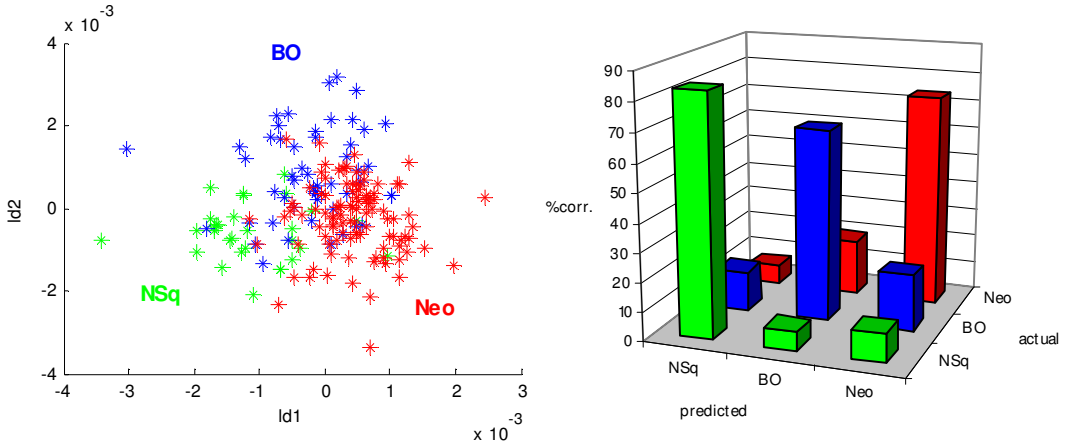

Figure 5-20: Three group Visionex tissue training classification model generated using data combined from before and after CCD replacement, with the background PCs removed

Table 5-6: The number of spectra in each group and the percentage of spectra correctly classified for the preliminary three group combined (pre and post alignment) PCA-LDA model with the background PCs removed

	# spectra correctly classified	% correct
Normal	25 (out of 30)	83.3
Barrett's	34 (out of 51)	66.7
Neoplasia	76 (out of 103)	73.8
Total	184	

The model performance was 73.4% with a sensitivity and specificity of 67.6-83.3% and 83.5-90.9% respectively.

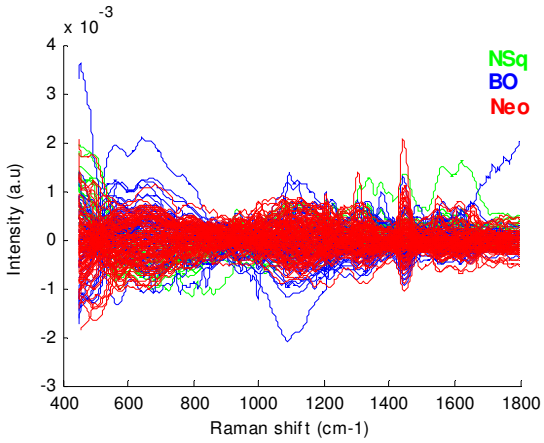

Figure 5-21: Mean centred spectra for the combined dataset reconstructed without background PCS (NSq – green, Barrett's – blue and neoplasia – red)

5.5.3 Removal of the probe backgrounds using energy sensitivity correction

As discussed previously, green glass calibration data had not been acquired routinely, however after analysis of all of the green glass calibration data acquired over the three years, it was evident that there was very little change from month to month and two distinct groups were clearly visible correlating with alignment variation which coincided with the CCD change. It was deemed sufficient to average the green glass correction files for both before and after the CCD change and use a generic correction file to correct each separate batch of spectra.

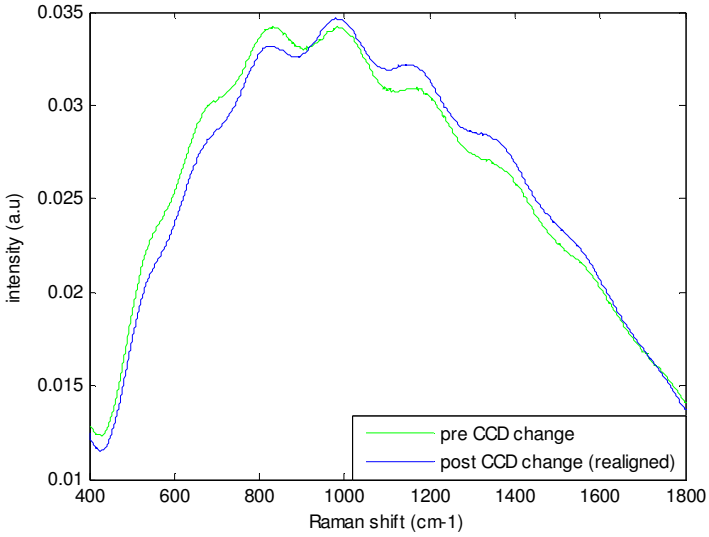

Figure 5-22: green glass calibration spectra (normalised) before and after system alignment problems following replacement CCD

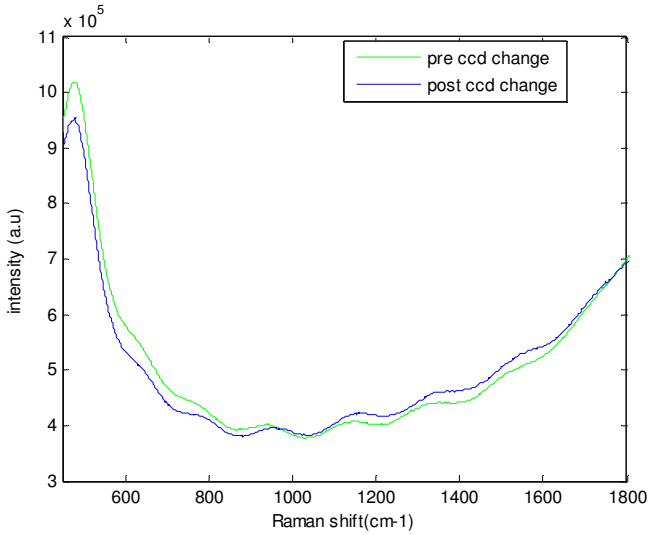

Figure 5-23: white light correction function (ratio of white light energy sensitivity function and the green glass calibration mean spectrum)

Figure 5-24 shows the two different datasets corrected using the green glass calibration mean spectrum. Although, general background is corrected, ripples are still evident and furthermore, there is still an obvious split in the dataset at approximately 900cm^{-1}.

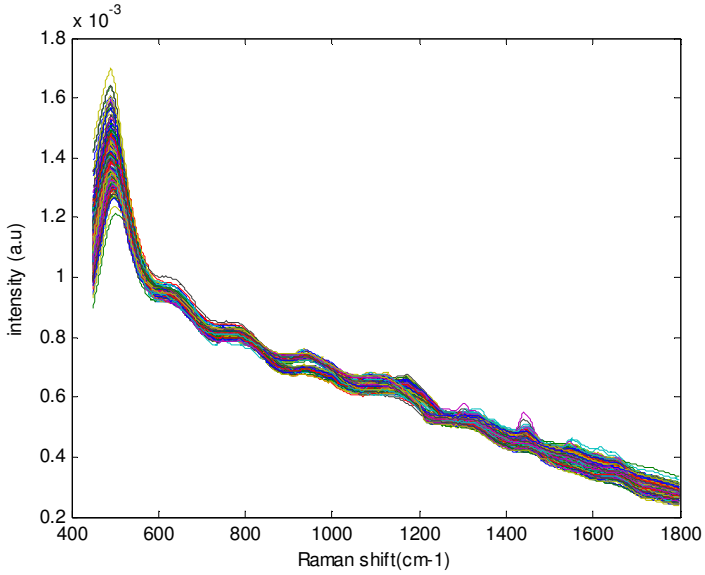

Figure 5-24: Green glass correction of the probes datasets before and after realignment following CCD replacement

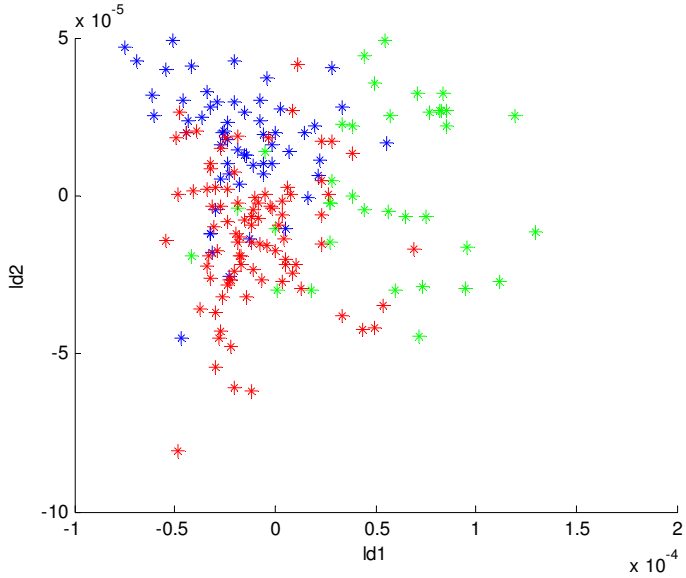

Figure 5-25: Three group PCA fed LDA scatter plot for the green glass corrected training model (pre and post alignment following CCD replacement)

5.6 Short acquisition (4 s) Visionex probe model

The Visionex model was re-generated with consensus pathology from 3 expert histopathologists (110 samples in total). Figure 5-26 shows the scatter plot and bar graph indicating the number of classifications and misclassifications. Model performance improved with consensus pathology opinion to train the model with an overall performance of 82%. The sensitivity and specificity were 77-86% and 87-95% respectively. The number of correctly classified samples is summarised in Table 5-7.

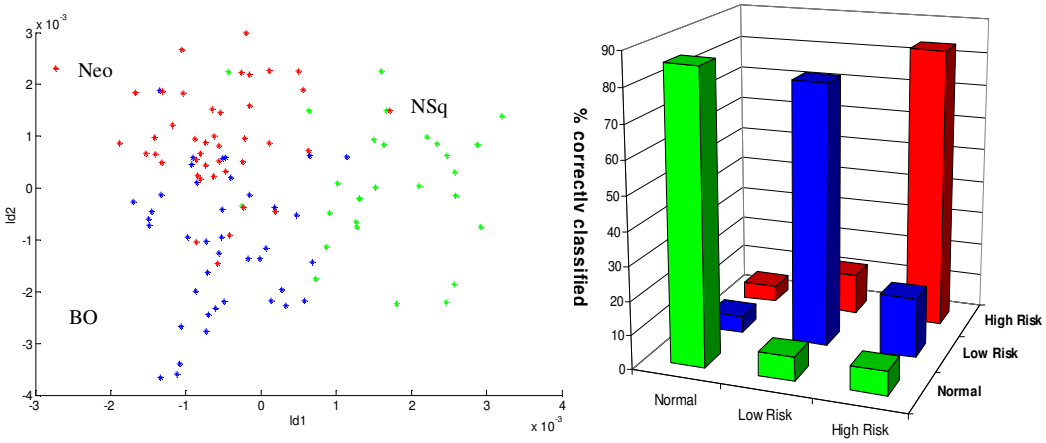

Figure 5-26: LDA tissue classification training model for the Visionex probe (4 s)

Table 5-7: Tissue classification training model for the Visionex probe (4 s)

	# samples correctly classified	% correctly classified
NSq	24 (out of 28)	86%
Barrett's	31 (out of 40)	78%
Neoplasia	35 (out of 42)	83%
Total	110	

5.7 Single output fibre probe tissue classification model

Comparing the collection efficiency by measuring the silicon standard peak at 520 cm^{-1} the single-fibre probe performed better than the multi-fibre Visionex probe (163 counts/mW/s and 74 counts/mW/s respectively).

The results from the novel single output fibre probe are also promising. The 4x15 s classification model (trained with consensus pathology) was able to discriminate normal, low risk and high risk with an overall performance of 90% with a sensitivity and specificity of 85-100% and 95-100% respectively.

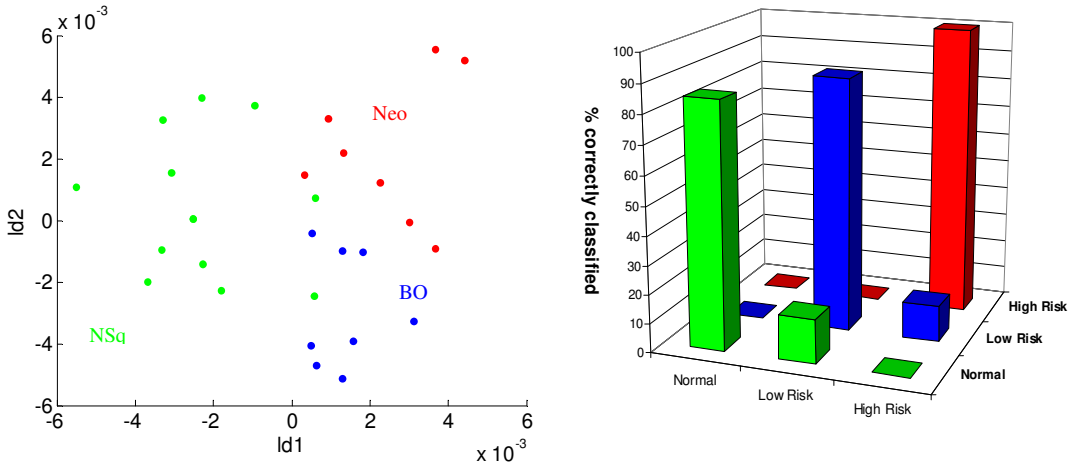

Figure 5-27: Classification model for the single output fibre probe (4x15 s)

Table 5-8: Tissue classification model for the single output fibre probe (4x15 s)

	# samples correctly classified	% correctly classified
NSq	11 (out of 13)	85
Barrett's	7 (out of 8)	88
Neoplasia	9 (out of 9)	100
Total	30	

Model performance of the single probe indicate that it is comparable with the multi-fibre Visionex probe, although sample numbers are very low, this produces an indication of similar future performance compared to the Visionex probe.

The results from the 4 s model were also promising with an overall model performance of 86% with a sensitivity and specificity of 86-88% and 88-100% respectively. Four seconds was chosen since optical components had not been optimised and it was thought to be possible to increase throughput by a factor of 4 leading to a potential sampling time of 1 s in the future. A comparison of raw and background subtracted tissue spectra

is shown below illustrating a reduction in background artefacts with the single fibre probe compared to the multi-fibre Visionex probe. The large background from the multi-fibre Visionex probe dominates the spectrum, whilst for the single fibre probe more tissue spectral peaks are evident. Comparing the silicon standard peak at 520 cm^{-1} the single-fibre probe performed better than the multi-fibre Visionex probe (163 counts/mW/s and 74 counts/mW/s respectively). This may be attributed to the beam steering since there is no penetration of 830 nm light in Si.

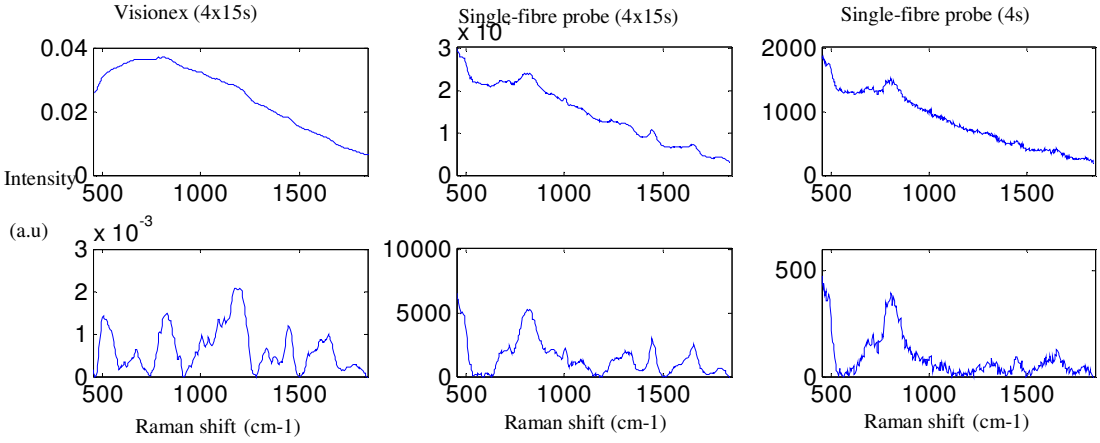

Figure 5-28: Comparison between Visionex probe spectra and single output fibre probe spectra acquired with an acquisition time shown in brackets. The top spectra are raw spectra, the bottom spectra are background subtracted (5th order polynomial)

Although the Visionex probe has been shown in this study and others to successfully classify pathologies,[158,202] a smaller probe with a reduced background Raman signal would be more suitable for *in vivo* diagnosis in the oesophagus, further more the Visionex probe is no longer manufactured and thus an alternative is required. Initial results from the single-fibre probe are encouraging, the sample size is small (30 samples from 30 different patients) and a larger study with more samples and patients is required to further validate the model. More samples will enable separation of a greater number of pathology groups. The sampling depth of the single-fibre probe is less than the Visionex probe and as a result should ensure that there is no spectral contribution from underlying stroma. Further work is required to verify this. Cross validation needs to be carried out to ensure the classification models are robust. Development of a large

consensus pathology model using the optimised design of the single-fibre probe is now required before *in vivo* use.

Cross validation was not carried out for this model since limited sample numbers did not permit this.

5.8 Summary

These results have shown that the Visionex probe can successfully discriminate three oesophageal pathology groups *ex vivo* with good sensitivity and specificity in a cross validated PCA fed LDA model. It was concluded that the current version of the Emvision probe was not suitable for oesophageal applications due to the large sampling depths, since as described previously, probing the superficial layers (~200 μm) will be most beneficial for detecting the earliest pre cancerous changes. As a result, the Emvision probe was not pursued for further investigation, however, the Emvision probe may have a role in detecting deeper cancers or with adaptation by the addition of an offset window for detecting more superficial pathologies. The novel single collection fibre probe proved to have potential with a resulting classification performance comparable with the Visionex, although a further large scale model is required in the future.

In summary, Raman probes (Visionex and novel single collection fibre) have been shown to have potential for biopsy targeting *ex vivo* and that improvements in the single output fibre design could result in further improvements. This implies that further time and effort should be invested in large scale *in vivo* trials once relevant modifications to the probe and housing have been carried out to make it suitable for *in vivo* use (i.e. C.E marking etc.).

In the future, targeted biopsy could be taken to the next step and provide *in vivo* diagnosis. This would have significant implications to clinical practice since *in vivo* diagnosis would allow immediate treatment at the time of diagnosis, resulting in reduced trauma to the patient since only one endoscopy session would be required, and would

also alleviate the stress of waiting for histology diagnosis. The results of this study can also be extended to other treatment sites, in particular other epithelial tissues which often follow the same route of carcinogenesis. This could also lead to a significant reduction in cost to patient surveillance programs by minimising the number of biopsies requiring detailed processing and histopathological analysis.

The classification model performance is consistent with published results using similar probes. Perhaps a two group model is more clinically realistic since this could be set at a level which reflects the clinical borderline between surveillance and opting for treatment. Biochemically, there is no foundation for merging Barrett's and NSq and this is potentially a source of error and should be avoided. Thus, as sample numbers permit, separation into more groups is likely to be more advantageous for improving classification performance rather than grouping dissimilar pathologies to bolster group numbers.

Chapter 6 Results and discussion: 2) Evaluating rapid Raman mapping for potential automated histopathology

6.1 A preliminary study of rapid Raman mapping parameters

Before the rapid mapping system could be used to its full potential, the system needed to be fully tested and evaluated. System parameters which needed investigation included the objective used (see section 6.1.1), grating selection (Section 6.1.2), signal to noise ratio (Section 6.1), step size and acquisition time (Sections 6.1-6.4). The substrate and thickness of tissue sections is also a consideration, and these were determined based on previous work within the group which concluded 15-20 µm sections on CaF_2 were optimum for Raman mapping.[108,121,123] Optimum system parameters also needed to be determined for future mapping studies and a potential large scale clinical mapping study.

6.1.1 Determining the optimum objective for rapid Raman mapping

A comparison of the two objectives was carried out and example spectra acquired with an acquisition time of 5 s can be seen in Figure 6-1.

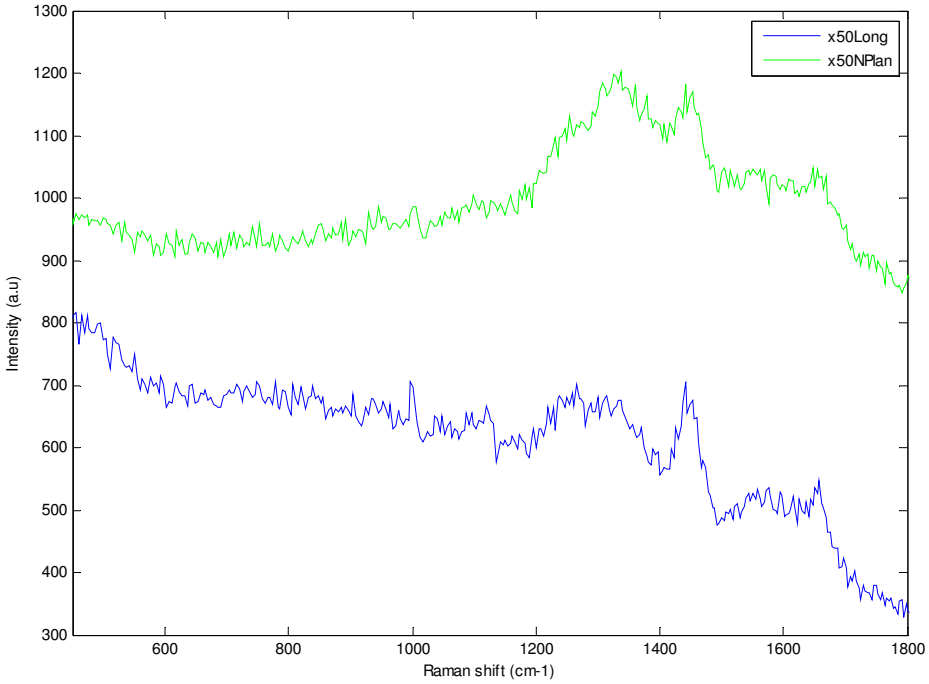

Figure 6-1: Raman spectra of connective tissue acquired using the prototype rapid Raman system (line focussed) at Renishaw Plc. (785 nm) with an acquisition time of 5 s – Nplan (green) and x50Long working distance (blue). An arbitrary offset has been applied since the spectra overlap

The Nplan x50 objective was recommended by the manufacturers but it was concluded that the signal to baseline ratio, and signal to noise ratio were comparable and as a results the Leica long working distance x50 objective was chosen since the reduction in the glass background was considered a significant advantage. Furthermore, peak assignment discrepancies due to the glass background present for the NPlan objective was also considered to be a potential problem for future tissue classification.

As an additional comparison, both objectives were used to obtain maps of a normal squamous epithelium island within Barrett's oesophagus. Raman maps were acquired with an acquisition time of 5s. Two different step sizes were used to ensure maps fitted into the allocated time slots available for the system. The pseudocolour PC score maps and corresponding PC loads (PCs 1-4) are shown in Figure 6-2. PC score images and

loads for PCs 5-8 can be seen in Appendix E. At the time of the mapping experiment the differences in signal to noise with varying step size/dataset size was not known (see following section for further details), but despite the difference in step size, it is still evident that there are background peaks evident in the PC loads (PC 1, 2 and 4),[†] and although other PC loads are similar, the objective background signal will make fitting biochemical constituents to the data difficult and also prevent comparison with previous tissue classification models. These results confirm that the Leica x50 long working distance objective is optimum for future Raman maps for potential automated histopathology.

[†] Recall that the maps were not mean centred, therefore the first PC load represents approximately the mean spectrum.

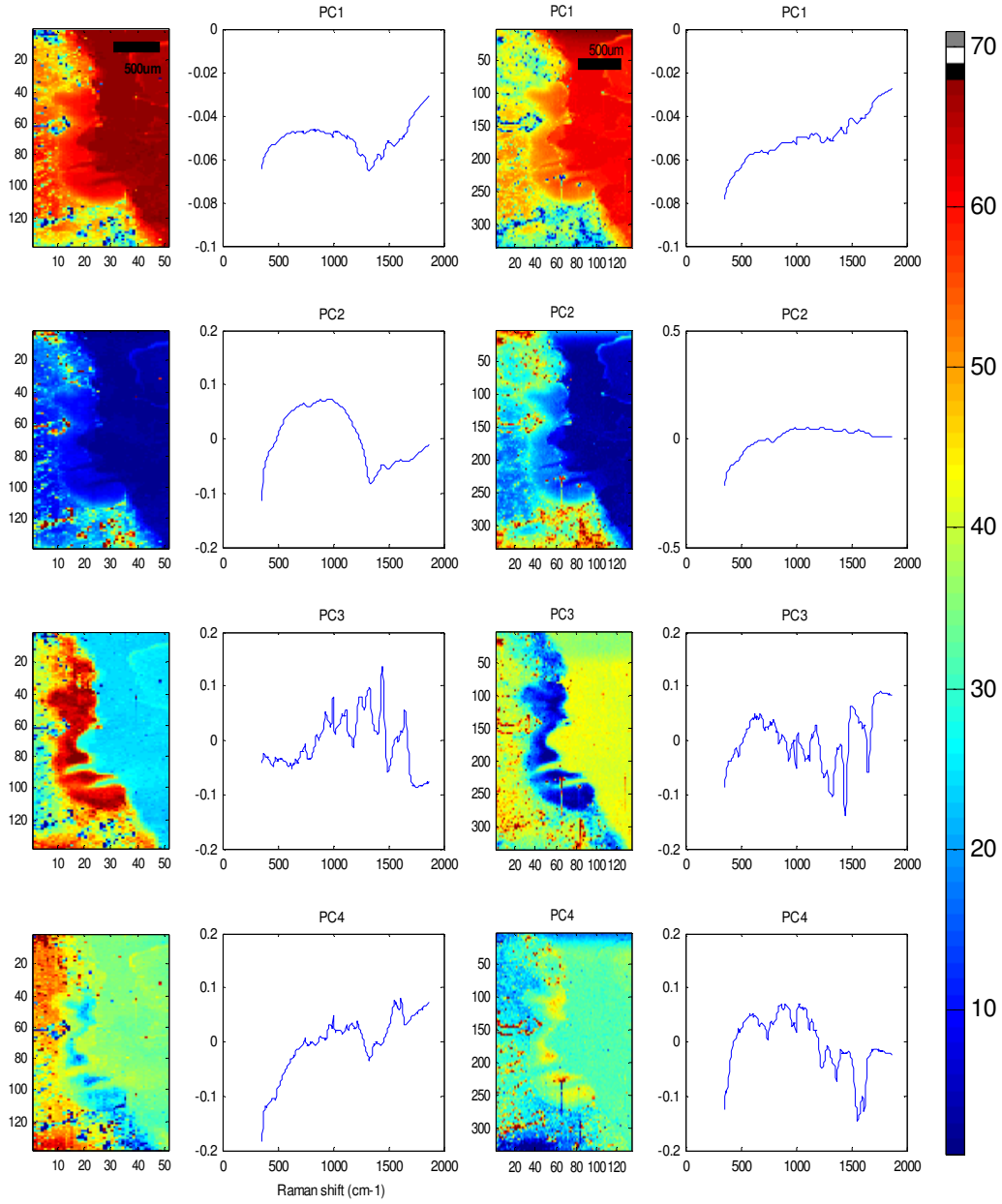

Figure 6-2: PCs 1-4 for comparison of maps acquired with the Nplan x50 objective, 5 s, 27.5 µm step size (left) and Leica x50 long working distance objectives, 5 s, 11 µm step size (right) Note that PC3 and PC4 for the Leica x50 objective, the colour bar is inverted and thus the PC load is also inverted

6.1.2 Rapid Raman mapping with high spectral resolution

An example map of a region of normal squamous epithelium mapped with the 1200lines/mm grating is shown in Figure 6-3. The wavenumber range was centred at 1100 cm^{-1}. The overall map time was approximately 15 hours.

Briefly, subtle biochemical variations are evident with what appears to by glycogen and protein peaks dominating the PC loads, however as previously mentioned this is inconclusive without the remainder of the fingerprint region.

Although initial results were promising it was difficult to attribute biochemical changes based on only a portion of the spectra fingerprint region.

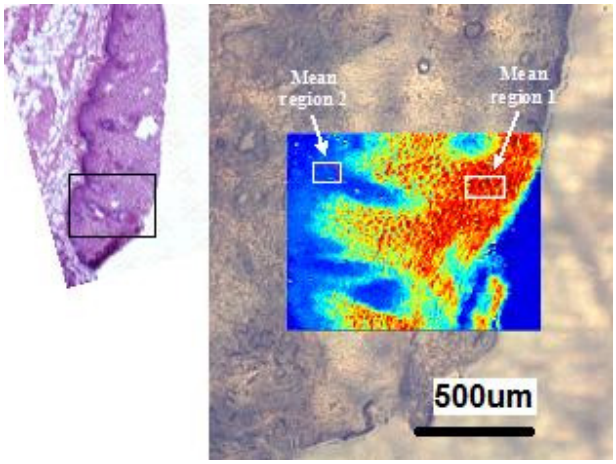

Figure 6-3:An example of a rapid Raman map of NSq epithelium acquired with a 1200 lines/mm grating, x50 NPlan objective, 8.8 µm step size and 30 s acquisition time

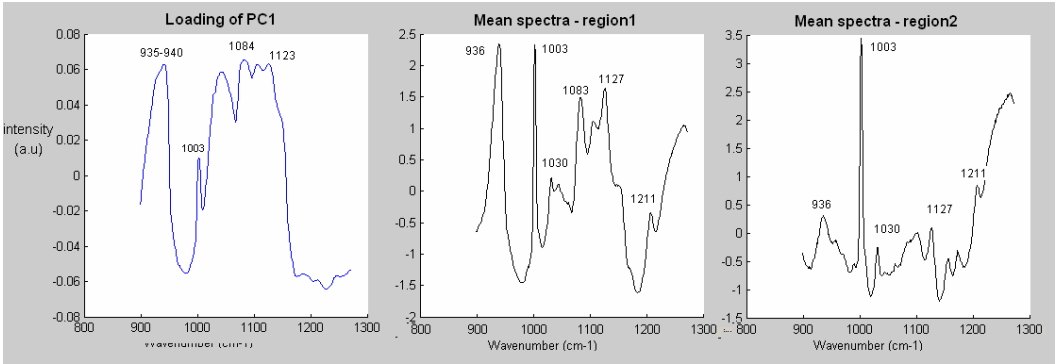

Figure 6-4: PC1 load (corresponding to pseudocolour PC score map in Figure 6-3), and mean regions 1 and 2 illustrated in Figure 6-3

Tentative peak assignments show that the main component separating the two regions is the glycogen, see peaks at 936, 1083 and 1127 cm^{-1}. However, this is difficult to confirm with the limited wavenumber range. Furthermore, collagen peaks in this wavenumber region (931-940, 1003, 1048 cm^{-1}) are very similar to glycogen, making this difficult to confirm. The peaks at 1003 and 1030 cm^{-1} could also be attributed to other protein structures other than collagen. A combination of the above mentioned constituents is likely.[201] To iterate this point, Figure 6-5 shows the similarities of glycogen and collagen IV in this spectral range. Identification of unique peaks (in this example) for glycogen at 492 cm^{-1} and for collagen at 1381 cm^{-1} would help biochemical analysis.

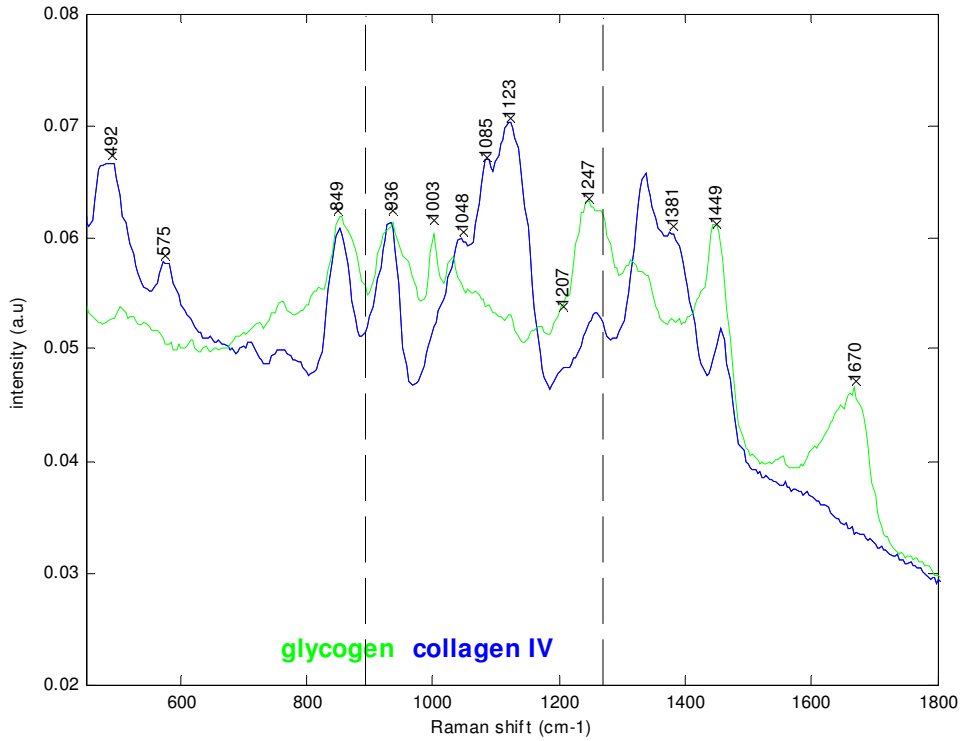

Figure 6-5: Comparison of (normalised) glycogen and collagen spectra (as shown previously, measured with the 785 nm

There is obviously the potential to repeat maps with the wavenumber range centred at different regions and subsequently stitch together retrospectively to form a larger wavenumber range. This is feasible for applications in the research laboratory (discussed

further in Section 6.5), but it is likely that this would be technically demanding and time consuming for application in the clinical environment. CCDs are available which enable high spectral resolution Raman spectra over a wider wavenumber range which may improve tissue classification for Raman mapping and as technology becomes cheaper this may become feasible.

It was concluded that future measurements would be carried out using the 300 line/mm grating since this spectral resolution has been shown to be sufficient for the separation of 9 pathology groups by Kendall *et al*.[1]

A comparison was also carried out with mid-IR absorption spectroscopy, the results for which can be seen in Appendix F.

6.2 Comparison of rapid Raman mapping with point mapping and line focus mapping

6.2.1 Comparison of rapid Raman map spectra with line focus spectra

Rapid Raman mapping provides a significant time advantage over traditional point and line focus mapping techniques as confirmed later in Table 6-3. However, for completeness, these rapid line maps were compared to traditional line focus mapping (described previously).

Considering the raw spectra there appeared to be degradation in the quality of the rapid Raman spectra compared to point Raman spectra. To investigate the sources of discrepancy, a 40s rapid Raman map spectrum was compared to a point spectrum, line map (high spatial resolution line map co-added), as shown in Figure 6-6. The signal to baseline ratio and magnitude of the peaks at 1000 and 1450cm^{-1} are shown in Table 6-1.

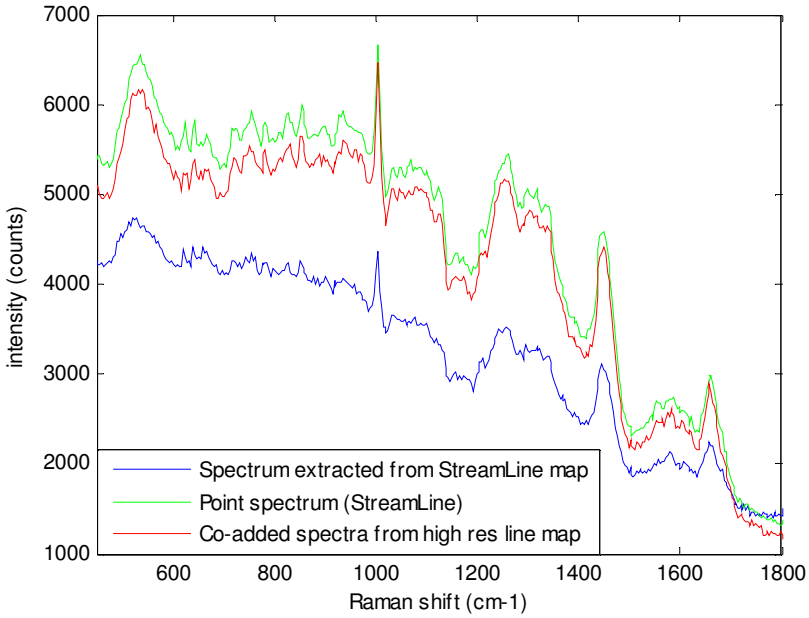

Figure 6-6: Spectrum extracted from a 40 s rapid Raman map (52.8 µm step size), 40 s point spectra, co-added line map (individual spectra from 1.1 µm spatially separated line map (1 laser length) co-added to simulate a point spectrum)

Table 6-1: Signal to baseline ratio and magnitude of the peak height at 1000 and 1450 cm^{-1}

	Signal to baseline ratio (at 1000 cm^{-1})	Magnitude (at 1000cm^{-1})	Signal to baseline ratio (at 1450 cm^{-1})	Magnitude (at 1450 cm^{-1})
Point spectrum	1.3	1431	1.6	1685
Line map (high spatial resolution co-added)	1.3	1574	1.6	1728
Spectrum extracted from rapid Raman map	1.2	748	1.5	968

There is good agreement between the co-added line spectrum and the point spectrum, visually and considering the magnitude of the peaks (Table 6-1), but there is a reduction in intensity of the rapid Raman map spectrum. This appears to be an intensity reduction since both the magnitude of the peak and signal to baseline ratio are reduced.

It is difficult to determine the origins of this discrepancy without access to in depth software and system settings and the difference was reported to the manufacturer. It is

expected that the Raman signal and background increase with acquisition time and that the signal to noise ratio improves according to the square root of n, due to the shot noise dependence. Therefore it is expected that for small step sizes, which are effectively spectra made up from additive multiple accumulations across the length of the laser line, the spectra would have a poorer signal to noise compared to spectra acquired using the entire laser length. In theory, the total intensities should be equal to that of the entire laser line, just split over multiple pixels. However, in this study there appears to be a reduction in signal intensity. From a research point of view it is sufficient to acknowledge the presence of this increased background and make suitable allowances to account for this when performing rapid mapping experiments.

6.2.1.1 ***Results – variation in signal to noise for rapid Raman line maps with step size***

Figure 6-7 shows typical spectra extracted from the centre of each rapid Raman line maps (line maps i.e. only one column of spectra with the centre spectrum halfway vertically in the map). Visually, there was a slight deterioration in SNR with extremely small step sizes (i.e. 3.2, 2.1 and 1.1 μm) but also a reduction in background. To quantify this, the signal to baseline, a method also used by Hayden *et al*., was determined to quantify this and the results are summarised in Table 6-2.

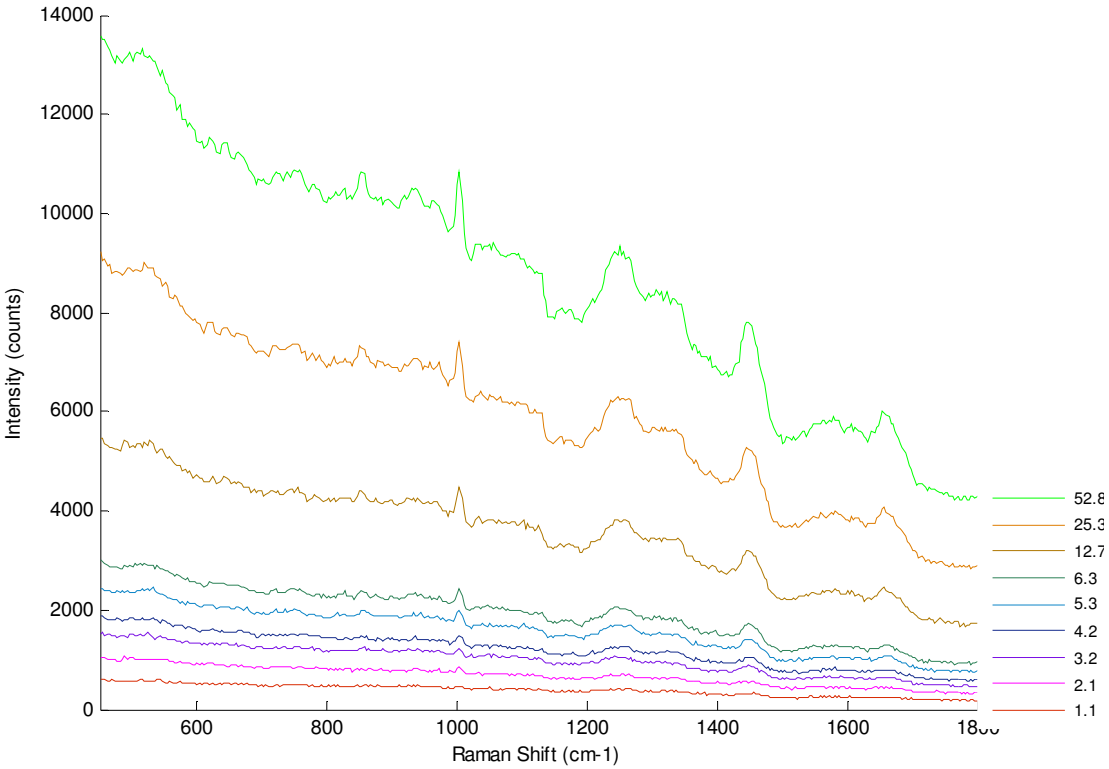

Figure 6-7: Spectra extracted (from the same positions) from rapid Raman maps acquired with different step sizes. The step size is shown to the right of each spectrum

The signal to baseline ratio (defined as the peak height divided by the average of the troughs either side of the peak, taking into account any noise present) was used as a comparison between the spectra since this eliminates variation in signal background. The overall magnitude of the signal was also considered along with the signal to noise ratio, although this quantity is difficult to quantify accurately for good and poor quality spectra. The SNR of the spectra were expected to decrease with decreasing step size since fewer CCD pixels were binned. Since it appeared, that the baseline signal was also increasing along with the Raman signal, spectra were also normalised and re-plotted to investigate whether or not normalisation was sufficient for eliminating background to enable direct comparison of the spectra. This is more evident in the normalised and offset plot shown in Figure 6-8.

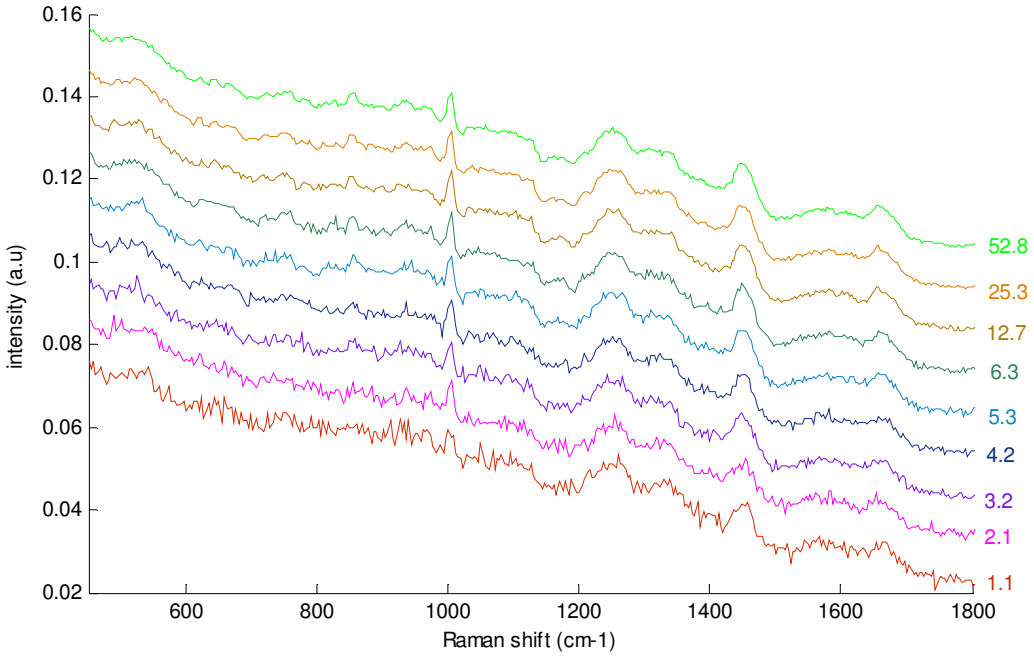

Figure 6-8: Central spectra from the rapid Raman line maps (normalized and plotted with an arbitrary offset)

Since each of spectrum is effectively an accumulation of the entire laser line length, the overall signal from a set of spectra spanning the length of the laser line should be equivalent to that from a single spectrum acquired using the entire laser profile, but as shown in the previous section, there is a slight discrepancy.

Table 6-2: Signal to noise ratio (at 1000 cm^{-1}) and signal to baseline ratio (at the 1000 cm^{-1} and 1450 cm^{-1}) for the series of rapid line maps acquired with varying step size and acquisition of 40 s

Step size	Map dimensions	Signal to noise ratio (at 1000 cm^{-1})	Signal to baseline ratio (at 1000 cm^{-1})	Signal to baseline ratio (at 1450 cm^{-1})
1.1	1 x 1000	5.1	1.09	1.19
2.1	1 x 501	6.7	1.10	1.20
3.2	1 x 335	9.1	1.11	1.21
4.2	1 x 253	11.7	1.11	1.21
5.3	1 x 203	16.2	1.11	1.21
6.3	1 x 170	17.8	1.11	1.21
12.7	1 x 86	25.0	1.11	1.21
25.3	1 x 44	34.5	1.11	1.19
52.8	1 x 22	35.5	1.09	1.19

It is evident that there is little difference in the signal to baseline ratio with step size, however, there does appear to be a slight reduction in the signal to baseline for small step sizes (below 3.2 μm), although to 1 decimal place, there appears to be no variation. This confirmed that taking the mean of a larger number of spectra counteracts the slight degradation in signal to noise with decreasing step size. This data was based on line maps acquired with rapid Raman mapping technology, but when mapping rectangular or square maps the total number of spectra increases by a square factor for each reduction in step size. Consequently, a reduction in noise would be further reduced by averaging effects. This is investigated in the following sections.

Figure 6-9 demonstrates the variation in signal intensity and SNR across the line profile of the laser, with 50 individual spectra acquired by spatial separation of the CCD. The profile from a map acquired of Si (1 s) is also shown to illustrate that the variation occurs due to the laser profile rather than an intensity variation in the tissue. In contrast, the rapid Raman map of the same region is shown which demonstrates that there is no variation with intensity of the laser profile and that this factor is no longer an issue. Bernard et al. also demonstrated this result in another study of rapid Raman mapping for geological applications.[203]

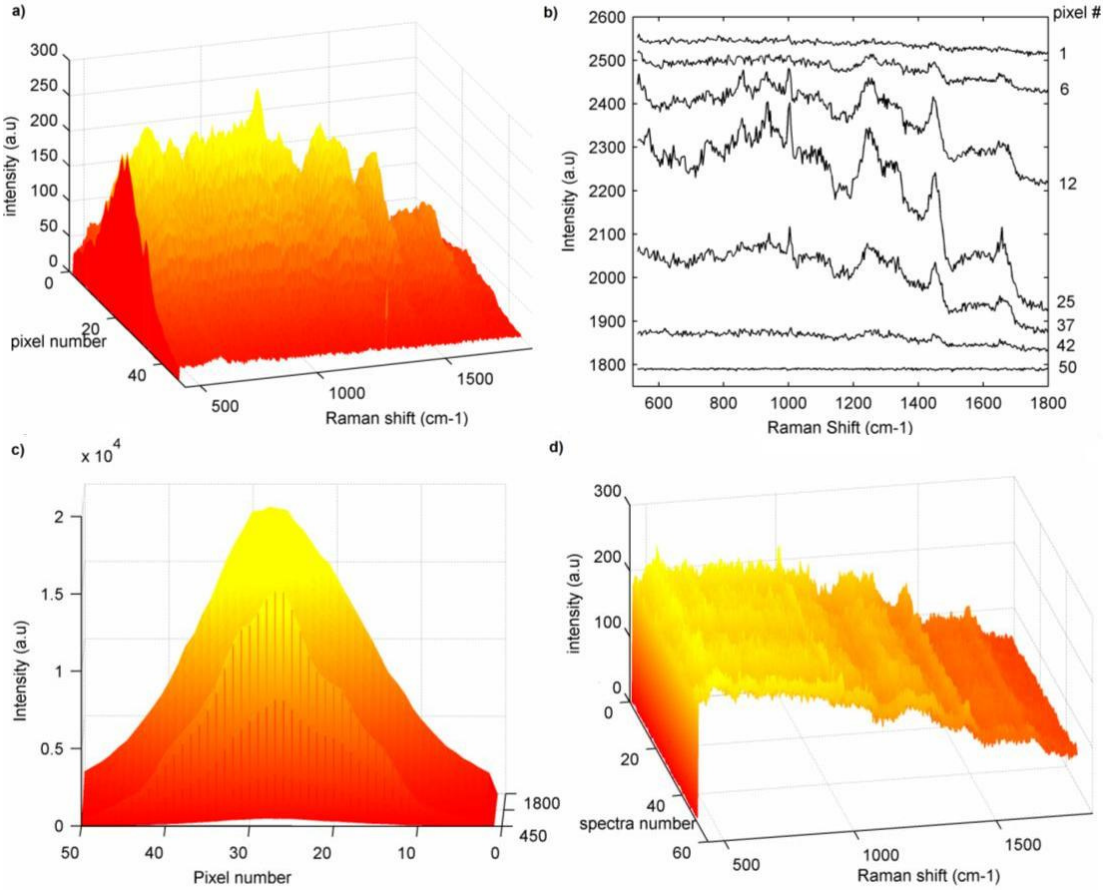

Figure 6-9: a) Variation in intensity along laser line of a line focused laser beam (left axis is 1µm step size along the sample and right axis is Raman shift 450-1850 cm^{-1}) measured on oesophageal tissue, b) Example oesophageal tissue spectra from the line focused line map illustrating the variation in SNR along the laser line (CCD pixels position is indicated to the right of each spectrum), c) Variation in signal intensity (at 520 cm^{-1} peak) along the line focused laser line (for line mapping) measured on a piece of silicon, d) Example spectra at 1.1 µm step size acquired using the rapid Raman mapping system on the same region of tissue as plots a and b, with the spectrum number equivalent to one pixel in plots a-c

6.3 Principal component analysis in combination with rapid Raman mapping for potential automated histopathology

6.3.1 Evaluation of rapid sampling parameters for Raman mapping technology for potential automated histopathology

The results of this study were published in Hutchings *et al.*[204,205] (the latter can be found in Appendix G). Figure 6-10 shows the H&E stained section, contiguous to the sample used in maps A-J, illustrating regions of fibrous connective tissue (FCT) and smooth muscle (SM). The contiguous section to the sample used in maps I-V is also shown illustrating circumferential normal squamous (NSq) and fibrous connective tissue.

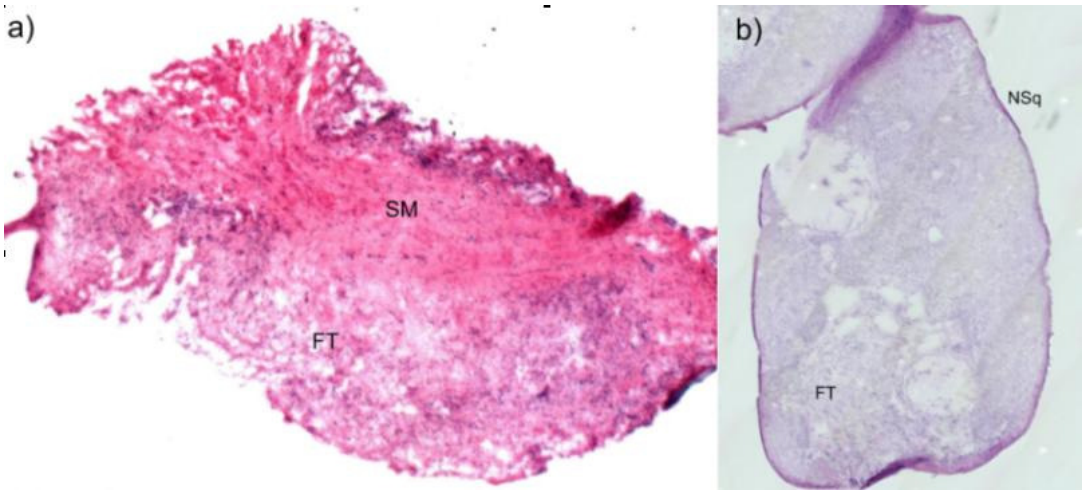

Figure 6-10: Annotated H&E (re-stained) section of the contiguous section to the frozen section used in the repeated mapping studies a) Maps A-J – sample containing areas of smooth muscle (SM) and fibrous connective tissue (FCT) are identified and b) Maps I-V – sample containing circumferential normal squamous epithelium (NSq) and fibrous connective tissue (FT)

PC loads 1-8 are shown in Figure 6-11. PC 5 was chosen for subsequent analysis since this map demonstrated the best biochemical and morphological fit with the pathology diagnosis of the tissue sample. This is further demonstrated in Figure 6-12 in a comparison between the difference spectrum of collagen and actin and PC load 5.

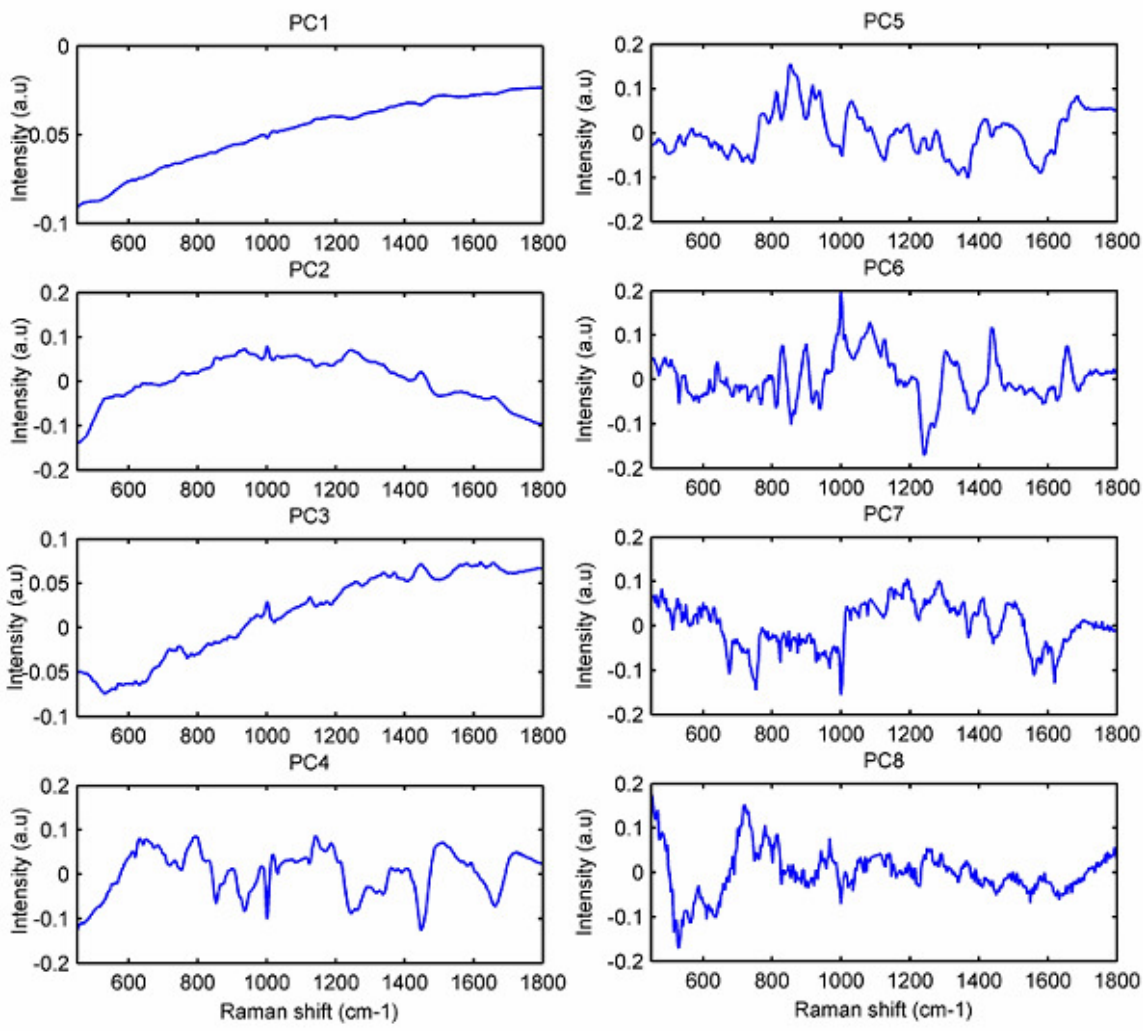

Figure 6-11: PCs 1-6 for map D

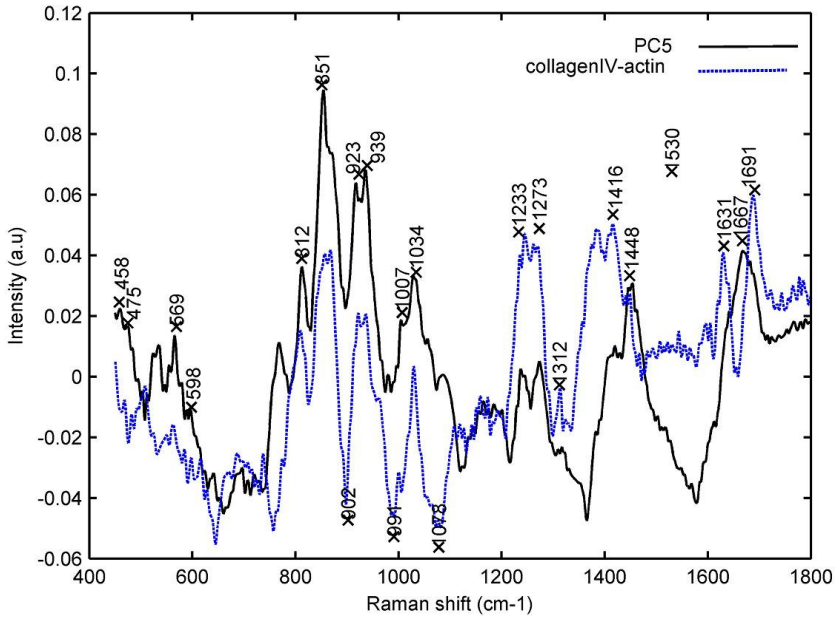

Figure 6-12: Difference spectra for collagen – actin (normalised and subtracted). NB Raman spectra were acquired at 785 nm

6.3.1.1 ***Signal to noise ratio variation in repeated maps***

Figure 6-13 shows pseudocolour score maps (PC5 for maps B-D, F-H and PC9 for maps A and E). Maps A-D were measured with varying acquisition time whilst maintaining a constant mapped area and step size of 25.3 µm.

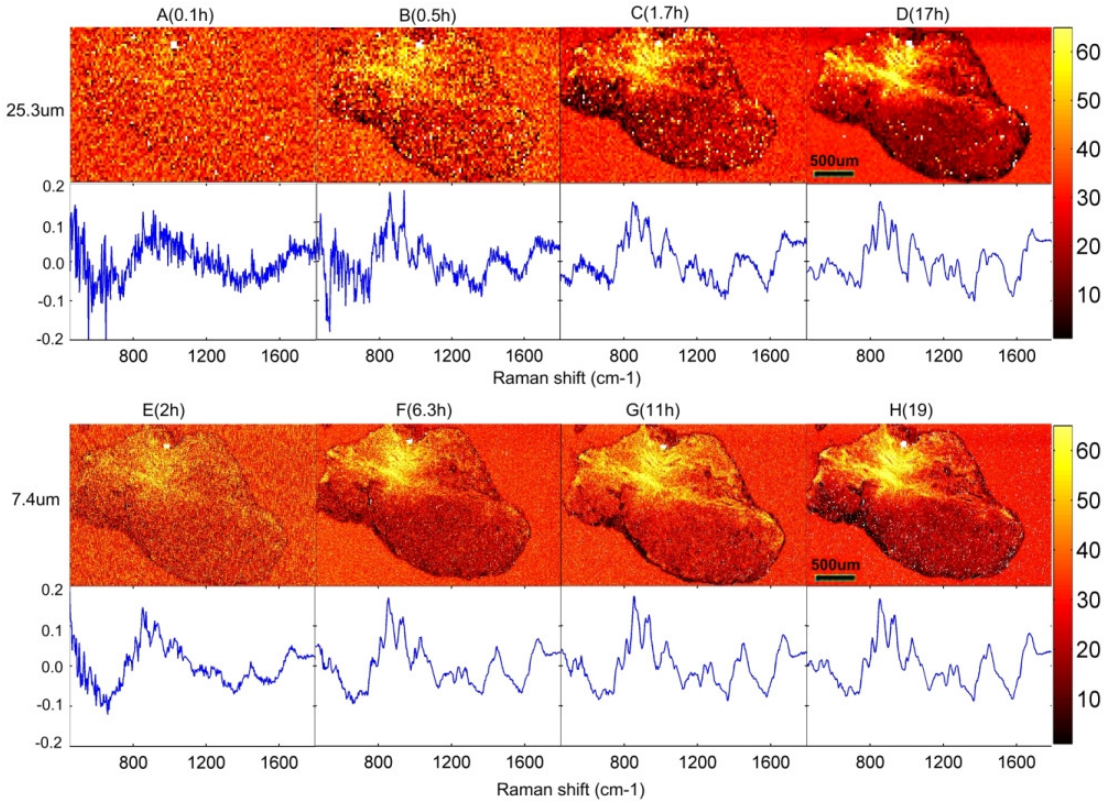

Figure 6-13: Fifth PC pseudocolour score map and corresponding principal component load (Maps A and E displays ninth PC). Maps A-D are for a constant step size of 25.3 µm with increasing acquisition time from left to right of 0.1, 0.5, 1.7 and 20.0 s. The total mapping time is shown in brackets for comparison. Maps E-H are repeated maps using a step size of 7.4µm with increasing acquisition time from left to right of 0.5, 1.7, 3 and 5 s (see Table 6-3 for mapping parameters)

Maps E-H show each of the various acquisition times whilst maintaining a constant mapped area and a step size of 7.4 µm. Maps C, I, J and F (Figure 6-14) show maps acquired with a constant acquisition time of 1.7 s with various step sizes. The fifth principal component load (PC9 for map A and E) exhibits opposing positive and negative peaks which are similar to the difference between actin and collagen spectra (see Figure 6-12 which compares PC5 and the difference spectra of collagen and actin – NB measured at 785 nm), which is consistent with the biochemical signatures of smooth muscle and connective tissue respectively. This agrees with results published by Koljenovic *et al*. who reported the biochemical difference between smooth muscle and fibrous connective tissue in bronchial tissue using PCA and K-means cluster analysis.[177]

However, further work is required to investigate biochemical differences in more detail since, as can be seen in Figure 6-12 there are discrepancies between the difference spectra and PC load indicating that there are contributions from other biochemical constituents.

Morphologically, this also agrees with pathology identified in the H&E sections. For maps A and E, PC 9 exhibited the same morphological appearance and similar loads and as a consequence were used instead of PC 5. PCs 1-4 (PC scores and loads can be seen in Appendix H) describe the mean spectra, difference between tissue and calcium fluoride substrate, small regions of luminescence, and protein distribution. Fibrous connective tissue and smooth muscle are in fact very similar biochemically and as a result this was a good test for detecting very subtle biochemical changes. Further detailed biochemical analysis with this data is possible (beyond the scope of this thesis) but this demonstrates that it is possible to detect gross biochemical changes even with poor SNR spectra.

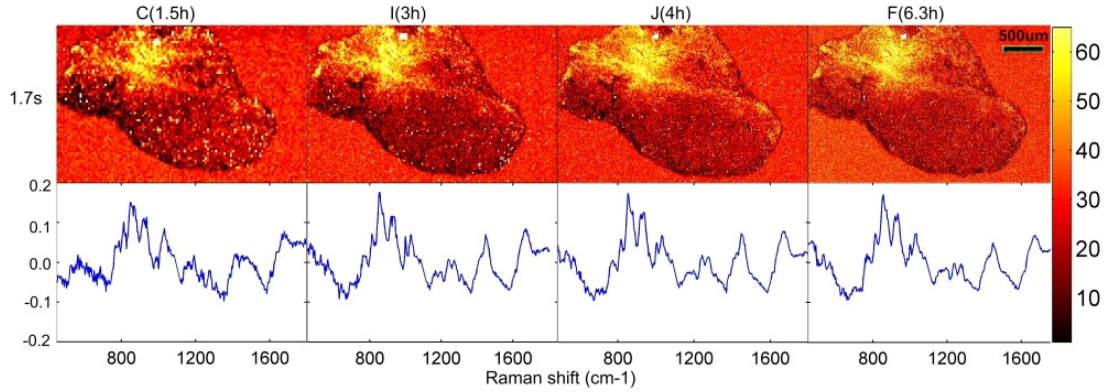

Figure 6-14: Fifth principal component pseudocolour score map and corresponding principal component load for maps C, I, J and F all with a constant acquisition time of 1.7 s with decreasing step size (thus increasing total number of spectra) from left to right of 25.3, 15.8, 10.6 and 7.4 µm (see Table 6-3 for mapping parameters)

Figure 6-15 shows typical raw spectra from maps with acquisition times of 0.5 s, 1.7 s and 20 s exhibiting the quality of the raw spectra within the maps.

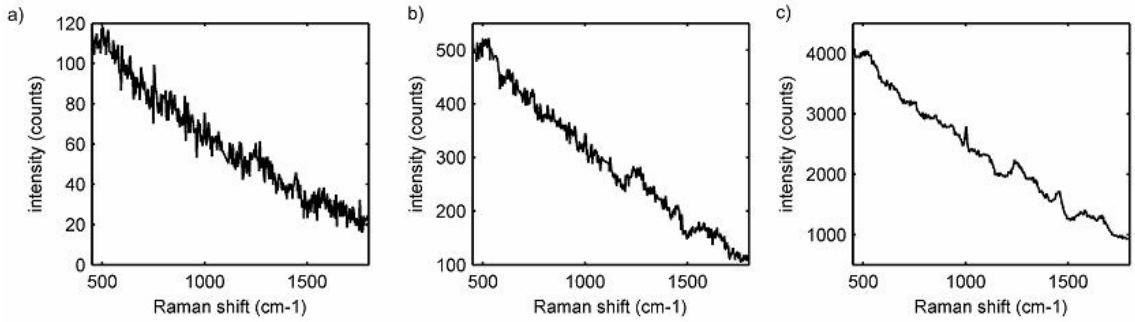

Figure 6-15: Typical raw spectra with an acquisition time of a) 0.5 s, b) 1.7 s and c) 20.0 s taken from map B, C and D respectively

The values for the RSD of the raw spectra calculated at the peak at 1000 cm^{-1} are shown in Table 6-5. They clearly demonstrate that the RSD reduces with increasing acquisition time as expected. For Map D, an RSD value of 2 was considered as a benchmark since the 20 s acquisition time provided a reasonable SNR of the raw spectra. The relative 'SNR' values measured at the 932 cm^{-1} peak of the principal component loads are also shown in Table 3. The corresponding 'SNR' for PC 5 load of map D was also high (>50) as expected. Similarly high 'SNR' values for the loads were achieved with shorter acquisition times provided the total number of spectra was large enough. As expected the relative 'SNR' of the loadings also increased with increasing number of total spectra with maps C, I, J and F. with the 'SNR' increasing from 12 to 44.

Figure 6-16 shows maps acquired with a constant mapping time of 4.5 hours. From left to right, maps I-V were acquired with increasing acquisition time and step size detailed in Table 6-4.

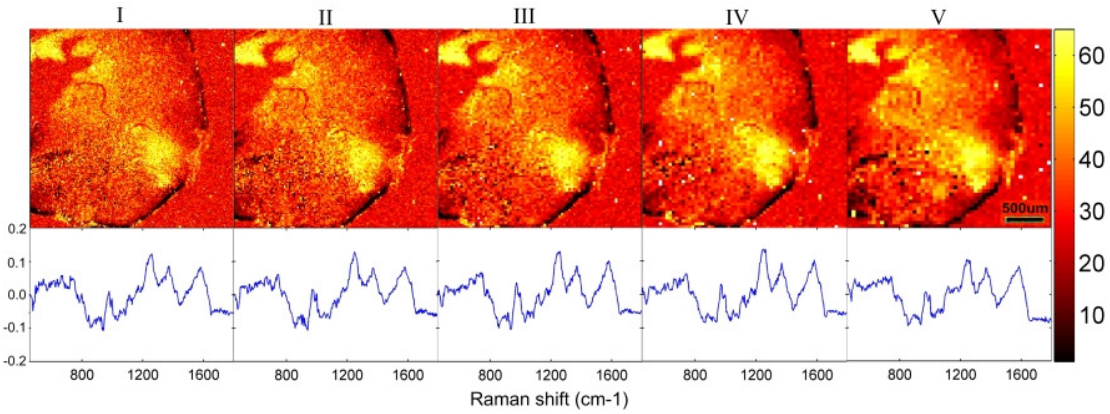

Figure 6-16: Fifth PC pseudocolour score map and corresponding PC load for maps I-V (left to right) all acquired with parameters adjusted to give a total mapping time of 4.5h (see Table 6-4 for parameter details)

There is good correlation with the pathology indicated on the H&E section with circumferential normal squamous identified by the negative peaks of the 5th PC load. Visually, the degradation in the spatial resolution is evident whilst there is little difference between the PC loads. The RSD and 'SNR' results are shown in, which demonstrates a slight decrease in the RSD as the acquisition time and step size are increased. This was mirrored for the previous set of maps (C, I, J and F), all acquired with an acquisition time of 1.7 s, illustrating that this increase in RSD is not linked to the reduction in spectral acquisition time, but more likely due to the number of spectra contained in the area sampled for the RSD calculation. The 'SNR' of the loads remains approximately constant. It should be noted that the 'SNR' values are not directly comparable with maps A-J since they have been measured on different samples obtained from two patients.

Table 6-3: Summary of mapping parameters for repeated maps. Maps A-D are for a constant step size of 25.3 µm, maps E-H are for a constant step size of 7.4 µm, maps C, I, J and F are for a constant acquisition time of 1.7 s. Overall mapping times are shown along with estimated mapping times for traditional point mapping (only applicable to the Renishaw system in these experiments)

Map ID	Step size (µm)	Acquisition time (s)	Total number of spectra	Total mapping time (hours)	
				Rapid mapping (actual)	Point mapping (estimated)
A	25.3	0.1	$0.9x10^4$	0.1	4.2
B	25.3	0.5	$0.9x10^4$	0.5	4.7
C	25.3	1.7	$0.9x10^4$	1.5	6.5
D	25.3	20	$0.9x10^4$	17	29.0
E	7.4	0.5	$10x10^4$	2.0	49.6
F	7.4	1.7	$10x10^4$	6.3	55.2
G	7.4	3.0	$10x10^4$	11	60.4
H	7.4	5.0	$10x10^4$	19	70.8
C	25.3	1.7	$0.9x10^4$	1.5	6.5
I	15.8	1.7	$2x10^4$	2.8	13.9
J	10.6	1.7	$5x10^4$	4.0	27.3
F	7.4	1.7	$10x10^4$	6.3	55.2

Table 6-4: Maps I-V are repeated maps of the sample with parameters adjusted to maintain a constant total mapping time of 4.5 hours. Overall mapping times are shown along with estimated mapping time for traditional point mapping (only applicable to the Renishaw system)

Map ID	Step size (µm)	Acquisition time (s)	Total number of spectra	Total mapping time (hours)	
				Rapid mapping (actual)	Point mapping (estimated)
I	9.5	2.4	$4x10^4$	4.5	23.6
II	12.7	3.0	$2x10^4$	4.5	15.7
III	19.0	4.7	$1x10^4$	4.5	9.6
IV	25.3	8.2	$0.6x10^4$	4.5	9.1
V	31.7	9.0	$0.4x10^4$	4.5	7.4

Table 6-5: Summary of the RSD for normalised spectra (16th of the total mapped area) within each map measured at the 1000 cm^{-1} peak and 'SNR' for the fifth principal component loading (PC9 for maps A and E) measured at the 932 cm^{-1} peak. Total mapping time (in hours) is shown in brackets next to the map ID for comparison

Map ID	RSD (normalised data)	PC (5^{th}) load 'SNR'
A(0.1h)	16	<2
B(0.5h)	7	4
C(1.5h)	4	12
D(17h)	2	>50
E(2h)	11	8
F(3.6h)	6	44
G(11h)	5	>50
H(19h)	4	>50
C(1.5h)	4	12
I(2.8h)	4	14
J(4h)	5	28
F(6.3h)	6	44
I (4.5h)	6	8
II(4.5h)	5	10
III(4.5h)	4	10
IV(4.5h)	4	8
V(4.5h)	4	11

*6.3.1.2 **Comparison with estimated point mapping times***

The ratio of the estimated point map time and overall mapping time for the rapid Raman maps, for various mapping parameters, is shown in Table 6-6. This illustrates the large reduction in mapping time achievable with rapid Raman mapping when compared to point mapping using a standard Renishaw Raman spectrometer.

Table 6-6: Summary of mapping parameters and comparison of total mapping times with traditional point mapping times indicated by the ratio of the estimated total map time using the point mapping technique and the total map time using the rapid mapping technique

Map ID	Acquisition time (s)	Ratio (estimated point map time/ rapid map time)
A	0.1	37.1
B	0.5	10.4
C	1.7	4.2
D	20.0	1.7
E	0.5	25.0
F	1.7	8.8
G	3.0	5.4
H	5.0	3.7
Map ID	Step size (µm)	Ratio (point map time/ rapid map time)
C	25.3	4.2
I	15.8	5.0
J	10.6	6.9
F	7.4	8.8
I	9.5	5.1
II	12.7	3.5
III	19.0	2.1
IV	25.3	2.0
V	31.7	1.6

There is a clear advantage of increasing the number of spectra within the map in terms of the performance of multivariate techniques. In this study, larger datasets were achieved by increasing the spatial resolution but this would also be achieved by mapping a larger sample with the same or lower spatial resolution. Factors limiting the size of the dataset include the 32-bit operating system addressable memory restriction and Matlab's requirement for the entire matrix to be held in a contiguous block. In the case of this study, memory restrictions limited the spatial resolution achievable for mapping the entire biopsy sample since smaller step sizes would have generated excessively large datasets (mapping the sample shown in Figures 3-4 with 1.1 µm step size would result in excess of $5x10^6$ spectra or $7.5\ x10^9$ data points (based on 1501 data points per spectrum).

6.3.1.3 Relative standard deviation (RSD) and signal to noise ratio (SNR) variation

From Figure 6-13 and Figure 6-14, for all maps shown except A and E, it is evident that the fifth PC load represents similar tissue features (in this example tentatively attributed

to collagen which is abundant in fibrous connective tissue and actin which is abundant in smooth muscle) in each of the repeated maps despite the variation in the number of spectra and acquisition time. For map A, noise dominated the ninth principal component load, although tissue peaks can be approximated. Considering map E, these spectral features appeared further down the PC loads at the 9th PC component.

For all maps except for D, for which an acquisition time of 20 s was used, the SNR of the raw spectra was very low (results not tabulated). Therefore the RSD measure was used to allow comparison. Ideally a high SNR would be desirable to ensure that subtle biochemical changes are detected but from these results it is evident that PCA is powerful enough to extract gross biochemical information even with a very low SNR. The RSD calculations on the normalised data (Table 6-5) illustrate the reduction in noise with increased acquisition time. The lowest RSD, as expected, was for the longest acquisition time of 20 s for map D. In general, this was mirrored on the raw data without normalisation (results not shown), although RSD values tended to be higher than expected for larger maps indicating a larger variance, likely to be caused by the presence of luminescent spectra and cosmic rays highlighting the difficulty in 'cleaning up' large datasets. This could also be caused by focusing issues across the sample area.

The relative 'SNR' values calculated for the PC loadings showed improved performance with longer acquisition times, in particular in the case of maps D and H for which the apparent noise was negligible with respect to the 932 cm^{-1} peak within the load.

As expected, the relative 'SNR' of the loadings also increased with increasing number of total spectra with maps C, I, J and F. An additional advantage of improved resolution is improved recognition of morphological features, which will make this technique more acceptable to the histopathologist.

When considering the maps acquired with a constant mapping time of 4.5 h (Maps I-V) it is evident that there is little difference regarding the loads but increased spatial resolution would be beneficial. The advantage afforded by rapid Raman mapping is also greater for higher resolution maps. Increased spatial resolution would also reduce the

effects of under-sampling and the possibility of missing crucial subcellular biochemical information. This would have little consequence for the samples in this study, but may become clinically significant for a sample containing a focus of disease.

The section shown in Figure 6-10 was initially thought to contain a region of inflammation or possibly adenocarcinoma to the bottom left, but this was inconclusive due to very poor staining. Following rapid Raman mapping, in which there was no evidence of a region of adenocarcinoma, this section was re-stained to obtain definitive diagnosis and found to only contain smooth muscle and fibrous tissue. This highlights a further potential advantage of spectroscopic diagnosis which could enable diagnosis of inconclusive sections based on distinguishing biochemical features from unstained tissue.

From Table 6-6 it is evident that rapid Raman mapping is significantly faster than traditional point mapping (from the same manufacturer). As expected there is a correlation between the step size and the speed of the map acquisition and thus there is an inverse correlation with the total mapping time. For a step size of 25.3 µm (maps A to D) rapid Raman mapping was approximately 3 times faster than point mapping for long acquisition times and up to 38 times faster for short acquisition times. Data published previously by Hutchings *et al.*[205] was based on best case scenario point mapping times which significantly underestimated overall mapping times for short acquisition times. With a step size of 7.4 µm (maps E to H) rapid Raman mapping was of the order of 4 times faster than point mapping for longer acquisition times (5 s) and 25 times faster for short acquisition times (0.5 s). Due to the large number of spectra within the dataset the advantage of rapid acquisition of spectra is accentuated.

One option, not considered in this investigation, is the potential to mismatch x and y step sizes to prevent under-sampling when using step sizes greater than the width of the laser line (7-8 µm). This is an area which will need further investigation before optimum mapping protocols can be determined. Further work must also be carried out to investigate the potential problems associated with under-sampling with regards to missing diagnostically significant information. The step size in this study has not been

reduced beyond that of the width of the laser line (7-8 µm for the x50 objective used in this study) due to size limitations on the datasets and also to prevent over-sampling but this is also an area for further investigation since this may provide further benefits with regards to increased spatial resolution and even larger datasets. This may be of particular interest when mapping cells at high resolution and leads to the possibility that biochemical changes within the tissue can now be investigated at the cellular level across larger areas of tissue. One consequence of this would be the need for improvement in computational facilities. The use of 64-bit computers has increased the datasets that can be managed since this work was undertaken.

There is also potential to investigate noise reduction techniques and smoothing of the spectral data such as those available within the Wire 3.0 software and those described by Sasic *et al*.[145]

Potential sample degradation has previously limited the maximum laser power that can be used with biological tissue samples, however with reduced acquisition times there is the potential to increase the laser power and thus improving the signal to noise ratio.

Before an automated screening technique can be developed, further work is also required to develop automated algorithms capable of identifying 'non-relevant' samples so that only diseased samples are forwarded for diagnosis by an expert histopathologist. It will also be beneficial to reduce the thickness of the mapped tissue sections towards the thickness used for H&E histopathology (7 µm), although potentially longer acquisition times may be required to counteract the reduction in Raman scattered photons with the thinner tissue section. One way to counteract this may be to use mirrored slides which maximises the return signal to the objective. This will also have an impact on the spatial resolution which can be achieved at smaller step sizes.

Each map contains a vast amount of biochemical detail and work is ongoing to explore information regarding the carcinogenesis process.

The use of PC load 'SNR' and RSD are relatively arbitrary methods of comparison, but methods were reproducibly determined for each of the maps to enable direct comparison between the repeated maps, however it must be noted that the values are not comparable between different samples due to differences in sample biochemistry and mapping conditions.

It should also be noted that there was no evidence of spectral difference between the first and the last map, furthermore, maps were acquired in a random order to prevent any systematic errors with time and sample state.

Rapid Raman mapping has enabled frozen tissue sections to be mapped on a clinically practicable timescale. The combination of large spectral datasets (generated by rapid Raman mapping) with multivariate analysis provides a powerful method of analysing tissue sections. The frozen tissue samples do not require preparation with histological stains, providing a significant advantage over current techniques. Frozen samples can be stored and subsequently stained if required. Furthermore, the process lends itself to automation using computed algorithms which removes the subjective element of histological diagnosis. Potentially a rapid pre-scan could be carried out at relatively low resolution with low SNR. Subsequent detailed high quality maps can then be acquired on regions of interest. In combination with multivariate classification models, there is the potential for the automated screening out of non-relevant samples, with those deemed as abnormal going on for diagnosis by an expert histopathologist. Consequently this would reduce the burden of 'non-relevant' samples which currently swamp the system and allow more time for analysis of the critically diseased samples.

A large amount of work will be needed to develop a comprehensive database of tissue spectra before Raman mapping can be used in the clinical environment. Rapid Raman mapping provides a method of acquiring such data which will enable verification of this technique on a timescale that was previously not possible.

Raman spectral mapping has historically been significantly slower than the complimentary technique of IR absorption spectroscopy and a rigorous comparison of the two techniques is now required.

There is a trade off with overall mapping time and signal to noise. Although the signal to noise ratio of the rapid Raman mapping spectra are not of the same quality as point mapping spectra (due to the line focusing and also the waterfall nature of reading the CCD which potentially translates residual CCD noise across the CCD), it is in effect a half way house or to word another way a technique which makes the compromise between rate of acquisition and the subsequent quality (and quantity) of the acquired spectra.

Advances in mapping technology have also facilitated the use of alternative wavelengths since shorter acquisition times can be used. Diem at al. used 514nm with an acquisition time of 0.5 s for mapping cells.[206] Considering the discussion previously regarding the spatial resolution achieved by Shlucker *et al*., this could potentially enable even higher spatial resolution Raman mapping in the future.

6.4 Raman mapping and linear discriminant analysis to evaluate the importance of lateral spatial resolution for histology diagnosis

The previous section has demonstrated the feasibility of measuring molecular signals from unstained tissue in relatively short time scales. Methodologies for utilising this information for clinical diagnosis are explained here, with particular emphasis on evaluating the spatial information for clinical utility. A portion of the results from this study have been submitted for publication (November 2008, Analyst),[207] a copy of the submitted manuscript can be seen in Appendix I.

6.4.1 Linear discriminant analysis of Raman maps

6.4.1.1 Principal component imaging

The results from one sample (Sample 1) are presented in detail, with the results from a second (Sample 2) sample added to demonstrate the technique can be used to identify other pathology groups. Figure 6-17 shows the white light montage image of Sample 1, acquired using a x2.5 objective. The small box indicates the region containing high grade dysplasia (HGD) and fibrous connective tissue (FCT) which was mapped repeatedly. It was noted that the regions between the HGD glands were also FCT. The H&E stained CaF_2 image (i.e. the mapped tissue section) and contiguous section stained with H&E for histology purposes are also shown.

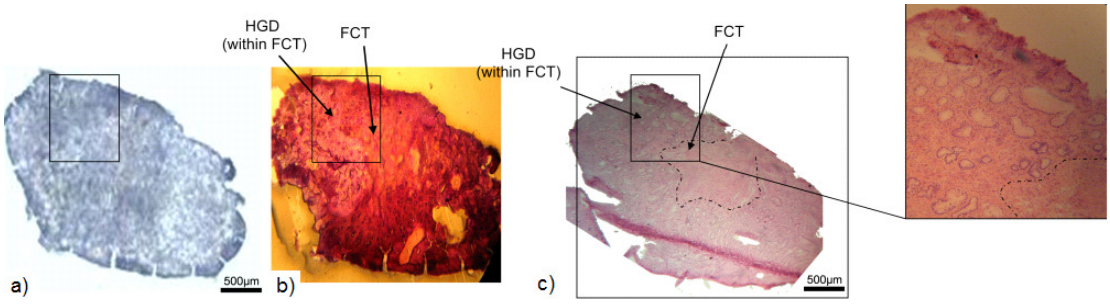

Figure 6-17: a) White light image and mapped area b) mapped tissue section stained with H&E (on CaF_2) c) contiguous 7 µm H&E stained section of Sample 1

Figure 6-18 shows PC2 as an example of a pseudocolour PC score images and corresponding PC load. The extremes of the colour bar are represented by a single colour, with the central portion remaining transparent. This allows the PC images to be overlaid, as shown in Figure 6-19, in which PCs 1-5 are shown overlaid with corresponding PC loads colour coded accordingly.

The biochemical information contained within the PC loads is shown to be similar (for the two maps acquired with 8.4 and 2.1 µm). Although the two different regions of tissue can be identified in both maps, it is much easier to identify morphological structure in the smaller step size map as glandular features and this further supports the presence of HGD.

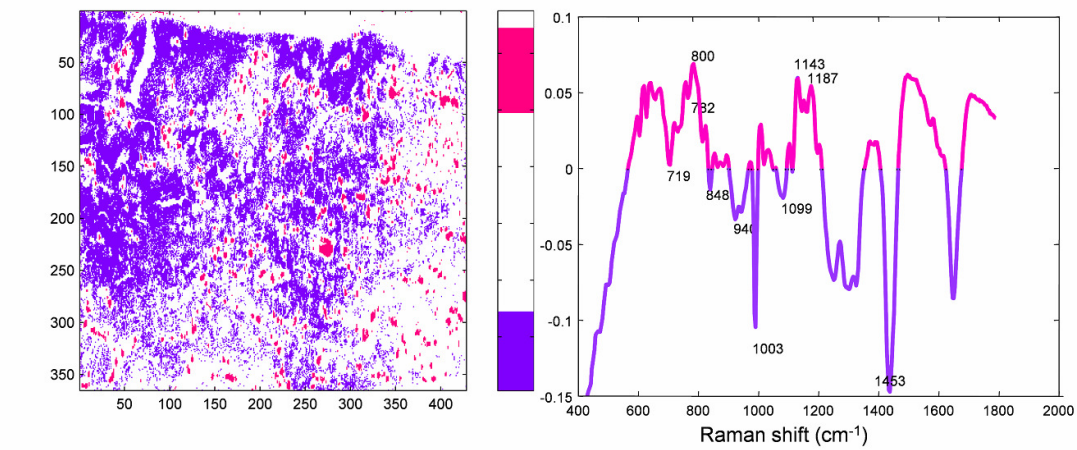

Figure 6-18: Example of how PC images are overlaid (pseudocolour PC 2 scores image and corresponding PC load for the 2.1 µm map)

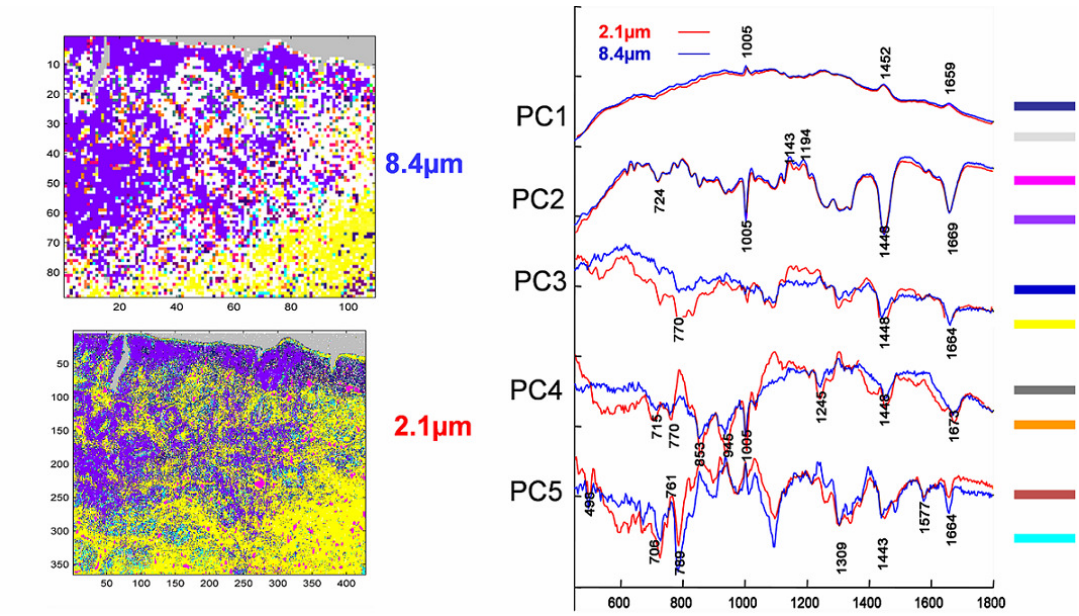

Figure 6-19: Pseudocolour PC score images overlaid for the 8.4 µm and the 2.1 µm step size map. PC loads are shown with corresponding colour coding

6.4.1.2 Linear discriminant analysis (LDA)

Initially, LDA models for six spectral groups were generated (see Table 6-7). As described previously, spectra were selected using thresholding of the PC score images, with ambiguous spectra (not clearly belonging to a single group) classed as 'unknown'. For the 8.4 µm map, the overall training performance of the LDA model was 70.1% with

the overall training performance degraded by the large number of misclassifications for spectra in the 'unknown' group and also the CaF_2 group. Sensitivity and specificity were 58.7–92.9% and 88.1–99.9% respectively. The number of spectra within each group and the percentage correctly classified by the LDA model is summarised in Table 6-7.

Table 6-7: Classification performance of the training (including the 'unknown' group) dataset of the LDA model (8.4 µm and 2.1 µm step sizes, 15 s acquisition time)

		CaF_2	TB	FCT	HGD	Lum	Unknown	% correctly classified
	CaF_2	354	27	0	0	0	0	94.4
	TB	62	111	3	0	0	13	82.7
8.4	FCT	0	0	920	1	0	79	99.3
µm	HGD	1	67	234	2608	0	752	88.0
	Lum	0	1	13	0	140	13	96.3
	Unknown	7	185	796	544	6	2655	71.7
	CaF_2	5713	371	0	0	0	0	93.9
	TB	150	1386	13	0	0	1	89.4
2.1	FCT	0	3	5145	0	0	252	95.3
µm	HGD	0	41	2952	52864	424	14322	74.9
	Lum	0	3	0	0	4070	0	99.9
	Unknown	2100	1528	13533	14152	5046	32151	46.9

For the 2.1 µm map, the overall training performance of the LDA model was 64.9%. As with the 8.4 µm model, the majority of the misclassified samples are from the 'unknown' group (as expected) which consequently skews the overall performance value. There are also misclassification of FCT spectra (predicted as 'unknowns') and some discrepancies with CaF_2 and tissue border. Table 6-7 shows the number of spectra within each LDA classification group. Sensitivity and specificity were 46.9 - 99.9% and 83.4 - 98.9% respectively, but again, these values are skewed by the large number of misclassifications within the 'unknown' group. As described earlier, the 'unknown' spectra were those which ambiguously belonged to more than one group i.e. spectra which were identified by the FCT PC scores image, but actually lay within the HGD region of the map. This will obviously have an effect on the model since spectra in the unknown group will not be similar biochemically since it is likely to contain a range of pathologies.

Figure 6-20 illustrates the model performance spatially to provide further insight. Figure 6-20a and Figure 6-20c identify spectra (as black pixels) which are misclassified by the LDA model for the 8.4 µm and 2.1 µm maps respectively. In Figure 6-20b and Figure 6-20d, these misclassified spectra (pixels) are colour coded according to the group in which the LDA model classifies them for the 8.4 µm and 2.1 µm maps respectively. This additional spatial information provides an insight into whether or not the LDA prediction is sensible which can potentially provide useful information regarding initial group. The process is also subjective to a certain extent, albeit based on biochemical information from the PC scores images, PC loads and pathology opinion.

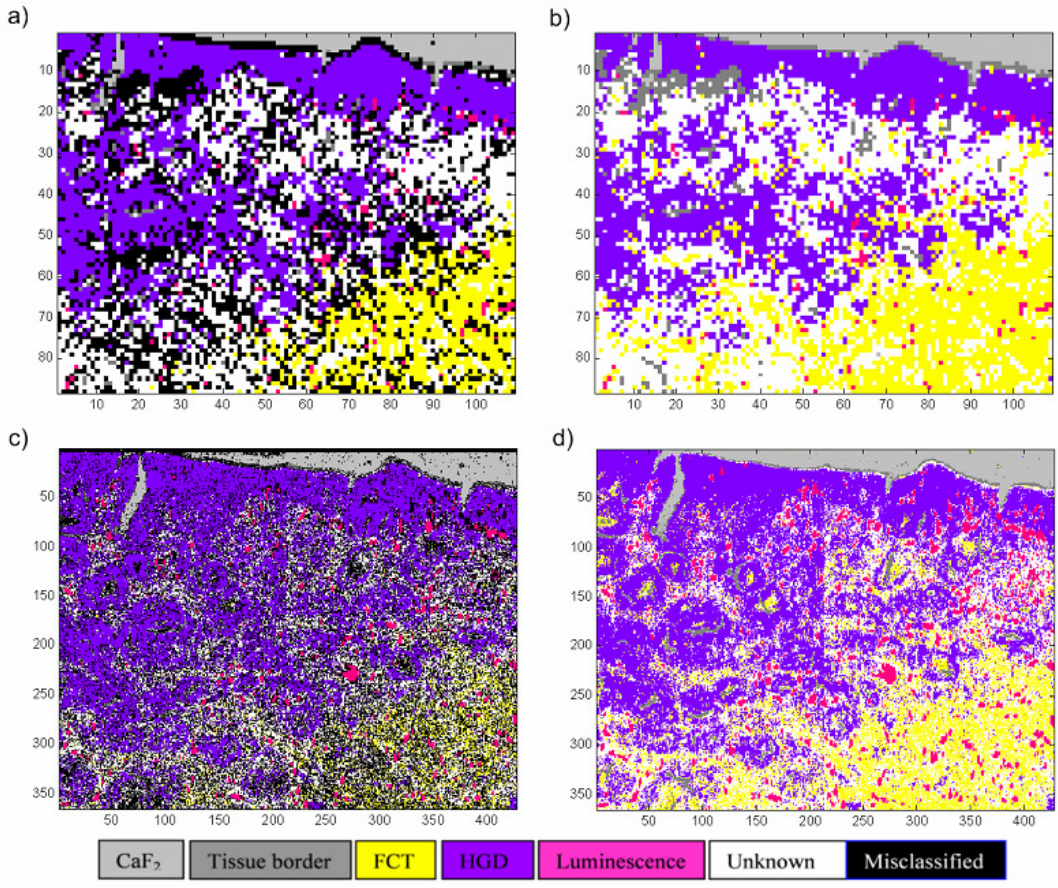

Figure 6-20: Pseudocolour LDA pathology images for the 8.4 µm (a-b) and 2.1 µm (c-d) maps colour coded with pathology. Figures 4a) and 4c) show the locations of the misclassified spectra/pixels, whilst Figures 4b) and 4d) show the predicted pathology according to the LDA model for each of the misclassified spectra

In the 2.1 μm map PC score image (Figure 6-19), the FCT appears to extend into regions between HGD glands. In the LDA pathology classification, although over 25000 spectra are misclassified as FCT, spatially, many of the inter-glandular spectra are still classified as "unknown" (white) and luminescence. This is likely to be due to initial choice of LDA groups for which the LDA process would try to separate the groups, but it could possibly be due to a biochemical difference in the FCT depending on the location of the tissue. This issue is addressed in the next section in which the 'unknown' group is extracted from the model and used as an independent test set. There is also the possibility there is spatial and spectral averaging of nearby HGD and further work is required to verify the actual spatial resolution achieved with rapid Raman mapping systems.

The central portions of the some of the glands appear to be misclassified as FCT, but again it is likely that a separate group would be required to account for these gland lumens which are likely to contain glandular mucin secretions etc. from the goblet cells. This may be based on protein signature of mucins, but further work is required to investigate this.

Luminescence also appears to be very structural within the tissue and mostly, within the regions of FCT. The location of the luminescence within the FCT is more evident with the small step size map, highlighting the potential importance of high lateral spatial resolution mapping.

Including spectra acquired from calcium fluoride in the mean centring may not be the optimum method, but it was concluded that calcium fluoride/other substrate would be an important constituent with any model since any discrepancy with substrate impurities may lead to misclassifications. This may also be important for regions of thin tissue which may contain contributions from both substrate and tissue. Further work will be needed to investigate this.

6.4.1.3 Projecting the 'unknown' group as an independent test set

Figure 6-21 shows the pseudocolour LDA image for the model generated excluding the 'unknown' group as a separate test set and later projecting these onto the model. Both the 8.4 µm and the 2.1 µm maps are comparable, with spectral predictions consistent with morphological features and location in the image.

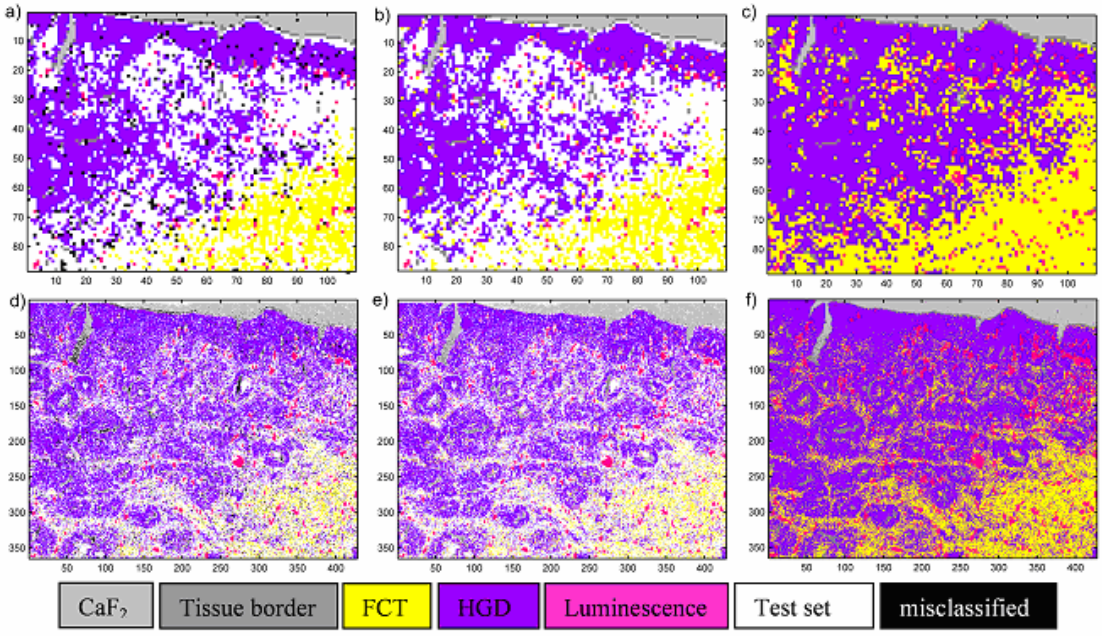

Figure 6-21: Projection of the test set onto the LDA model (generated excluding the 'unknown' group which was kept aside as a test set) for the 8.4 µm (a-c) and 2.1 µm (d-f) maps. Figures a) and d) illustrate tissue classification of the training set by the LDA model according to tissue pathology colour code with misclassifications as black pixels and the test set identified as white pixels. Figures b) and e) illustrate the predicted classification group of the misclassified spectra within the training set according to the LDA model and figure c) and f) show the projected test set results according to the classification by the LDA model

The overall performance of the training set models improved from 70.1% to 94.4% (79.4-99.0% sensitivity and 95.0-99.8% specificity) for the 8.4 µm step size model and from 64.9% to 93.7% (87.3-99.9% sensitivity and 95.2-100% specificity) when the unknown group was excluded as the test dataset.

As with previous LDA models which included the 'unknown' group, FCT appears to extend in between the glandular features of the HGD. Previously, this was only 2.1 µm

map, but when using the 'unknown' group as a test set this is also evident in the 8.4 μm map (Figure 6-21). Again, the centre of some of the glandular HGD structures are classified as FCT (especially evident in the small step size map). This is likely to be incorrect, and as discussed previously, a further group, tentatively attributed to mucin, may need to be added to the model to account for such regions. However, there is also the possibility that FCT, which is relatively transparent, is misclassified as tissue border since it comprises a lesser contribution from tissue spectral features and more CaF_2 due to spectral mixing with substrate spectra. Further work is needed to investigate the origins of these misclassifications. The projection model also suggests that regions of luminescence are surrounded by FCT.

To further investigate the projection of test dataset (and the presence of luminescence within the FCT), the LDA model was recalculated with fewer spectra in the training dataset. An additional 'unknown' margin around each pathology group was defined and allocated to the test dataset i.e. each region of luminescence was surrounded by a region of test set pixels/spectra. Similarly, the region between HGD and FCT was blocked out and allocated to the test set. Results indicate more strongly that luminescence is structural within the FCT. Pixels at the edge of the tissue and also the gland centres are also projected to be FCT, reiterating the need for an additional group within the model. The results are shown in Figure 6-22.

It is evident that reducing the training dataset does not impact on the ability to project the test set onto the classification model. Furthermore, improved training performance is achieved by ensuring the classification model is trained with well define spectral groups.

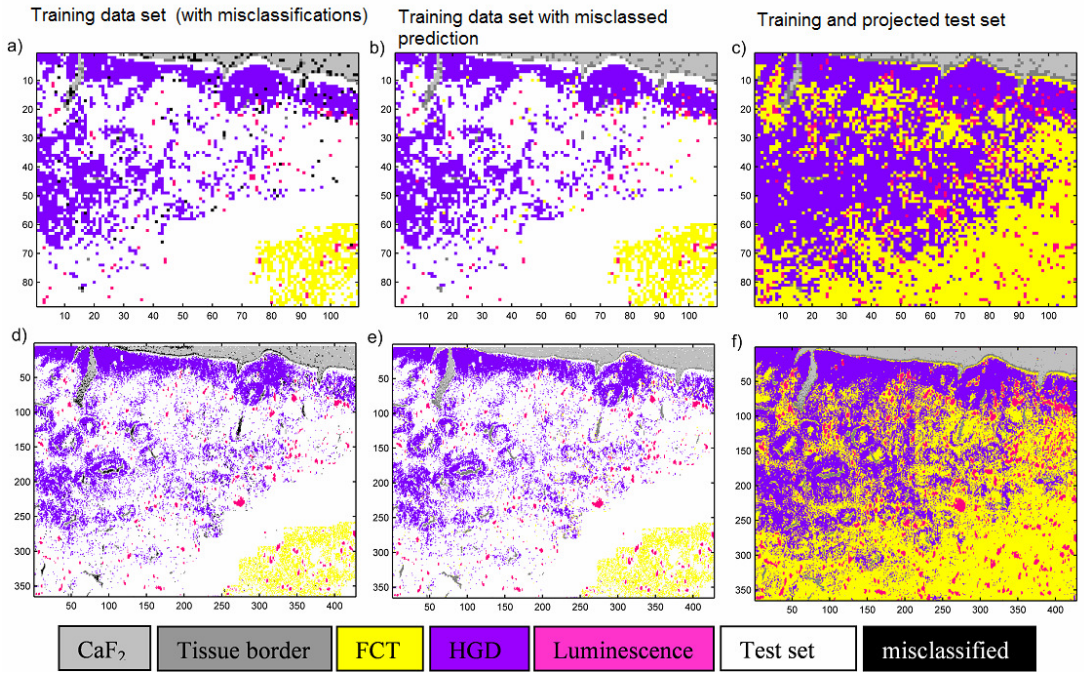

Figure 6-22: Projection of the larger test set (to account for tissue margins) onto the LDA model (generated excluding the test set) for the 8.4 µm (a-c) and 2.1 µm (d-f) maps. a) and d) illustrate tissue classification by the LDA model according to tissue pathology colour code with misclassifications as black pixels with the test set identified as white pixels. b) and e) illustrate the predicted classification group of the misclassified spectra according to the LDA model and figure c) and f) show the projected test set results according to the classification by the LDA model

6.4.1.4 An example of normal squamous epithelium (Sample 2)

The above process was repeated on a map (15 s acquisition and 8.4 µm step size) of Sample 2 (containing NSq and FCT), but in this case the size of the training dataset was reduced further.

Results are shown in brief in Figure 6-23, which shows the white light image and pseudo colour LDA image, the training set (defined by relatively small, but distinct regions of NSq, FCT and CaF_2), H&E of the contiguous section and also the mapped section stained with H&E (on CaF_2). It can be seen in the figure that there are no black pixels indicating a perfect overall training performance of 100%.

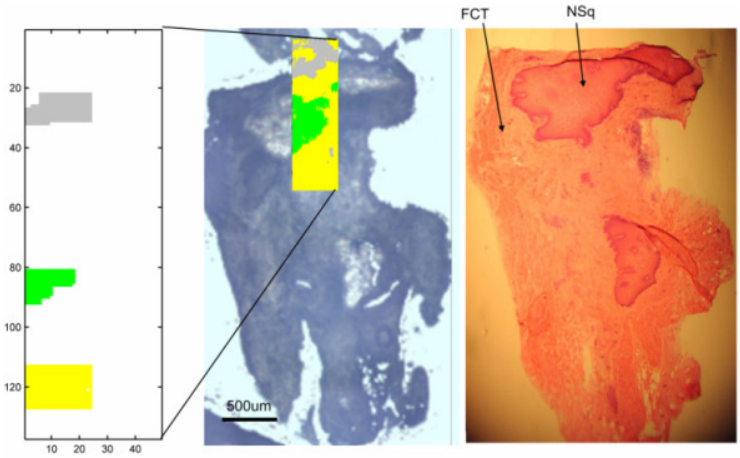

Figure 6-23: left) Model training set defined by small region of NSq (green) FCT (yellow) and CaF_2 (grey), centre) white light image of the sample with the projected tissue classification overlaid at the mapped region, right) annotated H&E of the consecutive section

6.4.1.5 ***Combined maps***

To further test the LDA projection of map data onto the tissue classification model, the two maps (15s acquisition time and 8.4 µm step size), were combined to form a large map containing HGD (sample 1), FCT (from samples 1 and 2), NSq (sample 2) and CaF_2 (from samples 1 and 2). The entire map was then reanalysed to investigate the feasibility of extending this to multiple tissue maps and tissue types.

Again, small, distinct regions of each tissue type (NSq, FCT and HGD) and also CaF_2 were defined as the training dataset, with the test set defined as the remainder of the dataset. The H&E images from each sample have been reconstructed to indicate the pathology of the combined map as shown in Figure 6-24, the regions selected for the training dataset are also indicated. The mean raw spectrum for each training set group (CaF2, FCT, HGD, NSq and Lum) is shown in Figure 6-25.

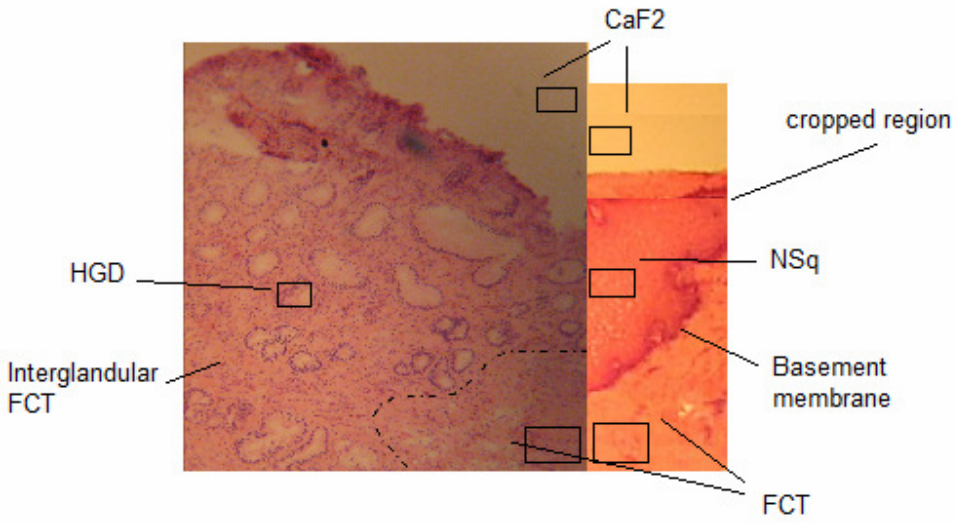

Figure 6-24: Reconstructed H&E for samples 1 and 2 to indicate pathology of combined map. The spectral regions selected for the training model are also indicated. Note the discontinuity in right hand H&E image which indicates the region cropped to ensure map dimensions agreed

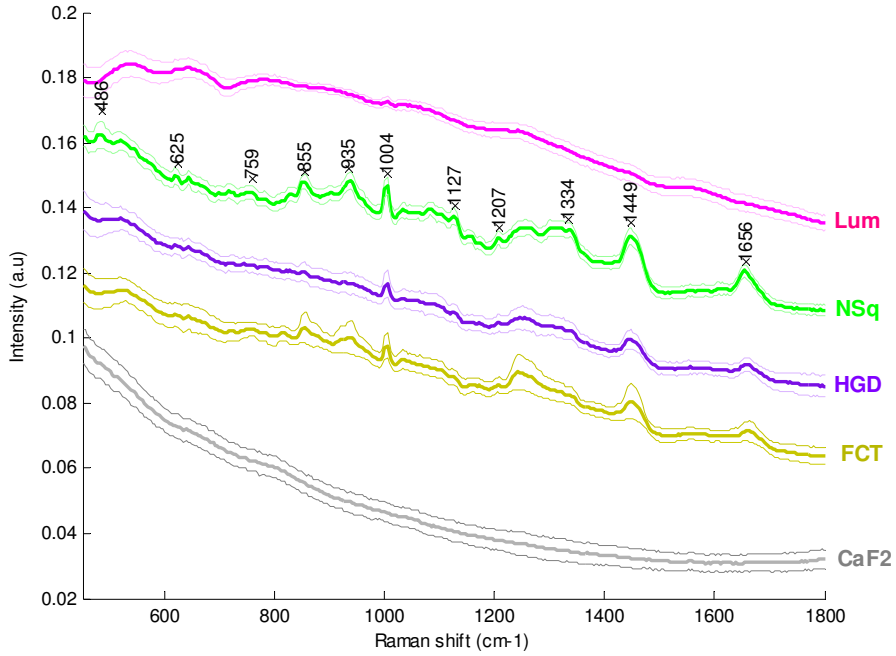

Figure 6-25: Mean spectra for the training dataset (for the combined LDA map for Sample 1 and 2). Plus and minus two standard deviations is also shown. Spectra have been plotted with an arbitrary offset for clarity

Further information can be gleaned from the difference spectra of the different groups. Examples of difference spectra between the NSq and the HGD training group spectra can be seen in Figure 6-26a and NSq and FCT in Figure 6-26b.

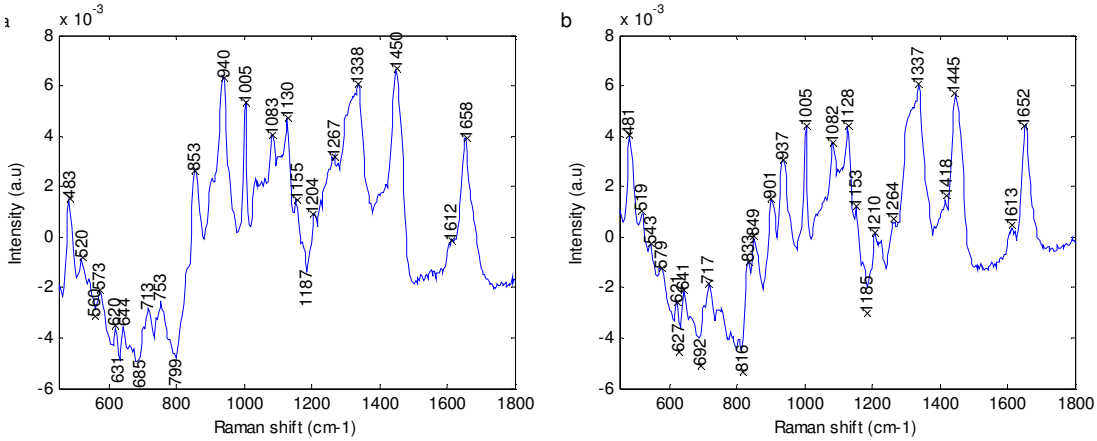

Figure 6-26: Difference spectra for the mean training set spectra a) NSq minus HGD and b) NSq minus FCT

Considering Figure 6-26, the 481(483), 884(853), 937(940), 1337(1338), 1450(1455) cm^{-1} peaks present in both can be attributed to glycogen, consistent with normal epithelial tissue. There is also relatively more protein content in NSq compared to FCT and HGD illustrated by the peaks 937, 1005, (1034 not labelled), 1329 (peak shoulder), 1458, 1655 cm^{-1}. In Figure 6-26a negative peaks at 685, 779 cm^{-1} may be due to DNA. In Figure 6-26b negative peaks at 874 and 920 cm^{-1} (not labelled) in the NSq minus the FCT could also potentially be attributed to collagen.

Figure 6-27c shows the classification for each spectra/pixel for the test dataset projected onto the LDA model generated using the training dataset.

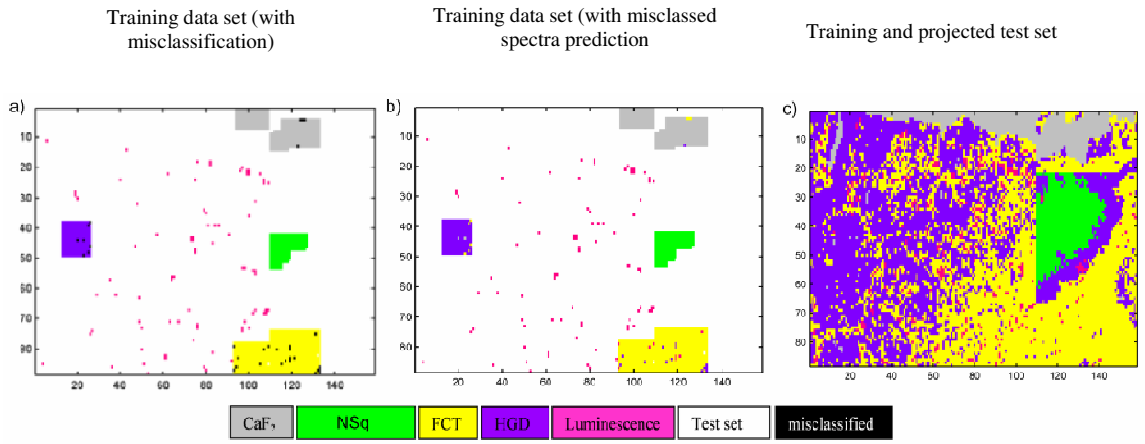

Figure 6-27: Classification model generated based on a training set taken from two samples (Sample 1 and 2 combined to one map) Sample 1 is the sample containing HGD and FCT and sample 2 contains FCT and NSq. a) shows the training set performance with correctly classified spectra classified according to pathology colour code with misclassified spectra highlighted as black pixels, b) illustrates the groups into which the misclassified spectra are predicted and c) illustrate the predicted classification for the test dataset (previously white pixels)

The overall accuracy of the training set classification model was 97.5% (98.8–100% sensitivity and 95.8 – 100% specificity). The number of correctly classified samples is summarised in Table 6-8.

Table 6-8: Classification performance of the training model generated with the combined maps (sample 1 and sample 2)

	CaF2	FCT	HGD	Lum	NSQ	Total	% correctly classified
CaF2	335	3	1	0	0	339	98.8
FCT	0	524	13	8	0	545	96.1
HD	2	5	161	0	0	168	95.8
Lum	0	0	0	82	0	82	100.0
NSq	0	0	0	0	158	158	100.0

In general, projection of the test dataset (Figure 8c) agrees with histology diagnosis (Figure 6-17- sample 1, Figure 6-23 – sample 2), however there are discrepancies which occur within the basement membrane region of the NSq (i.e. the border between NSq

and FCT) which gets projected as HGD. Regions of luminescence, not previously identified in Sample 2 are also detected within the FCT.

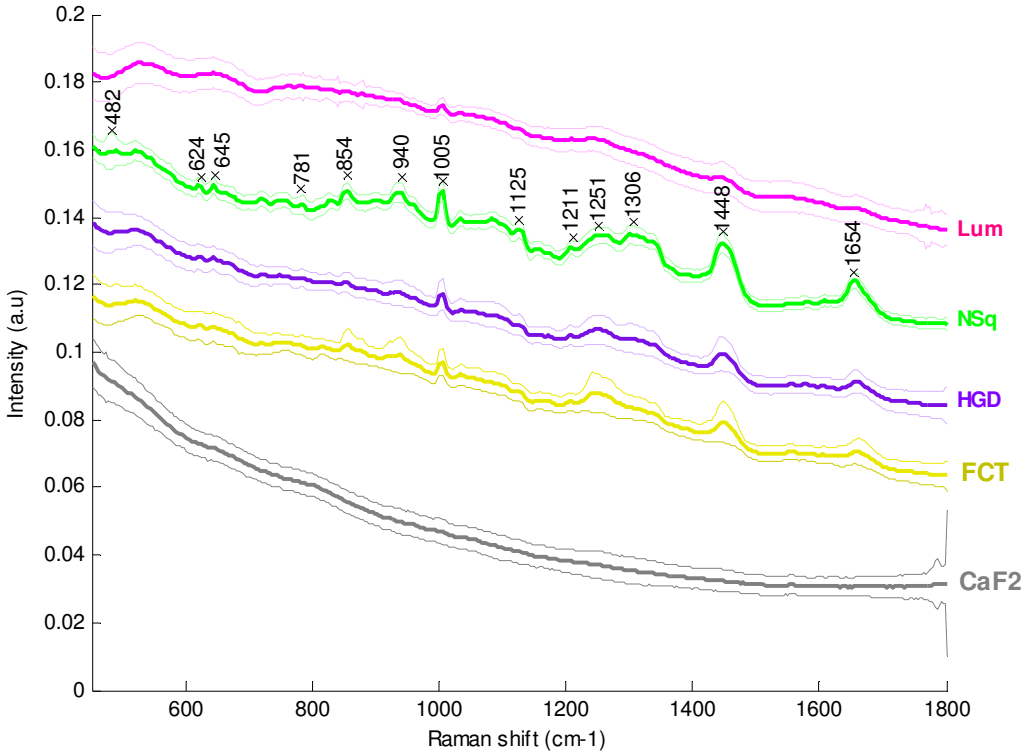

Figure 6-28: Mean spectra for the projected data set and training set

It can be seen from Figure 6-28 that there are a few a cases (in particular at the high wavenumber range of the CaF^2 and Lum group) where the standard deviation is large. This is caused by the presence of cosmic rays in the test set. It appears that the LDA process is relatively insensitive to the presence of cosmic rays, but further work is required to verify this.

The mean of the luminescence group for the projected spectra also contains evidence of Raman spectral peaks. This may be due to spectral mixing of adjacent pixels, but future work may reveal the biochemical composition of luminescent structures.

Admittedly this is not a full model containing all pathology groups, nor was the region of basement membrane included in the training dataset, but conclusions can still be drawn from this, since the result indicates that classification could be occurring based on biochemical signature of (potentially of dividing) cell nuclei densely packed in both HGD and also basement membrane regions. Furthermore, since epithelial cells originate at the basement membrane and migrate to the surface (where they are exfoliated), cells in the basement membrane region are also proliferating which could also further explain the misclassification. The misclassification could also be due to spectral mixing artefacts, as suggested by Bhargava *et al.* who also reported boundary epithelial pixels are misclassified as malignant.[150]

This result indicates that misclassifications are highly likely if sub tissue classes are not included into the training dataset, and perhaps suggests that spatial averaging may be advantageous to avoid such issues. Further work is required to determine the optimum number of classification groups for pathology diagnosis.

In a study by de Jong *et al.*, increased levels of DNA and RNA in inflammatory regions of Raman maps of bladder sections were reported (although data was not shown).[175] Concluding this study, de Jong *et al.* comment that spectral databases will need to include a reference dataset for inflammatory tissues to prevent misclassification. It was previously noted that inflammatory changes could not be detected with a Raman probe and point spectra and it is likely that spectral mixing overwhelms this subtle change which is only evident when mapping tissue sections. In the future, a thorough investigation of spectral mixing effects will be required to determine optimum number of pathology groups required for tissue diagnosis.

This study has shown that high lateral spatial resolution mapping is not necessarily needed for histological diagnosis. However, high lateral spatial resolution mapping does have advantages. There is the advantage of acquiring a large number of spectra which is amplified for reduced step sizes due to the square relation between step size and number of pixels. The additional spatial and spectral biochemical information could potentially facilitate the separation of more pathology groups.

LDA is a well known and accepted technique for spectral classification, and this thesis has shown its potential application in Raman imaging for histological diagnosis, supporting previously published work.[192-194] These works have been based on tissue classification models generated previously, with mapping data projected onto the model. This approach was not possible in this study since maps were acquired on a novel mapping system, with different optics to previously generated tissue classification models. Furthermore, due to the nature of rapid mapping technology, there are differences in the step size and sampled volume compared to previously acquired model data. In the future, large tissue classification models can be generated, more rapidly than previous studies due to the rapid mapping technique. Training dataset sizes will approach those reported in IR studies, for example Bird *et al*. reported a study in which 1.4 million spectra were analysed,[191] and this will easily be achievable with rapid Raman mapping. Further work is still required to investigate the extent to which the technique can be exploited with respect to automated imaging and also larger sample numbers need to be included in the model. In this preliminary study projection of an unknown dataset onto the model allows validation of the model to a degree but using spatial information relating to morphology, but rigorous validation and testing will still be required when further samples are added to the model. Nevertheless, this is an important step in the move towards clinical implementation of vibrational spectroscopy for automated histopathology.

Although, validating LDA as a potential method for automated histopathology was not the primary aim of this study, and it was merely used as tool of comparison, this study has shown that the technique holds promise for future application. Other groups have favoured various other cluster analysis techniques such as k-means and ANN, but these techniques have failings, namely they are extremely computer intensive, they also force spectra into distinct groups, which is not realistic for two reasons. First, pathology groupings do not have distinct boundaries, especially for lower spatial resolutions where spectral mixing is known to have an effect on 'boundary pixels' and, second,[150] in a similar manner, the carcinogenesis progression is not separated by distinct boundaries between pathologies. LDA has advantages over other, more widely used chemometric

techniques for spectral imaging, since the technique could potentially facilitate the visual and spectral representation of spectral mixing. This idea was also proposed by Mansfield *et al*. regarding FTIR imaging, in which the probability was described by a mixed colour palate which mirrored the probability of a spectrum/pixel belonging to more than one classification group, which could account for spatial averaging and also uncertainty in the pathology classification due to subtle spectral differences. E.g. for a pixel/spectrum which was predicted to be in two groups, say connective tissue (yellow) and cancer (red) with equal probability would be represented by an orange pixel. The shade of which could be further determined by the probability weightings.

Although LDA model performance provides a relatively arbitrary method of comparison, it allows a quick and easy method of comparing the maps acquired with different parameters. PC fed LDA models are also able to cope with low signal to noise spectra, where other techniques may fail. Since it is well known that the initial group choices are an important factor with LDA models, the initial grouping may play a large part in the model performance, but as the groups were the same in both the 8.4 and 2.1 μm models, it enabled direct comparison of the two maps. The use of this 'unknown' group as an independent test set to validate the model provided confirmation that the classification was reasonable, supported further by spatial information relating to morphology.

There is also the potential, as discussed above that the small step size map may identify more subtle biochemical features which may account for the larger number of misclassified spectra within the small (2.1 μm) step size map. As a result, the model performance for the small step size map could potentially be significantly better if the initial groupings are chosen more carefully. However, mapping at even smaller step sizes, may also induce greater heterogeneity in the maps, even from cells of the same pathology (due to sampling different parts of the cell within each image pixel). It remains a question what needs to be distinguished for a specific pathology application and this is discussed further in Section 7.3.

There is also scope to reduce map times in this study. Acquisition times of 15s were used to maximise tissue classification performance, but as shown in the previous chapter, PCA is able to cope with relatively poor SNR spectra providing spectral datasets are large enough. Map times were of the order of 12h for the high spatial resolution maps, whilst the rapid prescan was acquired in approximately 10 minutes. This was sufficient for visualising morphology in the PC scores image, but when reduced to well-defined rectangular training sets, the dataset size was not sufficient to deal with the poor signal to noise.

Further work ongoing within the group may lead to accurate biochemical fitting of the spectral maps and therefore images can be constructed of biochemical distributions also see Appendix D).[124,172]

In summary, rapid Raman spectral mapping with LDA discrimination has the potential for automated tissue classification in the future. Greater numbers of samples and patients (to cover the likely variability in the population of interest), with detailed histopathology will need to be included into the training model. It also appears from this initial study that high lateral spatial resolution mapping is not essential for clinical diagnosis of bulk tissue types, but may have advantages in the future for discriminating further tissue types.

This study has shown that the LDA projection imaging process can potentially be applied to multiple samples making it a suitable technique for automated histopathology in the future. Furthermore, spatial information from visually representing LDA classification as pseudocolour images can provide insightful information which will help to explain misclassifications based on morphological features which is not possible from traditional scatter plot representation. After a thorough search of the literature, this appears to be the first study in which multiple images are stitched together to investigate classifications between samples and also the first study to investigate misclassifications visually in this way.

6.5 Evaluation of rapid Raman mapping as a research tool to elucidate biochemical changes associated with carcinogenesis

6.6 Background - goblet cells and mucins

As described previously, Barrett's oesophagus (intestinal metaplasia) is characterised by the presence of goblet cells. Goblet cells are simple columnar epithelial cells found in many parts of the body, in particular in the intestinal and respiratory tract. The function of the goblet cell is to secrete mucus which is comprised mainly of mucins (glycoproteins in electrolyte solution).[208] Oesophageal submucosal glands have been shown to contain neutral, sialated, and sulphated mucins and furthermore this varies with Barrett's subtype (IM, CM and FM).[11,209,210] The presence of the sia-group in glycoproteins, which has been linked to cancers which metastasise, could be detected and potentially quantified using Raman spectroscopy using a peak at 880 cm^{-1}, although this peak is also attributed to tryptophan residues.[211]

It was hypothesised that Raman spectroscopic mapping could be used to obtain high spatial resolution images of goblet cells and furthermore gain insight into the biochemical constituents within goblet cells and potential biomarkers. This could help to understand the process of carcinogenesis and also provide biochemical evidence which may help to support tissue classification models which separate Barrett's subtypes and premalignant changes.

In order to elucidate subtle biochemical changes, a long acquisition time of 60 s was used to ensure good quality spectra. A step size of 1.1 µm was used. The entire sample was mapped, then cropped to the Barrett's gland to highlight variance within the region of interest. The H&E section and large area map can be seen in Figure 6-29. The pseudo colour PC scores images and corresponding PC loads can be seen in Figure 6-30.

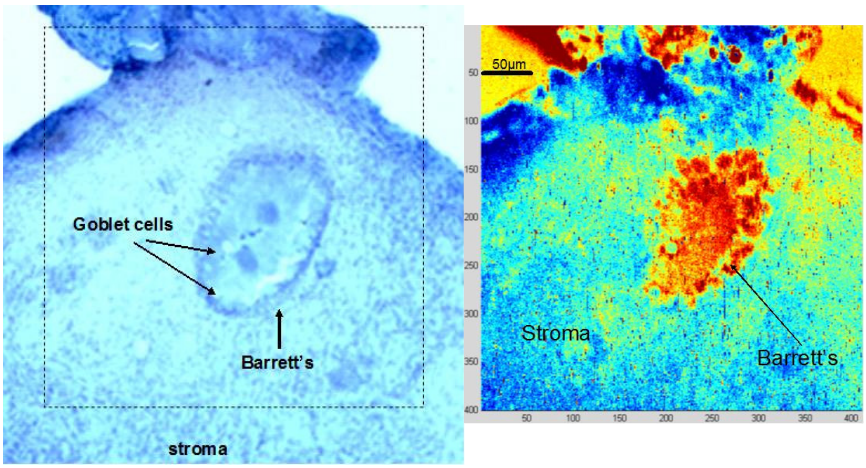

Figure 6-29: H&E stained section (of the mapped section on CaF_2) and PC2 scores image of a region of Barrett's (with goblet cells) surrounded by stromal fibrous connective tissue(FCT)

Of particular interest is the ability of resolve the 4 nuclei in the centre of the Barrett's gland in PC2 (indicated in Figure 6-30 with negative peaks (785, 859, 930, 1089, 1204, 1233, 1255, 1314 and 1325cm^{-1}) consistent with FCT and DNA.

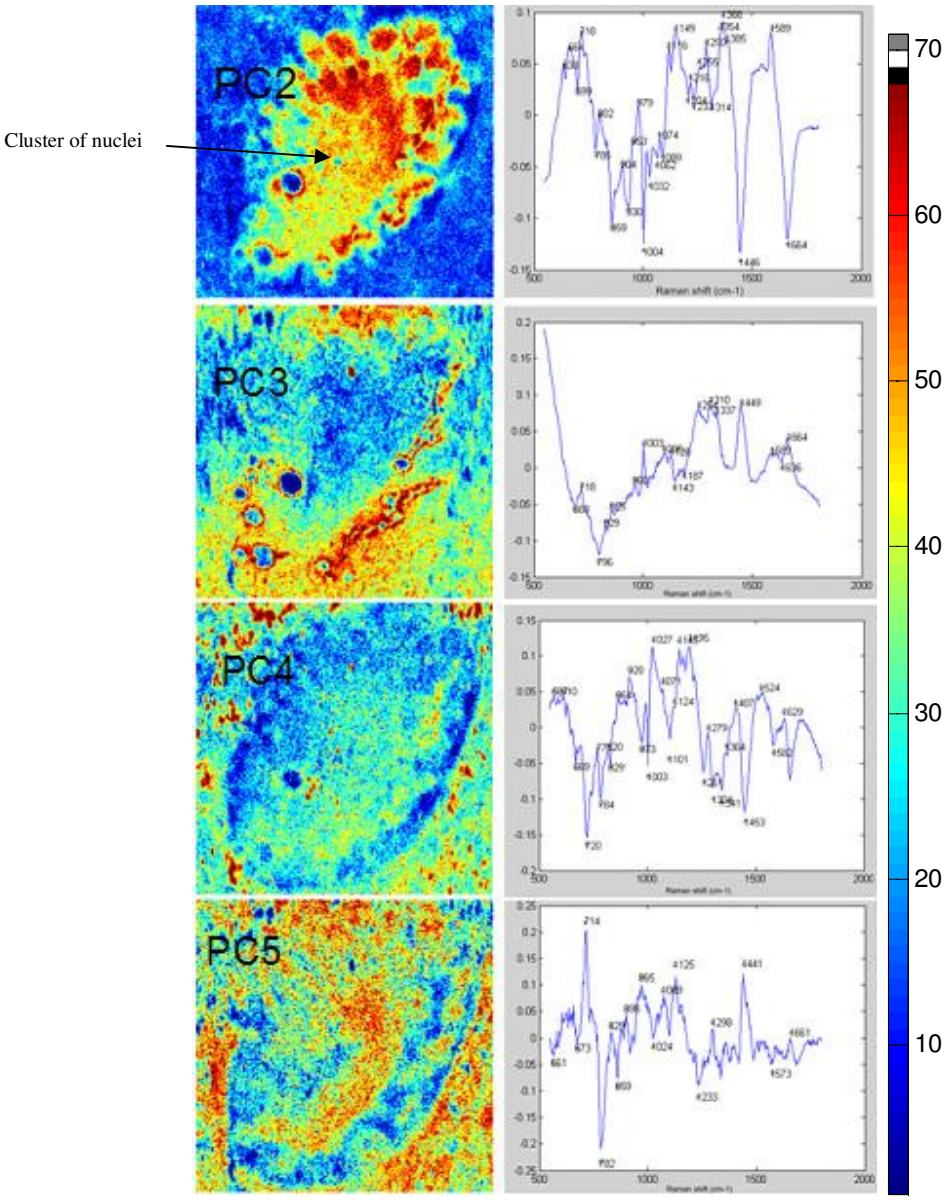

Figure 6-30: Pseudocolour PC score images (PC2-5) for the cropped region of interest containing Barrett's (with goblet cells) and surrounding FCT

There is potentially some evidence of the sia-group peak at 880 cm^{-1}, considering the negative peak in PC 5 but this was not conclusive in this sample.

A second sample of Barrett's was mapped with high spatial resolution, and the pseudocolour PC score images and corresponding PC loads can be seen in Figure 6-31. The glandular structure of the Barrett's is clearly evident.

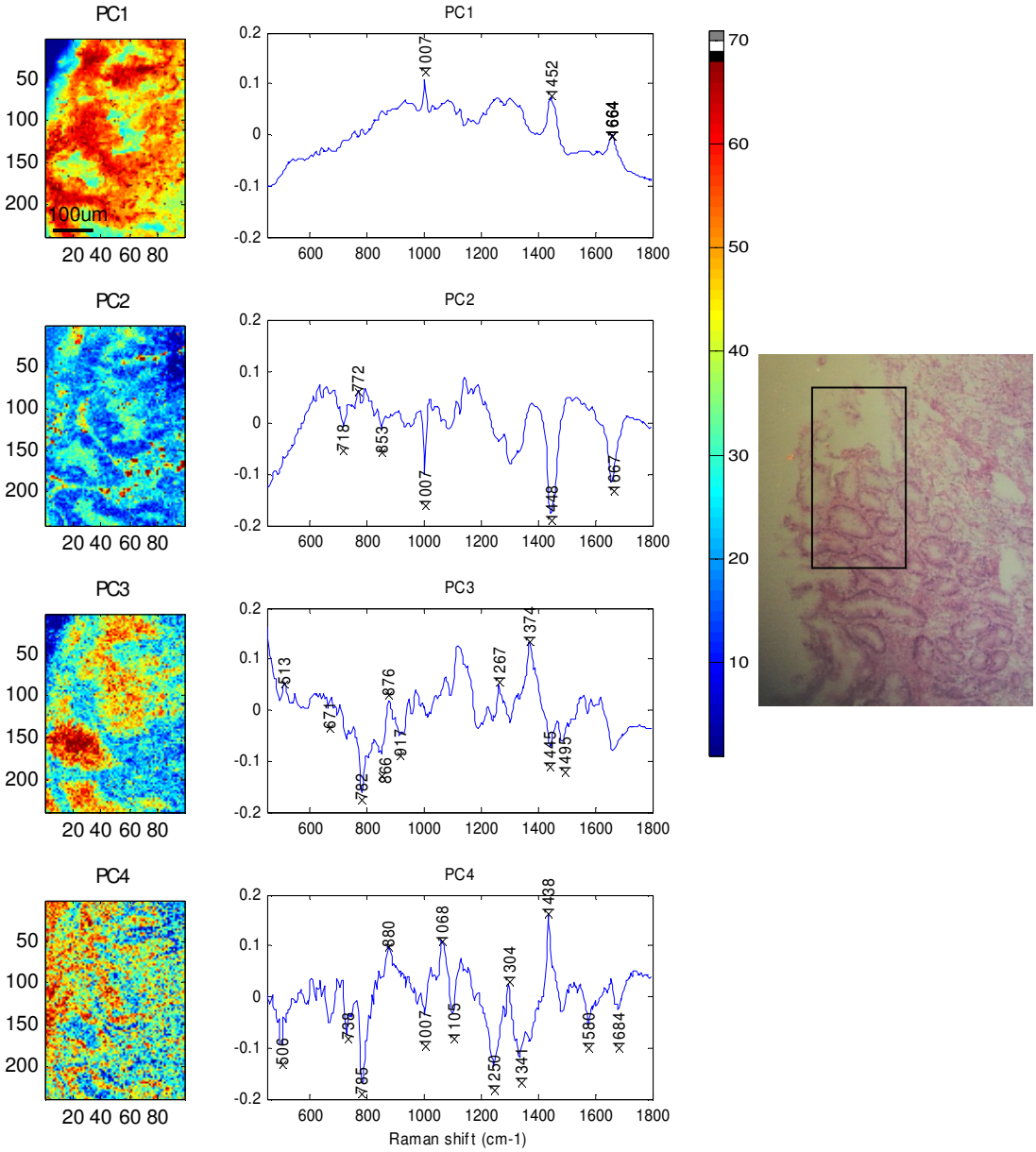

Figure 6-31: Pseudocolour PC score images (PC1-4) and corresponding PC load of a sample of Barrett's (with goblet cells) mapped with a 40 s acquisition time and step size of 2.1 µm. The H&E of the contiguous section is also shown

In the second sample, there were also peaks at 880 cm^{-1}, (positive peaks in PC 3 and 4). However, this is anecdotal at present and further work is required to investigate the presence of mucins in oesophageal tissue. Biochemical fitting may assist with this as suggested previously.

It should also be noted that luminescence was again detected within the FCT regions, in this case, in the inter-glandular FCT, this strengthens the observations noted in the previous section (HGD and FCT using LDA).

Chapter 7 Results and discussion: 3) Factors limiting translation of Raman optical diagnostic techniques into the clinical environment

7.1 Comparison with Raman microscopy system results

Figure 7-1 compares the normalised Raman spectra acquired from two oesophageal cancer tissue samples using both the Visionex probe and Renishaw microscopy system 1000 (labelled as system 1 - S1). The probe spectra were directly from the EMR, whilst the S1 spectra were acquired from the biopsy taken from the point of probe measurement.

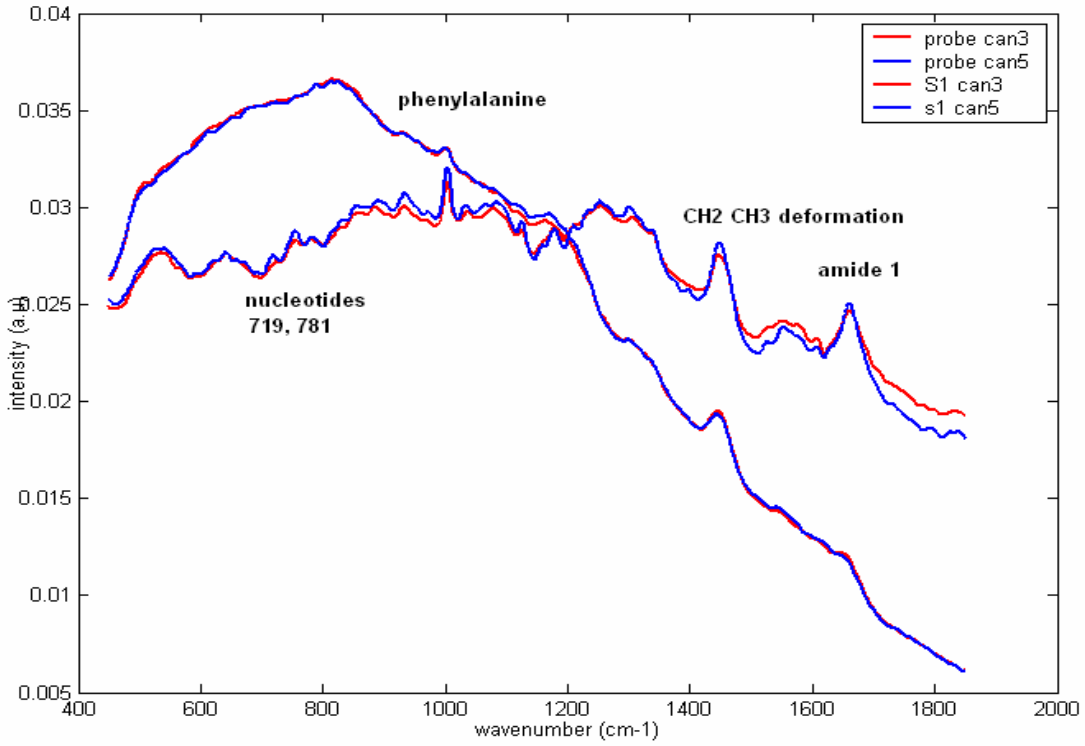

Figure 7-1: Comparison between probe (spectra with large background) and Renishaw system 1000 (S1) for two cancer samples (spectra with well defined peaks)

As discussed previously, the amide I band, CH_2, CH_3 deformation and phenylalanine peak at 1005 cm^{-1} is visible even with the large probe background. The inferior spectral quality is obvious, especially with respect to spectral resolution (peak width). It is also interesting to note the probe spectra appear to be very consistent and two cancer samples taken from the EMR sample are very similar, whereas the spectra acquired using S1 shows subtle differences, despite normalisation. This is likely to be caused by the smaller sampling volume of the microspectrometer. For the microspectrometer (x50 objective) the laser spot size is ~15x25 µm, (~7x50 µm line focussed) whilst the sampling volume for the Visionex probe is considerably larger (of the order of mm).

There is a possibility that the consistent probe background may be beneficial, since consistency is a key attribute when constructing tissue classification models. However, it is also likely that although the background is consistent, it is likely the background is masking subtle biochemical differences in the spectra. Further work is required to compare the two systems.

7.2 Practical considerations for implementing Raman spectroscopy in a clinical environment

7.2.1 Ambient light sources

Ambient light can pose a problem with Raman spectrometer systems. This is especially problematic when translation to a clinical environment is considered, and potentially more problematic for probe based systems compared to laboratory based systems, such as those which could potentially be used for automated histology.

LCD computer screens were found to be a very problematic source with very distinct peaks appearing in the Raman spectra as shown in Figure 7-2. Fluorescent lighting can also provide spectral artefacts.

LED light sources were found to over come these problems. Further work will be required to investigate endoscopic light sources for in vivo application and also effects from theatre lighting.

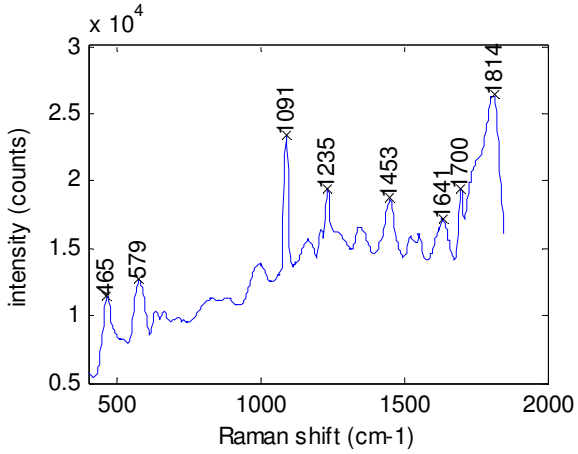

Figure 7-2: Raman spectra acquired using the Visionex probe of the LCD screen used in conjunction with the spectrometer computer control

7.2.2 Effect of ambient temperature

Table 7-1 shows the peak shifts which were noted in both System 1000 spectrometers for both the polymer standard and neon argon lamp. It is evident that there is potentially a contribution to the ambient temperature artefacts from both the spectrometer and laser. For the S100 probe system, a linear peak shift with temperature was not evident with the polymer standard so the range is stated.

Table 7-1: Summary of the peak shifts for polymer standard and Ne-Ar calibration lamp with variation in ambient temperature

System	Polymer peak shift	Ne-Ar lamp peak shift
S1000 (1)	0.4 cm^{-1}/ºC	0.1 cm^{-1}/ºC
S1000 (2)	0.6 cm^{-1}/ºC	0.5 cm^{-1}/ºC
S(100)	Range (max-min) 1.5 cm^{-1}	-0.1 cm^{-1}/ºC

7.2.2.1 *Ambient temperature study using Raman mapping*

Figure 7-3 shows a pseudocolour score map of the 1st principal component. The region of increasing temperature is clearly evident as a region of low scores (blue-purple). A repetitive stripe pattern is also evident once the temperature has stabilised and this is attributed to temperature oscillation as the air-conditioning maintains a constant temperature, consistent with that noted by Fukura *et al*[212]. The region of oscillation is consistent with a peak shift of approx 0.5 cm^{-1}. The 1st PC load (not shown) exhibits derivative spectral features which is consistent with characteristic peak shifts.

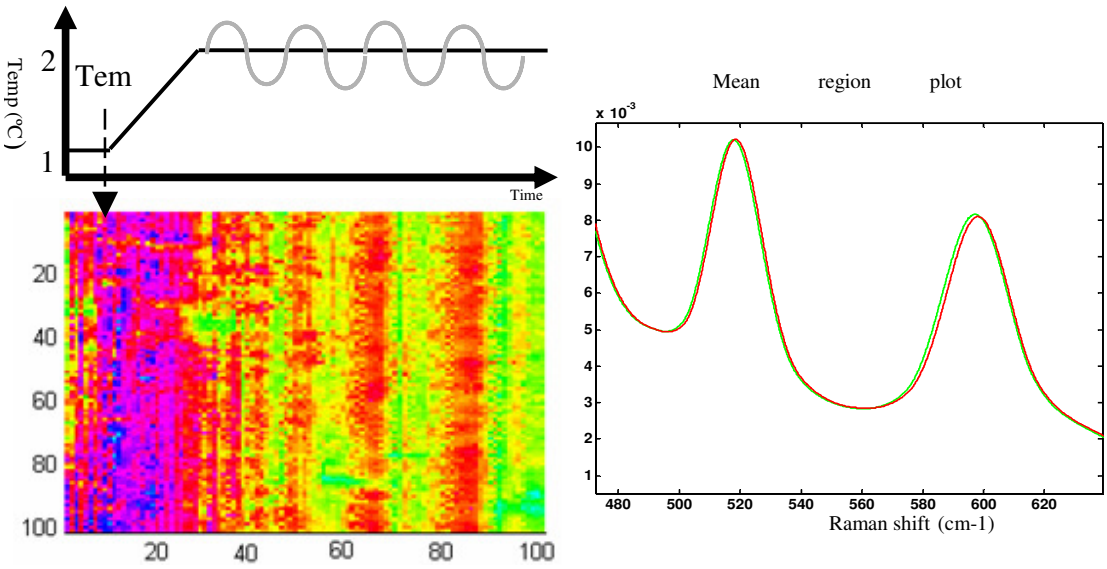

Figure 7-3: Raman map acquired with varying ambient room temperature. Left – pseudocolour PC score map of a polymer standard with correlating change in ambient temperature. Right – mean spectra taken from the red and green areas of the pseudocolour score map

The effect of peak shifts on a multivariate tissue classification model was also investigated. A classification model was generated using spectra acquired from S1000(1) at 23 ºC. Considering the effect of this on a tissue classification model, work in collaboration with another group member demonstrated that when spectral data modified with an artificial peak shift of 5 cm^{-1} was projected onto the original classification model the percentage correctly classified dropped from 94% to only 75%. This is an important result as it demonstrates the importance of temperature stability of Raman systems. A

copy of a poster presented at the International Conference of Vibrational Spectroscopy can be seen in Appendix J.

7.2.2.2 ***Summary***

Peak shifts can have significant effect on Raman spectra, and results are consistent with the literature.[213] Shifts occurred in both the polymer standard and neon argon spectra suggesting that shifts were caused by expansion or contraction of spectrometer components with temperature as well as a potentially significant contribution from the laser source. The apparent linear shift across the entire wavelength range would make correction easier than for example if a breathing artefact was apparent. Initial results suggest that the effect is less pronounced when using the compact S100 spectrometer which may be due to the simplicity of the spectrometer, or due to the lower resolution spectra, although further work is required to investigate this. This could potentially ease the transition to clinical application, in theatre for example. The detrimental effect of temperature induced peak shifts on a tissue classification model is demonstrated highlighting the importance of temperature stabilisation over short and long time periods.

7.2.3 Reproducibility and transferability

Comparison of Raman probes has generally relied on measuring the sampling efficiency and determining the focal depth using Si. Attempts at measuring the sampling volume off axis have also been made using diamond chips.[147] These measurements can give a good and simple method of comparing probes, but what is really of interest is the sampling volume and depth in tissue or a tissue equivalent material. Of interest is the ability to quantify a probe's ability to detect subtle differences in materials with different Raman signatures. For example the ability to detect a small region of cancer within a region of normal or Barrett's epithelium or a region of Barrett's within normal epithelium. This is a situation which is difficult to mimic in a phantom due to difficulties in replicating optical properties of different pathologies. However, considering a situation for which this would be easiest, the biomarker would be a substance with a unique Raman peak allowing the substance to be easily identified within surrounding tissue, for example a calcification in tissue. However, for substances, for example

collagen and glycogen, which may be easily distinguishable using Raman microscopy, this is more difficult with probe spectra due to large backgrounds, which are often dominant at the lower Raman shift range 400-900 cm^{-1}. A further aspect for consideration is the effect of substance concentration on a probe's ability to detect a certain substance within tissue.

7.2.4 A discussion of lateral spatial resolution: moving towards quantification when multivariate statistical techniques are used for imaging

This study also highlights an important aspect of spatial resolution for clinical diagnosis and raises the question: what is the spatial resolution in a Raman image. Although studies have looked at the impact of spatial resolution for spectral imaging,[148,180] this issue is non trivial since contrast and spatial resolution are inseparable for spectra data, an idea supported by other authors.[149] One concept is that due to the multidimensional nature of the spectroscopic information (for Raman mapping for example the 3D spectra data cube) there are many contributing factors to the contrast and spatial resolution that can be achieved. The multivariate techniques used for analysis may be of particular importance. To the author's knowledge there is nothing in the literature investigating this concept. Further work will need to be carried out in the future to investigate these concepts.

*7.2.4.1 **Initial phantom designs***

In order to test the limitations of the system and investigate how performance varies for detecting different substance, the design of a phantom would need to incorporate the concentration of a substance and Raman cross section. An alternative approach may be to construct the phantom with substances with a varying biochemical similarity, which can be measured by the degree of orthogonality.

To mimic the clinical situation, the background would be a substance with similar optical properties (less important for mapping phantoms since penetration/sampling depth is not really a consideration) and Raman signature to say for example, epithelial

tissue, Barrett's or stroma (or in the most simple of cases intralipid or intralipid/gelatine mixture), whilst the focal region may be a small region of cancer. It would be important to mimic the biochemical signature of the focal region for the phantom, or use a material with comparable orthogonality to the background tissue type chosen. Detecting HGD and LGD would require more subtle biochemical differences in the phantom which can be represented by a reduced concentration of a substance or more similar biochemical signature. Interpreting the results would become especially complex since multivariate techniques are often used to interpret Raman images.

Figure 7-4 shows some initial phantom designs which could potentially be used for quantifying spatial resolution and image contrast in Raman images. This could also be extended to depth and lateral spatial resolution for Raman probe and surface offset Raman spectroscopy.[66]

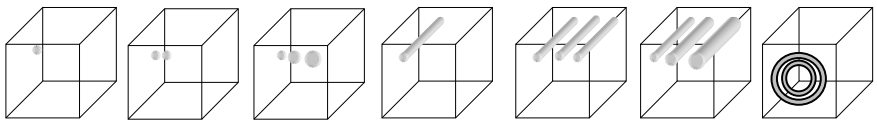

Figure 7-4: Initial phantom designs which can incorporate materials of varying concentration and volume to overcome limitations with current assessment of spatial resolution

7.3 The combination of chemometric analysis and Raman spectroscopy for pathology diagnosis – data quality versus data quantity

As touched upon in both the Raman probe for targeted biopsy and Raman mapping for automated histology studies, signal to noise ratio and dataset size are key parameters of multivariate tissue classification models. For Raman probe studies, spectra datasets sizes are relatively small, compared to Raman mapping studies, and whilst the SNR of the probe spectra is relatively good, spectral peaks are masked by probe backgrounds.

Considering Raman mapping experiments, to obtain Raman images in clinically practicable time frames, the SNR must be sacrificed

It was demonstrated previously (Figure 6-14), that the quality of the PC loads increases with dataset size. It has also been shown that fewer numbers of good quality probe spectra (albeit with few spectral peaks) can separate out three pathology groups.

Consensus pathology has also been shown to improve tissue classification by improving the training of the model.

A further consideration for automated histopathology and targeted biopsy techniques is how specifically the spectrum relates to the pathology, which is in effect a problem of spatial resolution since it relates to spectral mixing. To investigate this, the classification performance of different models was assessed from a perspective of practical clinical implementation, with the aim of determining optimum parameters for future clinical implementation studies. The number of pathology groups included, dataset size and spectral quality were considered. The overall experimental time and analysis time was also considered. The results are summarised in Table 7-2.

The quality and quantity of the data required will depend on the diagnostic requirements. For example if the ultimate aim is only to separate out normal from abnormal tissues then relatively crude spatial averaging and poor signal to noise spectra could be used however if the aim is to separate out tissue types, pre-cancers, cancers and even predict prognosis then more subtle biochemical features may need to be resolved. It will also depend on whether the histopathologist is confident in spectroscopic diagnosis without the additional morphological information represented in the form of a pseudocolour histology image. If not then crude step size maps could potentially provide a rapid and automated method of pathology diagnosis. Taking this idea to the extreme, it may be sufficient simply to use an *ex vivo* probe or collect a spectrum with a low magnification objective, averaged over a large area of tissue, although work will need to be carried out to verify the minimum level of signal mixing required to detect pathology changes. A combination of modalities may be advantageous, for example FTIR for mapping the

entire sample, followed by high lateral spatial resolution Raman mapping of regions of interest. The complementary nature of FTIR and Raman is being explored by many groups including ours.[137,190]

Table 7-2: Summary of training model performance for Raman probe and Raman mapping studies

Model summary	Samples/ spectra	Model parameters Acq. time, stepsize, pathology groups,	Training performance %
Novel probe – Limited dataset size, prelim. model	30/30	4s&60s,3gp(consensus)	86, 90
Visionex probe model – reasonable dataset size	184/184	4s, 3gp (consensus)	82
Raman map B – low SNR, large dataset	1/9000	0.5s, 25.3, N/A	N/A(PCA)
Sample 1 – LDA, poorly define dataset, low spatial res.	1/9592	15s, 8.4, 6gp	70.1
Sample 2 – LDA, poorly defined dataset, high spatial res.	1/156220	15s, 2.1, 6gp	64.9
Sample 1 – LDA, well defined dataset, high spatial res.	1/9592	15s, 8.4, 5gp	94.4
Sample 1 – LDA, well defined dataset, low spatial res.	1/156220	15s, 2.1, 5gp	93.7
Sample 2 – very well defined dataset, low spatial res.	1/500	15s, 8.4, 3gp	100
Sample1&2 – LDA, very well defined dataset, low spatial res.	2/1292	15s, 8.4, 5gp	97.5

These two points have considerable impact on the implementation of Raman spectroscopy as a clinical tool. It can be inferred that if small datasets are used (such as Raman probe studies, relatively good SNR spectra will be required until adequately large datasets are acquired. This implies that for future model generation, Raman spectra with a poorer SNR than initially conceived should be acquired in tandem with better quality spectra with the prospect of larger datasets in the future. The number of pathology groups which can be separated will be low until larger spectral datasets are acquired. In the future, it may become apparent that the limited spectral information within Raman probe spectra with high background and poor spectral resolution. However, the development of novel probe designs should improve Raman spectra.

The extent to which we attempt to separate out pathology information is a question of clinical need which, ultimately, will need to be answered by the histopathologist.

It is evident from the results of this thesis that there is promise for future clinical implementation of Raman spectroscopy for both targeted biopsy and automated histopathology. For the probe studies, the next step is to take the probe to the next phase

of development, dealing with issues such as sterilization and retesting in a clinical environment, whilst for the mapping studies, large pre-clinical trials are now required which will involve mapping many more samples to verify inter-compare patients and pathologies. The following sections summarise potential protocols for these studies based on lessons learned from this thesis.

7.3.1 Optimum parameters for future Raman probe for targeted biopsy studies

One factor which has arisen from these studies is the limits of SNR which can be pushed when used in combination with multivariate techniques. In any future study, SNR of measured spectra should be taken below what is thought feasible in the anticipation of measuring spectral datasets large enough to deal with limited SNR data. Acquiring both good and poor quality spectra from each sample enables robust training classification models to be generated.

A proposed protocol for ex vivo probe validation is to measure clinical samples in theatre, prior to clinical throughput for histology. Once samples have been formalin fixed and archived, samples can be extracted and reanalysed for consensus pathology. This will maximise sample numbers. This method may not be suitable for the probes with large sampling volumes, but for the novel probe this is not an issue. The acquisition times determined were 2x15 s, 1 s, and 0.1 s. The latter would feasibly allow large areas to be sampled or even imaged, with the clinician effectively able to sweep the probe over larger areas to survey for potential disease, however, spectrometer design may be needed to reduce dead time in CCD readout as with rapid Raman mapping. The proposed protocol is schematically described in Figure 7-5.

For probe studies with larger sampling volumes, the in vivo set up must be mimicked more closely, for example measuring EMRs or resected samples. Measuring in a theatre environment would maximise sample numbers.

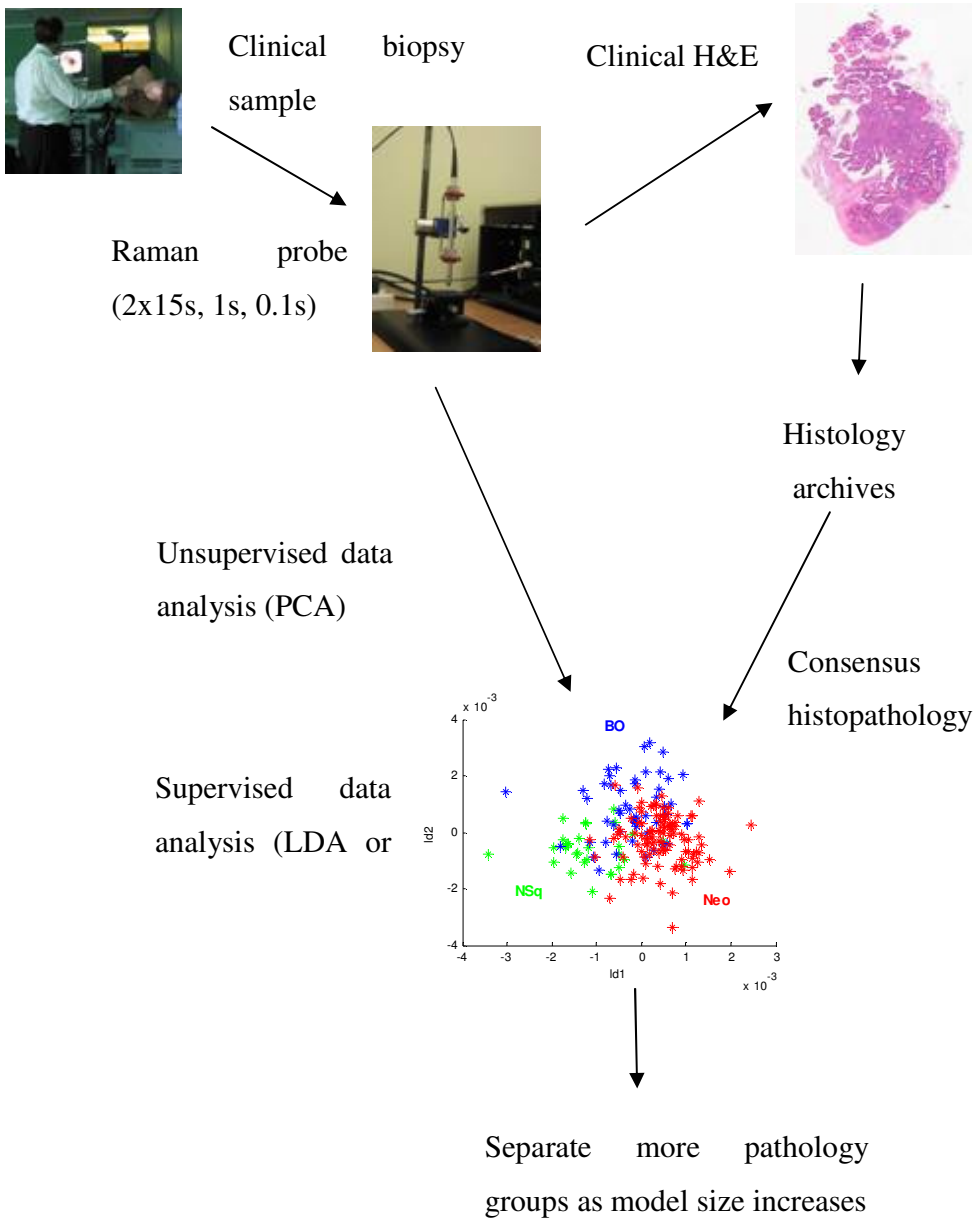

Figure 7-5: Proposed protocol for large scale ex vivo Raman probe study for targeted biopsy

7.3.2 Optimum parameters for future Raman mapping studies for automated histopathology

In order to determine optimum parameters, the method in which potential automated histopathology will be carried out needs to be considered. There are two possible ways

in which it could be utilised which require different approaches. The first approach is the use of relatively crude spatial resolution Raman mapping for filtering out non-relevant tissue samples (i.e. normal or low risk samples). The second would be to provide the histopathologst with a more detailed histology breakdown, and image.

Any potential future study would ideally encompass both eventualities. This would be easy to achieve since bulk discrimination of tissue types would likely to be carried out using crude spatial resolution with short acquisition times to minimise overall mapping times. For more detailed information, these maps can then be followed by longer acquisition time and/or high spatial resolution maps.

It appears that high spatial resolution is not necessarily required for bulk tissue classification which implies that mid-IR imaging may be a more suitable mapping technique, since it is more reliable and has greater SNR data. However, it is also implied that higher spatial resolution may have advantages, but until a larger scale trial is carried out, this cannot be ruled out. Furthermore, Raman has advantages over mid-IR techniques since sample preparation is simple (mid-IR absorption mapping is very sensitive to saturations caused by thick tissue samples). Continuity with in vivo studies would also be advantageous since this would enable biochemical validation of both techniques in tandem.

Considering Raman mapping technology is advancing it can be assumed that Raman mapping times will reduce further still in the future. Based on this, future large scale Raman mapping studies should be carried out, potentially in tandem with mid-IR imaging. Similar SNR factors apply to Raman mapping experiments as well as mid-IR imaging, and reducing the SNR of mid-IR spectra should also be investigated.

It is envisaged that the Raman spectrometer system will eventually be situated in the histology department. It has been shown that frozen sections can be stained on the substrate which enables comparison with contiguous sections (Figure 6-17). However, CaF_2 substrates (~£25) are not reusable once stained and coverslipped which implies that a cheaper alternative is required. Polished aluminium slides have been used in the

group for cell mapping studies which are cheaper than CaF_2, however they will need to be evaluated fully for tissue measurements and histopathology.

Raman mapping could be carried out in parallel with current clinical practice. A selection of biopsies will be snap frozen rather than formalin fixed and frozen sections and contiguous H&E sections taken. The remainder of the sample could then either be retained as a frozen sample, or formalin fixed and archived according to current clinical procedure.

Raman mapping would be used in a similar manner to traditional microscopy. A low magnification global image would be assessed, followed by higher magnification regions of interest. The initial aim would be to filter out non-relevant tissue samples (i.e. filter out normal samples), and for this only bulk tissue pathology discrimination would be required.

To mimic this process, a Raman mapping protocol should be adopted similar to that described in Section 4.6.4, additional rapid scans should be carried out in anticipation of larger datasets improving tissue classification. The proposed study would consist of several rapid pre-scan (0.1s, 25, 8 and 1-4μm), followed by and a longer acquisition time maps of regions of interest (5-15s, 8 and 1-4μm). For developing the training model, mapping the entire sample is not necessarily essential, as long each of the pathologies is well represented. However, this will be required for clinical implementation.

Investigating the effects of projecting poor quality spectra onto classification models with good SNR data may be an alternative to long mapping times in clinic since spectral libraries can be built in advance of clinical implementation.

It is likely that main-frame computing may be required for the analysis stage to handle large datasets until computer technology improves sufficiently.

Chapter 8 Future work

8.1 Multi-centre study of calibration standards and tissue equivalent phantoms

The previous section described potential protocols for large scale clinical trials for both Raman probes for targeted biopsy and Raman mapping for automated histopathology. Moving towards inter-departmental trials is another key step, but in order to achieve this, it is important to ensure system standardisation and transferability. This problem has been addressed within our laboratories between microscopy systems, using green glass intensity calibration. However, problems were experienced in this study for the Raman probe system. Further work is required to identify sources of these discrepancies and similar investigations carried out using novel probe designs.

Objective: To develop methods of transferring data and classification models between microscopy and laboratory Raman systems. This will enable probe data to be compared to previously developed classification models (from the Raman microscopy systems) and furthermore allow development of large scale spectral databases from different hospitals. If a reliable method can be developed, it will enable probe data to be compared to previously validated and published results.

It is anticipated that this should be carried out using test phantoms and calibration standards since measurements will need to be carried out internationally and reproducibly to obtain data to represent different instrumentation under different setups.

It is also proposed that a simple and homogeneous tissue sample is used to obtain multiple consecutive sections (with H&E sections in between) to enable more realistic comparison of different instrumentation. Obtaining a large tissue sample from an oesophagectomy may be one way of obtaining such a sample since regions of normal, or potentially Barrett's mucosa can be harvested away from the disease site.

8.2 Investigate and compare alternative pre-processing and multivariate analytical techniques

It has been discussed previously that there is a need for investigating pre-processing and calibration methods to ensure transferability of spectral data between systems. A comparison of multivariate techniques such as artificial neural network (ANN), support vector machines (SVM) and hierarchal cluster analysis (HCA) with LDA is also required.

8.3 Develop the prognostic model

The prognostic model investigates correlations between Raman signature and high risk patients with HGD, i.e. which high risk patients which are likely to progress to cancer. A poster presented at SPEC, Heidelberg (2006) which resulted from some data analysis carried out on behalf of Mr. Simon Dwerryhouse (formerly Biophotonics Research Group) can be seen in Appendix K. Following up patients from previous classification models, and those within this thesis may enable correlation with progression to cancer.

8.4 Biochemical fitting of rapid Raman mapping and a comparison with immunohistochemistry staining

One of the next steps towards automated Raman histopathology is fitting biochemical constituents to the rapid Raman maps. This so called biochemical mapping has been used by our groups and others to elucidate biochemical changes associated with carcinogenesis.[214,123,175] A further extension of this is to correlate the results with immunohistochemistry to identify the presence of mucins and other subtle biochemical changes with Raman mapping results and genetic mutation studies.

A collaborative project has already been established with Prof. Sir. N. Wright at CRUK, London and preliminary measurements have already commenced to identify different phenotypes in Barrett's crypts.

Chapter 9 Conclusions

9.1 Aim 1 – Classification model conclusions

The Visionex probe was shown to discriminate three different pathology groups with a good overall accuracy in a cross validated multivariate model. Promising results were obtained in a preliminary study of a novel single collection fibre probe. Although this model was small, it can be inferred that a similar and potentially improved performance as the Visionex probe will be achieved with a larger spectral dataset since raw spectra (and background spectra) can be seen to contain equivalent spectral information. It was also demonstrated that an acquisition time of as low as 4s could be used.

Sampling depth is considered to be an important parameter for probe design and as a result, the Emvision probe was ruled out as a potential *in vivo* probe for endoscopic use for early diagnosis of oesophageal premalignancies, however this probe may have other applications for probing deeper structures/resection margins.

In summary, both the Visionex and single collection fibre Raman probes have been shown to have potential for in vivo applications, and further efforts should now be committed to developing large tissue classification models and overcoming instrumentation issues prior to in vivo trials.

9.2 Aim 2 – Evaluation of rapid Raman mapping for potential automated histology

This study has demonstrated the advent of rapid Raman mapping technology in combination with multivariate techniques, has enabled mapping times to be reduced to a clinically practicable time scale.[204,205]

A further question of whether or not high spatial resolution mapping is required for automated histopathology was addressed. It was concluded that high spatial resolution

was not necessarily required and that a step size of 8μm was sufficient for separating bulk tissue pathologies. High spatial resolution imaging, does however, have visual advantages for the histopathologist since morphological structures can be identified more easily. Furthermore, there is the potential for separating out more pathology groups by reducing spectral mixing effects. Maps with different spatial resolutions were compared using linear discriminant analysis imaging of multiple maps demonstrating that technique could be applied between different samples. Rapid Raman mapping has been shown to be a useful research tool for elucidating biochemical changes associated with pathology.

This thesis and subsequent publications has served to improve the results within the literature which will hopefully enable scientists to make an informed choice when selecting a Raman imaging technique for biomedical and wider applications.

9.3 Aim 3 – Factors limiting translation of Raman optical diagnostic techniques into the clinical environment

Practical considerations for implementing Raman spectroscopy for both in vivo and ex vivo diagnostic applications were investigated. Ambient light sources such as LCD computer screens were found to be a significant problem, which can easily be overcome using shielding, switching off the screen or using alternative computer screens. LEDs can also provide an alternative light source. However, further work is required to investigate theatre lights and those used during endoscopy.

A variation in peak position with ambient temperature was also detected which highlights the importance of temperature stabilisation and calibration procedures. Peak shifts appear to be less of an issue for the probe based spectrometer.

Consideration of practical issues also led to the development of protocols for future large scale clinical studies. One conclusion was that the effectiveness of noise reduction using PCA should not be underestimated and it was recommended that this should be taken into account when devising study protocols.

The potential benefits of optical biopsy/automated histopathology are well known, namely that the technique is objective reproducible and in the case of *in vivo* diagnosis, can provide an immediate diagnosis. These factors will have patient outcome and cost benefits. This study has addressed some of the important issues which have previously limited the translation of Raman spectroscopy into the clinical environment for potential *in vivo* and *ex vivo* diagnosis of pathology.

Chapter 10 References

[1] Kendall, C., Stone, N., Shepherd, N., Geboes, K., Warren, B., Bennett, R. and Barr, H. (2003). Raman spectroscopy, a potential tool for the objective identification and classification of neoplasia in Barrett's oesophagus. *J. Pathol.,* 200(5), p. 602-609.

[2] Stone, N., Shepherd, N., Crow, P. and Barr, H. (2002). Near-infrared Raman spectroscopy for the classification of epithelial pre-cancers and cancers. *Journal of Raman Spectroscopy* 33, p. 564-573.

[3] Vander, A., Shermna, J. and Luciano, D. (1998). Genetic Information and Protein Synthesis, In: *Human physiology – The mechanisms of body function. Seventh edition*, edited by Vander, A., Shermna, J. and Luciano, D. WCB/McGraw-Hill, p. 89-109

[4] Perelman, L. T., and Backmann., V. (2002). Light Scattering Spectroscopy of Epithelial Tissues, In: *Handbook of Optical Biomedical Diagnostics,* edited by Tuchin, V. V. SPIE Press, p.675-773.

[5] Mudan, S. S. and Kang, J. Y. (2008). Epidemiology and Clinical Presentation in Esophageal Cancer. In: *Carinoma of the Esophagus*, edited by S. C. Rankin. Cambridge University Press, UK, p. 1-13.

[6] Cancer Research UK (2008). (http://info.cancerresearchuk.org/cancerstats/survival/latestrates/Cancer) (accessed 18th December 2008).

[7] Cancer research UK (2008). (www.cancerresearchuk.org/cancerstats/types/oesophagus/incidence) (Accessed 18th December 2008).

[8] Parkin, D. B. F., Ferlay, J. and Pisani, P. (2005). Global cancer statistics, 2002. *CA Cancer J Clin,* 55(2), p. 74-108.

[9] Cancer Research UK (2008). (http://info.cancerresearchuk.org/cancerstats/types/oesophagus/?a=5441) (Accessed 18th December 2008).

[10] Lagergren, J., Bergström, R., Lindgren, A. and Nyrén, O. Symptomatic Gastroesophageal Reflux as a Risk Factor for Esophageal Adenocarcinoma. *New England Journal of Medicine*, 340(11), p. 825-831.

[11] Goldblum, J. (2003). Barrett's Esophagus and Barrett's-Related Dysplasia. *Modern Pathology*, 16(4), p. 316–324.

[12] Kyrgidis, A., Kountouras, J., Zavos, C. and Chatzopoulos, D. (2005). New Molecular Concepts of Barrett's Esophagus: Clinical Implications and Biomarkers. *Journal of Surgical Research,* 125, p. 189–212.

[13] Barr, H., Kendall, C. and Stone, N. (2001). Review Article: the potential role for photodynamic therapy in the management of upper gastrointestinal disease. *Alimentary Pharmacology & Therapeutics,* 15, p. 311-321.

[14] Flejou, J. F. (2005). Barrett's oesophagus: from metaplasia to dysplasia and cancer. *Gut,* 54, Suppl 1, p. i6-12.

[15] Wani, S. and Sharma, P. (2006). The rationale for screening and surveillance of Barrett's metaplasia. *Best Practice & Research Clinical Gastroenterology*, 20(5), p. 829-842.

[16] Barrett's Oesophagus Foundation (2006). www.barrettsfoundation.org,uk/about_bo. (Accessed 14th March 2006).

[17] Riddell, H., Goldman, H., Ransohoff, D. F., Appelman, H. D., Fenoglio, C. M., Haggitt, R. C., Correa, P., Hamilton, S. R., Morson, B. C., Sommers, S. C. and Yardley, J. H. (1983). Dysplasia in inflammatory bowel disease: Standardized classification with provisional clinical application. *Human Pathology*, 14, p. 931–968.

[18] Reid, B. J., Haggitt, R. C., Rubin, C. E., Roth, G., Surawicz, C. M., Vanvelle, G., Lewin, K., Weinstein, W. M., Antonioli, D. A., Goldman, H., MacDonald, W. and Owen, D. (1988). Observer variation in the diagnosis of dysplasia in Barrett's esophagus. *Human Pathololog*y, 19(2), p. 166-78.

[19] Hurschler, D., Borovicka, J., Neuweiler, J., Oehlschlegel, C., Sagmeister, M., Meyenberger, C. and Schmid, U. (2003). Increased detection rates of Barrett's oesophagus without rise in incidence of oesophageal adenocarcinoma. *Swiss Med Wkly* 133(37), p. 507-514.

[20] Sampliner, R. E. (1998). Practice guidelines on the diagnosis, surveillance, and therapy of Barrett's esophagus. *American Journal of Gastroenterology*, 93(7), p. 1028-1032.

21 DaCosta, R. S., Wilson, B. C. and Marcon, N. E. (2006). Spectroscopy and fluorescence in esophageal diseases. *Best Practice & Research Clinical Gastroenterology,* 20(1), p. 41-57.

[22] www.seer.cancer.gov/csr/1973-1999/ (accessed 14th December 2006)

[23] Barr, H. (2003). The pathological implications of surveillance, treatment and surgery for Barrett's oesophagus. *Current Diagnostic Pathology,* 9, p. 242-251.

[24] Montgomery, E., Bronner, M. P., Goldblum, J. R., Greenson, J. K., Haber, M. M., Hart, J., Lamps, L. W., Lauwers, G. Y., Lazenby, A. J., Lewin, D. N, Robert, M. E., Toledano, A. Y., Shyr, Y. and Washington, K.(2001). Reproducibility of the diagnosis of dysplasia in Barrett esophagus: a reaffirmation. *Human Pathology,* 32(4), p. 368-378.

[25] Falk, G. W., Rice, T. W. (1999). Jumbo biopsy forceps protocol still misses unsuspected cancer in Barrett's esophagus with high-grade dysplasia. *Gastrointest Endosc* 49(2), p. 170.

[26] Dar, M. S., Goldblum, J. R., Rice, T. W. and Falk, G. W. (2003). Can the extent of high grade dysplasia in Barrett's oesophagus predict the presence of adenocarcinoma at oesophagectomy? *Gut,* 52(4), 486-489.

[27] Lennon, A. M. and Penman, I. D. (2008). Recent Advances in the Endoscopic Diagnosis of Esophageal Cancer., Epidemiology and Clinical Presentation in Esophageal Cancer. In: *Carinoma of the Esophagus,* edited by S. C. Rankin. Cambridge University Press, UK, p. 28-40.

[28] Sugimachi, K., Kitamura, K., Baba, K., Ikebe, M. and Kuwano, H. (1992), Endoscopic diagnosis of early carcinoma of the esophagus using Lugol's solution. *Gastrointestinal Endoscopy,* 38(6), p. 657-661.

[29] Kaffes, A. J. , Mishra, A., Simpson, S. B., Jones, D. B. (2002) Upper gastrointestinal endoscopic ultrasound and its impact on patient management: 1990-2000. *Internal Medicine Journal*, 32(8), p. 372-378.

[30] Lennon, A. M. and Penman, I. D. (2008). Endoscopic Ultrasound in Esophageal Cancer. In: *Carinoma of the Esophagus*, edited by S. C. Rankin. Cambridge University Press, UK, p. 44-61.

[31] Curvers, W. L., Kiesslich, R., Bergman, J. J. G. H. M. (2008). Novel imaging modalities in the detection of oesophageal neoplasia. *Best Practice & Research Clinical Gastroenterology*, 22(4), p. 687-720.

[32] Lao-Sirieix, P., Rous, B., O'Donovan, M., Hardwick, R. H., Debiram, I. and Fitzgerald, R. C. (2007). Non-endoscopic immunocytological screening test for Barrett's oesophagus, *Gut*, 56 (7), p. 1033-1034.

[33] Allum, W. H., Griffin, S. M., Watson, A., Colin-Jones, D. (2002). Guidelines for the management of oesophageal and gastric cancer. *Gut*, 50, (Suppl.V), v1–v23.

[34] Byrne, J. P., Armstrong, G. R. and Attwood, S. E. A. (1998). Restoration of the normal squamous lining in Barrett's esophagus by argon beam plasma coagulation. *The American Journal of Gastroenterology,* 93(10), p. 1810-1815.

[35] Gossner, L., May, A., Stolte, M., Seitz, G., Hahn, E. G., Ell, C. l. (1999). KTP laser destruction of dysplasia and early cancer in columnar-lined Barrett's esophagus. *Gastrointest. Endosc.* 49(1), p. 8-12.

[36] Sujendran, V., Sica, G., Warren, B. and Maynard, N. (2005). Oesophagectomy remains the gold standard for treatment of high-grade dysplasia in Barrett's oesophagus. *European Journal of Cardio-Thoracic Surgery,* 28(5), p. 763-766.

[37] Bergman, J. J. G. H. M, (2005) Endoscopic treatment of high-grade intraepithelial neoplasia and early cancer in Barrett oesophagus. *Best Practice & Research Clinical Gastroenterology*, 19 (6), p. 889–907.

[38] Vieth, M., Ell, C., Gossner, L., May, A. and Stolte, M. (2004). Histological analysis of endoscopic resection specimens from 326 patients with Barrett's esophagus and early neoplasia. *Endoscopy* 36(9), p. 776-781.

[39] Mason, R. (2008). The Role of Surgery in the Management of Esophageal Cancer and Palliation of Inoperable Disease. In: *Carinoma of the Esophagus*, edited by S. C. Rankin. Cambridge University Press, UK, p. 1-13.

[40] Sibille, A., Lambert, R., Souquet, J. C., Sabben, G. and Descos, F. (1995). Long-term survival after photodynamic therapy for esophageal cancer. *Gastroenterology*, 108(2), 337-344.

[41] Jankowski, J. A., Wright N. A., Meltzer, S. J., Triadafilopoulos, G., Geboes, K., Casson, A. G., Kerr, D. and Young, L. S. (1999). Molecular Evolution of the Metaplasia-Dysplasia-Adenocarcinoma Sequence in the Esophagus. *American Journal of Physiology*, 154(4), p. 965-973.

[42] McManus, D. T., Olaru, A., Meltzer, S. J. (2004). Biomarkers of esophageal adenocarcinoma and Barrett's esophagus. *Cancer Research,* 64(5), p. 1561-1569.

[43] Weston, A. P., Banerjee, S. K., Sharma, P., Tran, T. M., B.S., Richards, R. and Cherian, R. (2001). p53 protein overexpression in low grade dysplasia (LGD) in Barrett's esophagus: immunohistochemical marker predictive of progression. *Am. J. Gastroenterol.* 96(5), p. 1355-1362.

[44] Werther, M., Saure, C., Pahl, R., Schorr, F., Ruschoff, J., Alles, J, and Heinmoller, E. (2008) Molecular genetic analysis of surveillance biopsy samples from Barrett's mucosa – Significance of sampling. *Pathology – Research and Practice*, 204, p. 285–294.

[45] Deere, H. M. R. (2008). Pathology of Esophageal Cancer. In: *Carinoma of the Esophagus*, edited by S. C. Rankin. Cambridge University Press, UK, p. 14-27.

[46] Georgakoudi, I., and Van Dam, J. (2005). Characterization of dysplastic tissue morphology and biochemistry in Barrett's esophagus using diffuse reflectance and light scattering spectroscopy. *Techniques in Gastrointestinal Endoscopy,* 7(2), p. 100-105.

[47] Backman, V., Wallace, M. B., Perelman, L. T., Arendt, J., T., Gurjar, R., Müller, M. G., Zhang, Q., Zonios, G., Kline, E., McGillican, T., Shapshay, S., Valdez, T., Badizadegan, K., Crawford, J. M., Fitzmaurice, M., Kabani, S., Levin, S.H., Seiler, M., and Dasari, R., (2000). Detection of preinvasive cancer cells, *Nature*, 406(6791), p. 35-6.

[48] Tunnell, J. W., Desjardins, A. E., Galindo, L., Georgakoudi, I., McGee, S. A., Mirkovic, J., Mueller, M. G., Nazemi, J., Nguyen, F. T., Wax, A., Zhang, W., Dasari, R. R. and Feld, M. S. (2003). Instrumentation for Multi-modal Spectroscopic Diagnosis of Epithelial Dysplasia. *Technology in Cancer Research & Treatment,* 2(6), p. 505-514.

[49] Wallace, M. B., Perelman, Backman, V., Crawford, J. M., Fitzmaurice, M., Seiler, M., Badizadegan, K., Shields, S. J., Itzkan, I., Dasari, R. R., van Damm J. and Feld, M. S. (2000). Endoscopic detection of dysplasia in patients with Barrett's esophagus using light-scattering spectroscopy. *Gastroenterology,* 119(3), p. 677-682.

[50] Dhar, A., Johnson, K. S., Novelli, M. R., Bown, S. G., Bigio, I. J., Lovat, L. B. and Bloom, S. L. (2006). Elastic scattering spectroscopy for the diagnosis of colonic lesions: initial results of a novel optical biopsy technique. *Gastrointestinal Endoscopy,* 63(2), p. 257-261.

[51] Lovat, L. B., Johnson, K., Mackenzie, G. D., Clark, B. R., Novelli, M. R., Davies, S., O'Donovan, M., Selvasekar, C., Thorpe, S. M., Pickard, D., Fitzgerald, R., Fearn, T., Bigio, I. and Bown, S. G. (2006). Elastic scattering spectroscopy accurately detects high grade dysplasia and cancer in Barrett's oesophagus *Gut*, 55, p. 1078-1083.

[52] Raman, C. V. and Krishanan, K. S. (1928). A new type of secondary radiation, *Nature*, 121, p. 501-502 (1928).

[53] Smith, E., Dent, G. (2005). *Modern Raman Spectroscopy: A Practical Approach*, edited by, Smith, E., Dent, G. John Wiley and Sons.

[54] Hanlon, E. B., Manoharan, R., Koo, T-W., Shafer, K. E., Motz, J. T., Fitzmaurice, M., Kramer J. R., Itzkan, I., Dasari, R. R. and Feld M. S. (2000). Prospects for in vivo Raman spectroscopy, *Physics in Medicine and Biology,* 45(2), p. R1-59.

[55] Mahadevan-Jansen, A. and Richards-Kortum, R. (1996). Raman spectroscopy for the detection of cancers and precancers. *Journal of Biomedical Optics,* 1, p. 31-70

[56] Shim, M. G. and Wilson, B. C. (1997). Development of an in vivo Raman spectroscopic system for diagnostic applications. *Journal of Raman Spectroscopy,* 28, p. 131-142.

[57] Wong Kee Song, L. M. and Wang, K. K. (2003). Optical detection and eradication of dysplastic Barrett's esophagus. *Technol Cancer Res Treat,* 2(4), p. 289-302.

[58] Yu, C., Gestl, E., Eckert, K., Allara, D. and Irudayaraj, J. (2006). Characterization of human breast epithelial cells by confocal Raman microspectroscopy. *Cancer Detection and Prevention,* 30, p. 515–522.

[59] Treado, P. J. and Nelson M. P. (2001). Raman Imaging. In: *Handbook of Raman Spectroscopy: Practical Spectroscopy Series Vol. 28*, edited by I.R. Lewis and H.G.M Edwards, (Marcel Dekker, Inc., New York, p. 191-213.

[60] Duncan, M. D., Reintjes, J. and Manuccia T. J. (1982). Scanning coherent anti-Stokes Raman microscope. *Optics Letters,* 7, p. 350-352.

[61] Fleischmann, M., Hendra, P. J., and McQuillan, A.J., (1974). Raman spectra of pyridine adsorbed at a silver electrode. *Chemical Physics Letters*, 26(2), p. 163-166.

[62] Kneipp K., Wang Y., Kneipp H., Perelman L. T., Itzkan I., Dasari, R. R. and Feld, M. S. (1998). Detection and identification of a single DNA base molecule using Surface- Enhanced Raman Scattering (SERS). *Phys. Rev. E* , 57(6), R6281 - R6284.

[63] Sabatte, G., Keir, R., Lawlor, M., Black, M., Graham D., and Smith, W. E. (2008). Comparison of Surface Enhanced Resonance Raman Scattering (serrs) and Fluorescence for Detection of a Labelled Antibody. *Analytical Chemistry,* 80(7), p. 2351-2356.

[64] Faulds, K., Stewart, L., Smith, W. E. and Graham, D. (2005). Quantitative detection of dye labelled DNA using surface enhanced resonance Raman scattering (SERRS) from silver nanoparticles. *Talanta*, 67(3), p. 667-671.

[65] Stokes, R. J., Macaskill, A., Lundahl P. J., Smith, W. E., Faulds, K. and Graham, D. (2007). Quantitative Enhanced Raman Scattering of Labeled DNA from Gold and Silver Nanoparticles, *Small*, 3 (9), p. 1593-1601.

[66] Matousek, P., (2007). Deep non-invasive Raman spectroscopy of living tissue and powders. *Chem. Soc. Rev.*, 36, p. 1292–1304.

[67] Matousek, P., Everall N., Towrie M. and Parker A. W. (2005). Depth Profiling in Diffusely Scattering Media Using Raman Spectroscopy and Picosecond Kerr Gating. *Applied Spectroscopy,* 59, p. 200–205.

[68] Baker, P., Matousek, P., Ronayne, K. L., Parker, A. W., Rogers, K. and Stone, N. (2007). Depth profiling of calcifications in breast tissue using picosecond Kerr-gated Raman spectroscopy. *Analyst*, 132, p. 48–53.

[69] Matousek, P. and Stone, N. (2007). Prospects for the diagnosis of breast cancer by noninvasive probing of calcifications using transmission Raman spectroscopy. *Journal of Biomedical Optics,* 12(2), p. 024008.

[70] Morris, M. D., Matousek, P., Towrie, M., Parker, A. W., Goodship A. E. and Draper, E. R. C. (2005). *Journal of Biomedical Optics,* 10, p. 014014.

[71] Jackson, M. and Mantsch, H. H. (1992). Bio-analytical applications of Fourier transform infrared spectroscopy. *Trends in Analytical Chemistry*, 11(6), p. 206-210.

[72] Jackson, M., Haris, P. I. and Chapman, D. (1989). Fourier transform infrared spectroscopic studies of lipids, polypeptides and proteins. *Journal of Molecular Structure,* 214, p. 329-355.

[73] Krafft, C. and Sergo, V. (2006). Biomedical applications of Raman and infrared spectroscopy. *Spectroscopy*, 20, p. 195-218.

[74] Wang, J. S., Shi, J. S., Xu, Y. Z., Duan, X. Y., Zhang, L., Wang, J., Yang, L. M., Weng, S. F., Wu, J. G. (2003). FT-IR spectroscopic analysis of normal and cancerous tissues of esophagus. *World J. Gastroenterol.*, 9(9), p. 1897-1899.

[75] Maziak, D. E., Do, M. T., Shamji, F. M., Sundaresan, S. R., Perkins, D. G., Wong, P. T. T. (2007). Fourier-transform infrared spectroscopic study of characteristic molecular structure in cancer cells of esophagus: An exploratory study. *Cancer Detection and Prevention*, 31(3), p. 244-253.

[76] Wang, T. D., Triadafilopoulos, G., Crawford, J. M., Dixon, L. R., Bhandari, T., Sahbaie, P., Friedland, S., Soetikno, R., and Contag, C. H. (2007). Detection of endogenous biomolecules in Barrett's esophagus by Fourier transform infrared spectroscopy. *PNAS*, 104(40), p. 15864–15869.

[77] Ly, E., Piot, O., Wolthius, R., Durlach, A., Bernard, P. and Manfait, M. (2008) Combination of FTIR spectral imaging and chemometrics for tumour detection from paraffin embedded biopsies. *Analyst*, 133, p. 197-205.

[78] McIntosh, L. M., Jackson, M., Mantch, H. H., Stranc, M. F., Pilavdzic, D. and Crowson, A. N. (1999). Infrared Spectra of Basal Cell Carcinomas are Distinct from Non-Tumor-Bearing Skin Components *Journal of Investigative Dermatology*, 112, p. 951-956.

[79] Wood, B. R., Chiriboga, L., Yee, H., Quinn, M. A., McNaughton, D. and Diem, M. (2004). Fourier transform infrared (FTIR) spectral mapping of the cervical transformation zone, and dysplastic squamous epithelium. *Gynecologic Oncology*, 93, p. 59-68.

[80] Paluszkiewicz, C. and Kwiatek, M. (2001) Analysis of human cancer prostate tissues using FTIR microspectroscopy and SRIXE techniques. *Journal of Molecular Structure,* 565-566, p. 329-334.

[81] Fernandez, D. C., Bhargava, R., Hewitt, S. M. and Levin, I. W. (2005). Infrared spectroscopic imaging for histopathologic recognition. *Nature Biotechnololgy,* 23, p. 469-474.

[82] Petibois, C. and Deleris, G. (2006). Chemical mapping of tumor progression by FT-IR imaging: towards molecular histopathology. *Trends Biotechnol.*, 24, p. 455-462.

[83] Krafft, C., Shapoval, L., Sobottka, S. B., Geiger, K. D., Schackert, G., Salzer, R. (2006). Identification of primary tumors of brain metastases by SIMCA classification of IR spectroscopic images. *Biochimica et Biophysica Acta (BBA) - Biomembranes*, 1758(7), p. 883-891.

[84] Eckel, R., Huo, H., Guan, H. W., Hu, X., Che, X. and Huang, W. D. (2001). Characteristic infrared spectroscopic patterns in the protein bands of human breast cancer tissue. *Vibrational Spectroscopy.,* 27(2), p. 165-173.

[85] Alfano, R. R., Tata, D. B., Cordero, J., Tomashefsky, P., Longo, F. W., Alfano, M. A. (1984).Laser induced fluorescence spectroscopy from native cancerous and normal tissue. *IEEE Journal of Quantum Electronics*, 20(12), p. 1507-1511.

[86] Sokolov, K., Follen, M. and Richards-Kortum, R. (2002). Optical spectroscopy for detection of neoplasia. *Current Opinion in Chemical Biology,* 6(5), p. 651-658.

[87] Panjehpour, M., Overholt, B. F., Schmidhammer, J. L., Farris, C., Buckley, P. F. and Vo-Dinh, T. (1995). Spectroscopic diagnosis of esophageal cancer: new classification model, improved measurement system. *Gastrointest. Endosc.,* 41(6), p. 577-581.

[88] Bourg-Heckly, G., Blais, J., Padilla, J. J., Bourdon, O., Etienne, J., Guillemin, F. and Lafay, L. (2000). Endoscopic ultraviolet-induced autofluorescence spectroscopy of the esophagus: tissue characterization and potential for early cancer diagnosis. *Endoscopy,* 32(10), p. 756-765.

[89] Pfefer, T. J., Paithankar, D. Y., Paithankar, D. Y., Poneros, J. M., Schomacker, K. T. and Nishioka, N. S., (2003). Temporally and spectrally resolved fluorescence spectroscopy for the detection of high grade dysplasia in Barrett's esophagus. *Lasers Surg. Med.,* 32(1), p. 10-16.

[90] Wong Kee Song, L. M. and Wilson, B. C. (2005). Optical Detection of High-Grade Dysplasia in Barrett's Esophagus. *Techniques in Gastrointestinal Endoscopy ,* 7(2), p. 78-88.

[91] Endlicher, E., Knuechel, R., Hauser, T., Szeimies, R. M., Schölmerich, J. and Messmann, H. (2001). Endoscopic fluorescence detection of low and high grade dysplasia in Barrett's oesophagus using systemic or local 5-aminolaevulinic acid sensitisation. *Gut,* 48(3), p. 314-319.

[92] Fercher, A. F. (1990). In: *Ophthalmic interferometry Optics in Medicine, Biology and Environmental Research* ed. Gvon Bally and S Khanna (Amsterdam: Elsevier), p. 221–35.

[93] Hitzenberger (1991). Optical measurement of the axial eye length by laser Doppler interferometry. *Invest. Ophthalmol. Vis. Sci.*, 32(3), p. 616-624.

[94] Huang, H. D., Swanson, E. A., Lin, C. P., Schuman, J. S., Stinson, W. G., Chang, W., Hee, M. R., Flotte, T., Gregory, K., Puliafito, C. A. (1991) Optical coherence tomography. *Science,* 254, p. 1178–1181.

[95] Isenberg, G., Sivak, M.V., Chak, A., Wong, R. C. K. Willis, J. E, Wolf, B., Rowland, D. Y, Das, A. and Rollins, A., (2005). Accuracy of endoscopic optical coherence tomography in the detection of dysplasia in Barrett's esophagus: a prospective, double-blinded study. *Gastrointestinal Endoscopy,* 62(6), p. 825-831.

[96] Jenkins, M. W., Chughtai, O. Q., Basavanhally, A. N, Watanabe, M. and Rollins, A. M. (2007). In vivo gated 4D imaging of the embryonic heart using optical coherence tomography. *Journal of Biomedical Optics,* 12(3), p. 030505-1-030505-3.

[97] Holmes, J., Hattersley, S., Stone, N., Bazant-Hegemark, F. and Barr, H. Multi-channel Fourier domain OCT system with superior lateral resolution for biomedical applications. *Progress in Biomedical Optics and Imaging - Proceedings of SPIE*, 6847, art. no. 68470.

[98] Evans, J. A., Poneros, J. M., Bouma, B. E., Bressner, J., Halpern, E. F., Shishkov, M., Lauwers, G. Y., Mino-Kenudson, M., Nishioka, N. S. and Tearney, G .J. (2006). Optical Coherence Tomography to Identify Intramucosal Carcinoma and High-Grade Dysplasia in Barrett's Esophagus. *Clinical Gastroenterology and Hepatology* 4(1), p. 38-43.

[99] Poneros J. (2005). Optical coherence tomography and the detection of dysplasia in Barrett's esophagus. *Gastrointestinal Endoscopy*, 62(6), p. 832-833.

[100] Bazant-Hegemark, F. and Stone, N. (2008). Towards automated classification of clinical optical coherence tomography data of dense tissues. Article in Press.

[101] Fercher, A. F., Drexler, W., Hitzenberger, C.K. and Lasser, T. (2003). Optical coherence tomography - principles and applications. *Reports on Progress in Physics,* 66, p. 239–303.

[102] Lieber, C. A., Uratama, S., Rahim, N., Tu, R., Saroufeem, R., Reubner, B. and Demos, S. G., (2006). Multimodal near infrared spectral imaging as an exploratory tool for dysplastic esophageal lesion identification. *Optics Express* 14(6), p. 2211-2219.

[103] Huang, Z., Lui, H., Korbelik, M., Zeng, H. (2005). Raman spectroscopy in combination with background near-infrared autofluorescence enhances the in vivo assessment of malignant tissues. *Photochemistry and Photobiology,* 81(5), p. 1219-1226.

[104] Patil, C. A, Bosschaart, N., Keller, M. D., van Leeuwen, T. G. and Mahadevan-Jansen, A. (2008). Combined Raman spectroscopy and optical coherence tomography device for tissue characterization, *Opt. Lett.*, 33, p. 1135-1137.

[105] Chaves, P., Cardoso, P., Mendes de Almeida, J. C., Dias Pereira, A., Nobre Leitao, C., and Soares, J. Non-Goblet Cell Population of Barrett's Esophagus: An Immunohistochemical Demonstration of Intestinal Differentiation. *Human Pathology*, 30(11), p. 1291-1295.

[106] Lord, R. C and Yu, N. T. (1970). Laser-excited Raman spectroscopy of biomolecules. II. Native ribonuclease and alpha-chymotrypsin. *J. Mol. Biol.*, 51(2), p. 203-13.

[107] Goheen, S. C., Lis, L. J. and Kauffman, J. W. (1978). Raman spectroscopy of intact feline corneal collagen. *Biochimica et Biophysica Acta (BBA) - Protein Structure,* 536(1), p. 197-204.

[108] Stone, N. (2001). Raman spectroscopy of biological tissue for application in optical diagnosis of malignancy. PhD Thesis, Cranfield University.

[109] Puppels, G. J., Demul, F. F. M., Otto, C., Greve, J., Robernicoud, M., Arndtjovin, D. J. and Jovin, T. M. (1990). Studying single living cells and chromosomes by confocal Raman microspectroscopy Nature (347), 301-303.

[110] Turrell, G. and Corset, J. (1996). *Raman Microscopy: Developments and Applications*. Academic Press.

[111] Duindam, J., Vrensen, G. F., Otto, C., Greve, J. (1998). Cholesterol, phospholipid, and protein changes in focal opacities in the human eye lens. *Invest. Ophthalmol. Vis. Sci.,* 39(1), p. 94-103.

[112] Hirschfeld, T. and Chase, B. (1986). FT-Raman Spectroscopy: Development and Justification. *Applied Spectroscopy* 40(2), 133-137.

[113] Liu, C. H., Das, B. B., Sha, Glassman, W. L., Tang, G. C., Yoo, K. M., Zhu, H. R., Akins, D. L., Lubicz, S. S., Cleary, J., Prudente, R. (1992). Raman, fluorescence, and time-resolved light scattering as optical diagnostic techniques to separate diseased and normal biomedical media. *J. Photochem. Photobiol.* 16(2), p. 187-209.

[114] Mizuno, A. (1994). Near-infrared Fourier transform Raman spectroscopic study of human brain tissues and tumours. *Journal of Raman Spectroscopy,* 25, p. 265-269.

[115] Gniadecka, M., Wulf, H. C., Nielsen, O. F., Christensen, D. H. and Hercogova. J. (1997). Distinctive molecular abnormalities in benign and malignant skin lesions: studies by Raman spectroscopy. *Photochem Photobiol,* 66(4), p. 418-423.

[116] Caspers, P. J., Lucassen, G. W., Wolthuis, R., Bruining, H. A and Puppels, G. J. (1998). *In vitro* and in vivo Raman spectroscopy of human skin. *Biospectroscopy,* 4(5 Suppl.), p. S31-39.

[117] Adar, F (2001). Evolution and Revolution of Raman Instrumentation – Application of Available Technologies to Spectroscopy and Microstopy. In: *Handbook of Raman Spectroscopy. Practical Spectroscopy Series Vol. 28*, edited by I.R. Lewis and H.G.M Edwards, (Marcel Dekker, Inc., New York), p. 11-40.

[118] Pezzuti, J. A. and Morris, M.D., (1997). Progress in Analytical Raman Spectroscopy. *Analytical Communications*, 34, p. 5H–7H.

[119] Brennan, J. F., Wang, Y., Dasari, R. R., Feld, M. S. (1997). Near-Infrared Raman Spectrometer Systems for Human Tissue Studies. *Applied Spectroscopy,* 51(2), p. 201-208.

[120] Jobinyvon (2008). www.jobinyvon.com/Raman/laser-tutorial. (Accessed 19th December 2008).

[121] Kendall, C. (2002). A study of Raman spectroscopy for the early detection and classification of malignancy in oesophageal tissue. PhD Thesis, Cranfield University.

[122] Stone, N., Kendall, C., Smith, J., Crow, P. and Barr, H. (2004). Raman spectroscopy for identification of epithelial cancers. *Faraday Discuss*, 126, p. 141-57.

[123] Shetty, G., Kendall, C., Shepherd, N., Stone, N. and Barr, H. (2006). Raman spectroscopy: elucidation of biochemical changes in carcinogenesis of oesophagus. *British Journal of Cancer,* 94(10), p. 1460-1464.

[124] Shetty, G. (2006). Applications of Raman spectroscopy to the carcinogenesis of oesophagus. MD Thesis, Cranfield University.

[125] Utzinger, U. (2001). Near-Infrared Raman Spectroscopy for in Vivo Detection of Cervical Precancers. *Applied Spectroscopy* 55(8), p. 955-959.

[126] Lyng, F., Faolain, E. O., Conroy, J., Meade, A., Knief, P., Duffy, B., Hunter, M. B., Byrne, J. M., Kelehan, P., Byrne, H. J., (2007). Vibrational spectroscopy for cervical cancer pathology, from biochemical analysis to diagnostic tool. *Experimental and Molecular Pathology*, 82(2), p. 121-129.

[127] Crow, P., Stone, N., Kendall, C., Uff, J., Farmer, J. A. M., Barr, H. and Wright, M, P. J. (2003). The use of Raman spectroscopy to identify and grade prostatic adenocarcinoma in vitro. *British Journal of Cancer,* 89, p. 106-108.

[128] Koljenovic, S., Bakker Schut, T. C., Wolthuis, R., de Jong, B., Santos, L., Caspers, P. J., Kros, J. M. and Puppels G. J. (2005). Tissue characterization using high wave number Raman spectroscopy. *Journal of Biomedical Optics*, 10(3), p. 031116-1-11.

[129]Brozek-Płuska, B., Placek, I., Kurczewski, K., Morawiec, Z., Tazbir, M. and Abramczyk, H. (2008). Breast cancer diagnostics by Raman spectroscopy. *Journal of Molecular Liquids*, 141, p. 145–148.

[130] Haka, A. S., Shafer-Peltier, K. E., Fitzmaurice, M., Crowe, J., Dasari, R. R. and Feld, M. S. (2002). Identifying Microcalcifications in Benign and Malignant Breast Lesions by Probing Differences in Their Chemical Composition Using Raman Spectroscopy. *Cancer Research.* 62, p. 5375–5380.

[131] Rehman, S., Movasaghi, Z., Tucker, A. T, Joel, S. P., Darr, J. A., Ruban, A. V. and Rehman, I. U. (2007). Raman spectroscopic analysis of breast cancer tissues: identifying differences between normal, invasive ductal carcinoma and ductal carcinoma in situ of the breast tissue. *J. Raman Spectrosc.,* 38, p. 1345–1351.

[132] Malini, R., Venkatakrishna, K., Kurien, J., Pai K. M., Rao L., Kartha V. B., Murali Krishna, C. (2006). Discrimination of Normal, Inflammatory, Premalignant, and Malignant Oral Tissue: A Raman Spectroscopy Study. *Biopolymers*, 81, p. 179–193.

[133] Stone, N., Stavroulaki, P., Kendall, C., Birchall, M. and Barr, H. (2000). Raman Spectroscopy for Early Detection of Laryngeal Malignancy: Preliminary Results. *The Laryngoscope,* 110, p. 1756-1763.

[134] Lau, D. P., Huang, Z., Lui, H., Anderson, D. W., Berean, K., Morrison, M. D., Shen, L., and Zeng, H., (2005). Raman Spectroscopy for Optical Diagnosis in the Larynx: Preliminary Findings. *Lasers in Surgery and Medicine* 37, p. 192–200.

[135] Kumar, K. K., Anand, A., Chowdary, M. V. P., Keerthi, Kurien, J., Murali Krishna, C. and Mathew, S. (2007). Discrimination of normal and malignant stomach mucosal tissues by Raman spectroscopy: A pilot study. *Vibrational Spectroscopy*, 44(2), p. 382-387.

[136] Hanchanale, V. S., Rao, A. R. and Das, S. (2008). Raman spectroscopy and its urological applications. *Indian J Urol*, 24, p.444-50.

[137] Lin, S-Y., Li, M-J. and Cheng., W-T. (2007). FT-IR and Raman vibrational microspectroscopies used for spectral biodiagnosis of human tissues. *Spectroscopy*, 21, p. 1-30.

[138] de Paula, A. R. and Sathaiah, S. (2005). Raman spectroscopy for diagnosis of atherosclerosis: a rapid analysis using neural networks. *Medical Engineering & Physics,* 27, p. 237–244.

[139] Archer, J. K. J., Sudworth, C. D., Williams, R., How T., Stone, N., Mann, D. and Black, R. A. (2007). Improvements in Alzheimer Disease Diagnosis using Principal Component Analysis (PCA) in Combination with Raman Spectroscopy. SPIE Volume 6628 of Progress In Biomedical Optics And Imaging, paper 6628_37.

[140] Mahadevan-Jansen, A., Mitchell, M. F., Ramanujam, N., Utzinger, U. and Richards-Kortum, R. (1998). Development of a fiber optic probe to measure NIR Raman spectra of cervical tissue in vivo. *Photochem. Photobiol.,* 68(3), p. 427-31.

[141] Shim, M. G., Wong Kee Song, L. M., Marcon, N. E. and Wilson, B. C. (2000). In vivo near-infrared Raman spectroscopy: demonstration of feasibility during clinical gastrointestinal endoscopy. *Photochem. Photobiol.,* 72(1), p. 146-150.

[142] Hutsebaut, D., Vandenabeele, P. and Moens, L. (2005). Evaluation of an accurate calibration and spectral standardization procedure for Raman spectroscopy. *Analyst* 130, p. 1204-1214.

[143] Laserna, J. J. (1996). *Modern Techniques in Raman Spectroscopy*. Wiley.

[144] de Paula, A. R. and Sathaiah, S. (2005). Raman spectroscopy for diagnosis of atherosclerosis: a rapid analysis using neural networks. *Medical Engineering & Physics,* 27, p. 237–244.

[145] Sasic, S., Clark, D., Mitchell, J. and Snowden, M. (2005). Raman line mapping as a fast method for analyzing pharmaceutical bead formulations. *Analyst,* 130, p. 1530-1536.

[146] Sasic, S., Clark, D., Mitchell, J. and Snowden, M.(2004). A comparison of Raman chemical images produced by univariate and multivariate data processing—a simulation with an example from pharmaceutical practice. *Analyst*, 29, p. 1001-1007.

[147] Shim, M. G., Wilson, B., Marple, E. and Wach, M. (1999). Study of fiber-optic probes for in vivo medical Raman spectroscopy. *Applied Spectroscopy,* 53(6), p. 619-627.

[148] Hayden, C.A. and Morris M. D. (1996). Effects of Sampling Parameters on Principal Components

Analysis of Raman Line Images. *Applied Spectroscopy*, 50(6), p. 708-714.

[149] Lasch P. and Naumann D. (2006). Spatial resolution in infrared microspectroscopic imaging of tissues. *Biochimica et Biophysica Acta* , 1758**,** p. 814-829.

[150] Bhargava, R. (2007), Towards a practical Fourier Transform infrared chemical imaging protocol for cancer histopathology. *Anal. Bioanal. Chem.* 389, p. 1155-1169.

[151] Utzinger, U. and Richards-Kortum, R. (2003). Fiber optic probes for biomedical optical spectroscopy. *Journal of Biomedical Optics* 8(1), p. 121-147.

[152] De Lima, C. J., Sathaiah, S., Silveira, L., Zangaro, R. A. and Pacheco, M. T. T. (2000). Development of catheters with low fiber background signals for Raman spectroscopic diagnosis applications. *Artificial Organs,* 24(3), p. 231- 234.

[153] de Lima, C. J., Simoes, M., Pacheco, M. T. T., Silveira, L., Villaverde, A. B. Optical Fiber Catheter with Distal End Bending Mechanism Control for Raman Biospectroscopy. *Instrument. Sci. Technol.,*36, p. 1-13. (abstract only)

[154] Bakker Schut, T. C., Wolthuis, R., Caspers, P. J. and Puppels, G. J. (2002). Real-time tissue characterization on the basis of in vivo Raman spectra. *Journal of Raman Spectroscopy,* 33(7), 580-585.

[155] Crow, P., Molckovsky, A., Stone, N., Uff, J., Wilson, B., Wongkeesong, L. M. (2005). Assessment of fiberoptic near-infrared Raman spectroscopy for diagnosis of bladder and prostate cancer. *Adult Urology*, 65(6), p. 1126 - 1130.

[156] Teh, S. K., Zheng, W., Ho, K. Y., Teh, M, Yeoh, K. G. and Huang, Z.(2008). "Diagnostic potential of near-infrared Raman spectroscopy in the stomach: differentiating dysplasia from normal tissue", *British Journal of Cancer,* 98, p. 457-465.

[157] Boere, I. A., Bakker Schut, T.C. , van den Boogerta, J., de Bruina, R. W. F. and Puppels, G. J. (2003). Use of fibre optic probes for detection of Barrett's epithelium in the rat oesophagus by Raman spectroscopy. *Vibrational Spectroscopy,* 32(1), p. 47-55.

[158] Robichaux-Viehoever A., Kanter E., Shappell H., Bill-Heimer D., Jones III H., Mahadevan-Jansen, A. (2007). Characterization of Raman Spectra Measured in Vivo for the Detection of Cervical Dysplasia. *Applied Spectroscopy*, 61(9), p. 986-993.

[159] Huang Z., Zeng H., Hamzavi I., McLean D. and Lui H., (2001), Rapid near-infrared Raman spectroscopy system for real-time in vivo skin measurements. Opt Lett, 26:1782–4.

[160]Eikje, N. S., Ozaki, Y., Aizawa, K. and Arase, S. (2005). Fiber optic near-infrared Raman spectroscopy for clinical noninvasive determination of water content in diseased skin and assessment of cutaneous edema. *J. Biomed. Opt.,* 10(1), p. 1-13.

[161] Wong Kee Song, L-M., Molckovsky, A., Wang, K., Buttar, N., Burgart, L., Wilson, B., Dolenko, B. and Somorjai R. (2006). Diagnostic Accuracy of Raman Spectroscopy for the Classification of Dysplastic Lesions in Barrett's Esophagus. *Gastrointestinal Endoscopy* 63(5), AB89.

[162] Haka, A. S., Volynskaya, Z., Gardecki, J. A., Nazemi, J., Lyons, J., Hicks, D., Fitzmaurice, M., Dasari, R. R., Crowe, J. P. and Michael S. Feld (2006). In vivo Margin Assessment during Partial Mastectomy Breast Surgery Using Raman Spectroscopy. *Cancer Res.*, 66(6), p. 3317-3322.

[163] Molckovsky, A., Wong Kee Song, L-M., Shim, M. G., Marcon, N. E. and Wilson, B. C. (2003). Diagnostic potential of near-infrared Raman spectroscopy in the colon: Differentiating adenomatous from hyperplastic polyps. *Gastrointestinal Endoscopy*, 57, p. 396-402.

[164] Short, M. A., Lam, S., McWilliams, A., Zhao, J., Lui, H. and Zeng, H., (2008). Development and preliminary results of an endoscopic Raman probe for potential in vivo diagnosis of lung cancers, *Optics Letters*, 33(7), p. 711-713.

[165] Huang, Z., Mcwilliams, A., Lui, H., Mclean, D. I., Lam, S. and Zeng, H. (2003). Near-infrared Raman spectroscopy for optical diagnosis of lung cancer. *International Journal of Cancer* 107(6), p. 1047-1052.

[166] Boere, I. A., Bakker Schut, T. C., van den Boogerta, J., de Bruina, R. W. F. and Puppels, G. J. (2003). Use of fibre optic probes for detection of Barrett's epithelium in the rat oesophagus by Raman spectroscopy. *Vibrational Spectroscopy,* 32(1), p.47-55.

[167] Motz, J. T., Gandhi, S. J, Scepanovi, O. R., Haka, A. S., Kramer, J. R., Dasari, R. R. and Feld, M. S. (2005). Real-time Raman system for in vivo disease diagnosis. *Journal of Biomedical Optics,* 10(3) 031113-1-031113-7.

[168] Yamamoto, Y. S., Oshima, O., Shinzawa, H., Katagiri T., Matsuura, Y., Ozaki, Y. and Sato, H. (2008). Subsurface sensing of biomedical tissues using a miniaturized Raman probe: Study of thin-layered model samples. A*nalytica Chimica Acta*, 619, p.8-13.

[169] Nazemi, J. and Brennan III, J. F. (2008). Rapid lipid identification and quantification in coronary artery tissue via an optical fiber probe with Raman spectroscopy. *Cardiovascular Revascularization Medicine*, Volume 9, Issue 3, July-September 2008, Pages 197-198 (conference abstract).

[170] Delhaye, D., and Dhamelincourt, P. (1975). Raman microprobe and microscope with laser excitation. *Journal of Raman Spectroscopy,* 3, p. 33-43

[171] Kalasinsky, K., Hadfield, T,. Shea, A., Kalasinsky, V., Nelson, M., Neiss, J., Drauch, A., Vanni, G. S., and Treado, P. (2007). Raman Chemical Imaging Spectroscopy Reagentless Detection and Identification of Pathogens: Signature Development and Evaluation. *Anal. Chem*., 79, 2658 – 2673.

[172] Stone, N., Kendall, C., Barr, H. (2008). In: *Applications of Vibrational Spectroscopy in Medical Diagnosis*, edited by M. Diem, P. Griffiths and J. Chalmers (Wiley, UK).

[173] Stone, N., Hart Prieto, M., Kendall, C., Shetty, G. and Barr, H. (2008). Raman spectroscopic biochemical mapping of tissues. *P Soc Photo-Opt Ins (SPIE)* 6093-29

[174] Stone, N., Hart Prieto, M., Crow, P., Uff, J. and Ritchie, A. (2007). The use of Raman spectroscopy to provide an estimation of the gross biochemistry associated with urological pathologies. *Analytical and Bioanalytical Chemistry,* 387(5), p. 1657-1668.

[175] de Jong, B. W. D., Bakker Schut, T. C, Maquelin, K., van der Kwast, T., Bangma, C. H., Kok, D. J. and Puppels, G. J (2006). Discrimination between Nontumor Bladder Tissue and Tumor by Raman Spectroscopy. *Anal. Chem*., 78, p. 7761-7769.

[176] Koljenovic, S., Bakker Schut, T., van Meerbeeck, J., Maat, A., Burgers, S., Zondervan, P., Kros, J. and Puppels, G. (2004). Raman microspectroscopic mapping studies of human bronchial tissue. *Journal of Biomedical Optics,* 9(6), p, 1187-1197.

[177] Koljenovic, S., Bakker Schut, T., Vincent, A., Kros, J. and Puppels, G. (2005). Detection of Meningioma in Dura Mater by Raman Spectroscopy. *Anal. Chem*. 77, p. 7958-7965.

[178] Kneipp,J., Bakker Schut, T., Kliffen, M., Menke-Pluijmers, M. and Puppels, G. (2003). Characterization of breast duct epithelia: a Raman spectroscopic study. *Vibrational Spectroscopy*, 32, p. 67-74.

[179] Carden, A., Rajachar, R. M., Morris, M. D. and Kohn, D. H. (2003). Ultrastructural Changes Accompanying the Mechanical Deformation of Bone Tissue: A Raman Imaging Study. *Calcif. Tissue. Int*., 72, p. 166–175.

[180] Schlucker, S., Schaeberle, M. D., Huffman, S. W., Levin, I. W. (2003). Raman Microspectroscopy: A Comparison of Point, Line, and Wide-Field Imaging Methodologies. *Anal. Chem*., 75 (16), p. 4312-4318.

[181] Krafft, C., Knetschke, T., Siegner, A., Funk, R. and Salzer, R. (2003). Mapping of single cells by near infrared Raman microspectroscopy. *Vibrational Spectroscopy,* 32, p. 75-83.

[182] Krafft, C., Sobottka, S., Schackert, G. and Salzer, R. (2006). Raman and infrared spectroscopic mapping of human primary intracranial tumors: a comparative study. *Journal of Raman Spectroscopy,* 37, 367-375.

[183] Gendrin, C., Roggo, Y. and Collet, C. (2008). Pharmaceutical applications of vibrational chemical imaging and chemometrics: a review. *Journal of Pharmaceutical and Biomedical Analysis,* 48, p. 533-553.

[184] Bancroft, J. D and Palmer, J. (1996). Frozen and related sections, In: *Theory and Practice of histological techniques.* edited by Bancroft, J. D., Stevens, A (Churchill Livingstone)

[185] Faolain, E., Hunter, M. B., Byrne, J. M., Kelehan, P. McNamara, M., Byrne, H. J. and Lyng, F. M. (2005). A study examining the effects of tissue processing on human tissue sections using vibrational spectroscopy. *Vib. Spect*., 28, p. 121-127.

[186] Mobley, P. R., Kowalski, B. R., Workman, J. and Bro, R. (1996). Review of chemometrics applied to spectroscopy: 1985-95. Part 2. *Appl. Spectrosc. Rev., 31, p. 347-368.*

[187] Shaver, J. M. (2001). Chemometrics for Raman Spectroscopy, In: *Handbook of Raman Spectroscopy. Practical Spectroscopy Series Vol. 28*, edited by I.R. Lewis and H.G.M Edwards, (Marcel Dekker, Inc., New York), p. 292-298.

[188] Wold, S. (1987). Principal component analysis. *Chemometrics and Intelligent Laboratory Systems*

2(1-3), p. 37-52.

[189] Krishna, C. M., Prathima N.B., Malini, R., Vadhiraja, B. M., Bhatt, R. A., Fernandes D. J., Kushtagi, P., Vidyasagar, M. S., Kartha, V. B., (2006). Raman spectroscopy studies for diagnosis of cancers in human uterine cervix. *Vibrational Spectroscopy,* 41, p. 136–141.

[190] Isabelle, M., Stone, N., Barr, H., Vipond, M., Shepherd N., and Rogers, K. (2008). *Spectroscopy, An International Journal*, 22, p. 97.

[191] Bird, B., Miljkovic, M., Romeo, M. J., Smith J., Stone, N., George, M. W. and Diem, M. (2008). Infrared micro-spectral imaging: distinction of tissue types in axillary lymph node histology. *BMC Clinical Pathology*, 8(8).

[192] Koljenovic, S., Choo-Smith, L-P., Bakker Schut, T., Kros, J. M., van den Berge, H. J. and Puppels, G. J. (2002). Discriminating vital tumor from necrotic tissue in human glioblastoma tissue samples by Raman spectroscopy. *Laboratory Investigation*, 82(10), p. 1265-1278.

[193] Mansfield, J. R., McIntosh, L. M., Crowson, A. N., Mantsch, H. H. and Jackson, M. (1999). A LDA-guided search engine for the non-subjective analysis of microscopic maps. *Appl. Spectrosc.* 53, p. 1323-1330.

[194] Krafft, C., Thummler, K., Sobottka, S. B., Schackert, G. and Salzer, R. (2006). Classification of Malignant Gliomas by Infrared Spectroscopy and Linear Discriminant Analysis *Biopolymers*, 82, p. 301–305.

[195] Choo-Smith, L. P., Edwards, H. G. M., Endtz, H. P., Kros, J. M., Heule, F., Barr, H., Robinson, J. S., Bruining, H. A. and Puppels, G. J. (2002). Medical applications of Raman spectroscopy: From proof of principle to clinical implementation. *Biopolymers – Biospectroscopy,* 67(1), 1-9.

[196] Wolthuis, R., Bakker Schut, T. C. , Caspers P. J., Buschman, H. P., Römer, T. J., Bruining, H. A., and Puppels, G.J. (1999) Raman spectroscopy methods for in vitro and in vivo tissue characterization. In: *Fluorescent and luminescent probes for biological activity*, Edited by: Mason WT, San Diego: Academic Press, p. 433-455.

[197] Etz, E. S., Choquette, J. S. and Hurst, W. H. (2005). Development and Certification of NIST Standard Reference Materials for Relative Raman Intensity Calibration. *Microchimica Acta,* V149(3), p.175.

[198] Lieber, C.A., Mahadevan-Jansen, A.. (2003). Automated method for subtraction of fluorescence from biological Raman spectra. *Appl Spectrosc*., 57(11), p. 1363-1367.

[199] Lieber, C.A., Mahadevan-Jansen, A.. (2003). Automated method for subtraction of fluorescence from biological Raman spectra. *Appl Spectrosc*., 57(11), p. 1363-1367.

[200] Keller, M. D., Kanter, E. M., Lieber, C. L., Majumder, S. K., Hutchings, J., Ellis D. L., Beaven, R. B., Stone, N. and Mahadevan-Jansen, A. (2008) Detecting Temporal and Spatial Effects of Epithelial Cancers with Raman Spectroscopy. *Dis. Markers,* 25(6), p. 323-37.

[201] Jackson, M., Choo, L-P., Watson, P. H., Halliday, W. C. and Mantch, H. H. (1995). Beware of connective tissue proteins: assignment and implications of collagen absorptions in infrared spectra of human tissues. *Biochimica et Biophysica Acta*, 1270, p. 1-6.

[202] van de Poll, S. W. E., Kastelijn, K., Bakker Schut, T. C., Strijder, C., Pasterkamp, G., Puppels G. J. and van der Laarse, A. (2003). On-line detection of cholesterol and calcification by catheter based Raman spectroscopy in human atherosclerotic plaque ex vivo. *Heart,* 89, p. 1078-1082.

[203] Bernard, S., Beyssac, O. and Benzerara, K. (2008). Raman mapping using advanced line-scanning systems: Geological applications. *Applied Spectroscopy.* 62(11), p. 1180-1187.

[204] Hutchings, J., Kendall, C., Shepherd, N., Smith, B., Barr, H. and Stone, N. (2008). The potential for histological screening using a combination of rapid Raman mapping and principal component analysis. *Journal of Biophotonics,*. 2(1-2), p. 91-103.

[205] Hutchings, J., Kendall, C., Shepherd, N., Smith, B., Barr, H. and Stone, N. (2008). Rapid Raman microscopic imaging for potential histological screening. *P Soc Photo-Opt Ins (SPIE),* p. 6853A-33.

[206] Matthaus, C., Chernenko, T., Newmark, J., Warner, C. M., Diem, M. (2007). Label-Free Detection of Mitochondrial Distribution in Cells by Nonresonant Raman Microspectroscopy. *Biophysical Journal*, 93, p. 668-673.

[207] Hutchings, J., Kendall, C., Shepherd, N., Ludeman, L., Barr, H. and Stone, N. (2008) A Raman mapping study of high grade dysplasia in oesophageal tissue using linear discriminant analysis to evaluate the importance of spatial resolution for histopathology. *Submitted to Analyst (November 2008).*

[208] Verdugo, P. (1990). Goblet cells secretion and Mucogenesis. *Annu. Rev. Physiol.*, 52, p. 157-76

[209] Hopwood, D., Coghill, G. and Sanders, D. (1986). Human oesophageal submucosal glands. Their detection, mucin, enzyme and secretory protein content. *Histochemistry,* 86, p. 107–112.

[210] Arul, G. S., Moorghen, M., Myerscough, N., Alderson, D. A., Spicer, R. D. and Corfield, A. P. (2000). Mucin gene expression in Barrett's oesophagus: an in situ hybridisation and immunohistochemical study. *Gut*, 47, p. 753–761.

[211] Olenikov, V., Kryukov, E., Kovner, M., Ermishov, M., Tuzikov, A., Shiyan, S., Bovin, N. and Nabiev, I. (1999). Sialation sensitive bands in the Raman spectra of oligosaccharides and glycoproteins. *Journal of Molecular Structure,* 480-481, p. 475-480.

[212] Fukura, S., Mizukami, T., Odake, S. and Kagi, H. (2006). Factors Determining the Stability, Resolution, and Precision of a Conventional Raman Spectrometer. *Applied Spectroscopy,* 60 (8), p. 946-950.

[213] Nodland, E., Libnau, F. O., Kvalheim, O. M., Luinge, H. J. and Klaeboe, P. (1996). Influence and correction of peak shift and band broadening observed by rank analysis on vibrational bands from variable-temperature measurements. *Vibrational Spectroscopy*, 10, p. 105-123.

[214] Wang, T. D., Triadafilopoulos, G., Crawford, J. M., Dixon, L. R., Bhandari, T., Sahbaie, P., Friedland, S., Soetikno, R., and Contag, C. H. (2007). Detection of endogenous biomolecules in Barrett's esophagus by Fourier transform infrared spectroscopy, *PNAS*, 104(40), p. 15864–15869.

Appendix A Raman peak assignments in oesophageal tissue

Table A1: Characteristic Raman shift (δ=deformation, vstretch vibration, vs=symmetric vibration, vas=asymmetric vibration, adapted from Stone[110] *Kendall*[123] *and Shetty*[126]

	Assignment	Tissue/Substance
207	Calcium carbonate	Cholesterol
275	τCCC	Lactic acid
350	Ribose, cytosine	
370	δCCC	Lactic acid
385	Cytosine	
400	Silica	Fibre probe on cervix
424	δCCC	Human strateum corneum
425	δCCO	Lactic acid
429	Calcium hydroxyapatite	
430	Cholesterol	
430	δ(OPO)	Human tooth
435	Ribose	
451	O-P-O symmetric bend	Chicken leg bone
481	Glycogen	Sigma Aldrich G0885
492	ν_s (SiOSi)	silicone gel
500	Cytosine, guanine & disulphide	
500-550	Disulphide (S-S) stretch	Protein
505	ν (S-S)	Bovine serum albumin
507	Disulphide	Nails
509	Disulphide (S-S)	
510	Disulphide (C-S-S-C gauche-gauche-gauche)	Protein
518	Glucose	
525	Disulphide (C-S-S-C gauche-gauche-trans)	Protein
526	ν (S-S)	Strateum corneum
526	ν (S-S)	Human strateum corneum
528	ν (S-S)	Protein
529	Desmosine & isodesmosine (amino acids)	Elastin
530-1	ν (S-S)	Callus, psoriatic plaque
533	COC deformation (glycosidic ring)	
533	Glucose	Blood
540	Disulphide (C-S-S-C trans-gauche-trans)	Protein
541	νSS	AGP (glycoprotein)[*]
540	νOCO	Lactic acid
547	Cholesterol	Protein
553	Glucose	Blood
556	ν (S-S)	
574	Tryptophan	Eye lens
575	Cytosine, guanine & disulphide	
576	Glycogen	Sigma Aldrich G0885
576	Glycogen	Glycogen (Sigma Aldrich)[†]

[*] Kopecky, V. et al. (2003). Structure of human a1-acidn glycoprotein. *Biochemical and Biophysical Research Communications*, 300, p. 41-4.

[†] Hutchings J (Thesis, Section 1.2.3)

587	Calcium hydroxyapatite	Protein
591	Apatite	Human tooth enamel
591	δ(OPO)	Human tooth
600	ρ(CH) wagging	Human strateum corneum
607	Cholesterol	Protein
618	Phenylalanine(amino acid)	Collagen
620	Phenylalanine(amino acid)	Diseased breast tissue
620	Phenylalanine	
620-2	ν (C-S)	Callus, psoriatic plaque
620	Phenylalanine (AGP)	AGP (glycoprotein)*
622	Phenylalanine	
623	ν (C-S)	Human strateum corneum
623	ν (C-S)	Strateum corneum
624	Adenine	DNA (Z), RNA(Z)
625	Guanine in the C3' endo/syn form	DNA (Z)
626	Phenylalanine	
626		Cervix tissue
626	Silica	Fibre probe on cervix
637	Ribose & disulphide	Protein
640	Guanine	RNA(Z)
641	Tyrosine (AGP)	AGP (glycoprotein)*
642	Thymine	DNA (A), RNA (A)
643	ν (C-S), amide IV	Strateum corneum, Callus, psoriatic plaque
643	Tyrosine	
644	Tyrosine	
644	ν (C-S), Amide IV	Human strateum corneum
650	δC-COH	Lactic acid
665	Thymine	DNA (B)
668	Guanine in the C3' endo/anti form	DNA (A), RNA (A)
669	ν(C-S)	Bovine Serum albumin
669	ν(C-S)	
669	Thymine	
670	Breathing of aromatic ring of purine bases (guanine & adenine)	DNA
670	Guanine	DNA (C)
670	Guanine	
670	Thymine & guanine	
681	Guanine breathing ring	
682	Guanine in the C2' endo/anti form	DNA (B)
692	Creatine (O-C=O) deformation	
704	Calcium carbonate	Cholesterol
709	Glycogen	Sigma Aldrich G0885
700	Cholesterol	Brain
701	Cholesterol	
710	Adenine	
710	ν_s (Si-C)	silicone gel
710	νCS (AGP)	AGP (glycoprotein)*
717	phosphotidylcholine	Phosphotidylcholine(Sigma Aldrich)†
720	Nucleotides	Breast cancer in mouse
720	C-N vibration	Phospholipid membrane
722	Adenine	
724-7	Adenine	DNA (A), DNA(B), RNA(A)
725	C-S	Eye lens
725	CH_2 rocking	
727	=C-H in plane bend	Breast tissue, lipid
727	C-C stretch, proline	Normal breast tissue
727	=C-H in plane bend	
728	C-C stretch, proline	Oleic acid methyl ester

729	Adenine breathing ring	
729	Adenine	DNA (Z), RNA(Z)
730		DL-Lactic acid ($C_3H_6O_3$)
742-748	O-P-O	DNA (Z), RNA(Z)
743	in bovine albumin	Sigma Aldrich A2153
746	$\rho(CH_2)$	Human strateum corneum
748	Thymine	DNA (B)
749	Thymine breathing ring	
750	δOCO	Lactic acid
750	Cholesterol	Carotid artery
756	Tryptophan (AGP)	AGP (glycoprotein)*
759	Tryptophan (amino acid)	
759	Tryptophan (amino acid)	Human eye lens
760	Tryptophan (amino acid)	Rabbit & human cornea & Rabbit aqueous humour
760	Tryptophan & tyrosine	Rabbit lens
760	Tryptophan (amino acid)	
760	Tryptophan (amino acid)	
760	Tryptophan (amino acid)	
761	Glycogen	Sigma Aldrich G0885
762	Collagen	Sigma Aldrich C7774
770	Breathing of aromatic ring of pyrimidine bases (cytosine & thymine)	DNA
777	Thymine	DNA (A), RNA (A)
780	Cytosine	DNA (A), RNA (A)
780	Nnucleotides	Breast cancer in mouse
780	Uracil ring	
782	Cytosine ring breathing	DNA (B)
785	O-P-O	DNA (C)
787	Cytosine & uracil	
788	Thymine, cytosine, O-P-O	DNA
790	ν_s O-P-O	DNA
790	Acetone (C-C-C) stretch	
795	DNA	DNA (Sigma Aldrich)†
800		pyruvate
806-813 (809)	ν_s O-P-O	DNA (A)
811	Nucleotides	Breast cancer in mouse
814	ν_s O-P-O	DNA
814	ν_s O-P-O	RNA (A)
814	C-C stretch, backbone	Type I collagen (human placenta)
814	C-C stretch, backbone	Collagen
814	C-C stretch, backbone in collagen	Sigma Aldrich C7774
815	Phosphate	
816	C-C Proline ring	Collagen type I, normal skin dermis
817	C-C stretch, backbone	Infiltrating ductal carcinoma
817	C-C stretch, backbone	Diseased breast tissue
818	Haemoglobin	
818		Cervix tissue
818	Silica	Fibre probe on cervix
819	Tyrosine	
820	Structural protein	Breast
825-830	Tyrosine (amino acid)	Histones
825-842	O-P-O	DNA (B)
826	in bovine albumin	Sigma Aldrich A2153
827	δ(CCH) aliphatic	Human strateum corneum
828	Tyrosine (amino acid)	Sigma Aldrich T8909
830	C-COOH stretch	Lactate
830	C-COOH stretch	DL-Lactic acid ($C_3H_6O_3$) CH_3-

		CHOH-COOH
830	C-COOH stretch	Lactate
830	Tyrosine (amino acid)	Human eye lens
830	Tyrosine (amino acid)	
830	Tyrosine (amino acid)	
830	Tyrosine (amino acid)	
830	νC-COOH	Lactic acid
832	Tryptophan & tyrosine	Rabbit lens
832	Tyrosine	
832	Tyrosine	
833	ν_{as} O-P-O	DNA
833	Ribose phosphate	
834 (832-834)	Tyrosine (AGP)	AGP (glycoprotein)*
835	ν_{as} O-P-O	DNA (B)
840	Tyrosine (amino acid)	
840	Glucose	
840-860	Polysaccharides	
840-860	Polysaccharides	
840-880	Glucose	Blood
846	Tyrosine (amino acid)	Sigma Aldrich T8909
847	Glucose	Sigma
849		Breast
850	Proline	
850	Tyrosine (amino acid)	
850	Tyrosine (amino acid)	
850		Bovine albumin Sigma Aldrich A2153
850	δ(CCH) aromatic	Human strateum corneum
850-3	δ(CCH) aromatic	Strateum corneum, Callus, psoriatic plaque
852	Tyrosine (AGP)	AGP (glycoprotein)*
853	Tyrosine (amino acid)	Human eye lens
853	Tyrosine (amino acid)	DNA
853	Glycogen	Sigma Aldrich G0885
854-6	Tyrosine (amino acid)	Histones
855	Tyrosine	
855	C-C stretch Proline ring	Collagen
855	C-C stretch, proline	Type I collagen (human placenta)
856	Glycogen	Glycogen (Sigma Aldrich) †
856	Proline	Chicken leg bone
856		Polysaccharides in glioma grade III (human brain tissue)
856	CC strectch, COC stretch, 1,4 glycosidic link	
856	C-C stretch collagen backbone & Proline ring	Diseased breast tissue
856	collagen	Collagen IV (Sigma Aldrich)†
856	C-C stretch, proline	Infiltrating ductal carcinoma (breast)
856	ν(CC) skeletal vibrations, keratotic	Healthy human skin dermis
856	C-C stretch collagen backbone & Proline ring	
856	Tryptophan & tyrosine	Rabbit lens
856	C-C stretch Proline ring in collagen	Sigma Aldrich C7774
857	Tyrosine	
858	C-C stretch in elastin	Sigma Aldrich E1625
859	C-C Proline ring	Collagen type I, normal skin dermis
860	Collagen	Fibrocystic human breast tissue

860	Lactate	Human aqueous humour
865	Ribose, Tryptophan (amino acid)	Protein
866	Lactic acid	DL-Lactic acid ($C_3H_6O_3$) CH_3-CHOH-COOH
868	C-C stretch, hydroxyproline	Oleic acid methyl ester
870	C-C stretch, hydroxyproline	Normal breast tissue
870	Proline (amino acid)	Malignant breast tissue
870		Breast
872	C-C stretch of 4-hydroxyproline in collagen	Sigma Aldrich C7774
873	hydroxyproline	Chicken leg bone
873	Glycerol fragment vibration (Sialic acid)	AGP (glycoprotein) [‡]
874	C-C stretch, hydroxyproline	Type I collagen (human placenta)
874	C-C stretch of 4-hydroxyproline	Collagen
876	phosphotidylcholine	Phosphotidylcholine(Sigma Aldrich)[†]
876	C-C stretch, hydroxyproline	Infiltrating ductal carcinoma (breast)
876	C-C stretch of 4-hydroxyproline	Diseased breast tissue
878	Tryptophan (AGP)	AGP (glycoprotein)[*]
879	Tryptophan (amino acid)	Human eye lens
880	Tryptophan (amino acid)	
880	Tryptophan (amino acid)	
880	Tryptophan (amino acid)	
880	Tryptophan (amino acid)	Rabbit & human cornea
880	Tryptophan & tyrosine	Rabbit lens
880	Tryptophan (amino acid)	Rabbit aqueous humour
880	Sialic acid (Sia) (AGP)	AGP (glycoprotein)[‡]
883	CH_2 rocking,	Strateum corneum,
883	$\rho(CH_2)$	Human strateum corneum
885	Ribose, Tryptophan (amino acid)	Protein
890	Structural protein	Breast
890		Breast
890-1	CH_2 rocking,	Callus, psoriatic plaque
892	CH_2 rocking, collagen hydroxyproline	Skin
893		Bovine albumin Sigma Aldrich A2153
895	DNA backbone	DNA
896	Proline	Sigma Aldrich T8449
915	Ribose	Protein
917	Deoxyribose (CH_2 deformation)	DNA (B)
920	Glucose	Sigma
920	C-C stretch in elastin	Sigma Aldrich E1625
920	Lactic acid	DL-Lactic acid ($C_3H_6O_3$)
920	C-C stretch Proline ring	Diseased breast tissue, collagen
920	C-C Proline ring	Type I collagen (human placenta) & infiltrating ductal carcinoma (breast)
920	C-C stretch Proline ring in collagen	Sigma Aldrich C7774
921	C-C Proline ring	Collagen type I, normal skin dermis
921	C-C stretch Proline ring	Collagen
925	DNA backbone	DNA

[‡] Oleinikov, V., Kryukov, E., Kovner, K., Ermishov, M., Tuzikov, A., Shiyan, S., Bovin, N. and Nabiev, I. (1999). Sialylation sensitive bands in the Raman spectra of oligosaccharides and glycoproteins. *Journal of Molecular Structure*, 480-481, p. 475-480

928	DNA backbone, α helix	Protein
928-940	C-C Proline, valine	
930	Tryptophan (amino acid)	Protein
930	rCH_3	Lactic acid
931	CH_3 rocking, collagen proline	Skin
931	$\rho(CH_3)$, ρ(C-C) α-helix	Human strateum corneum
932	Skeletal C-C, α helix	DNA
932-5	CH_3 rocking, C-C stretch α helix keratin	Strateum corneum, Callus, psoriatic plaque
934	C-C stretch, backbone	Collagen
934	C-C Proline ring	Type I collagen (human placenta)
935-945	(C-C) skeletal vibrations, α helix	α-helix protein secondary structure
935	Collagen	Fibrocystic human breast tissue
936	C-C stretch backbone, hydroxyproline & collagen	Skin
936	C-C stretch, backbone in collagen	Sigma Aldrich C7774
937	C-C stretch collagen	Collagen IV (Sigma Aldrich)[†]
937	Glycogen	Sigma Aldrich G0885
937	Glycogen	Glycogen (Sigma Aldrich) [†]
937	C-C stretch, backbone	Diseased breast tissue
937	C-C Proline ring	Infiltrating ductal carcinoma (breast)
937	α-helix	nails
938	ν(C-C) skeletal vibrations, keratotic	Healthy human skin dermis
938	Peptide backbone stretch	
938	C-C backbone	Collagen
939	C-C-N stretching	Bovine Serum albumin
940	C-C-N stretching in bovine albumin	Sigma Aldrich A2153
940	ν(C-C) of proline and valine	Normal human skin
940	Triple helix vibrations	Collagen type I, normal skin dermis
941	C-C stretch	Protein
944	ν(C-C) (AGP)	AGP (glycoprotein)[*]
944	ν(C-C)	Asian skin
950	4-hydroxyproline	Malignant breast tissue
955	Hydroxyapatite	
956	Carotenoids	Human brain tissue, acoustic neuroma
956	$\rho(CH_3)$, δ(CCH) olefinic	Human strateum corneum
960	Calcification - hydroxyapatite	Human brain tissue, central neurocytoma
960	Calcification - hydroxyapatite	Aortic valve leaflets & coronary artery segments
960	P-O symmetric stretch	Chicken leg bone
960	P-O symmetric stretch	Atherosclerotic plaque calcified salts
960	Hydroxyapatite, P-O symmetric stretch	Calcified plaque
960	Cholesterol	
961	Apatite	Human tooth enamel
961	Y_s(PO) of PO_4^{3-} in apatite	Human tooth
961	Phosphate groups	Calcified atherosclerotic plaque
966	Hydroxyapatite	Calcified plaque
966	Desmosine & isodesmosine (amino acids)	Elastin
966	Triple helix vibrations	Collagen type I, normal skin dermis
968	C-OH	

972	=C-H out of plane deformation	Breast tissue
972	C-C Proline ring	Normal breast tissue, Oleic acid methyl ester
972	=C-H out of plane deformation	Breast
975	Ribose	Protein
975	Deoxyribose (CH_2 deformation)	DNA (B)
978	Symmetric phosphate ion stretching	Phospholipids, glucose-1-phosphate
978	Symmetric phosphate ion stretching	Human cervix
978	Phosphorylated proteins and nucleic acids	Human cervical biopsies
982	CH_2 rocking	Strateum corneum
1000-1100	Glucose	Blood
1000-1150	C-C skeletal vibrations	Phospholipid membrane, hydrophobic chains
1000-1250	Phosphate groups	DMPC (dimyristoylphosphatidycholine), a typical lipid, brain
1000-1200	C-C stretch – lipids	Healthy human skin
1000	Phenylalanine in bovine Albumin	Sigma Aldrich A2153
1001	Phenylalanine(amino acid)	Sigma Aldrich T8324
1001	Phenylalanine(amino acid)	Malignant breast tissue
1001	Phenylalanine(AGP)	AGP (glycoprotein)*
1001		Ovary
1001-1004	Phenyl ring breathing mode	
1002	υ(C-C) aromatic ring	Strateum corneum, Callus, psoriatic plaque
1002	(C-C) skeletal vibrations, β sheet	β-sheet protein secondary structure
1002	Phenylalanine(amino acid)	
1002	Phenylalanine(amino acid)	
1002	Phenylalanine(amino acid)	Collagen
1002	collagen	Collagen IV (Sigma Aldrich)†
1002	Hydroxyproline, tyrosine	Type I collagen (human placenta)
1002	ν(CC) aromatic ring	Human strateum corneum
1003	ν(CC) aromatic ring stretch of phenylalanine residue in keratin	Healthy human skin
1003	Phenylalanine(amino acid) breathing mode	Human brain tissue, protein
1003	C-N stretch	Urea
1003	C-N stretch of urea	Urea
1003	C-N stretch of urea	
1004	Phenylalanine(amino acid)	Rabbit lens, aqueous humour, cornea & human cornea
1004	Aromatic ring (breathing mode)	Normal human skin
1004	Phenylalanine(amino acid)	
1004	Phenylalanine(amino acid)	
1004	Phenylalanine(amino acid)	
1004	Phenylalanine(amino acid)	Diseased breast tissue
1004	Phenylalanine(amino acid)	Infiltrating ductal carcinoma (breast)
1004	Phenylalanine(amino acid) + Trp aromatic ring	Bovine Serum albumin
1004	Carotenoid	Beta carotene, Human breast carcinoma
1004	Phenylalanine in collagen	Sigma Aldrich C7774
1004	P-O symmetric stretch	Chicken leg bone
1005	Carotenoid	Normal human breast tissue
1005	Beta carotene	Breast
1005	Carotenoid	Human breast tissue

		Renal cell carcinoma (1003)
1005	Phenylalanine(amino acid)	Protein
1006	C-N stretch of urea	Urea, rabbit aqueous humour
1006	Phenylalanine, amino acid	Collagen, histones
1006	Phenylalanine, amino acid	Protein
1006	Carotenoids	Human brain tissue, acoustic neuroma
1008	C-N stretch	Urea NH_2-CO-NH_2
1008	Carotenoids	Carotenoids in normal colon
1010	C-N stretch	Human aqueous humour
1013	Urea N-C-N stretch	
1014	Tryptophan (amino acid)	
1015	Tryptophan (amino acid)	Protein
1016	Tryptophan – amino acid	DNA in water
1017	DNA backbone C-O stretch	
1029	Phenylalanine(AGP)	AGP (glycoprotein)*
1030	Collagen	Sigma Aldrich C7774
1031	Proline	
1031	ν(CC) skeletal cis conformation	Human strateum corneum
1031-32	υ(C-C) keratin	Strateum corneum, Callus, psoriatic plaque
1032	Phenylalanine(amino acid)	Rabbit & human cornea Rabbit lens Rabbit aqueous humour
1032	Phenylalanine(amino acid)	
1032	proline	Type I collagen (human placenta)
1034		Ovary
1035	Ribose, Phenylalanine(amino acid)	Protein
1035	C-C skeletal cis	
1043	Proline	Infiltrating ductal carcinoma (breast)
1043	Formalin artefact	breast tissue
1046	C-O stretch	carbohydrate§
1046	Lactic acid	DL-Lactic acid ($C_3H_6O_3$) CH_3-CHOH-COOH
1046	Glycogen	Glycogen (Sigma Aldrich) †
1048	Glycogen	Sigma Aldrich G0885
1050	νC-CH_3	Lactic acid
1050	CO stretch, CCC trans skeletal stretch	Healthy human skin dermis
1057	DNA backbone C-O stretch	
1060	δOD	Methyl lactate
1061	Lipid	Strateum corneum
1061	phosphotidylcholine	Phosphotidylcholine(Sigma Aldrich)†
1062	υ(C-C) skeletal trans conformation lipid	Strateum corneum
1062	ν(CC) skeletal trans conformation	Human strateum corneum
1064	C-C stretch	
1065	C-O stretch & C-O-C sym. stretch - phospholipids	Human brain tissue
1066	C-C stretch	Breast
1066	C-C stretch	breast tissue
1066	Proline	Normal breast tissue
1066	C-O, C-O-C stretch	Phospholipids
1066	Lipid	

§ Kast, R. E., Serhatkulu, G. K., Cao, A., Pandya, A. K., Dai, H., Thakur, J. S., Naik, V. M., Naik, R., Klein, M. D., Auner, G., W. and Rabah, R. (2008). Raman Spectroscopy Can Differentiate Malignant Tumors from Normal Breast Tissue and Detect Early Neoplastic Changes in a Mouse Model. *Biopolymers,* 89(3), p. 235-241.

1066		Ovary
1067	Proline	Oleic acid methyl ester
1069	Hydroxyapatite shifted due to environment	Human cervix
1070	Symmetric phosphate ion stretching	Glucose -1-phosphate, collagen
1070	Symmetric phosphate ion stretching	Human cervix
1070	Collagen/elastin	
1070		Cervix
1070	Phosphate / carbonate	Atherosclerotic plaque
1070	Phosphate / carbonate	
1071	apatite	Human tooth enamel
1071	$Y_{as}(PO)$	Human tooth
1072	P-O asymmetric stretch	Chicken leg bone
1074		Adipose tissue
1074	Triglycerides	Adipose tissue from human aorta
1078	C-N stretch	Benign breast tissue
1078-1090	C-C, C-O stretch in lipids. C-C, PO_2 stretch in nucleic acids	
1079	C-C stretch	Breast tissue
1079		Normal breast tissue
1079	C-C stretch	Breast
1080	C-C stretch & PO2- sym. stretch - phospholipids	Human brain tissue
1082	υ(C-C) skeletal random conformation lipid	Strateum corneum
1082		Oleic acid methyl ester
1082	PO2- vibration in phospholipids and nucleic acids	Normal human skin
1082	Lipid	Normal human breast tissue, Lipid (TPE)
1082	Lipid	Human breast tissue
1082	Lipid	
1082		Protein
1082	ν(CC) skeletal random conformation	Human strateum corneum
1083	Glycogen	Sigma Aldrich G0885
1084	Lactic acid	DL-Lactic acid ($C_3H_6O_3$) CH_3-CHOH-COOH
1084-90	ν(CC), ν(CN) (AGP)	AGP (glycoprotein)[*]
1085	Calcium carbonate	Cholesterol
1085	C-C stretch	Lipid
1085	Phenylalanine(amino acid)	Protein
1085	Phosopholipids	Malignant breast tissue
1086	C-C stretch, PO_2 stretch	Phospholipids
1087	Symmetric stretching of phosphate groups of the polynucleotide chain	DNA
1090	νCO	Lactic acid
1090	PO^-_2	DNA (C)
1091	PO^-_2	DNA (B)
1092	Glycogen	Glycogen (Sigma Aldrich) [†]
1094	DNA O-P-O	
1094	DNA O-P-O	
1095	ν_s of two ionised phosphate oxygens in the diphosphate ester	DNA (B)
1095	DNA	DNA (Sigma Aldrich)[†]
1095	PO^-_2	DNA (Z), RNA(Z)
1095	CC stretch, COC deformation 1-4 glycosidic link	
1097	phosphotidylcholine	Phosphotidylcholine(Sigma Aldrich)[†]
1099	PO^-_2	DNA (A), RNA(A)

1100	Formalin	Formalin
1100	PO_2 stretch	Protein
1100	ν_s of two ionised phosphate oxygens in the diphosphate ester	DNA (A)
1100	Lipid disorganised	
1100-1110	(C-C) skeletal vibrations	Unordered protein secondary structure
1104	C-C stretch lipid	
1108	Desmosine & isodesmosine (amino acids)	Elastin
1118		Normal breast tissue
1119		Oleic acid methyl ester
1119	C-C stretch	Breast tissue
1119	C-C stretch	Breast
1122	C-C stretch lipid	
1123	Glycogen	Sigma Aldrich G0885
1123	Glucose	Sigma
1125		
1125		Infiltrating ductal carcinoma (breast)
1126	C-N stretch	Protein
1126	C-C stretch - phospholipids	Human brain tissue
1126	ν(CC) skeletal trans conformation	Human strateum corneum
1127	υ(C-C) skeletal trans conformation lipid & keratin	Strateum corneum, Callus, psoriatic plaque
1127	Lipids	Strateum corneum
1127		Type I collagen (human placenta)
1128	C-C stretch	
1128	Heme vibrational mode	
1129	C-C stretch, lipid	Healthy human skin strateum corneum & epidermal membrane
1130	Trans C-C stretch – phospholipids	Human brain tissue, glioma grade III
1130	Lipid	Healthy human skin strateum corneum & epidermal membrane
1130	C-C stretch, lipid	
1130	C-O stretch glucose	
1130	Low density lipoproteins	
1131	Lactic acid	DL-Lactic acid ($C_3H_6O_3$)
1135	νCO, rCH_3	Lactic acid
1150	Carotenoid	Human artery
1150	C=C Carotenoid	Food
1150	Cholesterol	Carotid artery
1155	C-C stretch, δ(COH)	
1155	ν(CC), δ(COH)	Human strateum corneum
1156	CN stretch	Bovine Serum albumin
1156	Carotenoid	
1156	Carotenoid	Human breast carcinoma, Beta carotene
1157	Carotenoid	Normal human breast tissue
1157	Carotenoid	Human breast tissue Renal cell carcinoma (1155)
1157	Carotenoid	Human brain tissue, acoustic neurinoma, beta carotene
1158	Carotenoid	Carotid artery
1158	Carotenoid	Carotenoids in normal colon
1158	NH_2 rocking vibration	Urea
1159	C-N	Protein in eye lens
1160	Carotenoid	Blood plasma
1162	Ribose	

1166		Type I collagen (human placenta)
1167		Infiltrating ductal carcinoma (breast)
1172	ν(CC)	Human strateum corneum
1174	Tyrosine (AGP)	AGP (glycoprotein)*
1175	C-O stretching	Human cervical biopsies
1176	Tyrosine, Phenylalanine	Protein
1180		Cervix
1180	Tyrosine	Breast
1180	Tyrosine	
1180	Cytosine, guanine, adenine	
1197	Carotenoid	
1200-1700	Collagen	Dentine
1205	Tyrosine + Phenylalanine	Bovine albumin, Sigma Aldrich A2153
1206	4-hydroxyproline (amino acid), tyrosine	Diseased breast tissue
1206	4-hydroxyproline (amino acid)	Collagen
1206	Hydroxyproline, tyrosine	Type I collagen (human placenta) & infiltrating ductal carcinoma (breast)
1207	Tyrosine	Human eye lens
1207	Tyrosine (AGP)	AGP (glycoprotein)*
1207	Tyrosine + Phenylalanine (amino acid)	Bovine Serum albumin
1207		Ovary
1208	Thymine	DNA (B)
1210	hydroxyproline	Chicken leg bone
1210		Cervix
1210	Tryptophan, phenylalanine	
1211	Tyrosine, Phenylalanine, Thymine	Protein
1226-1243	Amide III - ν(C-N)	β pleated sheet protein secondary structure in β-Poly-L-alanine
1227	Heme vibrational mode	
1227-1247	Amide III (C-N stretch, N-H in plane bending) β-sheet	β-sheet protein secondary structure
1230	Uracil in RNA	Cultured breast cells
1230-1240	Amide III β-sheet	
1230-1245	Amide III - ν(C-N)	β pleated sheet protein secondary structure in β-Poly-L-glutamate
1234	Antisymmetric stretching of phosphate groups of the polynucleotide chain	DNA
1235-1270	Amide III (C-N stretch, N-H in plane bending) unordered	
1237	Amide III	Human eye lens
1238	Amide III, random coil	Rabbit & human cornea
1238	Amide III in elastin	Sigma Aldrich E1625
1238	Cytosine, uracil, Amide III	
1239	Thymine	DNA (A), RNA (A)
1240	Amide III - ν(C-N)	β pleated sheet protein secondary structure in β-Poly-L-lysine
1240	Vibration of pyrimidine bases (cytosine & thymine)	DNA
1240	Amide III ν(C-N)	Benign breast tumour
1240	Amide III	
1240	Amide III in collagen	Sigma Aldrich C7774
1240	Amide III - ν(C-N)	Uterus cancer
1240	Amide III	Caractous lens
1240	Thymine	Protein
1240-1260	Amide III unordered	
1243	Amide III	Liver - collagen
1243	Amide III	Chicken leg bone

1243	Amide III	Rabbit lens
1243-48	Amide III - ν(C-N)	irregular protein secondary structure in β-Poly-L-lysine pH4
1244	$\delta(CH_2)$ wagging, ν(CN) amide III disordered	Human strateum corneum
1245	νCO, δOH	Lactic acid
1245	Amide III, random coil	Human brain tissue, glioma grade III
1245	Keratotic	Healthy human skin dermis
1245		Cervix
1245	Amide III: keratin, disordered collagen	
1245-1305	Amide III (C-N stretch, N-H in plane bending)	Histones
1246	Amide III	Bovine Serum albumin
1246	Amide III ν(C-N)	Collagen & DNA
1246	Amide III ν(C-N)	Human cervix precancer
1246	Amide III (C-N stretching vibrations)	Human cervical biopsies
1246	Amide III (C-N stretching vibrations)	
1246	Amide III (C-N stretching vibrations)	Protein
1247	Amide III	Type I collagen (human placenta) & infiltrating ductal carcinoma (breast)
1247	Amide III	Diseased breast tissue
1247		Neutrogena sarcoma (brain) - collagen
1247	Amide III	Collagen
1247	Amide III - ν(C-N)	Endometrium cancer
1247	Collagen	Fibrocystic human breast tissue
1248	Amide III	Breast
1248	PO2- vibration in phospholipids and nucleic acids	Normal human skin
1248	Amide III (C-N stretch, N-H in plane bending)	Collagen
1249	Amide III - ν(C-N)	irregular protein secondary structure in β-Poly-L-glutamate pH 11
1250	Cytosine, uracil, Amide III	
1250	Amide III	Human artery
1250	Amide III	
1250	Cytosine	DNA (B)
1250	DNA	DNA (Sigma Aldrich)[†]
1250	Amide III	Collagen type I, normal skin dermis
1252	Amide III	Aorta
1253	Amide III random coil protein	Breast cancer in mouse
1254	Adenine	Protein
1254	Amide III (C-N stretch, N-H in plane bending)	Elastin
1255	Cytosine	Protein
1256	Glycogen	Sigma Aldrich G0885
1258-1304	Amide III (C-N stretch, N-H in plane bending)	α-helix protein secondary structure
1260-1310	Amide III (C-N stretch, N-H in plane bending)	α-helix protein secondary structure
1259	Amide III	Silicone gel
1260	Tyrosine	Unordered protein secondary structure
1260	Structural protein	Breast
1260	Symmetric CH_3 deformation	Silicone gel

1260	Amide III	Chicken leg bone
1260	Amide III	Malignant breast tissue
1260-1280	Amide III	Bovine Serum albumin
1261	Lipid	
1262	Amide III - ν(C-N)	Benign or normal cervix
1262	Amide III - ν(C-N)	Benign or normal uterus
1262	Amide III - ν(C-N)	Benign or normal endometrium
1262	Amide III - ν(C-N)	Benign or normal ovary
1264	Amide III in collagen	Sigma Aldrich C7774
1265-1300	Amide III (C-N stretch, N-H in plane bending)	α-helix protein secondary structure
1265-1348	Amide III - ν(C-N)	α-helix protein secondary structure in α-Poly-L-alanine
1265	=C-H in plane deformation	Breast
1265	=C-H in plane deformation	breast tissue
1265	Amide III	Normal breast tissue
1267	=C-H in plane deformation	
1267	Amide III	Infiltrating ductal carcinoma (breast)
1267	δ (=C-H)	Phospholipid membrane
1267	δ (=C-H)	Coronary Artery, unsaturated fatty acids
1267	Amide III	Lymph node
1267	Amide III	Diseased breast tissue
1267	Amide III	Collagen
1268	Amide III	Oleic acid methyl ester
1268	Amide III - ν(C-N) and δ(NH) in bovine albumin	Sigma Aldrich A2153
1269	Amide III	Type I collagen (human placenta)
1269	Amide III α-helix	Human brain tissue
1270		Cervix
1270	Amide III - ν(C-N)	Endometrium cancer
1271	Amide III - ν(C-N) and δ(NH)	Normal human skin
1271	Amide III (C-N stretch, N-H in plane bending)	Collagen
1273	Amide III	Collagen type I, normal skin dermis
1274	δ(NH) wagging, ν(CN) amide III α-helix	Human strateum corneum
1280	Amide III	Phospholipid membrane
1290	Amide III - ν(C-N)	α-helix protein secondary structure in α-Poly-L-glutamate
1295	Amide III - ν(C-N)	α-helix protein secondary structure in α-Poly-L-lysine
1296	$\delta(CH_2)$	Human strateum corneum
1296	Keratotic	Healthy human skin dermis
1296	$\delta(CH_2)$	Strateum corneum
1297	Lipid	Healthy human skin strateum corneum & epidermal membrane
1300	ν(C-C) ν(C-N)	Benign breast tissue
1300	Amide III	Bovine insulin
1300	C-H bending	Lipid
1300	Phospholipids - CH_2 twist and wagging	Human brain tissue
1300	Lipids – fatty acids	Breast
1300	δCH	Lactic acid
1300	Adenine , cytosine	
1300	phosphotidylcholine	Phosphotidylcholine(Sigma Aldrich)[†]
1302	Lipid	Lipid (TPE)
1302	Lipid	Human breast tissue
1302	Lipid	Normal human breast tissue

1302	Lipid	Human breast tissue
1303	CH_2 twisting	Breast
1303	Triglycerides	Adipose tissue from human aorta
1303	Adenine	
1303	δ CH_2	Phospholipid membrane
1303	CH_2 twisting	Normal breast tissue
1303	CH_3CH_2 twisting	Diseased breast tissue
1303	CH_3CH_2 twisting	Normal breast tissue & infiltrating ductal carcinoma
1304	CH_3CH_2 twisting	Oleic acid methyl ester
1306	Lipid	Human colon
1309	CH_2 twisting & wagging in lipids	Normal human skin
1310-16	$\Delta(CH_2)$	Callus, psoriatic plaque
1316	Histidine	Sigma Aldrich T8776
1316	Guanine	DNA (Z), RNA(Z)
1317	CH_2 twisting	Skin
1318	Guanine	DNA (A), RNA (A)
1319	CH_3CH_2 twisting	Type I collagen (human placenta)
1319	CH_3CH_2 twisting	Collagen
1320	Guanine	
1321	in bovine albumin	Sigma Aldrich A2153
1322	C-H	
1325	Tryptophan (amino acid) ring vibrations	
1325	Nucleic acid ring vibrations	
1330	Tryptophan (amino acid) ν(C-C)	Cervix cancer
1330	Tryptophan (amino acid) ν(C-C)	Uterus cancer
1330	Tryptophan (amino acid) ν(C-C)	Ovary cancer
1330	C-H	Nucleic acid bases & DNA, phospholipids
1330	C-H	Human cervix precancer
1330		Cervix
1330	DNA	Cultured breast cells
1330	δCH	Lactic acid
1332	DNA	DNA (Sigma Aldrich)[†]
1333	Glycogen	Sigma Aldrich G0885
1333	Guanine	DNA (B)
1334	CH deformation	
1335	Nucleic acids	Colon
1335	Adenine	DNA (A), RNA (A)
1337	Nucleic acid, purine bases (adenine, guanine)	Colon
1337	Nucleic acid, purine bases (adenine, guanine)	
1337	Purine bases (adenine, guanine)	DNA in water
1337	Adenylates	Colon mucosa
1338	Glycogen	Glycogen (Sigma Aldrich)[†]
1338	Tryptophan, amino acid	
1339	Adenine	DNA (B)
1339-41		Strateum corneum, Callus, psoriatic plaque
1340	Tryptophan (amino acid)	Rabbit & human cornea
1340	Tryptophan (amino acid)	Rabbit aqueous humour
1340	Nucleic acid	Colon adenocarcinoma
1343	CH_3CH_2 wagging	Diseased breast tissue
1343	CH_3CH_2 wagging	Collagen
1343	CH_3CH_2 wag	Type I collagen (human placenta) & infiltrating ductal carcinoma (breast)
1343		Rabbit aqueous humour
1343	Adenine	

1350	Glucose	Sigma
1358		Normal renal parenchyma & renal cell carcinoma
1359		Hepatocellular carcinoma
1360		Normal hepatic parenchyma
1360		Myoglobin
1360		Human aqueous humour
1361	Tryptophan	
1365	Guanine, tryptophan	
1372	Lipid	Human colon
1375		Myoglobin
1376	Thymine, guanine, adenine	
1377	Glycogen	Sigma Aldrich G0885
1380	δCH_3 δOH	Lactic acid
1382	Glycogen	Glycogen (Sigma Aldrich)[†]
1385	$\delta(CH_3)$ symm	Human strateum corneum
1400	Uracil, adenine	
1400		Cervix
1400	νCOO^-	AGP (glycoprotein)[*]
1401	Symmetric CH_3 bending in proteins	
1410	δOH	Methyl lactate
1412	Antisymmetric CH_3 deformation	Silicone gel
1420	δOH, νCO	Lactic acid
1421	$\delta(CH_3)$	Human strateum corneum
1421	Guanine, adenine	
1438	$\delta(CH_2)$ scissoring	Human strateum corneum
1438	CH_2 deformation	
1439	CH_2 scissoring deformation	breast tissue
1439	CH_3, CH_2 deformation	Normal breast tissue
1439	CH_2 deformation	Human breast biopsy
1439	CH_2 deformation due to lipids and proteins	Human brain tissue
1439	CH_2 scissoring deformation	Breast
1440	Lipid	
1441	CH_2 bending	Fibrous atherosclerotic plaque
1441	Lipid	Liver
1441	phosphotidylcholine	Phosphotidylcholine(Sigma Aldrich)[†]
1442	CH_3, CH_2 deformation	Oleic acid methyl ester
1442	Lipid	Human breast tissue Colon tissue
1442	Lipid	Normal human breast tissue
1442	Lipids – fatty acids	Normal breast tissue
1443	elastin	Sigma Aldrich E1625
1444	Lipid	Lipid (TPE)
1444	Triglycerides	Adipose tissue from human aorta
1445	$\delta(CH_2)$ or $\delta(CH_3)$	Cervix cancer
1445	$\delta(CH_2)$ or $\delta(CH_3)$	Uterus cancer
1445	$\delta(CH_2)$ or $\delta(CH_3)$	Benign or normal cervix
1445	$\delta(CH_2)$ or $\delta(CH_3)$	Benign or normal endometrium
1445	$\delta(CH_2)$ or $\delta(CH_3)$	Benign or normal ovary
1445	$\delta(CH_2)$ or $\delta(CH_3)$	Human breast tissue. Benign and Malignant tumours
1445	CH_2 deformation	breast tissue
1445	CH_2 bending mode	Normal breast tissue
1445	CH_3CH_2 deformation in collagen	Sigma Aldrich C7774
1447	$\delta(CH_2)$ (AGP)	AGP (glycoprotein)[*]
1447	CH_3CH_2 bending modes in bovine albumin	Sigma Aldrich A2153
1448	CH_2 deformation	Chicken leg bone

1448	Deoxyribose	DNA (B)
1448-9	$\Delta(CH_2)$ scissoring	Strateum corneum, Callus, psoriatic plaque
1449	CH_2 deformation	Lymph node
1450	Glucose	Blood
1450	CH bending	Rabbit & human cornea
1450	CH bending	Rabbit aqueous humour
1449	CH_3CH_2 bending modes	Bovine Serum albumin
1450	CH_3CH_2 deformation	Diseased breast tissue
1450	CH_2 bending	Human artery
1450	CH_2 bending mode	Diseased breast tissue
1450	$\delta(CH_2)$ or $\delta(CH_3)$	Endometrium cancer
1450		Elastin & collagen
1450	CH_3, CH_2 deformation	Infiltrating ductal carcinoma
1451	C-H bend	Normal human aorta
1451	CH_3, CH_2 deformation	Type I collagen (human placenta)
1451	CH_3CH_2 deformation	Collagen
1451	CH_2 bending	
1451-1454	CH_2 bending	Histones
1452	Structural protein	Breast
1452	$\delta(CH_2)$ scissoring in lipids & $\delta(CH_2)$ $\delta(CH_3)$ in proteins	Normal human skin
1452	CH_2 bending	Malignant breast tissue
1452	CH_2 in plane bending	Normal aorta
1453	$\delta(CH_2)$ or $\delta(CH_3)$	Ovary cancer
1453	$\delta(CH_2)$ or $\delta(CH_3)$	Benign or normal uterus
1453	C-H bending modes	Aorta
1454	CH_3 bending CH_2 scissors	Elastin & collagen & phospholipids
1454	CH_3 bending CH_2 scissors	Human cervix
1454	CH_3 asymmetric bending of proteins	
1454		Cervix
1455	δCH_3	Lactic acid
1455	Glycogen	Sigma Aldrich G0885
1455	CH_2 deformation	Breast
1456	CH_3 bending in elastin	Sigma Aldrich E1625
1456		Ovary
1457		DL-Lactic acid ($C_3H_6O_3$) CH_3-CHOH-COOH
1458	Nucleic acid	Colon adenocarcinoma
1460	Pentose sugar vibration due to δ CH_2	DNA
1462	Deoxyribose	DNA (B)
1475	δCH_3	Lactic acid
1475	DNA	DNA (Sigma Aldrich)[†]
1480	Vibration of purine bases (adenine & guanine)	DNA
1480	DNA	Cultured breast cells
1485	Nucleic acids	Colon
1485	Purine bases	DNA in water
1485	Nucleic acid, purine bases (adenine, guanine)	Colon
1485	Nucleic acid, purine bases (adenine, guanine)	
1487	Nucleic acid	Colon
1491	Formalin	
1500-1650	Heme	
1509	Phenylalanine	Bovine Serum albumin
1510	Adenine, guanine	
1512		Ovary

1517	Carotenoid	
1520-1670	Tryptophan & tyrosine	Cultured breast cells
1520	C=C Carotenoid	Food
1520	Carotenoid	Blood plasma
1522	Carotenoid	Carotid artery
1523	Carotenoid	Human breast tissue Renal cell carcinoma
1523	Carotenoid	Normal human breast tissue
1524	Carotenoid	Human brain tissue, acoustic neuroma
1525	Carotenoid	Beta carotene
1525	Carotenoid	Human breast carcinoma
1525	Carotenoid	Human breast carcinoma
1528	Carotenoid	Carotenoids in normal colon
1529	Carotenoid	Carotenoids in normal colon
1540	Amide II	Bovine insulin
1541	Tyrosine	
1547	Tryptophan	Human eye lens
1550	Tryptophan	
1552	Tryptophan (AGP)	AGP (glycoprotein)*
1552	δ(NH), ν(CN) Amide II	Human strateum corneum
1553	Tryptophan	
1554		Type I collagen (human placenta) & infiltrating ductal carcinoma (breast)
1555	Tryptophan	DNA in water
1556	Tryptophan	Bovine Serum albumin
1570	Vibration of purine bases (adenine & guanine)	DNA
1570	nucleotides	Breast cancer in mouse
1575	Guanine, adenine tryptophan	
1576	Nucleic acid	Colon adenocarcinoma
1577	Guanine, adenine	
1577	DNA	DNA (Sigma Aldrich)†
1580	nucleotides	Breast cancer in mouse
1580	DNA	Cultured breast cells
1580		Cervix
1585	Nucleic acid, purine bases (adenine, guanine)	Colon
1585	Nucleic acid, purine bases (adenine, guanine)	
1585	υ(C-O) olefinic	Strateum corneum, Callus, psoriatic plaque
1585	ν(C=C) olefinic	Human strateum corneum
1593	Purine bases	DNA in water
1600		
1602	Phenylalanine	
1602	Tyrosine	Tyrosine, colon adenocarcinoma
1606	Phenylalanine	Bovine Serum albumin
1607	Phenylalanine in bovine albumin	Sigma Aldrich A2153
1610	Tyrosine	Colon mucosa
1610	Tyrosine	Protein bands
1612	C=C stretching	Benzene
1615	Tyrosine (AGP)	AGP (glycoprotein)*
1616	Tyrosine	Bovine Serum albumin
1617	Tyrosine, phenylalanine	
1620	Tryptophan, tyrosine, phenylalanine, uracil	
1620	Tryptophan	Colon mucosa

1620	Tryptophan	Protein bands
1622	Tryptophan	DNA in water
1637	Amide I ν(C=O)	Diseased breast tissue
1637	Amide I ν(C=O)	Collagen
1640	OH bending	Water
1642	Amide I ν(C=O)	Collagen
1648-1661	Amide I ν(C=O)	Histones
1645	Bending mode	Water
1645	Amide I (C=O stretch)	α-helix protein secondary structure in α-Poly-L-lysine
1645-1660	Amide I (C=O stretch)	α-helix protein secondary structure
1665-1680	Amide I (C=O stretch)	β-sheet protein secondary structure
1660-1670	Amide I (C=O stretch)	Unordered protein secondary structure
1645-1655	Amide I (C=O stretch)	α-helix protein secondary structure
1665-1680	Amide I (C=O stretch)	β-sheet protein secondary structure
1655-1665	Amide I (C=O stretch)	Unordered protein secondary structure
1654-1662	Amide I (C=O stretch) α-helix	α-helix protein secondary structure
1665-1680	Amide I (C=O stretch)	β-sheet protein secondary structure
1654-1685	Amide I (C=O stretch)	Unordered protein secondary structure
1650	Amide I	Normal human aorta
1650	lipid	Colon mucosa
1650	Pyrimidine bases (cytidine, thymidine) ?	DNA in water
1650	C=C lipid bands	Colon
1650	Amide I ν(C=O)	Bovine insulin
1650		Ascorbate
1650		Rabbit aqueous humour
1650	Amide I (C=O stretch) ν(C=O)	Human artery
1650-1666	C=C vibration cis-isomer in fatty acid chain	Phospholipid membrane
1651	Amide I, ν(C=O)	Benign breast tissue and malignant tumours
1651-1664	Amide I, ν(C=O)	Healthy human skin
1651	Amide I, ν(C=O) in collagen	Sigma Aldrich C7774
1651	Amide I, (C=O stretch)	Ovarian cancer
1651-4	υ(C-O) Amide I, α helix	Strateum corneum, Callus, psoriatic plaque
1652	Lipid	Lipid (TPE)
1652	Lipid	Human breast tissue
1652	Amide I	α-helix protein secondary structure in α-Poly-L-glutamate
1652	ν(C=O) Amide I α-helix	Human strateum corneum
1653	Lipid	Human breast tissue Human colon
1653	Lipid	Normal human breast tissue
1653	Amide I protein	
1653	Amide I (C=O stretch) in bovine albumin	Sigma Aldrich A2153
1654	α-helix	nails
1654	C=C stretch Olefinic	Breast biopsy tissue
1654	C=C stretch	Breast tissue

1654	Amide I	Normal breast tissue
1654	C=C stretch	Breast
1655	C=C stretch of unsaturated fatty acid chains	Aorta
1655	Amide I	Oleic acid methyl ester
1655	Amide I protein (C=O stretch)	Coronary Artery
1655	Amide I (C=O stretch)	Lymph node
1655	Amide I (C=O stretch)	Endometrial cancer
1655	Amide I (C=O stretch)	α-helix protein secondary structure in α-Poly-L-alanine
1656	phosphotidylcholine	Phosphotidylcholine(Sigma Aldrich)[†]
1656	Amide I (C=O stretch)	Collagen
1656	Amide I (C=O stretch)	Human cervix
1656	Amide I (C=O stretch)	
1656		Cervix
1656	Amide I (C=O stretch)	Benign or normal endometrium
1656	Amide I (C=O stretch)	irregular protein secondary structure in β-Poly-L-glutamate pH 11
1657	Amide I (C=O stretch)	Cervical cancer
1657	Lipids – fatty acids	Breast
1657	Lipids	Colon
1657	Amide I (C=O stretch)	Malignant breast tissue
1657	Amide I	Infiltrating ductal carcinoma (breast)
1657	Amide I (C=O stretch)	Diseased breast tissue
1658	Amide I (C=O stretch)	
1658	Amide I	Aorta
1659	Amide I, ν(C=O)	Benign breast tumours
1659	Amide I (C=O stretch)	Benign or normal ovary
1659	Amide I (C=O stretch)	Benign or normal cervix
1659	Amide I (C=O stretch)	Benign or normal uterus
1659	Amide I (C=O stretch)	Uterus cancer
1659	Amide I (C=O stretch) ά helical	Human brain tissue
1659	Amide I (C=O stretch)	Bovine Serum albumin
1659	Amide I (C=O stretch)	
1661	Amide I ν(C=O) in elastin	Sigma Aldrich E1625
1661	Amide I ν(C=O)	Normal human skin
1662	Nucleic acid	Colon adenocarcinoma
1662	Triglycerides	Adipose tissue from human aorta
1662	Nucleic acids	Colon
1662	Amide I (AGP)	AGP (glycoprotein)[*]
1664	Amide I (C=O stretch)	Healthy human skin
1664		Ovary
1665	Amide I (C=O stretch)	irregular protein secondary structure in β-Poly-L-lysine pH 4
1665	Amide I (C=O stretch)	Collagen
1665	Amide I	Type I collagen (human placenta)
1665	Amide I (C=O stretch)	Liver - collagen
1665	Carbonyl vibration mode	Fibrous atherosclerotic plaque
1666	C=O stretching modes of pyrimidine bases	DNA
1667	Structural protein	Malignant breast
1668	Amide I (C=O stretch)	Elastin
1669	Amide I (C=O stretch)	Human eye lens
1669	Protein	Breast cancer in mouse
1669	Amide I (C=O stretch)	β pleated sheet protein secondary structure in β-Poly-L-alanine
1669	Amide I (C=O stretch)	Normal aorta

1670-1680	C=C vibration trans-isomer in fatty acid chain	Phospholipid membrane
1670	Amide I	Chicken leg bone
1670	Amide I (C=O stretch)	Pure protein - β pleated sheet
1670	Amide I (C=O stretch)	Collagen
1670	Amide I (C=O stretch)	
1670	Amide I (C=O stretch)	Rabbit lens
1670	Amide I (C=O stretch)	β pleated sheet protein secondary structure in β-Poly-lysine
1672	Amide I (C=O stretch)	β pleated sheet protein secondary structure in β-Poly-L-glutamate
1683	Amide I (C=O stretch)	Bound protein - regular uncharacterised secondary structure
1717	C=O stretching modes of purine bases	DNA
1725		Lactate
1725	νC=0	Lactic acid
1726	Lactate	
1736	ester stretching mode C=O	DMPC (dimyristoylphosphatidycholine), a typical lipid
1740	ν(C=O) -lipid	Food, coronary artery
1742	phosphotidylcholine	Phosphotidylcholine(Sigma Aldrich)†
1743		Oleic acid methyl ester, normal human breast tissue
1743	C=O stretch	Breast tissue
1743	C=O stretch	Breast
1743	ν(C=O) lipid	Human strateum corneum
1747	C=0 stretch	Aorta
1750	C=O	Normal skin dermis
1752	Triglycerides	Adipose tissue from human aorta
1768	ν(COO)	Human strateum corneum
2579	S-H stretch	Rabbit lens
2700-2880	Collagen C-H stretch	Dentine
2717-23	υ(CH) aliphatic	Strateum corneum, Callus, psoriatic plaque
2723	ν(CH) aliphatic	Human strateum corneum
2730		Breast
2800-3000	CH stretch – lipids	Healthy human skin
2850-2960	CH_3, CH_2 stretching in alkyl/ acyl chains	DMPC (dimyristoylphosphatidycholine), a typical lipid
2850	ν_s(C-H) in (Ethylene CH_2=CH_2)	Phospholipid membrane (constant with temperature)
2850	C-H stretching vibration	Normal skin dermis
2852	υ(CH_2) symmetric	Strateum corneum
2852	ν_s(CH_2) in lipids & proteins	Normal human skin
2852	ν_s(CH_3) - lipid	Healthy human skin
2852	ν(CH_2) symm	Human strateum corneum
2857	C-H stretch (-CH_3 sym.)	Breast tissue
2857	C-H stretch (-CH_2 sym.)	Breast
2872	υ(CH_2) asymmetric	Callus, psoriatic plaque
2875	C-H stretch (-CH_3 asym.)	Breast tissue
2875	C-H stretch (-CH_2 asym.)	Breast
2880	ν_{as}(C-H)	Phospholipid membrane
2880	C-H stretch	Human tooth enamel
2882	C-H stretch	Chicken leg bone
2883	υ(CH_2) asymmetric	Strateum corneum
2883	ν(CH_2) sym.- lipid	Healthy human skin

2883	$\nu(CH_2)$ symm, $\nu(CH_2)$ asymm	Human strateum corneum
2885	CH_3 stretch	Lactate
2886	C-H stretching vibration	Normal skin dermis
2898	C-H stretch (-CH_3 sym.)	Breast
2890	ν_{as}(C-H) in (Ethylene CH_2=CH_2)	Phospholipid membrane
2890	CH_2 symmetric stretch	Glucose
2890	CH_2 stretch	Rabbit & human cornea
2890	CH_2 stretch	Glucose
2890	CH stretch	Rabbit & human aqueous humour
2893	Glucose & lactate	Rabbit aqueous humour
2894-5	Lactate & glucose	
2898	C-H stretch (-CH_3 sym.)	Breast tissue
2918	C-H stretch	Chicken leg bone
2929	C-H stretch (-CH_3 sym.)	Breast tissue
2929	C-H stretch (-CH_3 sym.)	Breast
2930	$\nu(CH_2)$ – lipid	Coronary Artery
2931	$\upsilon(CH_3)$ symmetric	Strateum corneum, Callus, psoriatic plaque
2931	$\nu(CH_3)$ symm, $\nu(CH_2)$ asymm	Human strateum corneum
2932	C-H stretch	Human tooth enamel
2935	$\nu(CH_2)$ sym.- lipid	Healthy human skin
2935	C-H stretch	Rabbit lens
2939	Glucose & lactate	Rabbit aqueous humour
2942	C-H	
2942	$\nu_{as}(CH_3)$ – lipids and proteins	Normal human skin
2943	Glucose	
2945	CH stretch	Rabbit & human cornea
2945	CH_3 stretch	Lactate
2945	CH stretch	Rabbit & human aqueous humour
2945	Lactate	
2950	CH_2 anti-symmetric stretch	Glucose
2950	CH_2 stretch	Glucose
2958	$\nu(CH_3)$ asymm	Human strateum corneum
2960	C-H stretch (-CH_3 asym.)	Breast tissue
2960	C-H stretch (-CH_3 asym.)	Breast
2975	C-H stretch	
2982	Glucose & lactate	Rabbit aqueous humour
2983	$\upsilon(CH_3)$ symmetric	Strateum corneum, Callus, psoriatic plaque
2990	CH_3 stretch	Lactate
2995	Lactate	
3006	=C-H stretch	Breast tissue
3006	C-H stretch	Breast
3059-60	υ(CH) olefinic	Strateum corneum, Callus, psoriatic plaque
3060	ν(CH) olefinic	Human strateum corneum
3063	C-H stretch	Rabbit lens
3245	νOH	Methyl lactate
3390	OH mode	Rabbit lens

Appendix B Investigation of sample state using PCA

Following the Raman probe tissue classification, PCA analysis of the sample state (fresh and frozen) was investigated. It was found that no separation of the fresh and frozen samples was evident as shown below. PCA was carried out, and plots constructed colour coded for sample state – fresh (black), frozen once (green) and frozen twice (pink). There was no correlation/clustering for different sample state. The plot of PC1vPC3 shown in the figure, exhibited 5 outliers, which upon further investigation were found to be gastric samples exhibiting strong lipid peaks confirming that these samples should be removed from the model. No evidence was visible in the other PCs. There was no evidence in other PC plots.

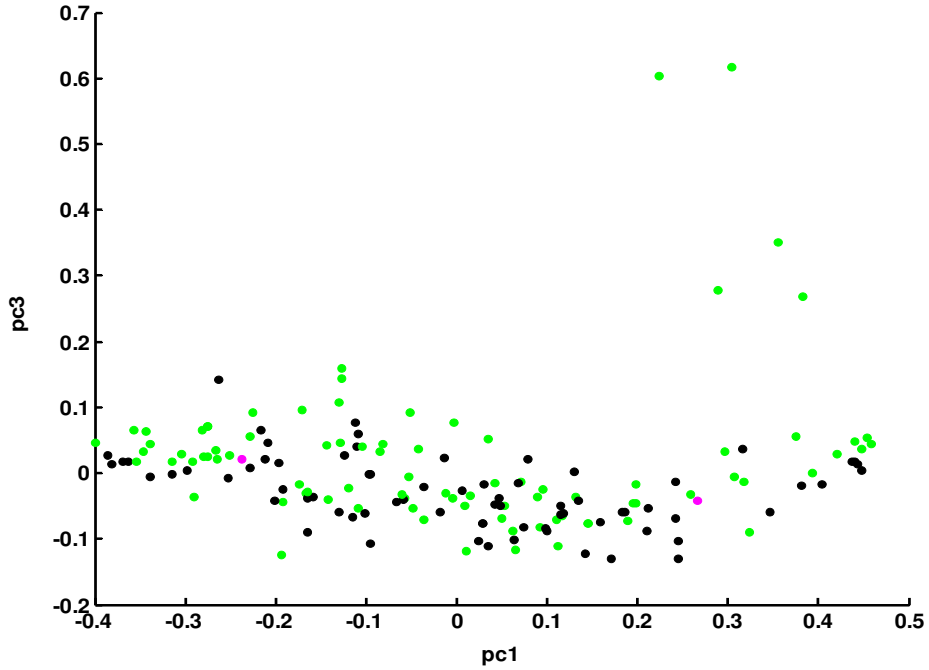

Figure C: PC1 vs PC3 (colour coded for sample state fresh (black), frozen once (green) and frozen twice (pink)

Appendix C Preliminary study of rapid Raman mapping

Rapid Raman maps were acquired using the prototype 785nm rapid mapping system at Renishaw. The sample contained a normal squamous island in Barrett's (with query LGD) as shown in Figure D1. PCA (using the Wire 3.0 Renishaw software), demonstrates that NSq is easily detectable with PC loads indicating presence of glycogen.

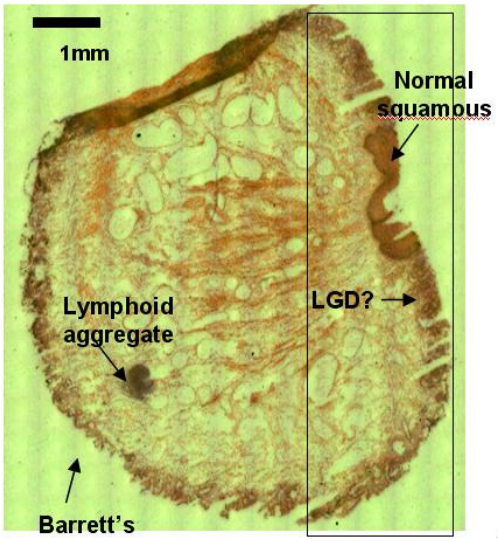

Figure C1: H&E of an oesophageal EMR section containing normal squamous, Barrett's (IM) and query low grade dyplasia (non conclusive).

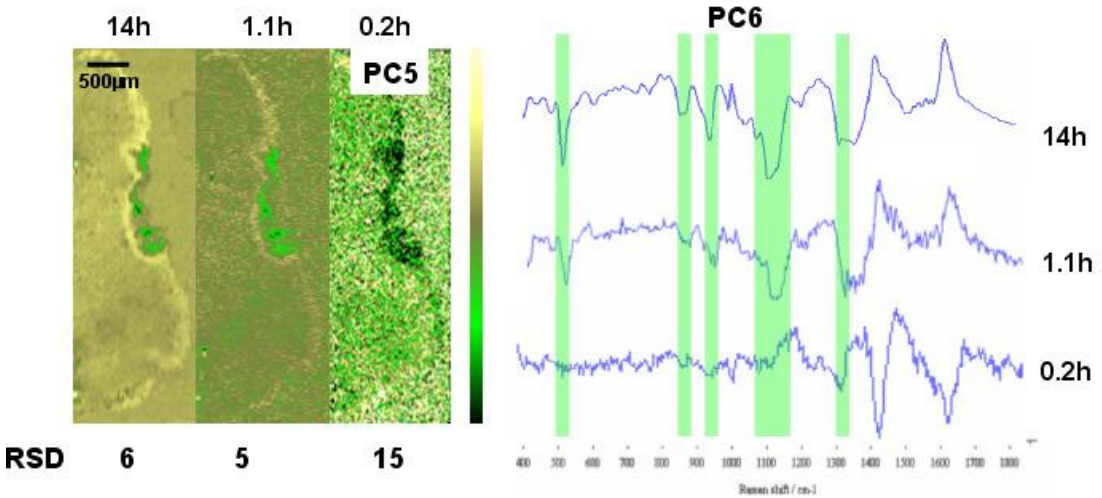

Figure C2: Rapid Raman maps (78x228=17784 total spectra) acquired with a step size 27.5 µm and acquisition times of 5, 0.5 and 0.1s. The 6th PC load (5th for the 0.1s map since the 6th PC was dominated by noise) are shown which exhibit peaks which can be attributed to glycogen (green bands) in normal tissue. The overall mapping time and relative standard deviation (RSD) is shown for comparison purposes.

Appendix D Previous mapping of oesophageal tissue (Shetty et al.[**])

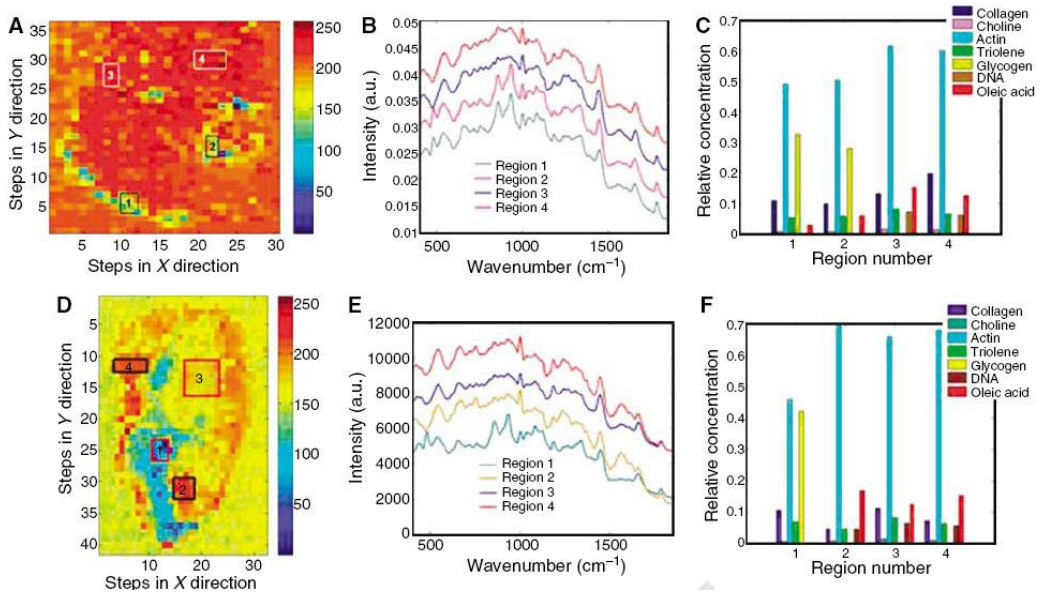

Figure D1: Examples Raman point maps of oesophageal two biopsy sections taken from Shetty et al. "Normal squamous and HGD sample (H&E stained section Figure 1A). (A) Third principal component score map with selected regions marked.

(B) Mean Raman spectra from selected regions. (C) Relative concentration of selected biochemical constituents calculated with mean spectra from selected

regions. Normal squamous and adenocarcinoma sample (H&E stained section Figure 1B). (D) Third principal component score map with selected regions

marked. (E) Mean Raman spectra from selected regions. (F) Relative concentration of selected biochemical constituents calculated with mean spectra from

selected regions."

[**] Shetty, G., Kendall, C., Shepherd, N., Stone, N. and Barr, H. (2006). Raman spectroscopy: elucidation of biochemical changes in carcinogenesis of oesophagus. *British Journal of Cancer,* 94(10), p. 1460-1464.

Appendix E Raman mapping objective comparison (PCs 5-8)

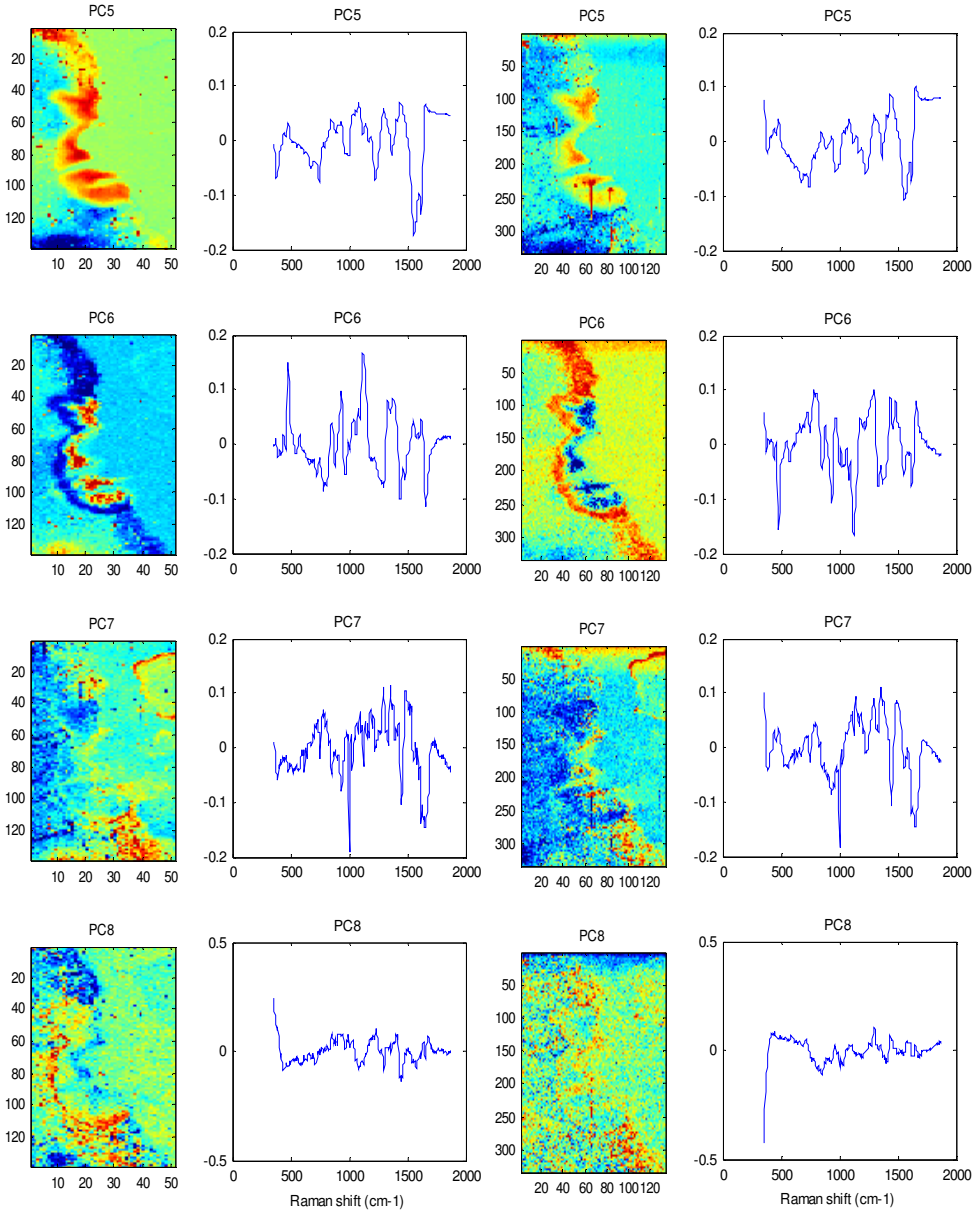

Figure E1: PCs 5-8 for comparison of maps acquired with the Nplan x50, 5 s, 27.5 µm step size (left) and Leica x50 long working distance, 5 s, 11 µm step size (right) objectives. Note that PC6 and PC8 for the Leica x50 obejctive, the colour bar is inverted and thus the PC load is also inverted.

Appendix F Raman Vs FTIR imaging

A comparison of Raman and FTIR mapping was carried out on a sample of NSq epithelium.

- 6.25µm step size
- Cropped to 15651 spectra
- 16 scans per pixel

- 6.6µm step size
- 141x111=15651 spectra
- acquisition time 30s

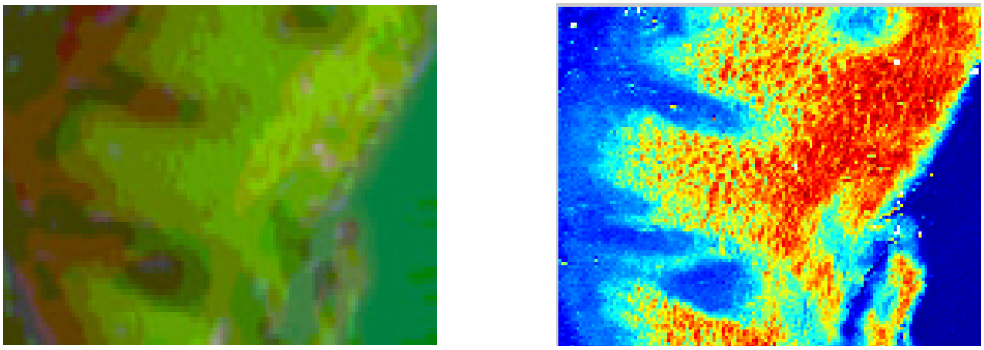

Figure F1: A comparison of Raman and FTIR maps acquired with the same mapped area, and similar signal to noise

Less data processing (cosmic rays etc) Higher SNR Quicker mapping times	More spectra peaks Potential for higher spatial resolution
PE Spotlight 300 - 1.4h	15h
With upgraded Spotlight 400 - 0.7h	~0.2-1h with optimised parameters

The conclusion of this study was that FTIR also has potential for automated histpathology, but it is limited by sample preparation, and furthermore, increasing the spatial resolution is not an option. However, reduced mapping times are extremely beneficial. Raman mapping would also provide continuity with in vivo studies.

Appendix G Hutchings et al. Journal of Biophotonics, 2(1-2), p. 91-103

(BLANK PAGE)

(BLANK PAGE)

Appendix H PCs 1-8 for the rapid Raman map D

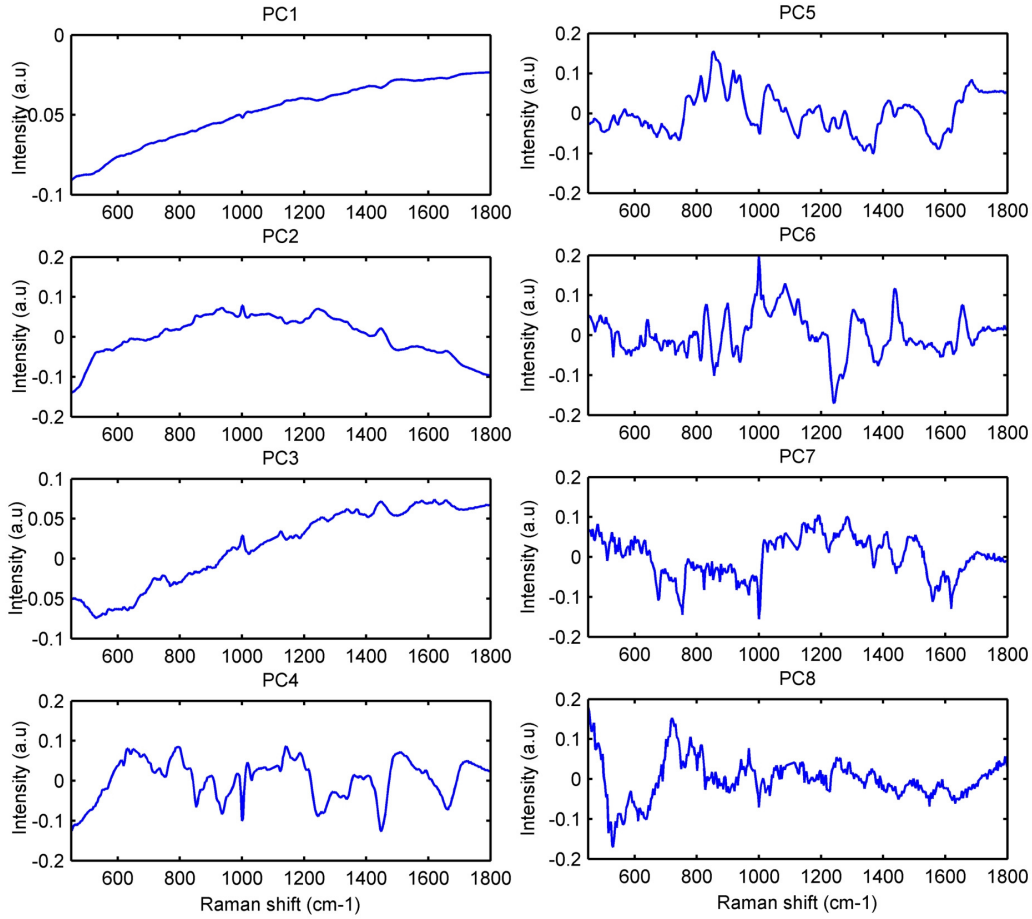

Figure H1: PC loads 1-8 for Map D

Appendix I Manuscript submitted to the Analyst (Nov 2008)

(BLANK PAGE)

Appendix J Ambient temperature poster

The effect of ambient temperature on a Raman classification model for the diagnosis of precancerous changes in the oesophagus

Gloucestershire Hospitals NHS NHS Foundation Trust

Hutchings J[1,2], Kendall C[1,2], Barr H[1,2] and Stone N[1,2]

1. Biophotonics Research Group, Gloucester Royal Hospital, Gloucester, GL1 3NN
2. Cranfield Health, Cranfield University, Silsoe, Bedfordshire, MK45 4DT

Cranfield UNIVERSITY

1. Introduction

- Raman spectroscopy has been used to successfully identify and classify precancerous changes in the oesophagus[1]
- Ambient temperature has been shown to affect Raman spectra[2] which is a possible limitation on the use of Raman spectroscopy in a clinical environment

Aim
To investigate spectral artefacts caused by variation in ambient temperature and to demonstrate the effect on a multivariate tissue classification model

2. Method

a) Peak shift investigation

- The air conditioning unit setting was altered in 2ºC intervals ranging from 19 to 31ºC (the actual room temperature was also measured)
- Polymer spectra were acquired using two Renishaw System 1000 spectrometers (830nm, 5s, x50objective) and a Visionex probe system in combination with a Renishaw System 100 spectrometer (830nm, 30s

- Spectra were also acquired from a neon argon lamp (1s)
- At each aircon setting, the systems were allowed to reach temperature equilibrium for 2hours
- Peak positions were plotted against actual room temperature
- A Raman map of the polymer standard was also acquired whilst ramping the temperature up from 19-28ºC using S1000(1).
- An 2mm square was mapped with a step size of 2µm, with acquisition time of 2s.

b) The effect of peak shifts on a multivariate tissue classification model

- A multivariate tissue classification model was tested by projecting spectral data with an artificial peak shift to illustrate the effect of ambient temperature on the model performance

3. Results

a) Peak shift investigation

- Peak shifts were noted in both System 1000 spectrometers for both the polymer standard and neon argon lamp

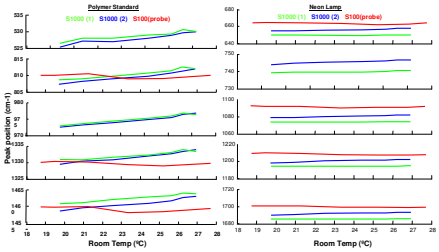

System	Polymer peak shift	Ne-Ar lamp peak shift
S1000 (1)	0.4cm^{-1}/ºC	0.1cm^{-1}/ºC
S1000 (2)	0.6cm^{-1}/ºC	0.5cm^{-1}/ºC
S(100)	Range (max-min) 1.5cm^{-1}	-0.1cm^{-1}/ºC

- It is evident that there is potentially a contribution to the ambient temperature artefacts from both the spectrometer and laser
- For the S100 probe system, a linear peak shift with temperature was not evident with the polymer standard so the range is stated

3. Results cont…

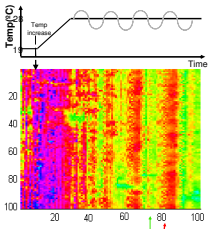

- The figure shows a psuedocolour score map of the 1st principle component
- The region of increasing temperature is clearly evident as a region of low scores (blue-purple)
- A repetitive stripe pattern is also evident once the temperature has stabilised and this is attributed to temperature oscillation as the air-conditioning maintains a constant temperature, consistent with that noted by Fukura et al[2]
- The region of oscillation is consistent with a peak shift of approx 0.5cm^{-1}

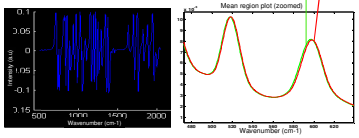

- The loading for the 1st PC exhibits discontinuities characteristic of peak shifts

a) The effect of peak shifts on a multivariate tissue classification model

- A classification model was generated using spectra acquired from S1000(1) at 23ºC
- An test set consisting of the original data set with an artificial peak shift of 5cm-1 was projected onto the original classification model

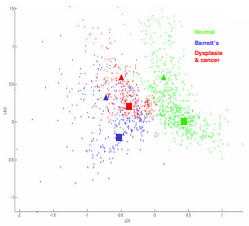

- The training set and test set centroids are illustrated in the figure with a square and triangle respectively
- The percentage correctly classified drops from 94% to 75%
- Note that the most significant shift is the misclassification of Barrett's as cancer with the shifted spectra
- This temperature shift would also have a detrimental effect on Raman maps of tissue sections

4. Conclusions

- Peak shifts can have significant effect on Raman spectra
- Shifts occurred in both the polymer standard and neon argon spectra suggesting that shifts were caused by expansion or contraction of spectrometer components with temperature as well as a potentially significant contribution from the laser source
- The apparent linear shift across the entire wavelength range would make correction easier than for example if a breathing artefact was apparent
- Initial results suggest that the effect is less pronounced when using the compact S100 spectrometer which may be due to the simplicity of the spectrometer, or due to the lower resolution spectra, although further work is required to investigate this. This could potentially ease the transition to clinical application, in theatre for example.
- The detrimental effect of temperature induced peak shifts on a tissue classification model is demonstrated highlighting the importance of temperature stabilisation over short and long time periods

5. References

1. Kendall C, Stone N, Shepherd, Geboes K, Warren B, Bennett and Barr H **Raman Spectroscopy, a potential tool for the objective identification and classification of neoplasia in Barrett's oesophagus.** Journal of Pathology; 2003; 200: 602-609
2. Fukura S, Mizukami T, Odake S and Kagi H. **Factors Determining the Stability, Resolution, and Precision of a Conventional Raman Spectrometer**. Applied Spectroscopy. 2006; 60 (8): 946-950 2006

Appendix K Prognostic model poster

Can Raman Spectroscopy be used to predict the prognosis of cancer in patients with high grade dysplasia (HGD)?

Joanne Hutchings[1], Simon Dwerryhouse[2], Nicholas Stone[1], Catherine Kendall[1], Hugh Barr[1]

1. Biophotonics Research Group, Gloucester Royal Hospital, Gloucester, GL1 3NN
2. Department of Surgery, Addenbrooke's Hospital, Cambridge, CB2 2QQ

email: Johutchings@hotmail.com

1. Introduction

Oesophageal Cancer

Oesophageal cancer is the 9th most common cancer in UK [1]. Over 7,500 people diagnosed per year in the UK [1]. 5-year survival 2 to 25%[2]. In most cases patients do not present until the disease is advanced at which point it is difficult to treat. The earlier we diagnose the cancer the easier to treat.

Endoscopic image of advanced oesophageal cancer

Barrett's Oesophagus

Barrett's oesophagus is a precursor condition to oesophageal cancer. Acid reflux causes normal stratified squamous epithelium that lines the stomach adapts over time to become columnar epithelium, similar to that found in the stomach. Patients with Barrett's oesophagus have a 30 fold chance of developing adencarcinoma[3].

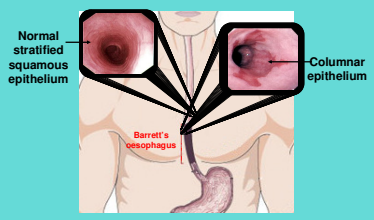

Currently, patients with Barrett's oesophagus undergo routine endoscopic surveillance. Biopsy samples are taken and analysed in histopathology to detect cancerous cells and premalignant changes such as dysplasia.

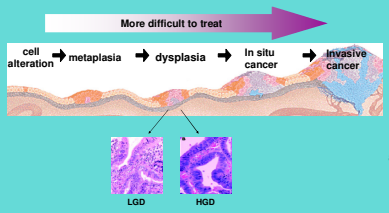

Dysplastic cells have 'malignant potential'

Precede cancer but do not always result in cancer

What is Raman Spectroscopy?

Raman Spectroscopy is based on the inelastic scattering of monochromatic light. Energy changes in the scattered light can be detected and used to characterise tissue samples.

Aim

To determine whether or not Raman spectroscopy can be used to detect those dysplastic cells with a higher probability of progressing to cancer.

2. Method

- 25 biopsies were obtained from 14 patients with Barrett's oesophagus
- 10-40 spectra measured on 1st biopsy diagnosed HGD (total 576)
- Acquired using customised Renishaw system 1000
- Excitation 830nm
- x80 objective
- Acquisition time of 30s

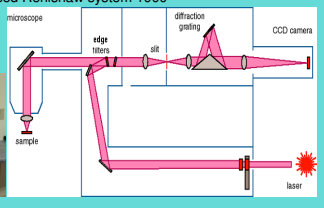

3. Data Analysis and Results

Raman on 1st biopsy
↓
Monitor patients over 2yrs
↓
Identify those who develop cancer
↓
Correlate pathology results with Raman spectra
↓
Develop model that predicts if a patient will develop cancer

Patient Groups

- Patients were grouped into one of four categories. The spectral prediction was compared to the histopathological results and the mean spectra determined.
  1) never developed cancer
  2) cancer at first biopsy
  3) cancer within 1 year
  4) cancer after 1 year

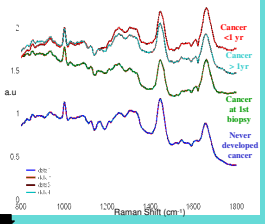

Multivariate Analysis

- A prognostic model was created using Matlab.
- Principal component analysis (PCA) was carried out and the first 15 components were fed into a linear discriminant model.
- The linear discriminant loads were used to create a scatter plot of the four different groups.

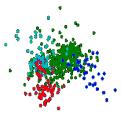

Performance of the Model

- The performance of the model can be seen in the bar chart which plots spectral prediction against actual outcome.
- The training performance, sensitivity and specificity are tabulated below.

Training performance	81.6%
Sensitivity	81-97%
Specificity	92-99%

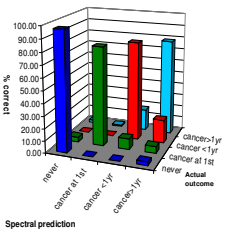

4. Conclusions

- This was a pilot study. More patients and samples (including LGD) are required to improve the reliability of the model. Cross validation will also be carried out. Other areas will also investigated such as the location of the cancer compared to the initial biopsy.
- Although further work is required, this pilot study demonstrates the potential for Raman spectroscopy to correctly predict the future development of cancer in patients with HGD. Hopefully in the future this will lead to the in vivo diagnosis and prognosis of patients with HGD and Barrett's oesophagus.

5. References

1. Cancer Research UK 2005
2. Parkin DM, Bray F, Ferlay J, Pisani P. Global Cancer Statistics, 2002 CA Cancer J Clin 2005; 55:74-108
3. Spechler SJ Managing Barrett's Oesophagus, BMJ 2003;326:892-894

Appendix L Grants, awards, publications and presentations

Grants

- Institute of Physics and Engineering in Medicine (IPEM) Research Training Fellowship – September 2006

Awards

- Barrett's Oesophagus Foundation National Meeting Scientific Poster Prize – London, March 2008
- PROBE Lay Persons Presentation Prize – London, March 2008
- BMLA Scientific Presentation Prize – Manchester, June 2007
- 3 Counties Cancer Research Network Scientific Poster Award – Cheltenham June 2006

Publications

- 2009 Hutchings, J., Kendall, C., Shepherd, N., Ludeman, L., Barr, H., Stone, N. 'A Raman mapping study of high grade dysplasia in oesophageal tissue using linear discriminant analysis to evaluate the importance of spatial resolution for histopathology' Submitted to Analyst

- 2009 Kendall, C., Isabelle, M., Hutchings, J., Babrah, J., Orr, L., Baker, R., Bazant-Hegemark, F., Stone, N., 'Vibrational spectroscopy: a clinical tool for cancer diagnostics' accepted in Analyst (Invited)

- 2008 Hutchings, J., Kendall, C., Smith, B., Shepherd, N., Barr, H., Stone, N., 'The potential for histological screening using a combination of rapid Raman mapping and principal component analysis' Journal of Biophotonics, 2(1-2), p. 91-103

- 2008 Keller, M.D., Kanter, E.M., Lieber, C.A., Majumder, S.K., Hutchings, J., Ellis, D.L., Beaven, R.B., Stone, N., Mahadevan-Jansen, A., 'Detecting Temporal and Spatial Effects of Epithelial Cancers with Raman Spectroscopy' Dis. Markers, 25(6), p. 323-37

- 2008 Hutchings, J., Kendall, C., Shepherd, N., Barr, H., Smith, B., Stone, N., 'Rapid Raman microscopic imaging for potential histological screening', Biomedical Optical Spectroscopy – Proceedings of SPIE 6853, art. No. 685305

- 2007 Hugh Barr, Joanne Hutchings, Catherine Kendall, Florian Bazant-Hegemark, Nicholas Stone. Endoscopic Approaches to the treatment of early malignancy and their relationship to clinical outcome. In: UK Key Advances in Clinical practice Series. The effective management of Upper Gastrointestinal malignancies, 2nd edition. Eds. Wendy L. Allen, Vicky Coyle and Patrick G. Johnston

Presentations and Posters **(International conferences in BOLD)**

- **High spatial resolution Raman mapping of epithelial tissues (Presentation) – SPEC 2008, Sao Jose dos Campos, Brazil.**
- Final year PhD presentation (presentation) – Cranfield Health, Sept 2008).
- Rapid Raman mapping of oesophageal tissue (Poster & presentation) – IPEM, Bath, Sept 2008
- **Optimised rapid Raman mapping of oesophageal tissue (Poster) - XXIst International Conference on Raman Spectroscopy, London, August 2008.**
- **A comparison of Raman probes for the early diagnosis of oesophageal cancer (Poster) – XXIst International Conference on Raman Spectroscopy, London, August 2008**
- **Rapid Raman mapping of oesophageal tissue (Poster), DASIM, Dublin 2008**
- Early diagnosis of Barrett's oesophagus using laser light (lay presentation and poster) – Barrett's Foundation, London, March 2008
- **Rapid Raman microscopic imaging for potential histological screening (Presentation) – SPIE, San Jose, Jan 2008.**
- RECaD presentation - Gloucestershire Hospitals NHS Trust, October 2007.
- Photodynamic therapy in Barrett's dysplasia: is it effective? (Presentation) – IPEM ASM, Cardiff, Sept 2007
- Evaluation of in vivo Raman probes for the diagnosis of precancerous changes in the oesophagus (Presentation) – IPEM ASM, Cardiff, Sept 2007
- Classification of precancerous changes in the oesophagus using a Raman probe (Presentation) – British Medical Lasers Association, Manchester, June 2007
- **Study of the effect of ambient temperature on a Raman classification model for the diagnosis of precancerous changes in the oesophagus (Poster) – International Conference of Applied Vibrational Spectroscopy, Corfu, June 2007**
- Can Raman Spectroscopy be used to predict the prognosis? (Poster) – House of Commons, March 2007
- The potential of Raman spectroscopy for in vivo cancer diagnosis in the oesophagus (Presentation) - Institute of Physics and Engineering in Medicine, Cambridge, Sept 2006
- The potential of Raman spectroscopy for in vivo cancer diagnosis in the oesophagus (Presentation) - British Medical Lasers Association, Manchester, June 2006
- **Can Raman Spectroscopy be used to predict the prognosis of cancer in patients with high grade dysplasia? (Poster) – SPEC, Heidelberg, May 2006.**
- Using Lasers to Diagnose Cancer (lay presentation) – British Medical Association, Cheltenham Feb 2006

Early View publication on
www.interscience.wiley.com
(issue and page numbers not yet assigned;
citable using Digital Object Identifier – **DOI**)

J. Biophoton. 1–13 (2009) / **DOI** 10.1002/jbio.200810070

Journal of
BIOPHOTONICS

FULL ARTICLE

The potential for histological screening using a combination of rapid Raman mapping and principal component analysis

Joanne Hutchings[1, 2], *Catherine Kendall*[1, 2], *Brian Smith*[3], *Neil Shepherd*[1, 2], *Hugh Barr*[1, 2], *and Nicholas Stone*[*, 1, 2]

[1] Biophotonics Research Group, Gloucester Royal Hospital, Great Western Road, Gloucester, GL1 3NN, UK
[2] Cranfield Health, Cranfield University, College Road, Cranfield, Bedfordshire, MK43 0AL, UK
[3] Renishaw Plc., Old Town, Wotton-under-Edge, Gloucestershire, GL12 7DW, UK

Received 9 September 2008, revised 18 December 2008, accepted 8 January 2009
Published online 28 January 2009

Key words: Raman, rapid, mapping, oesophagus, imaging, multivariate analysis, histopathology, screening, cancer

PACS: 00.00.Xx, 11.11.Yy

➡ **Supporting Material:** is available online under www.biophotonics-journal.org (abstract link of the article).

Rapid Raman mapping was carried out on 20 μm sections of oesophageal biopsy samples. Contiguous 7 μm sections were stained with haematoxylin and eosin (H&E) with histopathology provided by an expert pathologist. The step size and acquisition times were varied and the resulting spectra, principal component (PC) score maps and loads were compared. Overall mapping times were also compared to traditional Raman point mapping. The principal component loads for each of the maps were seen to be similar despite varying the acquisition time and number of spectra. Gross biochemical information was extracted showing good correlation with the H&E sections even for short overall mapping times (30–90 minutes for a 2 mm biopsy, 0.5 s acquisition time per 25.3 μm Raman pixel). This demonstrates that low signal to noise spectral maps are sufficient for the identification of histologically relevant biochemistry using principal component analysis as long as the spectral dataset is large enough.

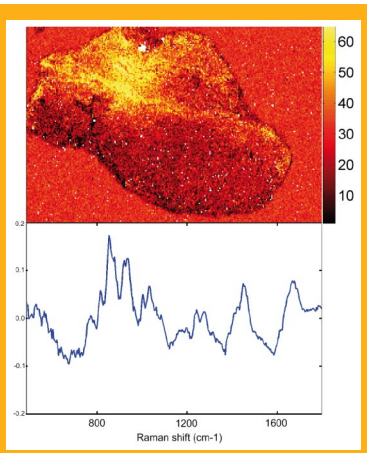

5th PC score map and corresponding load for a rapid Raman map (1.7 s acquisition, 10.6 μm step size, 5×10^4 total spectra, overall map time 4 h)

* Corresponding author: e-mail: n.stone@medical-research-centre.com,Phone: +448454 225485, Fax: +448454 225486

© 2009 by WILEY-VCH Verlag GmbH & Co. KGaA, Weinheim

Journal of
BIOPHOTONICS

1. Introduction

1.1. Oesophageal cancer

Barrett's oesophagus is a condition caused by long term gastro-oesophageal reflux. Patients with Barrett's oesophagus have an increased risk of developing adenocarcinoma [1]. As a result, patients undergo routine endoscopic surveillance during which biopsies are taken, formalin fixed, sectioned and stained with haematoxylin and eosin (H&E) for histopathological diagnosis. Approximately 90% of biopsies taken during routine endoscopic surveillance are not of clinical relevance resulting in unnecessary removal of tissue and stretched histopathological resources. A further problem is that histological diagnosis is subjective since the process of carcinogenesis is a continuum, and morphologically based classification can not reliably predict cancer risk [2]. An objective and reliable method of identifying non-relevant tissue samples would potentially relieve the huge burden of biopsy numbers on the histopathologist.

1.2. Raman Spectroscopy

Raman spectroscopy is an inelastic scattering technique that has been shown to be a promising method for distinguishing tissue pathologies based on a spectrum (effectively a biochemical fingerprint) not only in oesophageal disease [3], but also in other organ systems such as cervix [4, 5], stomach [6], breast [7, 8] colon [9] and parathyroid [10]. This technique could potentially be used as an aid to the histopathologist to classify more subtle biochemical changes occurring within the transition from Barrett's oesophagus, through dysplasia, to adenocarcinoma. Furthermore, it may be possible to detect molecular changes occurring before macroscopic morphological changes are evident at histopathological analysis.

Raman scatter is a relatively weak process compared to elastic scatter with as little as one in a million photons undergoing Raman scattering. As time has progressed technological advances have enabled the acquisition of Raman point tissue spectra in relatively short acquisition times. Imaging applications of Raman have generally relied on point mapping, which is widely regarded as a slow technique. However, there has been some use of flat field illumination coupled with liquid crystal tunable filters and array detection (ChemImage) [11].

In previous studies we have shown that Raman spectroscopy is capable of detecting and classifying pre-cancerous and cancerous changes with a high sensitivity and specificity [3]. Further studies have gone on to elucidate biochemical changes occurring during the progression to cancer in the oesophagus [12–14]. The first demonstration of Raman for the biochemical analysis of the bladder was made by Stone et al. [15]. Other groups have used Raman mapping to investigate cells [16, 17] and biological tissues in the bronchus [18], breast [19] and brain [20]. Raman mapping has also been used for pharmaceutical [21–23], materials [24, 25] and geological applications [26]. However, the long overall mapping times have limited the size of the datasets which can be acquired and consequently the biochemical information which can be gleaned using multivariate analysis. Furthermore, long overall mapping times have hindered the progression of the technique into the clinical environment.

1.3. Raman mapping

Details of Raman mapping techniques can be found in the following reference [27]. A brief overview of point and line mapping techniques is provided to illustrate the rapid mapping technique in context.

During point spectral mapping (Figure 1a), a point spectrum is acquired using effectively the entire length (actually the edges are removed to reduce noise) of the charged couple device detector (CCD) with the collection pixels region spanning the width of the laser line to maximise the collected signal. The rest of the CCD is not read out to minimise dark current readout noise and readout time. The sample is stepped along to the next position using an XY translational stage and the next spectrum is acquired and so on until a grid of spectra is obtained, often referred to as a spectral data cube. The overall mapping time is often limited by the acquisition time (per spectrum) when measuring tissue samples since they are not strong scatterers. The acquisition time may be of the order of 1–30 s depending on the tissue type and even as long as 120 s when measuring single cells [16]. Typically the total mapping time is roughly equal to the total number of spectra multiplied by the acquisition time. Additionally, there is a stage translation delay and CCD readout time delay for each of the spectra. This is of the order of 1.6 s (combined CCD readout and stage translation, calculated from a 0.1 s acquisition point map using a Renishaw system 1000 – see methods section for details). For shorter acquisition times, the speed of the XY translational stage and, often most significantly, the readout time of the CCD can significantly limit the rate at which spectra can be acquired. Furthermore, factors such as extended scanning and auto-focusing reduce the rate of spectral acquisition. In one study, Krafft et al. reported an acquisition rate of

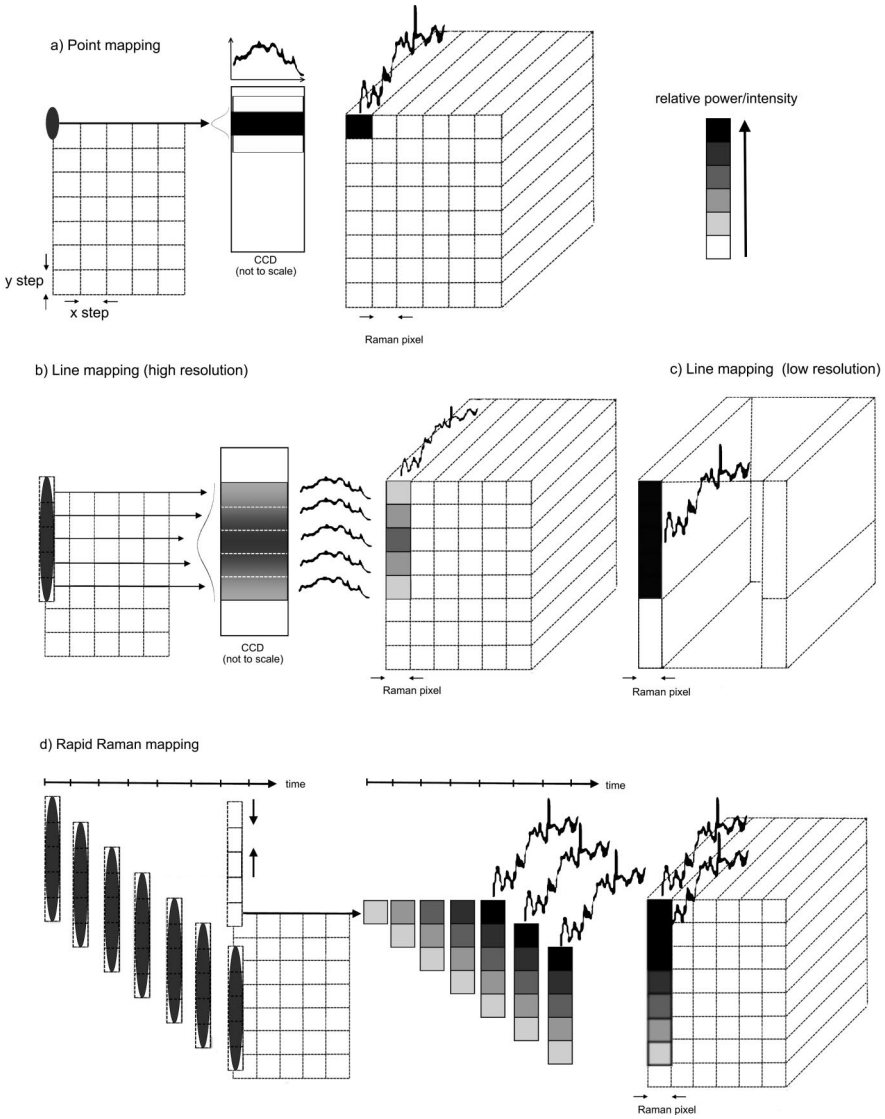

Figure 1 a) Illustration of traditional point Raman mapping in which a spectrum is acquired at each position on a grid, b) High spatial resolution line mapping using a barrel lens to produce a line focused laser. Many spectra are acquired simultaneously by separating out the lines on the CCD, c) Low spatial resolution line mapping in which the entire laser line is used to sample a large area of the sample utilising vertical binning of the CCD pixels and d) Illustration of rapid Raman mapping in which the CCD readout is synchronized with the movement of the stage to allow constant readout of Raman spectra thus reducing dead time between spectra. Note that relative intensity/power colour coding is for demonstrative purposes only and is not quantitative.

only 30 spectra per hour based on an acquisition time of 30 s whilst using autofocus during the mapping of brain tissue [28].

A development of point mapping was the introduction of a cylindrical lens to create a line-focused laser, often referred to as line mapping. A line focused laser can be used in two different ways as illustrated in Figure 1b and c. First, line mapping can achieve spatial separation of the laser line using the CCD pixels, resulting in an increased spatial resolution as illustrated in Figure 1b. This is achieved by reading out each CCD line separately creating multiple spectra, the trade off being a reduction in the signal of each spectrum since only a portion of the laser light is used to illuminate the area of the tissue imaged by that CCD pixel. A further drawback is that since the power varies along the length ($\sim$50 µm for the $\times$50 objective used in this study) of the laser line (approximately Gaussian) this method of line mapping results in a variation in the intensity of the spectra along the laser line as illustrated in Figure 2a and c. Consequently, there is a variation in the signal to noise ratio (SNR) as illustrated in Figure 2b. A correction can be performed, but this can be unreliable for inhomogeneous samples such as biological tissue. One further consequence of this correction process is that noise will be magnified at the edges of the line focused laser. As shown in Figure 2b, the SNR at the edges of the line-focused laser is less, therefore correction would result in the non-uniform magnification of the noise along the laser profile.

The second method for line mapping is to utilise the expanded laser line to sample the mapped region in fewer steps (Figure 1c). In this case, an increased signal to noise is achieved compared to the high resolution line-focused mapping (since the entire laser line is used to generate each spectrum), but the trade off is reduced spatial resolution.

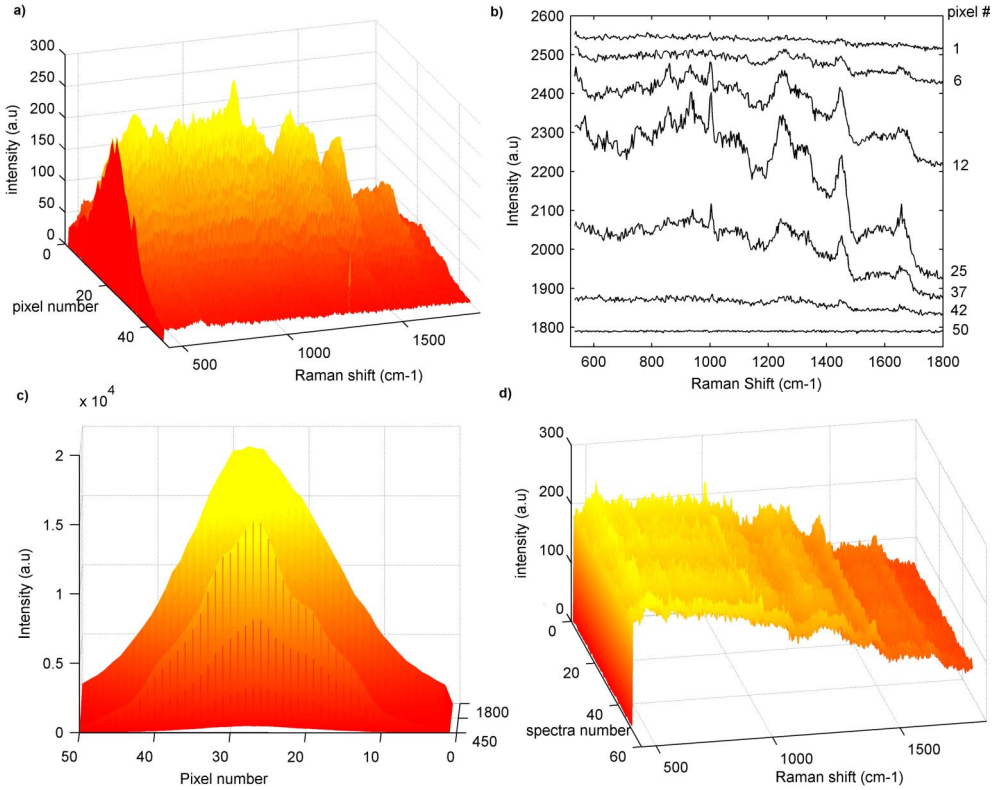

Figure 2 a) (online colour at: www.biophotonics-journal.org) Variation in intensity along laser line of a line focused laser beam (left axis is 1 μm step size along the sample and right axis is Raman shift 450–1850 cm^{-1}) measured on oesophageal tissue, b) Example oesophageal tissue spectra from the line focused line map illustrating the variation in SNR along the laser line (CCD pixels), c) Variation in signal intensity (at 520 cm^{-1} peak) along the line focused laser line (for line mapping) measured on a piece of silicon, d) Example spectra at 1.1 μm step size acquired using the rapid Raman mapping system on the same region of tissue as plots a and b, with the spectra number equivalent to one pixel in plots a–c.

Line mapping is still limited by CCD readout (especially for short acquisition times), although this is reduced when portions of the laser line read out independently for higher spatial resolution since the readout time is spread over multiple spectra. These two techniques were rigorously compared, along with wide field imaging concluding that depending on the application, line mapping was faster that point mapping [29].

Rapid mapping systems have been developed by several manufacturers including WITec (Ulm, Germany) and Renishaw. This paper focuses on Renishaw StreamLine, although the concepts discussed can potentially be applied to any imaging system capable of rapidly acquiring large Raman datasets. Considering StreamLine technology (Figure 1d), the sample is stepped along the laser line and the position of the stage is synchronised with the readout of the CCD (as illustrated in Figure 1b). Each spectrum is effectively made up of an accumulation of spectra as the entire laser line passes over each part of the sample. There is a short delay at the beginning of each column in the grid as the laser line passes over the first pixel and then following spectra are acquired at an increased rate. This enables high spatial resolution mapping without the Gaussian profile intensity trade off (associated with line mapping) and consequently eliminates the variation in SNR due to the laser profile, as illustrated in Figure 2d. There is still however a reduction in signal intensity and SNR compared to point mapping using the entire laser line. A further advantage is that constant readout (i.e. reduced dead time between sequential data points compared to point mapping) of spectral data results in the acquisition of spectra and maps at an increased rate. This uses the multichannel advantage of the CCD in two dimensions simultaneously. These advances have facilitated the acquisition of thousands of spectra within a matter of minutes compared to previous mapping techniques which took hours and even days. A previous study by our group evaluated rapid Raman mapping for spectroscopic analysis of oesophageal tissue by varying mapping parameters [30]. Bernard et al. have also investigated the use of rapid Raman mapping (referred to as advanced line-scanning) for geological applica-

tions, including a comparison with line mapping (static line scanning) [26].

1.4. Data analysis

Principal component analysis (PCA) has been applied by many groups as a spectroscopic image processing technique for both Raman and FT-IR applications [14, 16, 31]. Other techniques for vibrational imaging such as k-means [19, 28, 32], hierarchal cluster analysis (HCA) [17], and artificial neural networks (ANN) [33] have been applied to biological tissue. For further details on multivariate techniques for image analysis of Raman datasets, the reader is referred to the following references [34, 35].

Hayden et al. investigated the effects of sampling parameters for Raman line images using PCA, demonstrating that improved results were obtained using the higher magnification, concluding that this was due to an increased dataset size [31]. Work has also been carried out elsewhere to investigate the effects of reducing the acquisition time (from 30 s to 3 s) with Raman mapping of pharmaceutical beads analysed using principal component analysis as a pre-processing noise reduction method [21]. In this and a previous study [22], Sasic et al. used the relative standard deviation (RSD) to compare maps with varying degrees of noise within the raw spectra, but the effect of varying the size of the dataset was not considered. Since the performance of multivariate techniques improves with increased dataset size, the number of spectra within a map is an important variable to consider and this is the first paper to investigate the effects of this with Raman mapping. Krafft et al. also demonstrated that PCA could be used to evaluate low SNR data acquired from mapping single cells [16]. However, the focus of this paper was on the recovery of biochemical information rather than the implications of reducing the total mapping time. To date, little work has been carried out to investigate the effect of reducing the total mapping time on the data obtained from biological tissue samples.

It is well known that larger datasets improve the performance of multivariate techniques, and in particular PCA can be used to remove noise from large Raman datasets [35]. Subsequently it was hypothesised that using PCA sufficient diagnostic information, for screening out non-relevant samples, could be extracted from low SNR spectra providing that the dataset was sufficiently large. Therefore the SNR was monitored for a range of maps methodically acquired with various combinations of acquisition time and spatial resolution parameters (step size). This paper presents the results of this investigation and attempts to demonstrate that the total mapping time for oesophageal biopsies can potentially be reduced to a clinically practicable timescale.

This is the first paper reporting rapid Raman mapping of biological tissue. Raman maps containing larger numbers of spectra (100 000+ spectra) of biological tissue are presented. There is only one paper in the literature reporting Raman mapping of oesophageal tissue [14], in which maps contained approximately 2000 spectra, therefore, this paper presents a significant improvement over map size and image quality (total number of spectra and spatial resolution) due to an increase in the size of the spectral dataset. In combination with principal component analysis, this enables the elucidation of pathology dependent biochemical information. This is also the first paper to demonstrate that Raman mapping times for biopsies has reduced sufficiently to enable the technique to be used as a histological screening tool.

2. Experimental

2.1. Sample collection and preparation

Informed consent was obtained from patients undergoing routine upper gastrointestinal endoscopic surveillance of Barrett's oesophagus. Ethical approval for this study was obtained from Gloucestershire Local Ethics Committee. In this study, three samples from three different patients have been mapped.

Tissue samples were snap frozen in liquid nitrogen. A 20 μm frozen section was cut onto a calcium fluoride substrate for Raman spectral mapping. The thickness of the mapping section was chosen to maximise Raman scattered photons from the tissue section. A contiguous 7 μm section was obtained and stained with H&E for diagnosis by an expert gastrointestinal registry pathologist (Prof. Neil Shepherd). Due to the heterogeneous nature of the samples the pathologist annotated each sample with the various pathologies, classifying the regions as normal squamous, Barrett's, low grade dysplasia (LGD), high grade dysplasia (HGD) and adenocarcinoma. Inflammation, connective tissue (smooth muscle and fibrous tissue), oesophageal glands and ducts were also identified. Biopsy samples are typically 1–2 mm in diameter.

2.2. Raman spectral measurement

Typically, the core of the StreamLine instrument is a Renishaw inVia Raman microscope, although in these experiments the maps were acquired using a customised Renishaw Raman System 1000 spec-

Table 1 Summary of mapping parameters for repeated maps. Maps A–D are for a constant step size of 25.3 μm, maps E–H are for a constant step size of 7.4 μm, maps C, I, J and F are for a constant acquisition time of 1.7 s. Overall mapping times are shown along with estimated mapping times for traditional point mapping (only applicable to the Renishaw system).

Map ID	Step size (μm)	Acquisition time (s)	Total number of spectra	Total mapping time (h)	
				Rapid mapping (actual)	Point mapping (estimated)
A	25.3	0.1	0.9×10^4	0.1	4.2
B	25.3	0.5	0.9×10^4	0.5	4.7
C	25.3	1.7	0.9×10^4	1.5	6.5
D	25.3	20	0.9×10^4	17	29.0
E	7.4	0.5	10×10^4	2.0	49.6
F	7.4	1.7	10×10^4	6.3	55.2
G	7.4	3.0	10×10^4	11	60.4
H	7.4	5.0	10×10^4	19	70.8
C	25.3	1.7	0.9×10^4	1.5	6.5
I	15.8	1.7	2×10^4	2.8	13.9
J	10.6	1.7	5×10^4	4.0	27.3
F	7.4	1.7	10×10^4	6.3	55.2

trometer coupled to a microscope fitted with a Leica ×50 long working distance objective (NA 0.5). A diode laser with a wavelength of 830 nm was used with 70 mW at the sample (270 mW at source). A grating with 300 lines/mm was used to disperse the scattered light which was measured with a deep depletion charged couple device (CCD) detector.

Repeated maps were carried out on tissue sections, methodically varying the spectral acquisition time and step size. There are several variables to take into consideration – for a constant area map, a higher resolution map (i.e. smaller step size) results in a larger number of spectra compared to a lower resolution map (i.e. larger step size) of the same area. The total number of spectra is an important consideration since the size of the dataset has an impact on the reliability of any multivariate analysis used. However, for a lower spatial resolution map the total number of spectra is reduced, thus the acquisition time can be increased to obtain higher quality spectra in the same overall time scale. The quality of the spectral dataset is also an important factor when attempting to identify subtle biochemical changes using multivariate techniques.

Acquisition times ranged from 0.1–20 s as summarised in Table 1. For each acquisition time, the step size was also varied between 7.4–25.3 μm. The total mapping time was limited to a maximum of 24 h since longer maps were not practicable. The total number of spectra in each map varied between 0.9×10^4 and 10×10^4. The approximate mapping time using standard point mapping (using the Renishaw system) was calculated based on a CCD readout and XY translation delay of 1.65 s per spectrum (1.2 s per step reported by Schlucker et al. [29]). This value was determined by running a map (traditional point map mode) with an acquisition time of 0.1 s, step size of 6 μm and calculating the delay according to actual map time minus the best case scenario map time (i.e. number of spectra multiplied by the acquisition time) and dividing this by the total number of spectra in the map. To account for the difference in Raman signal intensity for the rapid Raman spectra compared to point mapping (which varies with step size, in a similar manner to line mapping), the acquisition time used in the estimate of the overall point mapping time was scaled by a factor equal to the step-size divided by the length of the laser line. In-

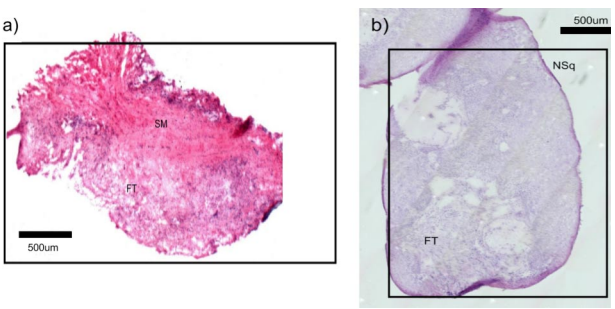

Figure 3 (online colour at: www.biophotonics-journal.org) Annotated H&E (restained) section of the contiguous section to the frozen section used in the repeated mapping studies a) Maps A–J – sample containing areas of smooth muscle (SM) and fibrous connective tissue (FT) are identified and b) Maps I–V – sample containing circumferential normal squamous epithelium (Nsq) and fibrous connective tissue (FT).

Table 2 Maps I–V are repeated maps of the sample with parameters adjusted to maintain a constant total mapping time of 4.5 h. Overall mapping times are shown along with estimated mapping time for traditional point mapping.

Map ID	Step size (μm)	Acquisition time (s)	Total number of spectra	Total mapping time (h)	
				Rapid mapping	Point mapping
I	9.5	2.4	4×10^4	4.5	23.6
II	12.7	3.0	2×10^4	4.5	15.7
III	19.0	4.7	1×10^4	4.5	9.6
IV	25.3	8.2	0.6×10^4	4.5	9.1
V	31.7	9.0	0.4×10^4	4.5	7.4

cluding this scaling factor ensured that the advantage of rapid Raman mapping was not overestimated.

Signal to noise (SNR) measurements were carried out on spectra measured on a relatively homogeneous tissue sample containing connective tissue and smooth muscle as diagnosed by an expert pathologist (Figure 3). Further SNR and relative standard deviation (RSD) measurements were made using a sample containing circumferential normal squamous epithelium. To determine the optimum mapping parameters, the step size (and thus total number of spectra) was varied from 9.5–31.7 μm whilst optimizing the acquisition time to maintain a constant total mapping time of 4.5 h (as detailed in Table 2).

2.3. *Data analysis*

Data analysis was carried out using Matlab and the PLS toolbox (Eigenvector Technologies, Manson, Washington, USA). Saturated spectra and cosmic rays were removed by replacement with the nearest neighbour. Principal components (PCs) were calculated and pseudocolour PC score maps were generated. Any remaining cosmic rays appearing in the score maps were blanked out and the PCs recalculated so as not to distort the loads. The relative standard deviation (RSD) (the ratio between the standard deviation and the mean at a given peak position [21]) measured at the 1000 cm^{-1} phenylalanine peak, expressed as a percentage, was used as a measure of the SNR to enable comparison between the different maps. This technique was adopted since the SNR of the raw spectra was low making it difficult to determine accurately. The focus of the laser causes variation in the spectral intensity and SNR at the edge of the sample and in areas where the calcium fluoride substrate has been measured. To overcome this, a region $1/16^{th}$ of the total map area was selected over the region of connective tissue for the RSD measurements. The area was kept constant for all maps to enable direct comparison. The RSD calculations were performed on normalised data to give an indication of SNR variation only. Spectra with saturations and cosmic rays were not included in the RSD calculations. Although not directly attributable to the acquired spectra, the 'signal to noise ratio' ('SNR') of the principal component loads was also calculated at the 932 cm^{-1} peak (the strongest peak in the 5^{th} PC load) to provide a relative comparison between the loadings for the different mapping parameters. This was done for the fifth principal component only. The fifth PC was chosen since the pseudocolour score map provided good correlation with the morphology of the H&E sections which was underpinned by good correlation biochemically with the PC load.

3. Results and discussion

Figure 3 shows the H&E stained section, contiguous to the sample used in maps A–J, illustrating regions of fibrous connective tissue (FT) and smooth muscle (SM). The contiguous section to the sample used in maps I–V is also shown illustrating circumferential normal squamous (NSq) and fibrous connective tissue.

3.1. *Signal to noise variation in repeated maps*

Figure 4 shows pseudocolour score maps (PC5 for maps B–D, F–H and PC9 for maps A and E). Maps A–D were measured with varying acquisition time whilst maintaining a constant mapped area and step size of 25.3 μm. Maps E–H show each of the various acquisition times whilst maintaining a constant mapped area and a step size of 7.4 μm. Maps C, I, J and F (Figure 5) show maps acquired with a constant acquisition time of 1.7 s with various step sizes. The fifth PC load (PC9 for map A and E) exhibits opposing positive and negative peaks consistent with the difference between actin and collagen spectra, which is consistent with the biochemical signatures of smooth muscle and connective tissue respectively,

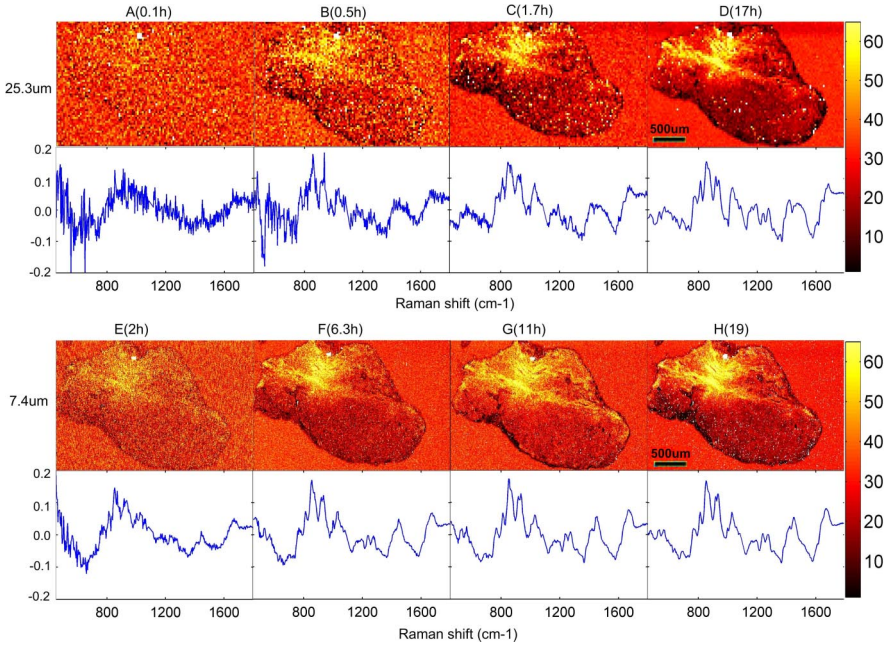

Figure 4 (online colour at: www.biophotonics-journal.org) Fifth principal component pseudo-colour score map and corresponding principal component load (Maps A and E display ninth PC). Maps A–D are for a constant step size of 25.3 μm with increasing acquisition time from left to right of 0.1, 0.5, 1.7 and 20.0 s. The total mapping time is shown in brackets for comparison. Maps E-H are repeated maps using a step size of 7.4 μm with increasing acquisition time from left to right of 0.5, 1.7, 3 and 5 s.

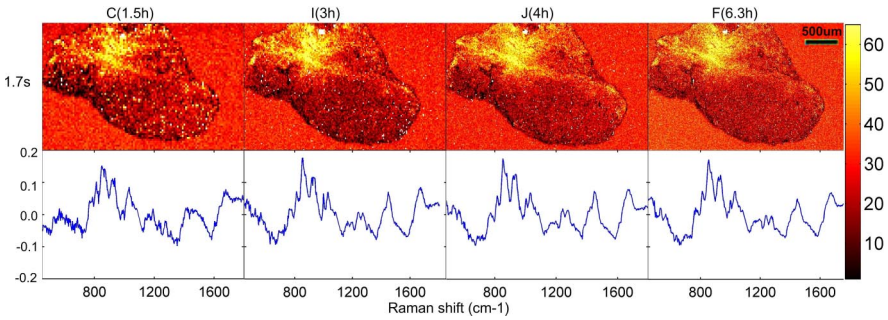

Figure 5 (online colour at: www.biophotonics-journal.org) Fifth principal component pseudo-colour score map and corresponding principal component load for maps C, I, J and F all with a constant acquisition time of 1.7 s with decreasing step size (thus increasing total number of spectra) from left to right of 25.3, 15.8, 10.6 and 7.4 μm.

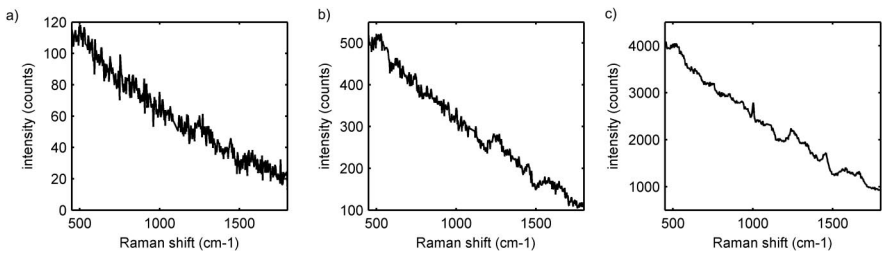

Figure 6 Typical raw spectra with an acquisition time of a) 0.5 s, b) 1.7 s and c) 20.0 s taken from map B, C and D respectively.

which is consistent with pathology identified in the H&E sections (see online supporting evidence S1). For maps A and E, PC 9 exhibited the same morphological appearance and similar loads and as a consequence were used instead of PC 5. PCs 1–4 (scores and loads not shown, but available online with the supporting evidence S2) describe the difference between tissue and calcium fluoride substrate, small regions of luminescence, and protein distribution. Fibrous connective tissue and smooth muscle are in fact very similar biochemically and as a result this was a good test of detecting very subtle biochemical changes. Further biochemical analysis will be published elsewhere but it is evident that it is possible to detect gross biochemical changes.

Figure 6 shows typical raw spectra from maps with acquisition times of 0.5 s, 1.7 s and 20 s exhibiting the quality of the raw spectra within the maps. The values for the RSD of the raw spectra calculated at the peak at 1000 cm^{-1} are shown in Table 3. They clearly demonstrate that the RSD reduces with increasing acquisition time as expected. For Map D, an RSD value of 2 was considered as a benchmark since the 20 s acquisition time provided a reasonable

Table 3 Summary of the RSD for normalised spectra (one 16th of the total mapped area) within each map measured at the 1000 cm^{-1} peak and 'SNR' for the fifth principal component loading (PC9 for maps A and E) measured at the 932 cm^{-1} peak. Total mapping time (in hours) is shown in brackets next to the map ID for comparison.

Map ID	RSD (normalised data)	PC (5th) load 'SNR'
A (0.1 h)	16	<2
B (0.5 h)	7	4
C (1.5 h)	4	12
D (17 h)	2	>50
E (2 h)	11	8
F (6.3 h)	6	44
G (11 h)	5	>50
H (19 h)	4	>50
C (1.5 h)	4	12
I (2.8 h)	4	14
J (4 h)	5	28
F (6.3 h)	6	44
I (4.5 h)	6	8
II (4.5 h)	5	10
III (4.5 h)	4	10
IV (4.5 h)	4	8
V (4.5 h)	4	11

SNR and RSD results are not comparable between maps A–J and I–V due to different samples and corresponding PC loads.

SNR of the raw spectra. The relative 'SNR' values measured at the 932 cm^{-1} peak of the principal component loads are also shown in Table 3. The corresponding 'SNR' for PC 5 load of map D was also high (>50) as expected. Similarly high 'SNR' values for the loads were achieved with shorter acquisition times provided the total number of spectra was large enough. As expected the relative 'SNR' of the loadings also increased with increasing number of total spectra with maps C, I, J and F. with the 'SNR' increasing from 12 to 44.

Figure 7 shows maps acquired with a constant mapping time of 4.5 h. From left to right, maps I–V were acquired with increasing acquisition time and step size detailed in Table 2. There is good correlation with the pathology indicated on the H&E section with circumferential normal squamous identified by the negative peaks of the 5th PC load. Visually, the degradation in the spatial resolution is evident whilst there is little difference between the PC loads. The RSD and 'SNR' results are shown in Table 3, which demonstrates a slight decrease in the RSD as the acquisition time and step size are increased. This was mirrored for the previous set of maps (C, I, J and F), all acquired with an acquisition time of 1.7 s, illustrating that this increase in RSD is not linked to the reduction in spectral acquisition time, but more likely due to the number of spectra contained in the area sampled for the RSD calculation. The 'SNR' of the loads remains approximately constant. It should be noted that the 'SNR' values are not directly comparable with maps A–J since they have been measured on different samples obtained from two patients.

3.2. Comparison with point mapping

The ratio of the estimated point map time and overall mapping time for the rapid Raman maps, for various mapping parameters, is shown in Table 4. This illustrates the large reduction in mapping time achievable with rapid Raman mapping when compared to point mapping using a standard Renishaw Raman spectrometer.

3.3. Discussion

There is a clear advantage of increasing the number of spectra within the map in terms of the performance of multivariate techniques. In this study, larger datasets were achieved by increasing the spatial resolution but this would also be achieved by mapping a larger sample at lower spatial resolution. Fac-

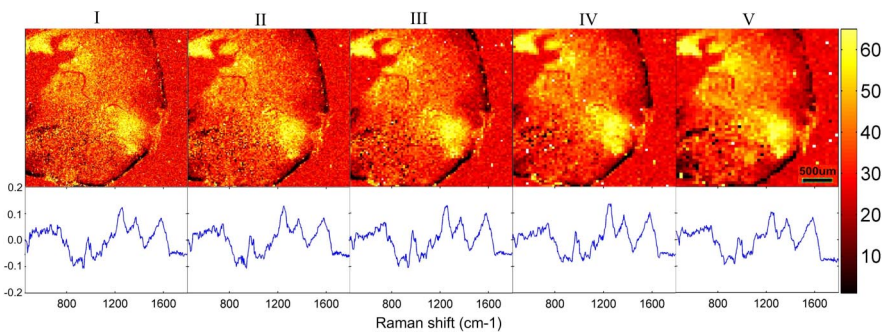

Figure 7 (online colour at: www.biophotonics-journal.org) Fifth principal component pseudo-colour score map and corresponding principal component load for maps I–V (left to right) all acquired with parameters adjusted to give a total mapping time of 4.5 h. See Table 2 for parameter details.

Table 4 Summary of mapping parameters and comparison of total mapping times with traditional point mapping times indicated by the ratio of the estimated total map time using the point mapping technique (Renishaw system) and the total map time using the rapid mapping technique.

Map ID	Acquisition time (s)	Ratio (estimated point map time/ actual rapid map time)
A	0.1	37.1
B	0.5	10.4
C	1.7	4.2
D	20.0	1.7
E	0.5	25.0
F	1.7	8.8
G	3.0	5.4
H	5.0	3.7
Map ID	**Step size (μm)**	**Ratio (estimated point map time/ actual rapid map time)**
C	25.3	4.2
I	15.8	5.0
J	10.6	6.9
F	7.4	8.8
I	9.5	5.1
II	12.7	3.5
III	19.0	2.1
IV	25.3	2.0
V	31.7	1.6

tors limiting the size of the dataset include the 32-bit operating system addressable memory restriction and Matlab's requirement for the entire matrix to be held in a contiguous block. In the case of this study, memory restrictions limited the spatial resolution achievable for mapping the entire biopsy sample since smaller step sizes would have generated excessively large datasets (mapping the sample shown in Figures 3, 4 with 1.1 μm step size would result in excess of 5×10^6 spectra).

3.4. Relative standard deviation (RSD) and signal to noise ratio (SNR) variation

From Figures 4 and 5, for all maps shown except A and E, it is evident that the fifth PC load represents similar tissue features (in this example tentatively attributed to collagen which is abundant in fibrous connective tissue and actin which is abundant in smooth muscle – see supporting evidence S1) in each of the repeated maps despite the variation in the number of spectra and acquisition time. For map A, noise dominated the ninth principal component load, although tissue peaks can be approximated. Considering map E, these spectral features appeared further down the PC loads at the 9th PC component.

For all maps except for D, for which an acquisition time of 20 s was used, the SNR of the raw spectra was very low (results not tabulated). Therefore the RSD measure was used to allow comparison. Ideally a high SNR would be desirable to ensure that subtle biochemical changes are detected but from these results it is evident that PCA is powerful enough to extract gross biochemical information even with a very low SNR. The RSD calculations on the normalised data (Table 3) illustrate the reduction in noise with increased acquisition time. The lowest RSD, as expected, was for the longest acquisition time of 20 s for map D. In general, this was mirrored on the raw data without normalisation (results not shown), although RSD values tended to be higher than expected for larger maps indicating a larger variance, likely to be caused by the presence of luminescent spectra and cosmic rays highlighting the difficulty in 'cleaning up' large datasets. This could also be caused by focusing issues across the sample area.

The relative 'SNR' values calculated for the PC loadings showed improved performance with longer acquisition times, in particular in the case of maps D and H for which the apparent noise was negligible with respect to the 932 cm^{-1} peak within the load.

As expected, the relative 'SNR' of the loadings also increased with increasing number of total spectra with maps C, I, J and F. An additional advantage of improved resolution is improved recognition of morphological features, which will make this technique more acceptable to the histopathologist.

When considering the maps acquired with a constant mapping time of 4.5 h (Maps I–V) it is evident that there is little difference regarding the loads but increased spatial resolution would be beneficial. The advantage afforded by rapid Raman mapping is also greater for higher resolution maps. Increased spatial resolution would also reduce the effects of undersampling and the possibility of missing crucial biochemical information. This would have little consequence for the samples in this study, but may become clinically significant for a sample containing a focus of disease.

The section shown in Figure 3 was initially thought to contain a region of inflammation or possibly adenocarcinoma to the bottom left, but this was inconclusive due to very poor uptake of the H&E stain with the frozen section. Following rapid Raman mapping, in which there was no evidence of a region of adenocarcinoma, this section was re-stained to obtain definitive diagnosis and found to only contain smooth muscle and fibrous tissue. This highlights a

further potential advantage of spectroscopic diagnosis which could enable diagnosis of inconclusive sections based on distinguishing biochemical features.

3.5. Comparison with point mapping

From Table 4 it is evident that rapid Raman mapping is significantly faster than traditional point mapping (from the same manufacturer). As expected there is a correlation between the step size and the speed of the map acquisition and thus the total mapping time. For a step size of 25.3 μm (maps A to D) rapid Raman mapping was approximately 3 times faster than point mapping for long acquisition times and up to 37 times faster for short acquisition times. Data published previously [30] was based on best case scenario point mapping times which significantly underestimated overall mapping times for short acquisition times. With a step size of 7.4 μm (maps E to H) rapid Raman mapping was of the order of 4 times faster than point mapping for longer acquisition times (5 s) and 25 times faster for short acquisition times (0.5 s). Due to the large number of spectra within the dataset the advantage of rapid acquisition of spectra is accentuated. Bernard et al. reported a similar reduction in overall mapping time (13 times faster, although maps were not acquired with the same acquisition times or step size) compared to traditional line mapping [26].

3.6. Future work

One option, not considered in this paper, is the potential to mismatch x and y step sizes to prevent under-sampling when using step sizes greater than the width of the laser line (~7 μm for the ×50 objective used in these experiments). This is an area which will need further investigation before optimum mapping protocols can be determined. Further work must also be carried out to investigate the potential problems associated with undersampling with regards to missing diagnostically significant information. The step size in this study has not be reduced beyond that of the width of the laser line (~7 μm for the ×50 objective used in this study) due to size limitations on the datasets and also to prevent oversampling but this is also an area for further investigation since this may provide further benefits with regards to increased spatial resolution and even larger datasets. This may be of particular interest when mapping cells at high resolution and leads to the possibility that biochemical changes within the tissue can now be investigated at the cellular level across larger areas of tissue. One consequence of this would be the need for improvement in computational facilities. The use of 64-bit computers has increased the datasets that can be managed since this work was undertaken.

There is also potential to investigate noise reduction techniques and smoothing of the spectral data such as those described by Sasic et al. [21].

Potential sample degradation has previously limited the maximum laser power that can be used with biological tissue samples. However with reduced acquisition times there is the potential to increase the laser power and thus improve the signal to noise.

Before an automated screening technique can be developed, further work is also required to develop automated algorithms capable of identifying 'non-relevant' samples so that only diseased samples are forwarded for diagnosis by an expert histopathologist. It will also be beneficial to reduce the thickness of the mapped tissue sections towards the thickness used for H&E histopathology (7 μm), although potentially longer acquisition times may be required to counteract the reduction in Raman scattered photons with the thinner tissue section.

Each map contains a vast amount of biochemical detail and work is ongoing to explore information regarding the carcinogenesis process.

4. Conclusion

Rapid Raman mapping has enabled frozen tissue sections to be mapped on a clinically practicable timescale. The combination of large spectral datasets (generated by rapid Raman mapping) with multivariate analysis provides a powerful method of analysing tissue sections. The frozen tissue samples do not require preparation with histological stains, providing a significant advantage over current techniques. Frozen samples can be stored and subsequently stained if required. Furthermore, the process lends itself to automation using computed algorithms which removes the subjective element of histological diagnosis. Potentially a rapid pre-scan could be carried out at relatively low resolution with low SNR. Subsequent detailed high quality maps can then be acquired on regions of interest. In combination with multivariate classification models, there is the potential for the automated screening out of non-relevant samples, with those deemed as abnormal going on for diagnosis by an expert histopathologist. Consequently this would reduce the burden of 'non-relevant' samples which currently swamp the system and allow more time for analysis of the critically diseased samples.

A large amount of work will be needed to develop a comprehensive database of biochemical information before Raman mapping can be used in

the clinical environment. Also the progression to supervised multivariate classification may require further evaluation and Bhargava has demonstrated that there was a relation between the SNR of IR absorption spectra and classification accuracy, although a combination of univariate and multivariate techniques were used as an alternative to PCA [36]. Rapid Raman mapping provides a method of acquiring such data which will enable verification of this technique on a timescale that was previously not possible. Raman spectral mapping has historically been significantly slower than the complimentary technique of IR absorption spectroscopy and a rigorous comparison of the two techniques is now required.

Acknowledgements The authors would like to thank Geraint Evans, Tim Smith and Ian Bell of Renishaw for their support of this work, Christine Braun and Jo Motte for their assistance with sample preparation. Financial support from Institute of Physics and Engineering in Medicine (IPEM) Research Training Fellowship, Royal Society Dorothy Hodgkin Research Fellowship and National Institute of Health Research Career Scientist Fellowship.

Joanne Hutchings received her BSc. degree in Physics with Medical Physics from University of Wales, Cardiff in 2002 and her Masters degree in Medical Radiation Physics from University of Wales, Swansea in 2005. She is in the final stages of a PhD (Cranfield University) based in the Biophotonics Research Group in Gloucestershire Hospitals NHS Foundation Trust researching optical diagnostic techniques as part of a Research Training Fellowship funded by the Institute of Physics and Engineering in Medicine.

Catherine Kendall studied physics in Bristol and Bordeaux. She trained as a medical physicist, undertaking clinical placements and obtained her Masters degree from the University of Exeter. In 2002 she received her PhD from Cranfield University investigating the application of Raman spectroscopy to oesophageal cancer diagnosis. Dr. Kendall is now a Royal Society Dorothy Hodgkin Fellow at Cranfield University, based in the Biophotonics Research Group, Gloucestershire Hospitals NHS Foundation Trust.

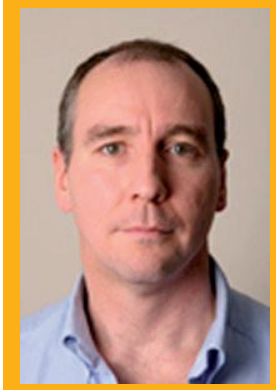

Brian Smith received his BSc (Theoretical physics) and PhD (Raman spectroscopy) from the University of London. Following postdoc at Queen Mary College materials department and CCD camera software development at Wright Instruments he moved to Renishaw to develop Raman spectroscopy instrumentation and applications. Dr. Smith is now design manager of the Spectroscopy Products Division with interests in many areas related to Raman spectroscopy.

Neil Shepherd is a Consultant Histopathologist within the Gloucestershire Hospitals NHS Foundation Trust. He qualified from St. Bartholomew's Hospital, London and trained in pathology at St. Bartholomew's and St. Mark's Hospitals, London. Professor Shepherd has clinical and research interests in gastrointestinal (GI) pathology. He has written 5 books, over 30 chapters and more than 150 original articles and reviews. He holds an Honorary Clinical Professorship at the University of Cranfield.

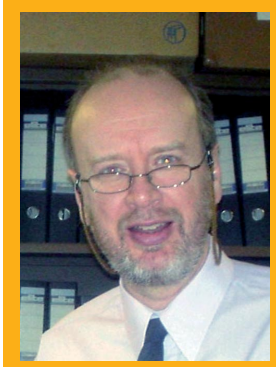

Hugh Barr is a Consultant Upper Gastrointestinal Surgeon. His specialist interests include Barrett's oesophagus, endoscopic mucosal resection, photodynamic therapy, laser therapy and oesophagus gastric cancer. Professor Barr is the foundation Dean of the Faculty of Medicine and Bioscience, Cranfield University and the local lead clinician for the National Cancer Research Network. He has led the clinical consortium developing this work and holds a patent. He has published over 100 papers and 25 book chapters.

Nicholas Stone is a Consultant Clinical Scientist and Heads up the Biophotonics Research Unit at Gloucestershire Hospitals NHS Foundation Trust. He initially trained as a Medical Physicist, including a couple of Masters degrees, finally obtaining a PhD in Tissue spectroscopy from Cranfield University in 2001. He recently received a Health Executive MBA from Keele University and this helps with product commercialization aspects of his role. Dr. Stone is dedicated to pioneering the translation of novel optical technologies to the clinic to enhance timely diagnosis of early treatable disease (especially cancers).

References

[1] J. Lagergren, R. Bergstrom, A. Lindgren, and O. Nyren, N Engl. J. Med. **340**, 825 (1999).
[2] R. Haggitt, Human Pathology **25**(10), 982 (1994).
[3] C. Kendall, N. Stone, N. Shepherd, K. Geboes, B. Warren, R. Bennett, and H. Barr, J. Pathol. **200**, 602 (2003).
[4] A. Robichaux-Viehoever, E. Kanter, H. Shappell, D. Billheimer, H. Jones III, and A. Mahadevan-Jansen, Appl. Spectrosc. **61**, 986 (2007).
[5] F. Lyng, E. O. Faolain, J. Conroy, A. Meade, P. Knief, B. Duffy, M. B. Hunter, J. M. Byrne, P. Kelehan, and H. J. Byrne, Experimental and Molecular Pathology **82**, 121–129 (2007).
[6] K. K. Kumar, A. Anand, M. V. P. Chowdary, Keerthi, J. Kurien, C. Murali Krishna, and S. Mathew, Vib. Spectrosc. 44, 382 (2007).
[7] B. Brozek-Pluska I. Placek, K. Kurczewski, Z. Morawiec, M. Tazbir, and H. Abramczyk, Journal of Molecular Liquids **141**, 145 (2008).
[8] A. S. Haka, K. E. Shafer-Peltier, M. Fitzmaurice, J. Crowe, R. R. Dasari, and M. S. Feld, Cancer Research **62**, 5375 (2002).
[9] J. Taylor, C. Kendall, N. Stone, and T. Cook. British Journal of Surgery, **94**, 6 (2007).
[10] K. Das, N. Stone, C. Kendall, C. Fowler, and J. Christie-Brown, Lasers Med. Sci. **21**, 192 (2006).
[11] M. Schaeberle, V. Kalasinsky, J. Luke, E. Lewis, J. Levin, and P. Treado, Anal. Chem. **68**, 1829 (1996).
[12] N. Stone, C. Kendall, and H. Barr, Raman spectroscopy as a potential tool for early diagnosis of malignancies in esophageal and bladder tissue, in: Applications of Vibrational Spectroscopy in Medical Diagnosis, edited by M. Diem, P. Griffiths, and J. Chalmers (Wiley, 2008), pp. 203–230.
[13] N. Stone, M. Hart Prieto, C. Kendall, G. Shetty, and H. Barr, Proc. SPIE **6093**, Article number 60930U (2006).
[14] G. Shetty, C. Kendall, N. Shepherd, N. Stone, and H. Barr, BJC **200**, 602 (2006).
[15] N. Stone, M. Hart Prieto, P. Crow, J. Uff, and A. Ritchie, Analytical and Bioanalytical Chemistry **387**, 1657 (2007).
[16] C. Krafft, T. Knetschke, A. Siegner, R. Funk, and R. Salzer, Vib. Spectrosc. **32**, 75 (2003).
[17] C. Matthaus, T. Chernenko, J. A. Newmark, C. M. Warner, and M. Diem, Biophysical Journal **93**, 668 (2007).
[18] S. Koljenovic, T. Bakker Schut, J. van Meerbeeck, A. Maat, S. Burgers, P. Zondervan, J. Kros, and G. Puppels, Journal of Biomedical Optics **9**, 1187 (2004).
[19] J. Kneipp, T. Bakker Schut, M. Kliffen, M. Menke-Pluijmers, and G. Puppels, Vib. Spectrosc. **32**, 67 (2003).
[20] S. Koljenovic, T. Bakker Schut, A. Vincent, J. Kros, and G. Puppels, Anal. Chem. **77**, 7958 (2005).
[21] S. Sasic, D. Clark, J. Mitchell, and M. Snowden, Analyst **130**, 1530 (2005).
[22] S. Sasic, D. Clark, J. Mitchell, and M. Snowden, Analyst **129**, 1001 (2004).
[23] D. F. Steele, P. M. Young, R. Price, T. Smith, S. Edge, and D. Lewis, The AAPS Journal, **6**, Article 32.
[24] N. L. Jestel, J. M. Shaver, and M. D. Morris, Appl. Spectrosc. Volume **52**, 64 (1998).
[25] S. Nakashima, J. Phys.: Condens. Matter **16**, S25 (2004).
[26] S. Bernard, O. Beyssac, and K. Benzerara, Appl. Spectrosc. **62**, 1180 (2008).
[27] P. J. Treado and M. P Nelson, in: Handbook of Raman Spectroscopy, edited by I. R. Lewis and H. G. M Edwards, Practical Spectroscopy Series Vol. 28 (Marcel Dekker, Inc., New York, 2001), pp. 191–213.
[28] C. Krafft, S. Sobottka, G. Schackert, and R. Salzer, J. Raman Spectrosc. **37**, 367 (2006).
[29] S. Schlucker, M. D. Schaeberle, S. W. Huffman, and I. W. Levin, Anal. Chem. **75**, 4312 (2003).
[30] J. Hutchings, C. Kendall, N. Shepherd, B. Smith, H. Barr, and N. Stone, Proc. SPIE, Volume 6853, Article number 685305 (2008).
[31] C. A. Hayden and M. D. Morris, Appl. Spectrosc. **50** (6), (1996).
[32] P. Lasch, W. Hansch, D. Naumann, and M. Diem, Biochimica et Biophysica Acta **1688**, 176–186 (2004).
[33] P. Lasch, M. Diem, W. Hansch, and D. Naumann, J. Chemometrics **20**, 209 (2006).
[34] P. J. Treado and M. P Nelson, in: Handbook of Raman Spectroscopy, edited by I. R. Lewis and H. G. M. Edwards, Practical Spectroscopy Series Vol. 28 (Marcel Dekker, Inc., New York, 2001), pp. 213–216.
[35] J. M. Shaver, Chemometrics for Raman Spectroscopy, in: Handbook of Raman Spectroscopy, edited by I. R. Lewis and H. G. M. Edwards, Practical Spectroscopy Series Vol. 28 (Marcel Dekker, Inc., New York, 2001), pp. 292–298.
[36] R. Bhargava, Anal. Bioanal. Chem. **389**, 1155 (2007).

ARTICLE TYPE www.rsc.org/xxxxxx | XXXXXXXX

A Raman mapping study of high grade dysplasia in oesophageal tissue using linear discriminant analysis to evaluate the importance of spatial resolution for histopathology

Joanne Hutchings,[a] Catherine Kendall,[a] Neil Shepherd,[b] Linmarie Ludeman,[b] Hugh Barr[c] and Nicholas Stone*[a]

Received (in XXX, XXX) Xth XXXXXXXXX 200X, Accepted Xth XXXXXXXXX 200X
First published on the web Xth XXXXXXXXX 200X
DOI: 10.1039/b000000x

Surveillance programs to detect pre-cancers in the oesophagus generate large numbers of tissue samples. Rapid Raman mapping has the potential application for automated histopathology, by providing an adjunct to the histopathologist by screening out normal samples. Linear discriminant analysis (LDA) is suggested as a potential chemometric technique for automated classification of Raman tissue maps. This paper investigates the effect of tissue classification based on Raman maps acquired with different lateral spatial resolution using LDA as a means of comparison. Model performances of 94.4% (79.4-99.0% sensitivity and 95.0-99.8% specificity and 93.7% (87.3-99.9% sensitivity and 95.2-100% specificity) were obtained for LDA models generated using 8.4 μm and 2.1 μm step sizes respectively. Initial results suggest that high lateral spatial resolution is not necessarily required for classifying tissue pathologies but the advantage of additional morphological information is advantageous and could facilitate separation of sub tissue groups in the future.

Introduction

Clinical motivation

The current gold standard for diagnosing oesophageal pre-cancers and cancers is endoscopic biopsy followed by histological staining with Haematoxylin and Eosin (H&E). Surveillance programs to detect pre-cancers in the oesophagus generate large numbers of tissues samples which places a strain on histology resources. There are also inadequacies associated with the histopathology diagnosis, namely that the technique is subjective and morphologically based.[1]

Raman spectroscopy is an inelastic scattering technique which effectively provides a biochemical fingerprint that allows the classification of different tissue types and pathologies. Consequently, the technique has the potential to provide automated, objective and reproducible diagnosis of tissue pathologies. Our group and others have shown that the technique is a promising method to distinguish normal, precancerous and cancerous changes in unstained oesophageal tissue using a laboratory based Raman system.[2,3] Applications in other tissues have been reported including the cervix,[4] bronchus,[5] colon,[6] breast,[7] and brain.[8] The technique also has the potential to be used in vivo.[9]The main text of the article should appear here. Headings and subheadings should be formatted using the relevant button from the “Styles” toolbar.

Raman spectral mapping

Raman has been shown previously to separate out 9 pathologies based on multivariate classification models.[2] This paper develops the idea of using the combination of multivariate analytical techniques and rapid Raman spectral mapping as a potential technique for automated histopathology. In previous publications, we have shown that technological advances have reduced Raman mapping times to a level which has made implementation in a clinical environment a future possibility and Raman spectroscopic mapping could potentially be used as an aid to the histopathologist.[10,11] One question which remained unanswered was whether or not the potential additional information gained from high (lateral) spatial resolution Raman mapping would be a useful adjunct for the histopathologist.

Raman has the potential for high lateral spatial resolution mapping (micrometer to sub micron level).[12] However, applications on biological tissue sections have been limited due to the size of these spectral datasets (and mapped areas) due to lengthy overall mapping times.

FT-IR imaging has provided an alternative with biochemical information provided by many studies of biological tissue.[13,14] Other studies have used both Raman and FR-IR as complimentary techniques.[15,16] The spatial resolution of laboratory based FT-IR systems however is difraction limited,[17] and at mid-IR wavelengths this can cause problems with signal to noise in the low wavenumber region of the spectrum with apertures smaller than 10-15μm. Higher lateral spatial resolutions can be achieved with synchrotron sources,[18] and attenuated total reflection (ATR), whereby a high refractive index crystal enables light to contact the sample at relatively smaller spot size. However, there are still issues due to the fact that contact is required between the ATR crystal and the sample over the whole field of interest.

Spatial resolution is considered to be one of the most critical measurement parameters in spectroscopic imaging.[17]

However, an in depth quantification of the lateral spatial resolution is beyond the scope of this paper, but for the purposes of this study it is sufficient to use the step size as a rough indication of the relative lateral spatial resolution that can be achieved. For further information, the reader is referred to the aforementioned publications.

In previous studies by the authors using rapid Raman mapping, the step size was not reduced beyond 7.4μm (approximately the width of the line focused laser line using the x50 objective), due to limitations caused by the dataset size and also to prevent over-sampling. Improvements in programming, software and computer power have since enabled larger datasets to be handled. From one perspective this has increased the total areas which can be mapped and also increased the spatial resolution which could be utilised. The detrimental effects of under-sampling are clear with the possibility of missing an area of focal disease. This paper explores this and demonstrates the potential for mapping with high lateral spatial resolution. The limitation of the system is a 1.1 μm step size using a x50 objective, and since the advantage of StreamLine™ (outlined elsewhere[11]) is greater for smaller step sizes, large datasets (of the order of hundreds of thousands of spectra) can be generated in a practicable time frame.

Many studies have reported the use of principal component analysis (PCA) for Raman imaging purposes. This paper extends the multivariate analysis to include PC fed linear discriminant analysis (LDA), which is not only proposed as a potential multivariate technique for future automation of Raman histopathology, but it is also used as a tool for comparing maps acquired with different mapping parameters. Other multivariate techniques have been used for Raman and IR imaging such as cluster analysis and but the drawback of this is the high computational requirements.[13] Artificial neural networks (ANN) has also been used as a supervised classification method,[19] but comparison of these with LDA is beyond the scope of this paper.

Materials and Methods

Sample collection and preparation

Informed consent was obtained from patients undergoing routine upper gastrointestinal endoscopy and surgical resection. Gloucestershire Local Ethics committee granted ethical approval for this study.

Fresh tissue samples were immediately snap frozen in liquid nitrogen and stored in a -80°C freezer until measurements were carried out. For each sample, a 15 μm frozen section was cut onto a calcium fluoride substrate for Raman spectral mapping. The thickness of the mapping section was chosen to maximise Raman scattered photons from the tissue section (whilst not taking the section beyond 1-2 cells thick). A contiguous 7 μm section was obtained and stained with H&E for diagnosis by an expert gastrointestinal registry pathologist. The diagnosis was verified on the mapped section H&E (on CaF) by a second histopathologist. Regions of connective tissue (smooth muscle (SM) and fibrous connective tissue (FCT)), normal squamous (NSq), Barrett's (BO), low grade dysplasia (LGD), high grade dysplasia (HGD) and adenocarcinoma (Ad) were identified. Biopsy samples are typically 1-2 mm in diameter.

Mapped samples were also stained with H&E following Raman mapping to enable better correlation with morphological features.

Two samples from two different patients have been mapped in this study.

Raman spectral measurement

Raman maps were acquired using a customised Renishaw Raman System 1000 spectrometer with StreamLine technology (Renishaw Plc. Wotton-under-Edge, Gloucestershire, UK). In brief, the system comprises an NIR diode laser (830nm), a Leica microscope with a Leica x50 (NA 0.5) long working distance objective was used to focus (line focussed) and collect the Raman scattered photons. A metal oxide edge filter was used to remove the elastically scattered light and a grating with 300 lines/mm was used to disperse the inelastically scattered light which was measured with a deep depletion charged coupled device (CCD) detector.

An initial rapid pre-scan was carried out using a crude step size (26.4μm) and short acquisition time (0.5s). Further maps were acquired with step size of 8.4, 4.2 and 2.1μm with a 15 s acquisition time (to achieve spectra with good signal to noise ratio). It was decided that it was optimum to generate the tissue classification model using good quality spectra.

Data Analysis

Cosmic rays were removed by interpolating between the data points either side of the cosmic ray peak. Saturated spectra were also removed. Subsequently each map dataset was normalised and mean-centred. Principal component analysis (PCA) was carried out in Matlab using the PLS toolbox (Eigenvector Technologies, Manson, Washington, USA). Any remaining cosmic rays which were still evident were in the PC loads were blanked out, removed the calculation and PCs re-generated. Pseudocolour PC score maps were then plotted. The pixels of the Raman map were colour coded with the upper and lower extremes of the PC scores and those pixels falling into the central range of the scores were left transparent to enable the images to be overlaid. This represented the pixels/spectra with the most significant contributions from the positive and negative aspects of the PC loads, respectively. The corresponding PC loads were colour coded accordingly to enable correlation of biochemical constituents from peaks within the PC loads with morphological information from the pseudocolour PC score image.

To compare the different step size maps, PC fed LDA was carried out (using the first 10 PCs). Spectra were classified as either calcium fluoride (CaF_2), tissue border (TB), high grade dysplasia (HGD), fibrous connective tissue (FCT) and luminescence (Lum). For the remaining spectra, for which their grouping was ambiguous (either due to the fact that there

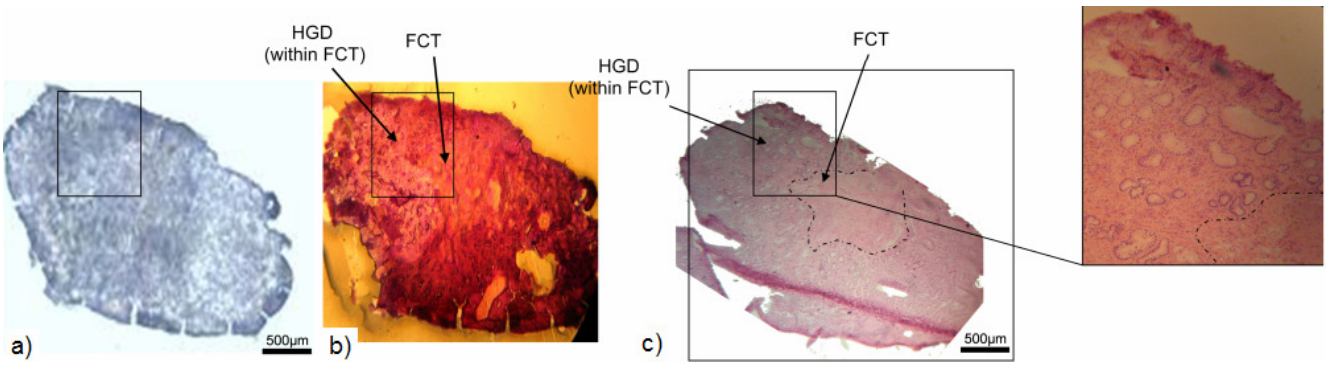

Fig. 1 Sample 1 a) White light image and mapped area b) mapped tissue section stained with H&E (on CaF_2) c) contiguous 7μm H&E stained section

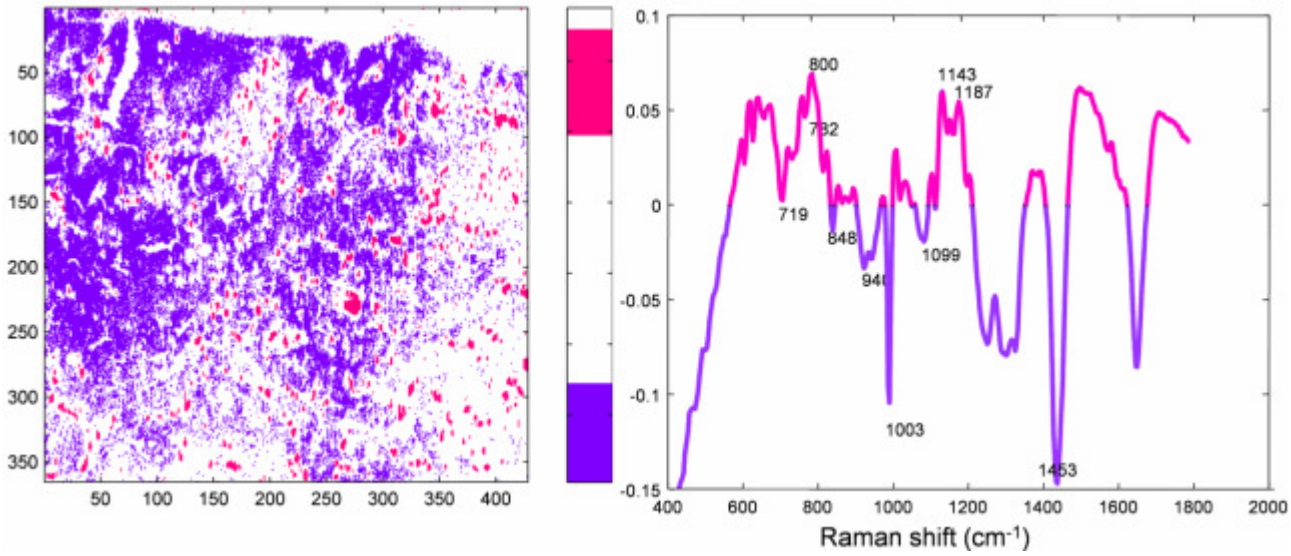

Fig. 2 Example of how PC images are overlaid. (psuedocolour PC 2 scores image and corresponding PC load for the 2.1 μm map)

is not a distinct boundary between tissue or the spectra found to have overlapping PC load contributions) were classed as unknown.

Two PC fed LDA models were generated for each map. The first with the unknown group included as a separate group to investigate misclassifications within the LDA. For the second model, the unknown group was excluded from the model and subsequently projected onto the classification model as an independent test set.

As a first step toward automated histopathology, bulk tissue discrimination was tested i.e. discrimination between connective tissue and glandular (HGD) tissue. In the future separation of further sub tissue types may be possible.

Results

Principal component imaging

The results from one sample (Sample 1) is presented in detail, with the results from a second (Sample 2) sample added to demonstrate the technique can be used to identify other pathology groups. Figure 1 shows the white light montage image of Sample 1, acquired using a x2.5 objective. The small box indicates the region containing high grade dysplasia (HGD) and fibrous connective tissue (FCT) which was mapped repeatedly. It was noted that the regions between the HGD glands were also FCT. The H&E stained CaF_2 image (i.e. the mapped tissue section) and contiguous section stained with H&E for histology purposes are also shown.

Figure 2 shows PC2 as an example of a psuedocolour PC score images and corresponding PC load. The extremes of the colour bar represented by a single colour, with the central portion remaining transparent. This allows the PC images to be overlaid, as shown in Figure 3, in which PCs 1-5 are shown overlaid with corresponding PC loads colour coded accordingly.

The biochemical information contained within the PC loads is shown to be similar (for the two maps acquired with 8.4 and 2.1 μm). Although the two different regions of tissue can be identified in both maps, it is much easier to identify morphological structure in the smaller step size map as glandular features and this further supports the presence of HGD.

Linear discriminant analysis (LDA)

Initially, six group LDA models were generated (see Table 1 for detailed). For the 8.4 μm map, the overall training

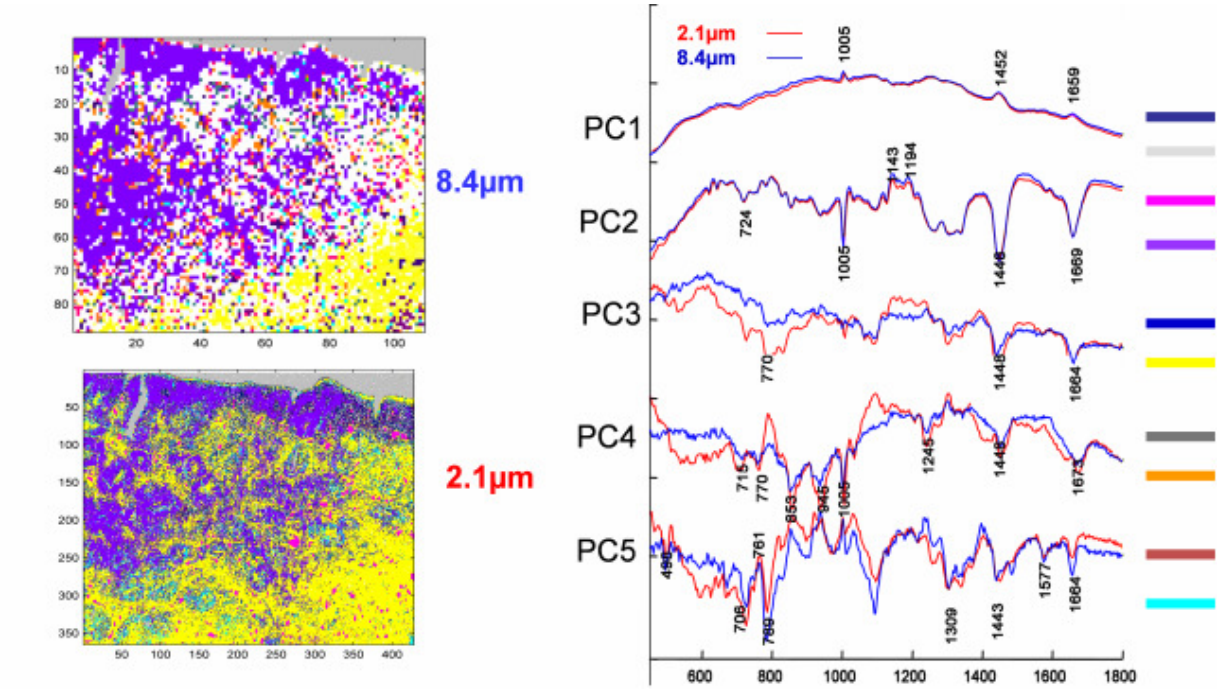

Fig.3 Pseudocolour PC score images overlaid for the 8.4 µm and the 2.1 µm step size map. PC loads are shown with corresponding colour coding

Table 1 Classification performance of the training (including the 'unknown' group) dataset of the LDA model (8.4 µm and 2.1 µm step sizes, 15s acquisition time)

		CaF_2	TB	FCT	HGD	Lum	Unknown	% correctly classified
8.4 µm	CaF_2	354	27	0	0	0	0	94.4
	TB	62	111	3	0	0	13	82.7
	FCT	0	0	920	1	0	79	99.3
	HGD	1	67	234	2608	0	752	88.0
	Lum	0	1	13	0	140	13	96.3
	Unknown	7	185	796	544	6	2655	71.7
2.1 µm	CaF_2	5713	371	0	0	0	0	93.9
	TB	150	1386	13	0	0	1	89.4
	FCT	0	3	5145	0	0	252	95.3
	HGD	0	41	2952	52864	424	14322	74.9
	Lum	0	3	0	0	4070	0	99.9
	Unknown	2100	1528	13533	14152	5046	32151	46.9

performance of the LDA model was 70.1% although the overall performance is degraded by the large number of misclassifications in the 'unknown' group (see data analysis for explanation) and also the CaF_2 group. Sensitivity and specificity were 58.7–92.9% and 88.1–99.9% respectively. The number of spectra within each group and the percentage correctly classified by the LDA model is summarised in Table 1.

For the 2.1 µm map, the overall training performance of the LDA model was 64.9%. As with the 8.4 µm model, the majority of the misclassified samples are from the 'unknown' group (as expected) which consequently skews the overall performance value. There are also misclassification of FCT spectra (predicted as 'unknown's) and some discrepancies with CaF_2 and tissue border. Table 1 shows the number of spectra within each LDA classification group. Sensitivity and specificity were 46.9 - 99.9% and 83.4 - 98.9% respectively, but again, these values are skewed by the large number of misclassifications within the 'unknown' group.

Figure 4 illustrates the model performance spatially to provide further insight. Figures 4a and 4c identify spectra (pixels) which are misclassified by the LDA model for the 8.4 µm and 2.1 µm maps respectively. In Figures 4b and 4d, these misclassified spectra (pixels) are colour coded according to the group in which the LDA model classifies them for the 8.4 µm and 2.1 µm maps respectively. This additional spatial information provides an insight into whether or not the LDA prediction is sensible which can potentially provide useful information regarding initial group.

In the 2.1 µm map PC image (Figure 3), the FCT appears to extend into regions between HGD glands. In the LDA pathology classification, although over 25000 spectra are

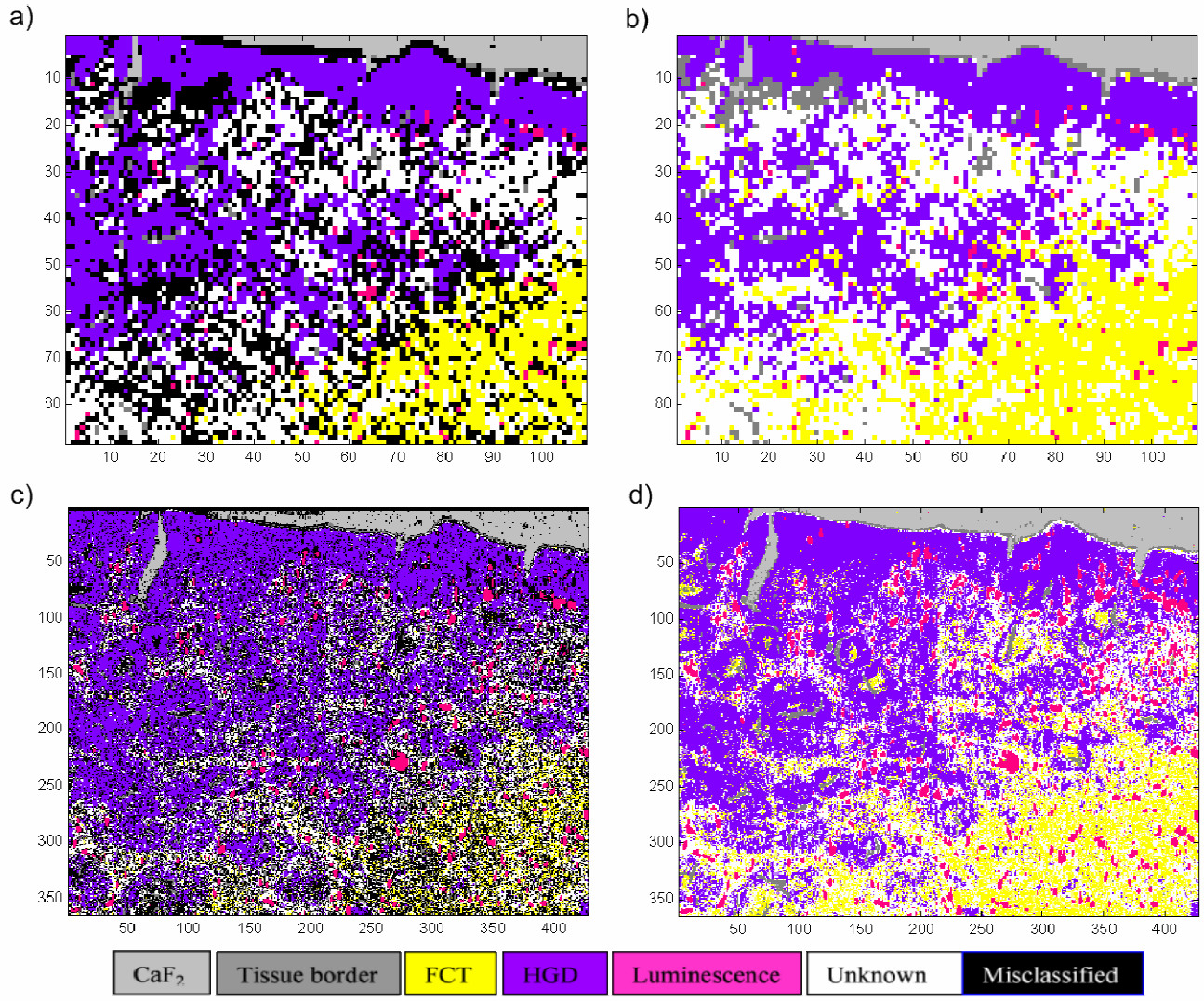

Fig. 4 Pseudocolour LDA pathology images for the 8.4 µm (a-b) and 2.1 µm (c-d) maps colour coded with pathology. Figures 4a) and 4c) show the locations of the misclassified spectra/pixels, whilst Figures 4b) and 4d) show the predicted pathology according to the LDA model for each of the misclassified spectra.

misclassified as FCT, this is not within the inter glandular regions which appear to remain as "unknown" (white) and luminescence. This is likely to be due to initial choice of LDA groups for which the LDA process would try to separate the groups, but it could possibly be due to a biochemical difference in the FCT depending on the location of the tissue. This issue is addressed in the next section in which the 'unknown' group is extracted from the model and used as an independent test set. There is also the possibility there is spatial and spectral averaging of nearby HGD and further work is required to verify the actual spatial resolution achieved with rapid Raman mapping systems.

The central portions of the glands appear to be misclassified as FCT, but again it is likely that a separate group would be required to account for these gland lumens which are likely to contain glandular mucin secretions etc. from the goblet cells. This may be an important classification for diagnosis, but further work is required.

Luminescence also appears to be very structural within the tissue. Mostly, within the regions of FCT. The location of the luminescence within the FCT is more evident with the small step size map, highlighting the potential importance of high lateral spatial resolution mapping.

Including spectra acquired from calcium fluoride in the mean centring process is possibly not the optimum method, but it was concluded that calcium fluoride/other substrate would be an important constituent with any model since any discrepancy with substrate impurities may lead to misclassifications. This may also be important for regions of thin tissue which may contain contributions from both substrate and tissue. Further work will be needed to investigate this.

Projecting the 'unknown' group as an independent test set Figure 5 shows the pseudocolour LDA image for the model generated excluding the 'unknown' group as a separate test set and later projecting these onto the model. Both the 8.4 µm and

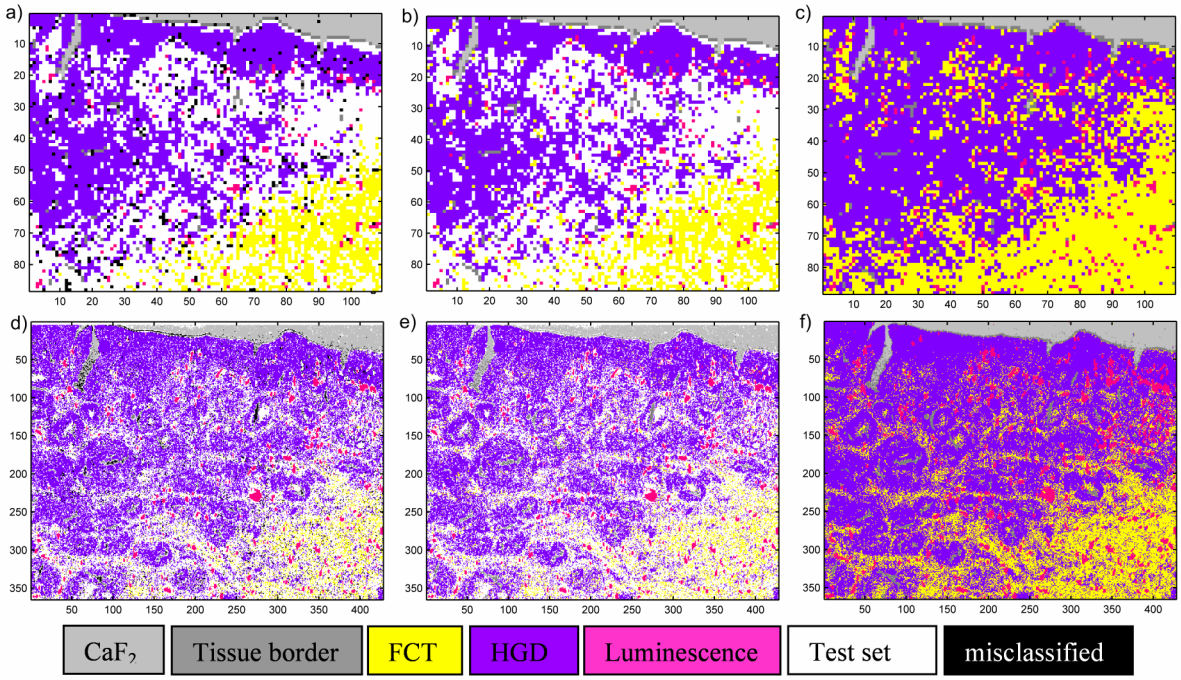

Fig. 5 Projection of the test set onto the LDA model (generated excluding the 'unknown' group which was kept aside as a test set) for the 8.4 µm (a-c) and 2.1 µm (d-f) maps. Figures a) and d) illustrate tissue classification of the training set by the LDA model according to tissue pathology colour code with misclassifications as black pixels and the test set identified as white pixels. Figures b) and e) illustrate the predicted classification group of the misclassified spectra within the training set according to the LDA model and figure c) and f) show the projected test set results according to the classification by the LDA model. Caption

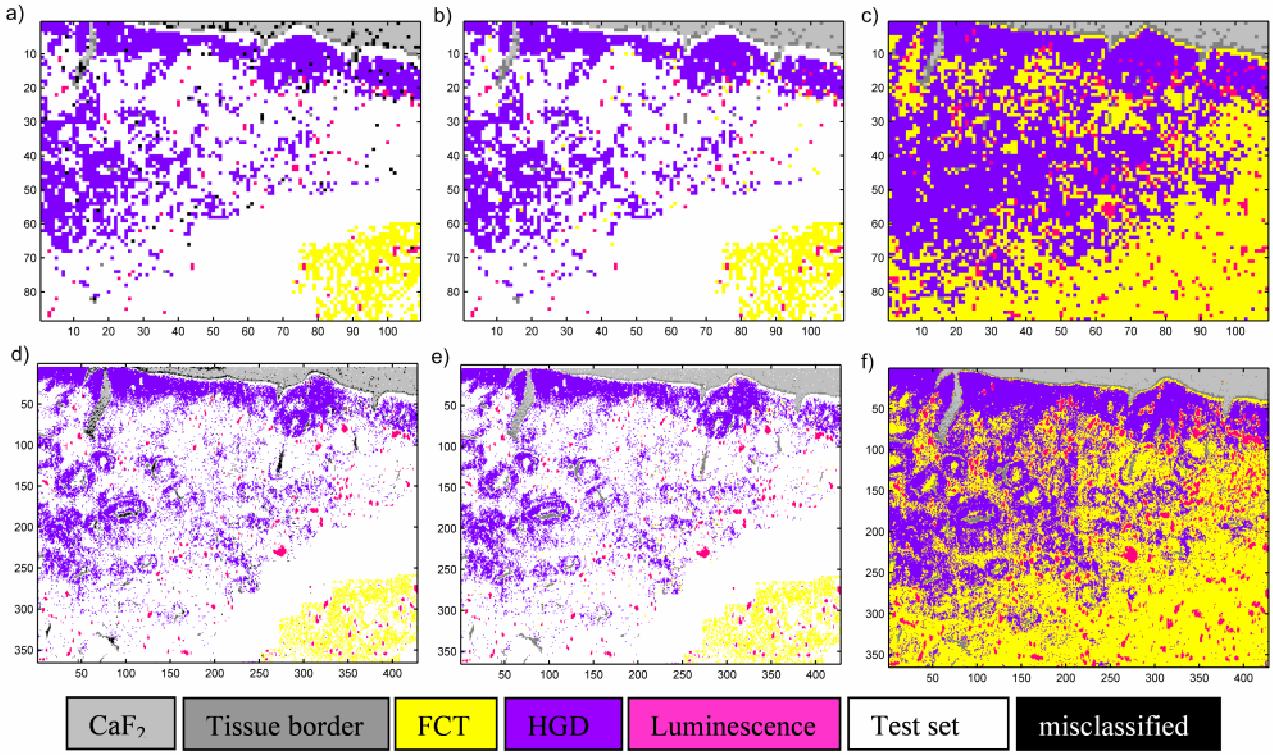

Fig. 6 Projection of the larger test set (to account for tissue margins) onto the LDA model (generated excluding the test set) for the 8.4 µm (a-c) and 2.1 µm (d-f) maps. Figures a) and d) illustrate tissue classification by the LDA model according to tissue pathology colour code with misclassifications as black pixels with the test set identified as white pixels. Figures b) and e) illustrate the predicted classification group of the misclassified spectra according to the LDA model and figure c) and f) show the projected test set results according to the classification by the LDA model.

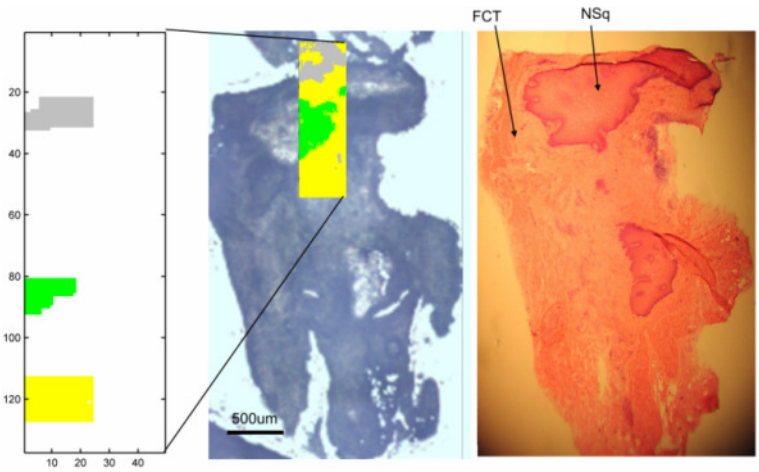

Fig. 7 LDA model trained with a small region of normal squamous (green) fibrous connective tissue (yellow) and CaF_2 (grey).

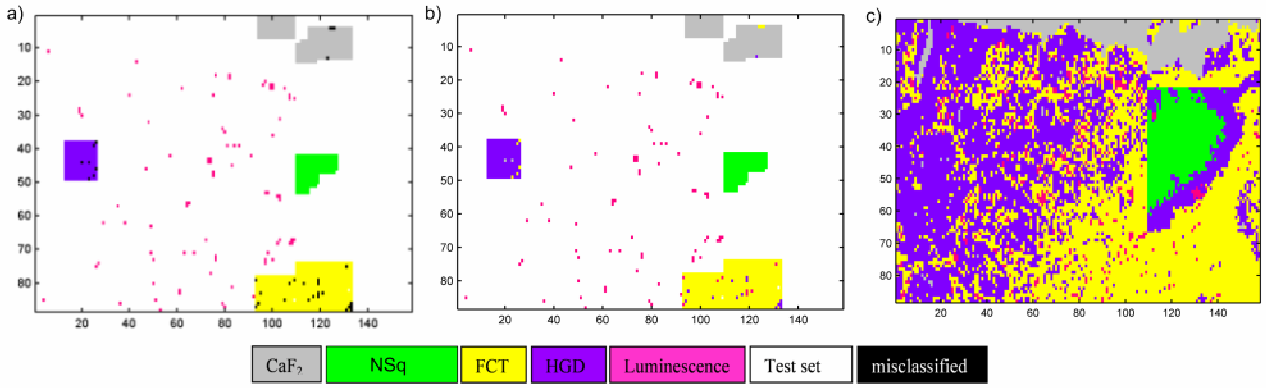

Fig. 8 Classification model generated based on a training set taken from two samples (Sample 1 and 2 combined to one map) Sample 1 is the sample containing HGD and FCT and sample 2 contains FCT and NSq. a) shows the training set performance with correctly classified spectra classified according to pathology colour code with misclassified spectra highlighted as black pixels, b) illustrates the groups into which the misclassified spectra are predicted and c) illustrate the predicted classification for the test dataset (previously white pixels)

the 2.1 µm maps are comparable, with spectral predictions consistent with morphological features and location in the image.

The overall performance of the training set models improved from 70.1% to 94.4% (79.4-99.0% sensitivity and 95.0-99.8% specificity) for the 8.4 µm step size model and from 64.9% to 93.7% (87.3-99.9% sensitivity and 95.2-100% specificity) when the unknown group was excluded as the test dataset.

As with previous LDA models which included the 'unknown' group, FCT appears to extend in between the glandular features of the HGD. Previously, this was only 2.1µm map, but using in Figure 5 this is also evident in the 8.4 µm map. The centre of some of the glandular HGD structures are classified as FCT (especially evident in the small step size map). This is likely to be incorrect, and as discussed previously, a further group, tentatively attributed to mucin, may need to be added to the model to account for such regions. However, there is also the possibility that FCT, which is relatively transparent, is misclassified as tissue border since it comprises a lesser contribution from tissue spectral features and more CaF_2 due to spectral mixing with substrate spectra. Further work is needed to investigate the origins of these misclassifications.

The projection model also suggests that regions of luminescence are within FCT surrounds the regions of luminescence.

To further investigate the projection of test dataset (and the presence of luminescence within the FCT), the LDA model was recalculated with fewer spectra in the training dataset. An additional 'unknown' margin around each pathology group was defined and allocated to the test dataset i.e. each region of luminescence was surrounded by a region of test set pixels/spectra. Similarly, the region between HGD and FCT was blocked out and allocated to the test set. Results indicate more strongly that luminescence is structural within the FCT. Pixels at the edge of the tissue and also the gland centres are also projected to be FCT, reiterating the need for an additional group within the model. The results are shown in Figure 6.

It is evident that reducing the training dataset does not

impact on the ability to project the test set onto the classification model.

An example of normal squamous epithelium

The above process was repeated on a map (15s acquisition and 8,4 µm step size) of Sample 2 (containing NSq and FCT), but in this case the size of the training dataset was reducted further still.

Results are shown in brief in Figure 7, which shows the white light image and pseudo colour LDA image, the training set (defined by relatively small, but distinct regions of Nsq, FCT and CaF_2), H&E of the contigous section and also the mapped section stained with H&E (on CaF_2).

Combined maps

To further test the LDA projection of map data onto the tissue classification model, the two maps (15s acquisition time and 8.4 µm step size), were combined to form a large map containing HGD (sample 1), FCT (from samples 1 and 2), NSq (sample 2) and CaF_2 (from samples 1 and 2). The entire map was then reanalysed to investigate the feasibility of extending this to multiple tissue maps and tissue types.

Again, small, distinct regions of each tissue type (NSq, FCT and HGD) and also CaF_2 were defined as the training dataset, with the test set defined as the remainder of the dataset (Figure 8a and b). Figure 8c shows the classification for each spectra/pixel for the test dataset projected onto the LDA model generated using the training dataset.

The overall accuracy of the training set classification model was 97.5% (98.8–100% sensitivity and 95.8 – 100% specificity).

In general, projection of the test dataset (Figure 8c) agrees with histology diagnosis (Figure 1 - sample 1, Figure 7 – sample 2), however there are discrepancies which occur within the basement membrane region of the NSq (i.e the border between NSq and FCT) which gets projected as HGD. Regions of luminscence, not previosuly identified in Sample 2 are also detected within the FCT.

Admittedly this is not a full model containing all pathology groups, nor was the region of basement membrane included in the training dataset, but conclusions can still be drawn from this, since the result indicates that classification could be occurring based on biochemical signature of cell nuclei which are rapidly proliferating and densely packed in both HGD and also basement membrane regions. Furthermore, this indicates that misclassifications are highly likely if sub tissue classes are not included into the training dataset, and perhaps suggests that spatial averaging may be advantageous to avoid such issues. In the future, work is required to determine optimum number of pathology groups required for tissue diagnosis.

Discussions

This study has shown that high lateral spatial resolution mapping is not necessarily needed for histology diagnosis. However, high lateral spatial resolution mapping does have advantages. There is the advantage of acquiring a large number of spectra which is amplified for reduced step sizes due to the square relation between step size and number of pixels. The additional spatial and spectral biochemical information could potentially facilitate the separation of more pathology groups.

LDA is a well known and accepted technique for spectral classification, and this paper has shown its potential application in Raman imaging for histology diagnosis. Further work is still required to investigate the extent to which the technique can be exploited with respect to automated imaging and also larger sample numbers need to be included in the model. The projection of an unknown dataset onto the model allows validation of the model to a degree but using spatial information relating to morphology, but rigorous validation and testing will still be required when further samples are added to the model. Nevertheless, this is an important step in the move towards clinical implementation of vibrational spectroscopy for automated histopathology.

Although LDA model performance provides a relatively arbitrary method of comparison, it allows a quick and easy method of comparing the maps acquired with different parameters. PC fed LDA models are also able to cope with low signal to noise spectra, where other techniques fail. Since it is well known that the initial group choices are an important factor with LDA models, the initial grouping may play a large part in the model performance, but as the groups were the same in both the 8.4 and 2.1 µm models, it enabled direct comparison of the two maps. The use of this 'unknown' group as an independent test set to validate the model provided confirmation that the classification was reasonable, supported further by spatial information relating to morphology.

There is also the potential, as discussed above that the small step size map may identify more subtle biochemical features which may account for the larger number of misclassified spectra within the small (2.1 µm) step size map. As a result, the model performance for the small step size map could potentially be significantly better if the initial groupings are chosen more carefully. However, mapping at even smaller step sizes, may also induce greater heterogeneity in the maps, even from cells of the same pathology (due to sampling different parts of the cell within each image pixel).

It remains a question of how much separation is required for a specific pathology application. For example if the ultimate aim is only to separate out normal from abnormal then relatively crude spatial averaging and poor signal to noise spectra could be used however if the aim is to separate out tissue types, pre-cancers, cancers and even predict prognosis then more subtle biochemical features may need to be resolved. It will also depend on whether the histopathologist is confident in spectroscopic diagnosis without the additional morphological information represented in the form of a pseudocolour histology image. If not then crude step size maps could potentially provide a rapid and automated method of pathology diagnosis. Taking this idea to the extreme, it may be sufficient simply to use an ex vivo probe or collect a spectrum with a low magnification objective, averaged over a large area of tissue, although work will need to be carried out to verify the minimum level of signal mixing required to detect pathology changes. A

combination of modalities may be advantageous, for example FTIR for mapping the entire sample, followed by high lateral spatial resolution Raman mapping of regions of interest. The complementary nature of FTIR and Raman is being explored by many groups including ours.[16, 17]

The extent to which we attempt to separate out pathology information is a question of clinical need which, ultimately, will need to be answered by the histopathologist.

Conclusions

In conclusion, rapid Raman spectral mapping with LDA discrimination has the potential for automated tissue classification in the future. Greater numbers of samples and patients, to cover the likely variability in the population of interest, with detailed histopathology will need to be included into the training model. It also appears from this initial study that high lateral spatial resolution mapping is not essential for clinical diagnosis of bulk tissue types, but may have advantages in the future for discriminating further tissue types.

This study has shown that LDA projection imaging process can be potentially be applied to multiple samples making it a suitable technique for automated histopathology in the future. Futhermore, spatial information from visually representing LDA classification as psuedocolour images can provide insightful information which will help to explain misclassifications based on morphological features which is not possible from traditional scatter plot representation.

Acknowledgements

The authors would like to thank Christine Braun for her assistance with sample preparation. Financial support from Institute of Physics and Engineering in Medicine (IPEM) Research Training Fellowship, Royal Society Dorothy Hodgkin Research Fellowship and National Institute of Health Research Clinical Fellowship is gratefully acknowledged.

Notes and references

[a*] *Biophotonics Research Group, Leadon House, Gloucester Royal Hospital, Great Western Road, Gloucester, Gloucestershire, GL1 3NN, UK. Fax: 00448454 225485; Tel: 0044845 225486; E-mail: n.stone@medical-research-centre.com*

[b] *Department of Histopathology*

[c]. *Department of Surgery*

† See DOI: 10.1039/b000000x/

1 R. Haggitt, *Human Pathology*, 1994, **25**, 982;

2 C. Kendall, N. Stone, N. Shepherd, K. Geboes, B Warren, R. Bennett and H. Barr, *Journal of Pathology*, 2003, **200**, 602;

3 G. Shetty, C. Kendall, N. Shepherd, N. Stone and H. Barr, British Journal of Cancer, 2006, **200**, 602;.

4 A. Robichaux-Viehoever, E. Kanter, H. Shappell, D. Bill-Heimer, H. Jones III, A. Mahadevan-Jansen, *Applied Spectroscopy*, 2007, **61**, 986;

5 S. Koljenovic, T. Bakker Schut, J. van Meerbeeck, A. Maat, S. Burgers, P. Zondervan, J. Kros and G. Puppels, *Journal of Biomedical Optics*, 2004, **9**, 1187;

6 J. Taylor, C. Kendall, N. Stone and T. Cook. *British Journal of Surgery*, 2007, **94**, 6;

7 J. Kneipp, *Vibrational Spectroscopy*, 2003, **32**, 67;

8 S. Koljenovic, T. Bakker Schut, A. Vincent, J. Kros and G. Puppels, *Anal. Chem.,* 2005, **77**, 7958;

9 E.B. Hanlon, R. Manoharan, T-W. Koo, K.E. Shafer, J.T. Motz, M. Fitzmaurice, J.R. Kramer, I. Itzkan, R.R. Dasari and M.S. Feld, *Phys. Med. Biol.*, 200, **45** R1;

10 J. Hutchings, C. Kendall, N. Shepherd, B. Smith, H. Barr and N. Stone, *P Soc Photo-Opt Ins (SPIE)*, 2008, 6853A;

11 J. Hutchings, C. Kendall, B. Smith, N. Shepherd, H. Barr and N. Stone N, accepted in *J. Biophotonics* November 2008

12 S. Schlucker, M. Schaeberle, S. Huffman and I.W. Levin, *Anal. Chem*, 2003, **75**, 4312;

13 P. Lasch, W. Haensch, D. Naumann and M. Diem, *Biochimica et Biophysica Acta,* 2004, 1688, 176;

14 B. Bird, M. Miljkovic, M.J. Romeo, J. Smith, N. Stone, M.W. George and M. Diem, *BMC Clinical Pathology,* 2008, **200**, 8;

15 C. Krafft, D. Codrich, G. Pelizzo, and V, Sergo, *Vibrational Spectroscopy*, 2008, **46**, 141;

16 M. Isabelle, N. Stone, H. Barr, M. Vipond, N. Shepherd and K. Rogers, *Spectroscopy: An International Journal,* 2008, *22*, 97;

17 P. Lasch and D. Naumann, *Biochimica et Biophysica Acta* , 2006, **1758,** 814;

18 L. Miller and P. Duma, *Biochimica et Biophysica Acta*, 2006, **1758**, 846;

19 P. Lasch, M. Diem, W. Hänsch, D. N.aumann, *Journal of Chemometrics*, 2006, **20**(5), 209;